To the Graduate Council:

I am submitting herewith a dissertation written by Russell Paul Wong entitled "The Effects of Calcification on the Structure and Properties of Biomedical Polyurethanes." I have examined the final copy of this dissertation for form and content and recommend that it be accepted in partial fulfillment of the requirements for the degree of Doctor of Philosophy, with a major in Polymer Engineering

Roberto S. Benson, Major Professor

We have read this dissertation
and recommend its acceptance:

Accepted for the Council:

Vice Provost
and Dean of The Graduate School

THE EFFECTS OF CALCIFICATION ON THE STRUCTURE AND PROPERTIES OF BIOMEDICAL POLYURETHANES

A Dissertation

Presented for the

Doctor of Philosophy

Degree

The University of Tennessee, Knoxville

Russell Paul Wong

May 1991

Copyright © Russell Paul Wong, 1991
All rights reserved

ACKNOWLEDGEMENTS

The author expresses his sincere appreciation to the faculty and staff of the Department of Materials Science and Engineering at the University of Tennessee, Knoxville for their assistance and support during his studies. To each of the people who directly or indirectly aided in the completion of this work, he will always be grateful.

The author expresses his gratitude to his fellow students who have assisted him in countless ways. He thanks the fellow members of his group, Mr. Paul (H.J.) Kim, Ms. Xinli Liu, and Mr. Steve (M.W.) Lee for their help in conducting experiments. In particular, he thanks Ms. Trishna Ray-Chaudhuri for her assistance in all facets of life in graduate school.

The author particularly acknowledges the technical assistance of the machine and electronics shops. The machining and design work of Mr. Larry Smith and Mr. Doug Fielding was exceptional. The instrumentation and electronics assistance of Mr. Ron Johnson and Mr. Gregory Jones was outstanding. Mr. Johnson's expertise was extremely helpful in software development and operation of the Fourier transform infrared spectrometer.

The author also wishes to express his special appreciation to the members of his advisory committee, Drs. J.E. Spruiell, P.J. Phillips and J.D. Landes for their helpful suggestions in all phases of this project.

They served the author as a fine definition of an advisory committee.

The author acknowledges a grant from the Whitaker Foundation who provided financial support for this research. He is also grateful for the support of the Center for Materials Processing of the University of Tennessee. The contributions of Biomer from Ethicon, Inc. and Pellethane from Dow Chemical Co. are also acknowledged. The polymers were contributed exclusively for this study.

The author sends his love to his parents and brother for their kind encouragement throughout his years in graduate school.

Finally, the author thanks his advisor, teacher, and friend, Dr. Roberto S. Benson for helping the author shape his research and professional goals. Dr. Benson's advice helped to focus this research. His encouragement taught one to be persistent when faced with challenges. His friendship will always be most treasured.

ABSTRACT

The formation of calcium salt deposits has been shown to cause premature failure of biomedical implant devices in several clinical cases. Although several mechanistic theories exist regarding the causes of calcification, it was necessary to consider the nature of the interaction of the calcium salts with the implant material to eventually understand how to prevent calcification.

This study examined the effects of blending calcium chloride into the biomedical polyurethanes Biomer (Ethicon, Inc.) and Pellethane (Dow Chemical Co.) on tensile mechanical and molecular orientation properties. In addition, the pure polyurethanes were exposed to an aqueous solution of calcium chloride in physiological concentrations. Fracture properties and molecular orientation associated with the fracture phenomenon were measured using FTIR dichroism and a specially designed tensile stretching device. This device allowed for simultaneous measurements of stress, strain and orientation.

The results of this study indicated that calcium chloride salts caused reductions in fracture toughness and stress distributions surrounding cracks. The effects were attributed to salt saturation of the soft segment matrix with calcium chloride followed by disruption of the domain structure at higher salt concentrations. The uptake of

calcium chloride from aqueous solution showed changes in mechanical properties which were mediated by the soft segment matrix.

In mechanical strain orientation studies, the domain structure of Biomer appeared to have its long axis in a direction perpendicular to the chain axes. Upon drawing, the domains oriented in the draw direction, causing the chain axes to display a negative orientation. Pellethane domains did not display this behavior because of less extensive hydrogen bonding in the domains.

TABLE OF CONTENTS

CHAPTER PAGE

1. INTRODUCTION....1

2. LITERATURE SURVEY....11

2.1. Biomedical Polymers....12

2.2. Polyurethanes....16
2.2.1. Chemical Structure....16
2.2.2. Micro Structure....17
2.2.3. Metal Ion Complexation....23
2.2.4. Mechanical Properties....30

2.3. Mechanical Properties of Elastomers....38
2.3.1. Ideal Rubber Elasticity....39
2.3.2. Load-Extension Behavior....42
2.3.3. Structure of the Crack Tip....48
2.3.4. Environmental Effects and Fracture Properties....50

2.4. Theory of Fracture....53
2.4.1. Linear Elastic Fracture....58
2.4.2. Nonlinear Elastic Fracture....64
2.4.2.1. Experimental Determination of J for Polymers....82
2.4.2.2. Measurements of J for Polymers....87

2.5. Infrared Spectroscopy....94
2.5.1. Interpretation of Infrared Spectra....95
2.5.2. Infrared Dichroism and Orientation Functions....100

2.6. Literature Conclusions....108

3. EXPERIMENTAL....110

3.1. Materials....110

3.2. Instrumentation and Equipment....112
3.2.1. The Fourier Transform Infrared Spectrometer....112
3.2.2. Tensile Mechanical Testing Instrument....113
3.2.2.1. Hardware....113
3.2.2.2. Software....116

3.3. Data Reduction and Analysis....120
3.3.1. Infrared Spectroscopy....120
3.3.2. Fracture Property Measurements....124

CHAPTER PAGE

3.4. Experimental Methods.....126
3.4.1. Fracture Property Changes with Calcium Chelation.....126
3.4.2. Molecular Orientation of Polyurethanes.....126
3.4.3. Orientation of the Crack Tip Field.....127
3.4.4. Changes in Mechanical Properties with Calcium Uptake.....129

4. RESULTS.....131

4.1. Fracture Property Changes with Calcium Chelation.....131

4.2. Molecular Orientation of Polyurethanes.....150

4.3. Orientation of the Crack Tip Fields.....162

4.4. Changes in Mechanical Properties with Calcium Uptake.....204

5. DISCUSSION.....227

5.1. Fracture Testing.....227
5.1.1. Fracture Property Changes with Calcium Chelation.....229
5.1.1. Summary of Fracture Testing.....244

5.2. Molecular Orientation of Polyurethanes.....246

5.3. Orientation of the Crack Tip Fields.....260

5.4. Summary of Polyurethane-Calcium Chloride Blend Studies.....271

5.5. Polyurethane Uptake of $CaCl_2$.....272

6. CONCLUSIONS.....291

7. FURTHER WORK.....295

LIST OF REFERENCES.....298

APPENDICES.....307

APPENDIX A. SOFTWARE MACROS DEVELOPED FOR THE DIGILAB 3240-SPC MICROCOMPUTER.....308

CHAPTER PAGE

APPENDIX B. SOURCE CODE OF PASCAL PROGRAMS FOR TENSILE TESTING.....309

APPENDIX C. MECHANICAL DRAWINGS USED TO MACHINE VERTICAL POSITIONING AND CLAMPS FOR STEP MOTOR LINEAR ACTUATORS.....324

VITA.....331

LIST OF FIGURES

FIGURE PAGE

1. Hydrogen bonding in adjacent polyurethane hard segments.[39].....19

2. Domain-matrix morphology.....20

3. The crown ether, 18-crown-6.[54].....24

4. Loss tangent versus temperature measured from dynamic mechanical analysis at 11 Hz for various calcium concentrations.[8].....27

5. Infrared spectra of polyurethanes for various calcium concentrations.[8].....28

6. Stress versus time for initial loads of 1.1, 1.3, 1.75, and 2.55 MPa for Pellethane.....33

7. Tensile stress-strain curves for Pellethane blended with urea.[14].....36

8. Tensile stress-strain curves for Biomer blended with urea.[14].....37

9. Theoretical and experimental stress-strain curves for simple elongation of gum-vulcanized rubber from Treloar.[65].....43

10. Load-extension curves for a typical polymer tested at four temperatures showing different regions of mechanical behavior. (a) Brittle fracture, (b) ductile failure, (c) necking and cold-drawing, and (d) homogeneous deformation (quasi-rubber-like behavior). From Ward.[66].....45

11. Blunted crack tip with craze.....49

12. Effects of environment on crack propagation. (a) Sample immersed in stabilizing fluid requiring greater crack growth to store same energy as (b) sample in atmosphere.....52

13. Stress concentration distributions visualized in terms of lines of force (similar to fluid flow about an obstacle).....56

FIGURE PAGE

14. Center cracked notch panel under uniaxial load.[80].....60

15. Planar conditions to determine for stress distribution about a crack tip.[80].....63

16. Definition of the J integral along path ABCDEF, where T is the traction on path segment, ds.[114].....68

17. J contour around contour Γ at a crack tip. From Paris.[17].....70

18. Calculated non-linear elastic crack tip stress model (a) Approximate location of yield boundary and geometrical shape of constant stress near the crack tip. (b) Yield boundary; detail very near the crack tip. From Rice and Rosengren.[18].....74

19. Experimental principal stress map (isoclinics shown as broken lines) at (a) T = 0.16 kg/cm and (b) T = 0.65 kg/cm. From Andrews.[82].....75

20. Andrews' proposed method for measuring craze energy.[115].....81

21. (a) Load-displacement curves of cracked specimens having various crack lengths. (b) stored strain energy versus crack length for a given displacement l, and (c) notation used in (a) and (b). From Landes and Begley.[86].....84

22. Simple extension specimen with a cut in one edge. Dotted line shows the integration path chosen to evaluate the J-integral. From Oh.[89].....88

23. (a) Effect of temperature on Jc, Kc, dJ/d(a) and m for LDPE. (b) Effect of temperature on Jc, Kc, dJ/d(a) and m for LLDPE. From Hashemi and Williams.[93].....90

24. Diagram of the interaction of an oscillating electric field (light) with a vibrating dipole. From Koenig.[118].....96

25. Commonly observed infrared vibrations.....98

FIGURE PAGE

26. Model for infrared dichroism for uniaxially oriented systems.[98,99].....102

27. Calculation of dichroic ratio, D, from infrared absorbance spectrum.....106

28. Chemical structure of polyurethane elastomers used in this study.....111

29. Layout of infrared microscope and tensile testing equipment.....114

30. Flow diagram of software written for tensile test control.....118

31. Flow diagram of software written for analysis of infrared spectra. Initializing the program and sort data.....122

32. Flow diagram of software written for analysis of infrared spectra. Executing a comparison search and termination.....123

33. Map indicating positions analyzed for stress induced orientation using infrared micro-dichroism.....128

34. Stress versus strain data for pure Biomer films with varying crack growth to failure.....132

35. Strain energy to failure versus initial crack length for pure Biomer.....134

36. Strain energy to failure versus crack growth to failure for pure Biomer.....135

37. Stress versus strain data for Biomer blended with 1% wt. calcium chloride with varying crack growth to failure.....136

38. Strain energy to failure versus initial crack length for Biomer blended with 1% wt. calcium chloride.....137

39. Strain energy to failure versus crack growth to failure for Biomer blended with 1% wt. calcium chloride.....138

FIGURE PAGE

40. Stress versus strain data for Biomer blended with 5% wt. calcium chloride with varying crack growth to failure.....139

41. Strain energy to failure versus initial crack length for Biomer blended with 5% wt. calcium chloride.....140

42. Strain energy to failure versus crack growth to failure for Biomer blended with 5% wt. calcium chloride.....141

43. Stress versus strain data for Biomer blended with 10% wt. calcium chloride with varying crack growth to failure.....142

44. Strain energy to failure versus initial crack length for Biomer blended with 10% wt. calcium chloride.....143

45. Strain energy to failure versus crack growth to failure for Biomer blended with 5% wt. calcium chloride.....144

46. Stress versus strain data for pure Pellethane films with varying crack growth to failure.....146

47. Strain energy to failure versus initial crack length for pure Pellethane.....147

48. Strain energy to failure versus crack growth to failure for pure Pellethane.....148

49. Stress versus strain data for Pellethane blended with 1% wt. calcium chloride with varying crack growth to failure.....149

50. Strain energy to failure versus initial crack length for Pellethane blended with 1% wt. calcium chloride.....151

51. Strain energy to failure versus crack growth to failure for Pellethane blended with 1% wt. calcium chloride.....152

52. Stress versus strain data for Pellethane blended with 5% wt. calcium chloride with varying crack growth to failure.....153

FIGURE PAGE

53. Strain energy to failure versus initial crack length for Pellethane blended with 5% wt. calcium chloride.....154

54. Strain energy to failure versus crack growth to failure for Pellethane blended with 5% wt. calcium chloride.....155

55. Stress versus strain data for Pellethane blended with 10% wt. calcium chloride with varying crack growth to failure.....156

56. Strain energy to failure versus initial crack length for Pellethane blended with 10% wt. calcium chloride.....157

57. Strain energy to failure versus crack growth to failure for Pellethane blended with 10% wt. calcium chloride.....158

58. Mid-infrared absorbance spectrum of Biomer.....159

59. Mid-infrared absorbance spectrum of Pellethane.....160

60. Polarized infrared absorbance spectra for pure Biomer at various strains; N-H stretch.....163

61. Polarized infrared absorbance spectra for Biomer blended with 1% calcium chloride; at various strains; N-H stretch.....164

62. Polarized infrared absorbance spectra for Biomer blended with 5% calcium chloride; at various strains; N-H stretch.....165

63. Polarized infrared absorbance spectra for Biomer blended with 10% calcium chloride; at various strains; N-H stretch.....166

64. Polarized infrared absorbance spectra for pure Pellethane at various strains; N-H stretch.....167

65. Polarized infrared absorbance spectra for Pellethane blended with 1% calcium chloride; at various strains; N-H stretch.....168

FIGURE PAGE

66. Polarized infrared absorbance spectra for Pellethane blended with 5% calcium chloride; at various strains; N-H stretch.....169

67. Polarized infrared absorbance spectra for Pellethane blended with 10% calcium chloride; at various strains; N-H stretch.....170

68. Polarized infrared absorbance spectra for pure Biomer at various strains; C-H stretch.....171

69. Polarized infrared absorbance spectra for Biomer blended with 1% calcium chloride; at various strains; C-H stretch.....172

70. Polarized infrared absorbance spectra for Biomer blended with 5% calcium chloride; at various strains; C-H stretch.....173

71. Polarized infrared absorbance spectra for Biomer blended with 10% calcium chloride; at various strains; C-H stretch.....174

72. Polarized infrared absorbance spectra for pure Pellethane at various strains; C-H stretch.....175

73. Polarized infrared absorbance spectra for Pellethane blended with 1% calcium chloride; at various strains; C-H stretch.....176

74. Polarized infrared absorbance spectra for Pellethane blended with 5% calcium chloride; at various strains; C-H stretch.....177

75. Polarized infrared absorbance spectra for Pellethane blended with 10% calcium chloride; at various strains; C-H stretch.....178

76. Stress relaxation with time for crack tip orientation studies of Biomer blended with calcium chloride.....180

77. Stress relaxation with time for crack tip orientation studies of Pellethane blended with calcium chloride.....181

FIGURE PAGE

78. Polarized infrared absorbance spectra for pure Biomer surrounding the crack tip; N-H stretch.....183

79. Polarized infrared absorbance spectra for pure Biomer surrounding the crack tip; C=O stretch.....184

80. Polarized infrared absorbance spectra for Biomer blended with 1% wt. calcium chloride; surrounding the crack tip; N-H stretch.....185

81. Polarized infrared absorbance spectra for Biomer blended with 1% wt. calcium chloride; surrounding the crack tip; C=O stretch.....186

82. Polarized infrared absorbance spectra for Biomer blended with 5% wt. calcium chloride; surrounding the crack tip; N-H stretch.....187

83. Polarized infrared absorbance spectra for Biomer blended with 5% wt. calcium chloride; surrounding the crack tip; C=O stretch.....188

84. Polarized infrared absorbance spectra for Biomer blended with 10% wt. calcium chloride; surrounding the crack tip; N-H stretch.....189

85. Polarized infrared absorbance spectra for Biomer blended with 10% wt. calcium chloride; surrounding the crack tip; C=O stretch.....190

86. Polarized infrared absorbance spectra for pure Pellethane surrounding the crack tip; N-H stretch.....191

87. Polarized infrared absorbance spectra for pure Pellethane surrounding the crack tip; C=O stretch.....193

88. Polarized infrared absorbance spectra for Pellethane blended with 1% wt. calcium chloride; surrounding the crack tip; N-H stretch.....194

FIGURE PAGE

89. Polarized infrared absorbance spectra for Pellethane blended with 1% wt. calcium chloride; surrounding the crack tip; C=O stretch.....195

90. Polarized infrared absorbance spectra for Pellethane blended with 5% wt. calcium chloride; surrounding the crack tip; N-H stretch.....196

91. Polarized infrared absorbance spectra for Pellethane blended with 5% wt. calcium chloride; surrounding the crack tip; C=O stretch.....197

92. Polarized infrared absorbance spectra for Pellethane blended with 10% wt. calcium chloride; surrounding the crack tip; N-H stretch.....198

93. Polarized infrared absorbance spectra for Pellethane blended with 10% wt. calcium chloride; surrounding the crack tip; C=O stretch.....199

94. Polarized infrared absorbance spectra for pure Biomer surrounding the crack tip; C-H stretch.....200

95. Polarized infrared absorbance spectra for Biomer blended with 1% wt. calcium chloride; surrounding the crack tip; C-H stretch.....201

96. Polarized infrared absorbance spectra for Biomer blended with 5% wt. calcium chloride; surrounding the crack tip; C-H stretch.....202

97. Polarized infrared absorbance spectra for Biomer blended with 10% wt. calcium chloride; surrounding the crack tip; C-H stretch.....203

98. Polarized infrared absorbance spectra for pure Pellethane surrounding the crack tip; C-H stretch.....205

FIGURE PAGE

99. Polarized infrared absorbance spectra for Pellethane blended with 1% wt. calcium chloride; surrounding the crack tip; C-H stretch.....206

100. Polarized infrared absorbance spectra for Pellethane blended with 5% wt. calcium chloride; surrounding the crack tip; C-H stretch.....207

101. Polarized infrared absorbance spectra for Pellethane blended with 10% wt. calcium chloride; surrounding the crack tip; C-H stretch.....208

102. Stress versus strain data for Biomer after 30 days in aqueous calcium chloride solution with varying crack growth to failure.....209

103. Strain energy to failure versus initial crack length for Biomer after 30 days in aqueous calcium chloride solution.....210

104. Strain energy to failure versus crack growth to failure for Biomer after 30 days in aqueous calcium chloride solution.....211

105. Stress versus strain data for Pellethane after 30 days in aqueous calcium chloride solution with varying crack growth to failure.....212

106. Strain energy to failure versus initial crack length for Pellethane after 30 days in aqueous calcium chloride solution.....213

107. Strain energy to failure versus crack growth to failure for Pellethane after 30 days in aqueous calcium chloride solution.....214

108. Polarized infrared absorbance spectra for Biomer after 30 days in aqueous calcium chloride solution, at various strains; N-H stretch.....216

109. Polarized infrared absorbance spectra for Biomer after 30 days in aqueous calcium chloride solution, at various strains; C-H stretch.....217

FIGURE PAGE

110. Polarized infrared absorbance spectra for Pellethane after 30 days in aqueous calcium chloride solution, at various strains; N-H stretch.....218

111. Polarized infrared absorbance spectra for Pellethane after 30 days in aqueous calcium chloride solution, at various strains; C-H stretch.....219

112. Polarized infrared absorbance spectra for Biomer after 30 days in aqueous calcium chloride solution, surrounding the crack tip; N-H stretch.....220

113. Polarized infrared absorbance spectra for Biomer after 30 days in aqueous calcium chloride solution, surrounding the crack tip; C=O stretch.....221

114. Polarized infrared absorbance spectra for Pellethane after 30 days in aqueous calcium chloride solution, surrounding the crack tip; N-H stretch.....222

115. Polarized infrared absorbance spectra for Pellethane after 30 days in aqueous calcium chloride solution, surrounding the crack tip; C=O stretch.....223

116. Polarized infrared absorbance spectra for Biomer after 30 days in aqueous calcium chloride solution, surrounding the crack tip; C-H stretch.....224

117. Polarized infrared absorbance spectra for Pellethane after 30 days in aqueous calcium chloride solution, surrounding the crack tip; C-H stretch.....225

118. Normalized strain energy to failure versus initial crack length for pure Biomer.....230

119. Normalized strain energy to failure versus initial crack length for Biomer blended with 1% wt. calcium chloride.....232

FIGURE PAGE

120. Normalized strain energy to failure versus initial crack length for Biomer blended with 5% wt. calcium chloride.....233

121. Normalized strain energy to failure versus initial crack length for Biomer blended with 10% wt. calcium chloride.....235

122. Comparison plot of normalized strain energy to failure versus initial crack length for Biomer blended with various calcium chloride concentrations.....237

123. Normalized strain energy to failure versus initial crack length for pure Pellethane.....238

124. Normalized strain energy to failure versus initial crack length for Pellethane blended with 1% wt. calcium chloride.....240

125. Normalized strain energy to failure versus initial crack length for Pellethane blended with 5% wt. calcium chloride.....241

126. Normalized strain energy to failure versus initial crack length for Pellethane blended with 10% wt. calcium chloride.....242

127. Comparison plot of normalized strain energy to failure versus initial crack length for Pellethane blended with various calcium chloride concentrations.....243

128. The N-H stretch vibration. High frequency (shorter period) vibration corresponds to free N-H; low frequency (longer period) vibration corresponds to hydrogen bonded N-H.....247

129. Change in N-H orientation function with strain for various calcium chloride concentrations in Biomer.....250

130. Change in N-H orientation function with strain for various calcium chloride concentrations in Pellethane.....251

FIGURE PAGE

131. Schematic depiction of hard segment domains for Biomer. Disruption of hydrogen bonding due to calcium chloride.....253

132. Schematic depiction of hard segment domains for Pellethane. Disruption of hydrogen bonding due to calcium chloride.....254

133. Change in C-H orientation function with strain for various calcium chloride concentrations in Biomer.....255

134. Change in C-H orientation function with strain for various calcium chloride concentrations in Pellethane.....256

135. Maximum stress at fixed strain for various calcium chloride concentrations in Biomer.....258

136. Maximum stress at fixed strain for various calcium chloride concentrations in Pellethane.....259

137. Crack tip N-H orientation maps of Biomer for various calcium chloride concentrations.....262

138. Crack tip C=O orientation maps of Biomer for various calcium chloride concentrations.....263

139. Crack tip N-H orientation maps of Pellethane for various calcium chloride concentrations.....264

140. Crack tip C=O orientation maps of Pellethane for various calcium chloride concentrations.....265

141. Crack tip C-H orientation maps of Biomer for various calcium chloride concentrations.....266

142. Crack tip C-H orientation maps of Pellethane for various calcium chloride concentrations.....267

143. Comparison plot of normalized strain energy to failure versus initial crack length for pure Biomer and the Biomer uptake study.....274

FIGURE PAGE

144. Comparison plot of normalized strain energy to failure versus initial crack length for pure Pellethane and the Pellethane uptake study.....275

145. Change in N-H orientation function with strain for Biomer and the Biomer uptake study.....276

146. Change in C-H orientation function with strain for Biomer and the Biomer uptake study.....278

147. Change in N-H orientation function with strain for Pellethane and the Pellethane uptake study.....279

148. Change in C-H orientation function with strain for Pellethane and the Pellethane uptake study.....280

149. Maximum stress at fixed strain for Biomer and the Biomer uptake study.....281

150. Maximum stress at fixed strain for Pellethane and the Pellethane uptake study.....282

151. Crack tip N-H orientation maps for Biomer and the Biomer uptake study.....284

152. Crack tip C=O orientation maps for Biomer and the Biomer uptake study.....285

153. Crack tip N-H orientation maps for Pellethane and the Pellethane uptake study.....286

154. Crack tip C=O orientation maps for Pellethane and the Pellethane uptake study.....287

155. Crack tip C-H orientation maps for Biomer and the Biomer uptake study.....289

156. Crack tip C-H orientation maps for Pellethane and the Pellethane uptake study.....290

1. INTRODUCTION

The growth of polymers for biomedical applications has been rapid in recent decades. With the approval of the United States Food and Drug Administration, (FDA), blood contact polymers have been applied in different configurations with little knowledge of long term degradation properties. The FDA primarily examines the effects of the polymer on the body with less emphasis on the effects the body has on the polymer. This is a matter which only recently has been addressed in the literature.

Polyurethane copolymers are most commonly used when contact with blood is required. Their relative biocompatibility with blood components and stability in the harsh physiological environment of the human body has been a great advantage in numerous cases. The versatility of these materials for this and other biomedical applications is attributed to the ease with which their properties can be tailored for specific applications in the body. Although the material has been successful in several short term applications, only limited success has been achieved in long term applications where blood contact is continuous. These applications include the total artificial heart, ventricular assist devices, artificial blood vessels, cardiac pacemaker housings and artificial kidney dialysis.[1-5] Failure of these materials

in many cases was attributed to changes in mechanical properties which led to fracture, leakage, or compliance mismatch.

In the wake of several literature reports of premature failure of Pellethane in long term implantable devices, the polymer manufacturer, Dow Chemical Company, has removed Pellethane from the long term medical implant market as of April 1, 1992.[6,7] Dow further recommended that manufacturers seek other sources of polyurethanes for their applications because the cost of long term technical support was not in line with the volume of the material demand. Pellethane will continue to be available only for short term implantable applications.

There continues to be a strong industrial demand for a long term implantable polyurethane material. A replacement material will have to demonstrate long term resistance to cracking and calcification to receive acceptance by the medical device manufacturers as well as the FDA. The present goal of biomaterial science is to isolate the causes of mechanical failure and select replacement materials for the future.

Because of the complexity of polymer degradation processes in the body, an ideal study would identify all degradation processes before selecting candidate materials. Such a task, however, is well beyond the scope of any single study. This study specifically examined the

material properties in an attempt to understand the calcium interaction with polyurethane. It was restricted to in vitro studies of aqueous calcium salt solutions to simplify the analysis of the polymer-environment interaction.

Another goal of this study was to examine a possible mechanism of calcification of polyurethane in the body. Calcification is one of the major causes of a loss of elastic properties. Calcification in the body can be initiated by:[8,9]

1. Fragments of devitalized cells.[10]

2. Proteins and lipids at accumulation sites in surface defects and subsurface voids.[11]

3. Sites of stress concentration due to alteration of local domain structure.[11]

4. Accumulation by the polymer following a metal ion chelation with the polyether segment of the polyurethane.[12,13]

In addition to examining each cause individually, one should not ignore the interdependence of the effects. For example, sites of high stress may accelerate cell fragmentation. Loading and unloading cycles may increase surface and subsurface void formation. Protein deposition in subsurface regions generally results in calcium deposition which may be enhanced by metal ion chelation. As a result, the mechanism of calcification in

polyurethanes is not at all clear. Other complications of the physiological environment include the productivity of osteoblasts (calcium phosphate mineral producing cells) in the body as well as the health, age and sex of the patient.

One should not ignore other blood components either. Studies by Warner et al.[8] showed that blending urea and ionic salts into polymers results in an increase in elastic modulus, causing embrittlement and a general reduction in the compliance of the material. These significant changes were observed when urea and ionic salts were introduced in concentrations well below those found in blood. The same study concluded that the salt interactions occurred by way of a chelation mechanism. Evidence of chelation was observed by infrared spectroscopy, which had been used to observe other complexations mechanisms.[8,14] The study also employed differential scanning calorimetry (DSC) and dynamic mechanical analysis to observe shifts in the glass transition temperature with chelation. The shifts were directly attributed to the formation of the complexes.

From the viewpoint of polymer science, it is necessary to understand the structure of the polymer molecules as they interact physically and chemically in the body. The body's effects on chain stiffness, crystallinity and morphology must be accounted for,

particularly as they relate to elastic properties. Unfortunately there continues to be much disagreement on the physical structure of polyurethanes and their copolymers prior to implantation. There is some agreement, however, on the effects of different processing variables. The areas which were relevant to this study are reviewed in section 2.2.

As an engineering phenomenon, calcification appears to be a chemically mediated physiological response to mechanical stress. This is similar to the restructuring of bone by the body in response to stress. In biomechanics, this concept is known as Wolff's law. Wolff's law proposes that bone material is deposited in response to stresses applied over a long term. If the stresses are removed, the bone material is removed by the body. The mechanism by which bone cells sense stress is not well understood. Mechanical stresses lead to unknown structural/conformational changes in polyurethanes which enhance calcium deposition.

In a recent study, Golomb and Wagner[15] attempted to model polyurethane calcification by an in vitro experiment. They introduced pores into Pellethane by extracting pre-embedded polyethylene glycol from solvent cast films. The films were then introduced to a metastable aqueous calcium phosphate solution for periods of 2, 4, and 6 weeks. The study showed that calcium

deposits increased with prolonged incubation periods and repeated incubation.

Two important points were made by Golomb and Wagner in their conclusions. The porosity of the material directly affected calcium uptake by polyurethane. One might expect this result since porosity is directly related to surface area available for mass transfer. The second point suggested that this model may be useful as a pre-screening method for the evaluation of biomedical polymers to calcify. This suggestion must be viewed critically. By use of a metastable calcium phosphate solution Golomb and Wagner have overemphasized the chemistry of calcification. In fact, a metastable solution or supersaturated solution will precipitate calcium phosphate upon the slightest disruption. One might therefore expect that any surface placed in the metastable solution will have calcium phosphate deposits with time.

In vivo studies of polyurethane leaflet heart valves showed that calcification is the major cause of premature failure. Lo et al.[16] evaluated a tricuspid leaflet valve in the mitral position of eight growing Jersey calves. Upon autopsy, the cause of death of the calves was due to valve dysfunction. Massive calcium deposits formed on the moving parts of the valves (stents). The deposits restricted their ability to prevent back flow of blood.

The authors noted that although all blood contact surfaces were covered with the same polyurethane, calcification occurred only on the flexing polyurethane stents. This and other similar studies leads one to believe that calcification is a form of a response to the stress distribution in the polyurethane.

Stress risers have been correlated to the calcification process. Two of the aforementioned calcification mechanisms are directly related to the formation of voids or surface imperfections during processing. The introduction of random structural flaws causes local stresses to exceed the design stresses during use. The phenomenon is known as stress intensification. Generally, material stresses are at a maximum in the vicinity of the void and decrease with distance from it. The stresses depend on the shape of the void, the applied stresses, and the elastic properties of the material. At critical stresses, voids may grow or coalesce into larger structural cracks, with the greatest stress intensification near the crack tip. It is clear, therefore, that stress intensification combined with the calcification effects of the physiological environment will have an adverse effect on the structural integrity of the implant material.

Under the appropriate environmental and mechanical conditions, stresses of the crack tip fields can exceed

the material yield stress without crack propagation. In this study, regions of plastic deformation were observed in the form of stress induced molecular orientation in the direction of the local stress. Micro-FTIR dichroism was used to map orientation with displacement from the crack tip. By analogy, this was referred to as an "orientation field". It was hypothesized that there is a critical orientation above which crack growth will initiate.

Upon determination of the geometry of an orientation field, it was desirable to compare it to the shape and position of the corresponding stress and strain field. Although a direct measure of stresses to map the crack tip stress field was not possible, the stresses have been modeled using fundamental fracture theories.[17-19] Furthermore, bulk sample stress-strain-orientation curves were generated which were used to correlate local stresses and strains from measured orientation functions.

Stress and strain intensity fields have been modeled in the literature assuming both linear and nonlinear elasticity. The more prominent of these theories and their applicability are discussed in the literature review. Because of the inherently nonlinear (rubber) elastic behavior of polyurethanes and other rubbery type materials, it was assumed that a nonlinear elastic model stress field was most appropriate. At small deformations, however, a linear elastic model may provide a good first

approximation. The choice of a model will also depend on the molecular structure changes induced by the environmental effects.

To summarize the main points of this discussion:

(1) Calcium present in blood has been shown to degrade the mechanical properties of polyurethanes used for long term implant materials. The complexation of calcium salts with polyurethane copolymers can be detected by infrared spectroscopy, DSC, and dynamic mechanical testing.

(2) Stress intensification in a material is determined by the geometry, applied stresses, and the elastic properties (linear and nonlinear) of the material. Because the elastic properties are adversely affected by the presence of calcium, it follows that the crack tip stress field and fracture properties will also be determined by the effects of the salt environment.

(3) Stresses surrounding the crack tip may induce molecular orientation in the direction of local stresses. Molecular orientation may be affected by the presence of calcium.

(4) Orientation can be mapped as a function of position with respect to the crack tip and can be referred to as an "orientation field".

(5) The geometry of the orientation field may be related to the geometry of the crack tip stress field as calculated by fracture theories.

2. LITERATURE SURVEY

Recent studies reported in the biomaterials community indicate a tendency of polyurethanes to calcify in the physiological environment. Calcification has led to embrittlement and a loss of mechanical properties. The loss of mechanical properties subsequently led to premature failure through the formation of cracks and fissures in the implant. Little is known about the specific mechanism of these failures, hence it was difficult to hypothesize how to prevent it. It was the purpose of this study to examine one of the possible calcification mechanisms and to determine if it increased the tendency to form cracks in polyurethanes.

Fracture is defined as the formation of new surfaces in a material. A fracture process is any process which stores energy through the formation of new surfaces. This study examined the mechanical formation of cracks in polyurethane and how the presence of calcium ions affected their stability. The first three sections in this review discuss properties which affect the formation of cracks. Because this study was motivated by the properties of polymers in the physiological environment, the survey begins with a general discussion of the biomedical properties of polymers with a discussion of their use in the body. This is followed by a review of the material

properties of biomedical polyurethane elastomers. (The material properties which are relevant to this study are discussed in detail; references are provided for the less relevant properties.) The mechanical properties of polyurethanes were included because it is essential to understand the properties on the molecular level. A review of the mechanical properties of elastomers was included because of the dependence of fracture on elastic properties.

Fracture properties of materials are reviewed with a particular emphasis on the nonlinear elastic behavior of elastomers. Simple methods for determining the tearing energy of rubber based on nonlinear elastic fracture mechanics are discussed. Tearing energy data can also be used to calculate stresses and strains surrounding the crack tip. The crack tip stress fields were correlated with molecular orientation measurements.

Orientation functions obtained by infrared dichroism were reviewed with examples of their use with polyurethane copolymers. It was believed that micro infrared dichroism was a useful tool for measuring orientation on the microscopic level or for collecting localized orientation measurements.

2.1. Biomedical Polymers

The ideal replacement material for a failed organ is the same material as the tissues of the original organ

without the medical defects. This is the goal of much research in genetic engineering and cell cloning. The best solutions currently require the use of synthetic polymers such as polyurethanes. Polyurethanes have demonstrated a few cases of long term compatibility. The loss of biocompatibility takes place as the body's immune system initiates a foreign body response. This usually follows a series of steps within the body:[20,21]

1. Implantation of the material followed immediately by protein deposits. The protein deposits attract cellular organisms to the site.
2. If the foreign body is small, encapsulation of the foreign body by giant cells and a membrane of fibrous tissue to isolate it from the rest of the body. Typically, artificial organs are too large to be encapsulated by the body.
3. Release of degradative enzymes by the cellular organisms on to the implant material surface in an attempt to destroy the foreign body. If encapsulation does not take place, the body is exposed to harmful degradative enzymes leading to inflammation.
4. If encapsulation does take place, a gradual migration of the capsule out of the body.

For long term implant materials, it is desirable to interrupt the foreign body response at step 1.

Analysis of biological rejection is also a matter that is under current investigation. The problem is commonly addressed from a biological approach but rarely as a polymer material problem. The focus of much of the literature, therefore, is on the biological effects with little emphasis on the structure and properties of the polymer.

As noted in the introduction, polyurethanes are the most commonly selected polymers for biomedical implant materials requiring blood contact. They can be synthesized with a wide variety of mechanical properties by varying the type and/or molecular weight of the flexible polyether segment, hence they may be synthesized for use as hard tissue replacements as well as soft tissue replacements. In addition to favorable mechanical properties, polyurethanes are relatively inert to the major blood components which include water, proteins, enzymes, oxygen, and blood cells.

Other polymers have been used for specific applications of blood contact. They often lack chemical stability or the proper mechanical properties to be used in other applications, however. As an example, poly(ethylene terephthalate) (PET) used for large diameter blood vessels is successful because an initial deposition of blood proteins along the inner surface forms a protective layer, the pseudoneointima, which isolates the

polymer from blood flow. Small diameter PET blood vessels (such as those which might be used for coronary arteries) also form pseudoneointima which completely impede flow within a few days of implantation, rendering the implant useless.

Although the mechanism of polyurethane biocompatibility is poorly understood, some general observations can be made. A common observation is that the chemical repeat groups which form polyurethanes occur naturally in the body in the form of proteins, amino acids and other biopolymers. The close chemical compatibility effectively slows the body's immune response toward rejection of the implant.

Hung et al.[3] showed that there was a direct correlation between thermal properties of polyurethane and the results of biocompatibility tests. It was believed that the magnitude of the biological response was highly correlated with the thermal and physical properties of the polymer. Tissue cultures, hemolysis, intramuscular implant, intradermal irritation, systemic toxicity, and histopathological rating, and the cumulative biological response index were shown to correlate also with kinetic parameters derived from thermogravimetry.

In more detailed studies, other interactions have been shown to affect biocompatibility. Because blood flow is naturally non-turbulent, turbulent flow can result in

the destruction of blood cells. The immune system recognizes cellular debris resulting in a foreign body response. Through a series of complex biochemical interactions, it detects abnormal solid and fluid mechanical properties. Blood flow is generally pulsatile, reversible and laminar during a single heartbeat. It is believed that slight changes in the complex flow patterns result in a breakdown of blood cell membranes, the release of intracellular debris and initiation of an immune response toward that debris. Compliance mismatching at the anastomosis between polymers and the tissues result in rapid occlusion of artificial arteries.[22] The occlusion is attributed to an exaggerated wound healing response of the body due to the detection of hemolysis (destruction of red blood cells). Hemolysis was attributed to turbulent flow at the anastomosis of the artificial and natural artery. The interaction of polyurethane with the physiological environment therefore requires mechanical compatibility as well as chemical compatibility. The mechanical properties of an implant material must, therefore, be similar to that of the tissue which it is replacing.

2.2. Polyurethanes

2.2.1. Chemical Structure

Biomedical polyurethanes are synthesized from a diisocyanate (O=C=N-R-N=C=O) and a diol (OH-R'-OH) to form

a polyether based polyurethane. The copolymer is formed in a two step process. The initial reaction is the endcapping reaction of a polyether glycol with a diisocyanate to form a prepolymer. The second reaction is the coupling of the prepolymer with a diol or diamine to form a poly(ether-urethane) or a poly(ether-urethane-urea), respectively. The typical chemical structure of a polyurethane is shown below:

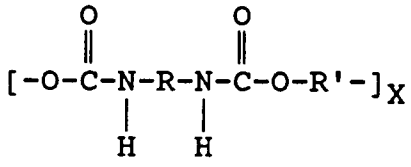

Most biomedical grade polyurethanes are synthesized from a diisocyanate of methylene bis (phenylisocyanate) (MDI) and a 2, 3 or 4 carbon based polyether. The resulting structure is of a rigid (hard) urethane segment copolymerized to a flexible (soft) polyether segment. Increasing the molar ratio of the hard segment molecular weight to the soft segment molecular weight increases the chain stiffness of the resulting copolymer.

2.2.2. Micro Structure

The elastomeric nature of polyurethane requires the polymer to have the form of a crosslinked structure. If the crosslink can be broken and reformed without degradation of the chemical structure, the elastomer can

be easily processed from the melt or solution. Such is the nature of the polyurethane physical crosslinks.

Referring to the preceding section on polyurethane chemical structure, the hard segments urethane groups form the physical crosslinks in the molecule. Hard segments of individual copolyurethane molecules tend to align with adjacent hard segments because hydrogen bonds form between the oxygen atoms, (both C=O and C-O), and the hydrogen of the N-H group.[23-26] A urethane segment tends to be more rigid because of hydrogen bonding with adjacent amide groups, as shown in Figure 1. Because of strong interactions between hard segments and their chemical incompatibility with the soft segments, copolyurethanes tend to form a phase separated, domain-matrix morphology as shown in Figure 2.[27,28] The urethane or urethane-urea (hard) blocks tend to aggregate to form ordered <u>domains</u> which are dispersed in a <u>matrix</u> of amorphous polyether (soft) segments. To process the polyurethane, the hydrogen bonds must be broken by melting or dissolution in a solvent.

The structure of polyurethanes and their copolymers has been reported in the literature, particularly with respect to the unit cell of the crystalline domains. Although there is considerable debate over the crystal structure (hexagonal versus orthorhombic versus triclinic) of polyurethane hard segment domains, there appear to be

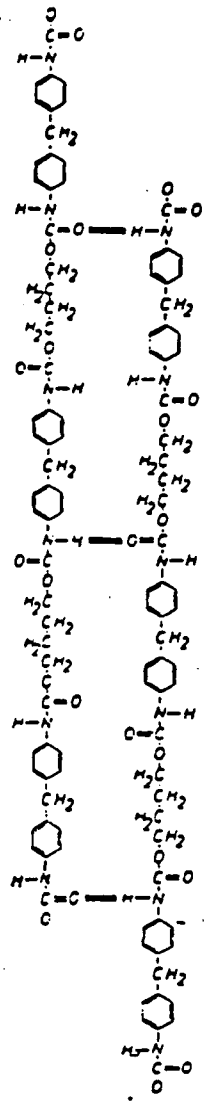

Figure 1: Hydrogen bonding in adjacent polyurethane hard segments.[39]

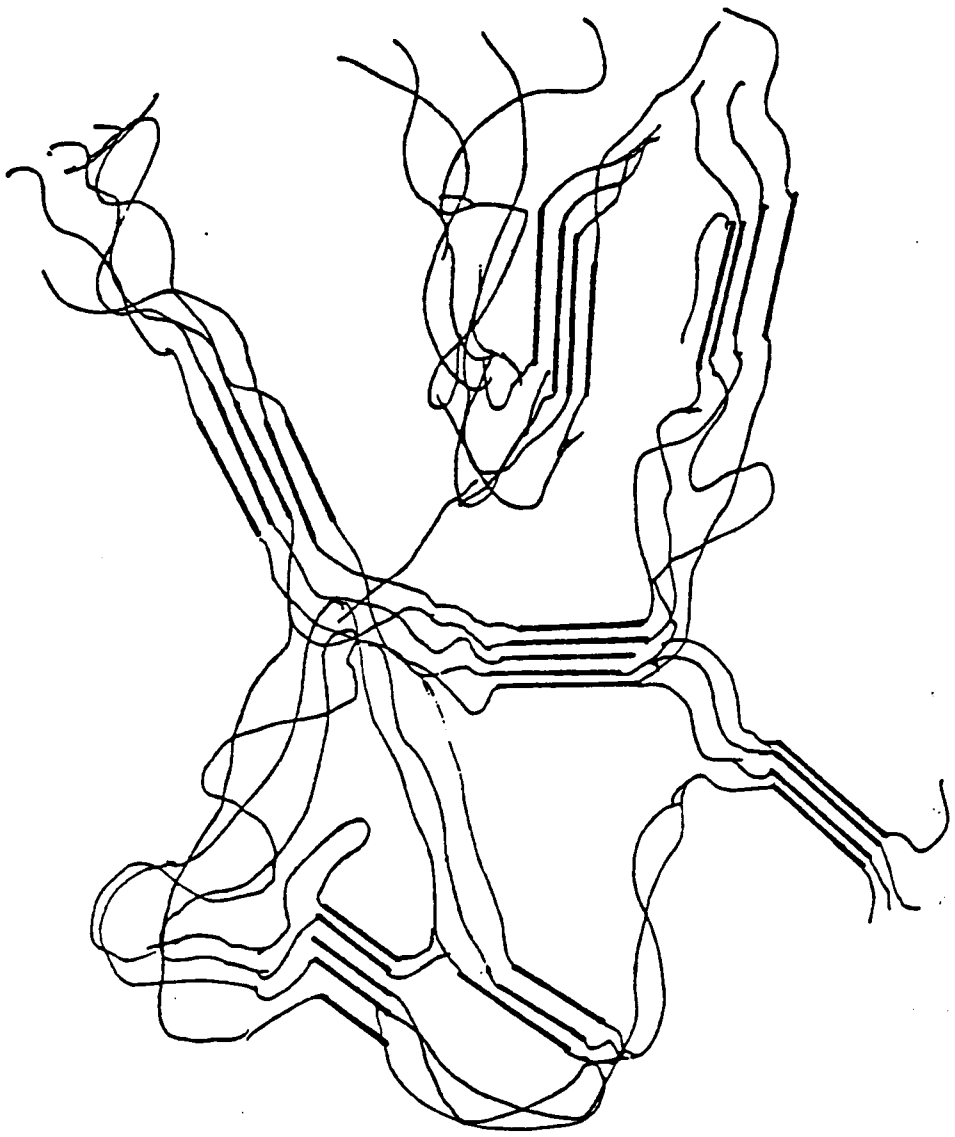

Figure 2: Domain-matrix morphology.

some points of agreement. The effects of energy barriers to rotational freedom, temperature[29-32], the stability of polymer conformations,[33] synthesis method,[34] length and chemical structure of the hard segment,[1,35,36] molecular weight and chemical structure of the soft segment, and the structure of the diisocyanate[23-25,37-41] have been studied as they relate to polyurethane structure.[26,42-50] Studies correlating the structure of polyurethanes with macroscopic properties have also been reported.[29,51]

Polyurethane hard segment domains tend to orient upon drawing, although the unit cell of the crystalline domains remains a subject of controversy. The most recent evidence from wide angle x-ray studies indicates evidence of three unit cell lattices including hexagonal, triclinic, and orthorhombic for MDI based urethane groups.[24,52] Because of uncertainty in the crystalline structure of the hard segments, it is difficult to use WAXD to examine the crystalline orientation of the polymer. The uncertainty also complicates the understanding of biological interactions, particularly with respect to binding of proteins to the polyurethane.

It is generally accepted that the choice of the chain extender, the soft segment chemical structure, and their respective molecular weights will determine the properties of the polyurethane. Furthermore, a low molecular weight hard segment domain will act as a physical crosslink to

give the copolymer a rubber network structure. Previous studies of hydrogen bonding of polyurethane-urea elastomers using infrared dichroism showed that the hydrogen bonded systems were not true network junctions but displayed rubber elastic behavior at small elongations.[53] This concept is acceptable if one considers the high molecular weight polyether group to be "crosslinked" by the hydrogen bonding urethane groups. Because the crosslinking is based on secondary bonding and not primary bonds, these are not true chemically crosslinked systems. Furthermore, the urethane hydrogen bonds can be broken by heating (thermoplastic elastomer) or dissolution; the crystalline domains are reformed upon cooling or precipitation, respectively. At high elongations, a breakdown of lamellar structure occurs due to high orientation of both the domain and matrix regions of the copolymer.[53]

2.2.3. Metal Ion Complexation

Prior to examining the complex problem of biological calcification, it is necessary to examine the possibility of direct interaction of calcium with the polyurethane in a simple, stable environment. This section examines the literature which details molecular binding of cations by polymers which have similar structures to polyurethanes.

Polyurethanes have demonstrated moderately strong selectivity in their ability to extract cations.[45] The

absorption of metal ions is dependent on the chemical structure and molecular weight of the polyether segment. Because of their flexibility, polyethylene oxide soft segments have been shown to be the most efficient extractors. The extractability of cations is also strongly dependent on the anions present; large polarizable anions have been shown to be most effective in increasing sorption of cations.

Oxygen atoms in the main chain allow structures to form which accommodate metal ions. These structures are similar to those formed by crown ethers with metal ions. Complexes of crown ethers with molecular guests were studied extensively,[54,55] particularly with regard to the formation of inclusion compounds. A structure of particular interest is the unsubstituted 1,4,7,10,13,16-hexaoxacyclooctadecane that has 18 atoms within the cyclic structure with an oxygen every third atom, also known as 18-crown-6. The 18-crown-6 molecule can accommodate various molecular guests through changes in molecular conformation. The structure of this molecule is shown in Figure 3. Note that the 18-crown-6 structure is a cyclic version of polyethylene oxide.

The mechanism of extraction is referred to as cation-chelation.[54,55] It suggests that a polyether segment can wrap around a cation to form a complex by the attraction of the ether oxygen to the cation. The selectivity of the

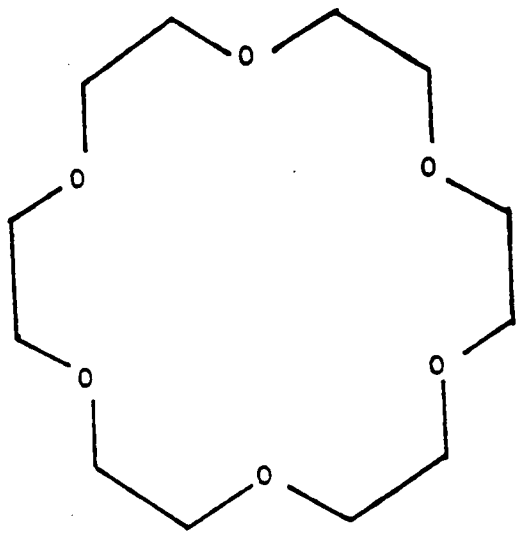

Figure 3: The crown ether, 18-crown-6.[54]

polyether is based on the size of the cation. The chemical structure of the polyether determines the shape and size of the conformation. The selectivity of the cation complex is affected by the extraction of the anion which must allow for charge balance.

Infrared measurements have been used to support the cation-chelation mechanism of ion extraction. Shifts of about 30 cm^{-1} in the ether vibrational modes near 1100 cm^{-1} were observed when Co(II) was absorbed from sodium thiocyanate solution. Co(II) formed a complex metal anion with the thiocyanate; the complex was absorbed by chelated sodium ions so that the polyether had no direct interaction with the cobalt. There was an increase in T_g associated with this system. The behavior was attributed to two effects. The first is a linear compression of the polyether chains as they spiral around the cation. The second effect is by electrostatic attractions between two chelated univalent cations on different polymer chains and one bivalent anion resulting in a crosslink between polymer chains.[9]

Killis, et al.[57] used dynamic mechanical properties to study the effects of sodium tetraphenylborate on the mechanical properties of chemically crosslinked polyether-urethanes. The crosslinked structure was synthesized from polyethylene oxide or polypropylene oxide with a triisocyanate with the salt blended into the polyether

prior to polymerization. For the polyethylene oxide systems, a decrease in T_g was observed at low salt concentrations followed by an increase at higher salt concentrations. The polypropylene oxide networks displayed increases in T_g for all salt concentrations. These shifts in the glass transition indicate the presence of significant cation-polyether interactions.

Warner, Wong and Benson[8] studied the effect of several salts on the structure of a polyether-urethane-urea copolymer synthesized from polypropylene oxide, methylene bis(phenyl isocyanate) and ethylene diamine. In that study, salts were blended into polymer solutions. Film samples were cast from the solution and tested by dynamic mechanical testing, infrared spectroscopy, and tensile loading. The loss tangent curves displayed a major peak corresponding to the glass transition temperature, T_g. As shown in Figure 4, increasing the calcium concentration caused T_g values to increase to higher values indicating that polyether segments required more energy to achieve main chain motion. Infrared spectra of the polymer salt blends are shown in Figure 5. Increasing calcium concentration (a to d), caused shifts of the carbonyl absorption at 1730 cm^{-1} to 1650 cm^{-1} which was the same shift observed for carbonyl compounds which are chelated with metal ions.[9] The broad ether absorption at 1110 cm^{-1} in the pure polyurethane sample sharpened and

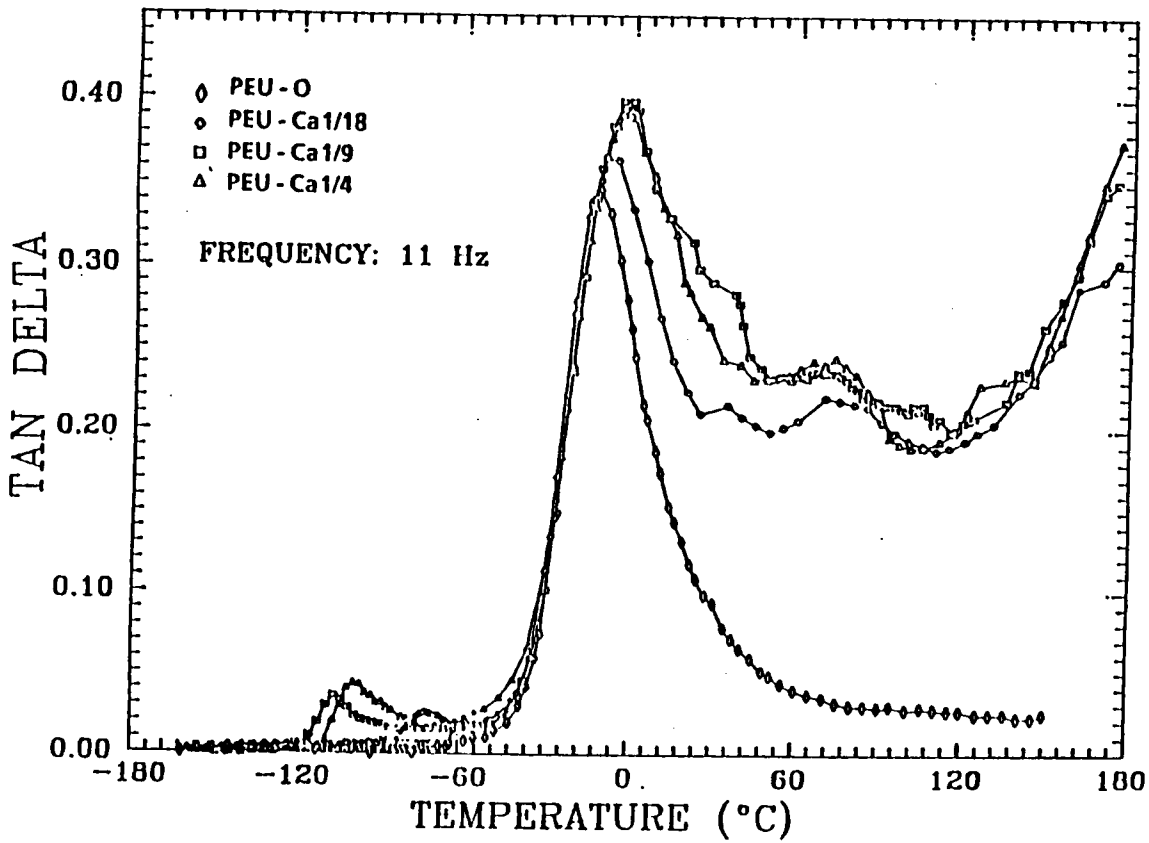

Figure 4: Loss tangent versus temperature measured from dynamic mechanical analysis at 11 Hz for various calcium concentrations.[8]

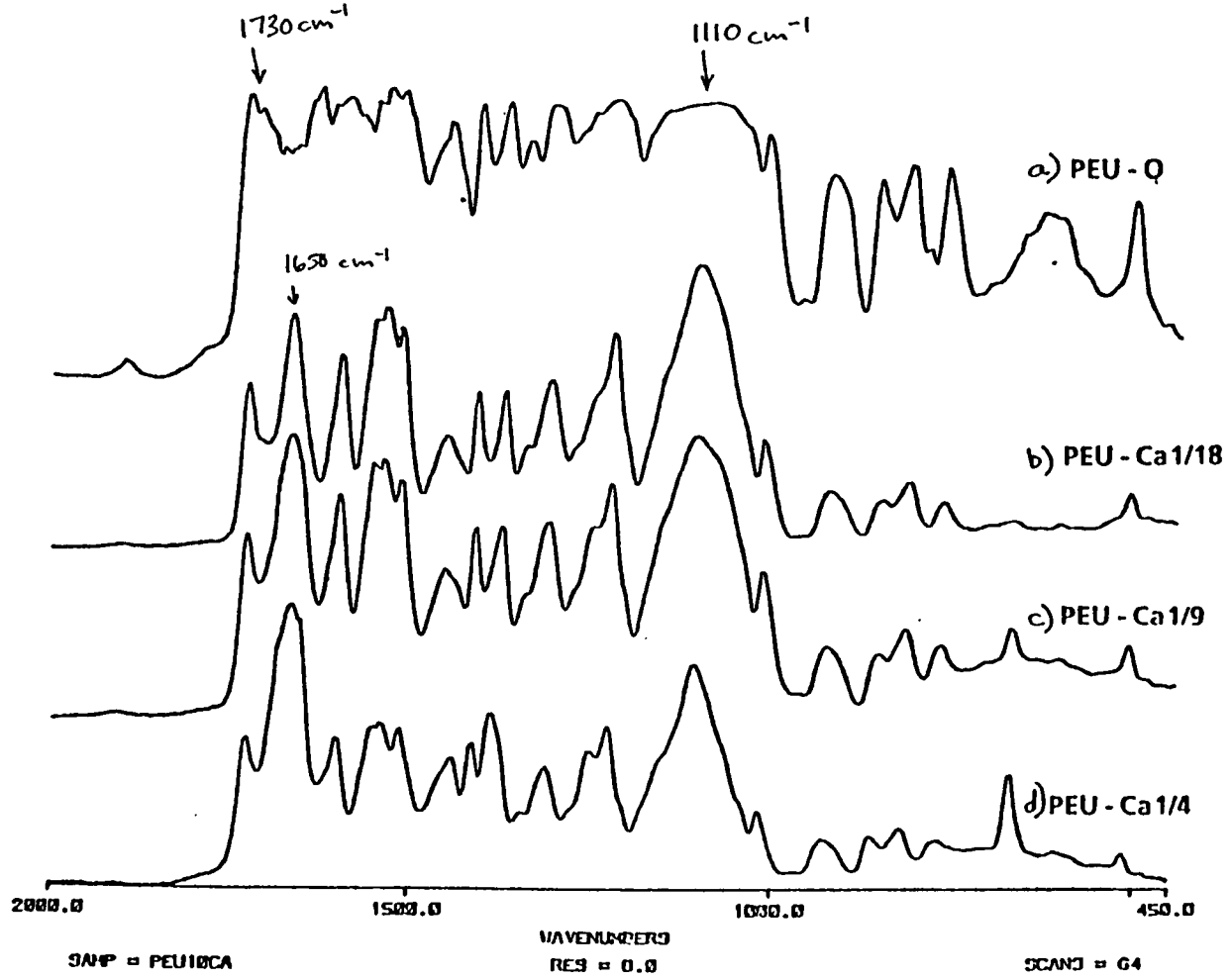

Figure 5: Infrared spectra of polyurethanes for various calcium concentrations.[8]

shifted toward 1075 cm^{-1} indicating metal ion chelation. In tensile measurements, the elastic modulus passed through a maximum, indicating that there is an optimum chelation concentration beyond which the excess salt acted as a plasticizer. In another study, Benson, et al.[12] showed that the addition of lithium salts to the poly(ether-urethane-urea) resulted in an altered structure which demonstrated a significant increase in water absorptivity. While this may not seem unusual upon the addition of a hygroscopic material, the fact that the effect persisted upon removal of the added salt suggested that a lasting alteration had occurred.

Lithium and calcium salts and strongly hydrogen bonding materials such as urea, thiourea, and guanidine hydrochloride were all found to be effective in producing measurable changes in structure.[9,11,12] An infrared study of the hydrogen bonded and non-hydrogen bonded urethane and urea carbonyls showed structure changes resulted from an interaction between salts and urethane carbonyls. The cation is believed to interact with two hard segments to form a spacer. The larger spacing between the polymer chains interferes with normal hydrogen bonding of the hard segments. When the salt is removed by leaching, the hard segments do not have sufficient mobility to form the crystalline structure. In fact, the polar groups of the polymer remain available for interactions with water.

Metal ions in the physiological environment have been shown to adversely affect mechanical properties of polyurethanes by changing the mobility of the soft segments.[8] In the case of blood contact biomedical implants, metal ions are introduced from the blood plasma which may be modeled as a buffered aqueous solution. Complexation of ions on the polymer surface depends primarily on the surface structure of the polymer. In an infrared study of polyurethane surfaces, Knutson and Lyman[1] observed that polyether segments tended to concentrate at the mold surface to a much greater extent than the urethane segments. In an aqueous salt solution, the polyether segments can readily form complexes with metal ions at the surface.

2.2.4. Mechanical Properties

The mechanical properties of polyurethanes may vary from elastomeric to rigid, depending on the relative molecular weights of the hard and soft segments. Varying the length of the flexible chain between physical crosslinks (domains) leads to differences in chain mobility. Furthermore, varying the domain size and shape greatly affects ultimate properties. The mechanical properties, in this study, are determined largely by the chemical structure.

If the molecular weight of the urethane segment is on the same order of magnitude as the molecular weight of the

polyether group, the copolymer will display rigid, brittle mechanical properties. Walsh, et al.[58] showed that polyurethanes containing short chain polyethers have a greater deviation from ideal rubber elasticity. If the polyether segment is long compared to the urethane segment, the polymer will display rubbery behavior, as the hydrogen bonded domains act effectively as crosslinks. Hydrogen bonding which enhances phase separation also contributes to the stiffness of the domains. The flexibility of the polyether segments similarly affects the overall flexibility of the copolyurethane.[12,13]

Dzierza[58] used stress relaxation properties to investigate the viscoelastic behavior of polyurethanes. Using a three element Maxwell model, Dzierza observed that a slow relaxation process depends on orientation of the hard segment domains. A fast relaxation process was related to a disruption of covalent and hydrogen bonds. At the molecular level, stress relaxation was attributed to a disruption of urethane segment hydrogen bonds, a decrease in the number of free entanglements and limited slippage of trapped entanglements. At temperatures roughly below 373 K, the mechanical relaxation was attributed to the soft polyether segments; above that temperature there were relaxation contributions of the hard urethane segments. Dzierza's experiments indicate

that polyurethane mechanical properties can be directly correlated to structure.

Figure 6 shows the results of a series of room temperature stress relaxation experiments of Pellethane, from our laboratory. Samples were rapidly loaded to 1.1, 1.3, 1.75 and 2.55 MPa respectively within 1.2 minutes to a constant strain. Within the first two minutes the stress relaxed by roughly 10% for all loadings. After the first two minutes, however, the stresses appear to have a gradual, constant decay with the higher stressed samples relaxing at a proportionately higher rate. At these stresses, the fast relaxation process may be attributed to the recoil of the polyether segments. The hydrogen bonded urethane segments maintained a more ordered structure which may have contributed to the remaining slow relaxation. An exponential fit to the single element Maxwell model did not yield a reasonable approximation of the stress relaxation curves because of the rapid initial relaxation followed by the slow relaxation of the remaining stresses. It is likely that a multi-element viscoelastic model may approximate the behavior with a spectrum of relaxation times. The results of this preliminary study showed that a delay of 2 minutes following step loading allowed for reproducible results in orientation measurements.

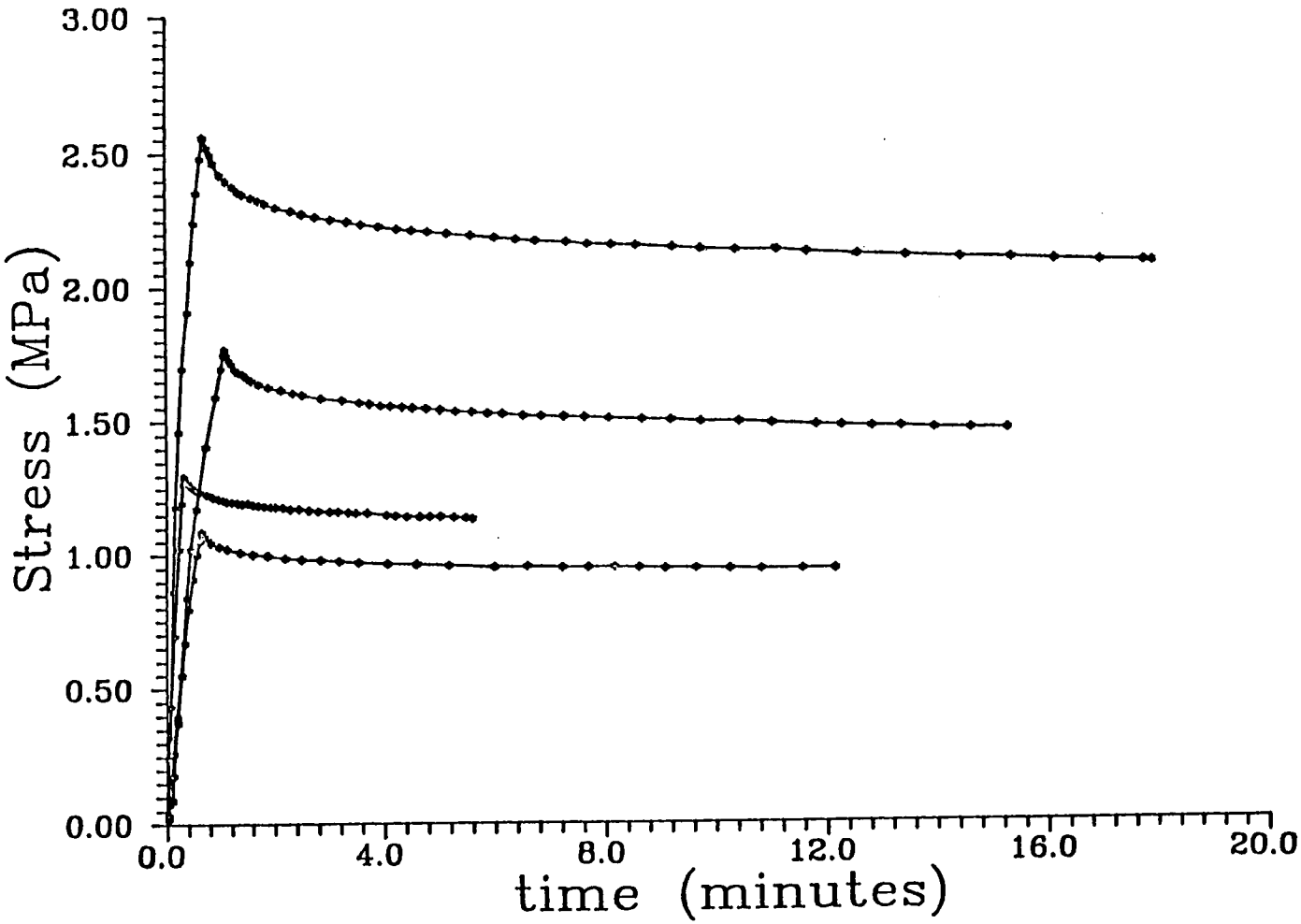

Figure 6: Stress versus time for initial loads of 1.1, 1.3, 1.75, and 2.55 MPa for Pellethane.

Wilkes, et al.[59] examined thermally induced time dependent mechanical behavior in biomedical grade polyurethanes, including poly(ether-urethanes) (Pellethane) and poly(ether-urethane-ureas) (Biomer). Using differential scanning calorimetry, tensile testing and small angle x-ray scattering, they observed time dependent changes in mechanical properties which were attributed to changes in the degree of micro-phase separation of the domain-matrix structure. The copolymers with significant amounts of urea linkages demonstrated little or no time dependent changes in structure or properties following annealing at 160°C for 5 minutes and rapid quenching. This difference may be attributed to a higher degree of hydrogen bonding resulting from the urea groups. Unfortunately, these conclusions may be called into question because the test samples of Biomer were solvent cast while the Pellethane samples were compression molded. Wilkes, et al. note that the solution cast films were given similar thermal and pressure treatments in order to ensure that no differences in properties resulted from the two different methods of preparation. The processing surface (glass versus steel) will affect the surface structure as the polyether segments tend to be attracted toward the glass surfaces. One might also expect that there is an associated change in the bulk morphology as well. Nevertheless, the study demonstrated

that annealing led to increases in modulus for poly(ether urethanes) which are compression molded.

In a more recent study, Rek and Govorcin[60] used differential scanning calorimetry, wide angle x-ray scattering, tensile mechanical and dynamic mechanical analysis to examine the effect of annealing on the domain structure of polyester based polyurethanes. They observed an increase in the crystallinity of the domains upon annealing, however, they also observed greater mixing between the hard and soft segments. The study may suggest that annealing enhances the crystallinity of the domains which, in turn, may enhance the strength of the physical crosslink through more extensive hydrogen bonding.

In a study of the effects of other blood components on polyurethanes, Benson and Wong[14] examined the effects of urea on mechanical properties. The tensile measurements are shown in Figures 7 and 8. The blending of small concentrations of urea to Biomer resulted in increases in the initial modulus. At low concentrations, Pellethane demonstrated small increases in modulus with the addition of urea; at 10% urea, however, the excess urea acted as a plasticizer by effectively interfering with the hydrogen bonding of the urethane segments.

Other studies examined fracture mechanics phenomena to understand the nature of crack propagation in polyurethanes. Caspary and Schnecko[49] observed the

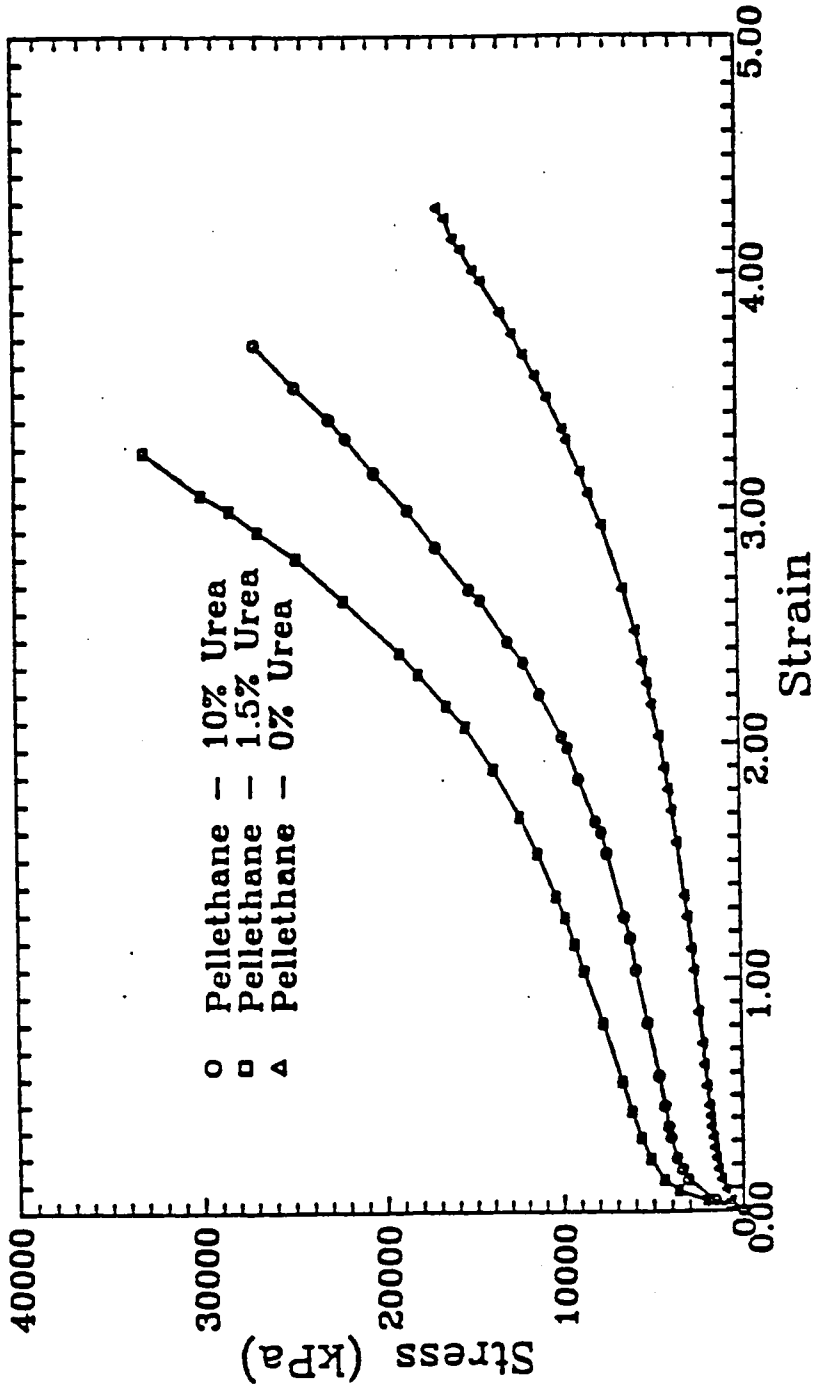

Figure 7: Tensile stress-strain curves for Pellethane blended with urea.[14]

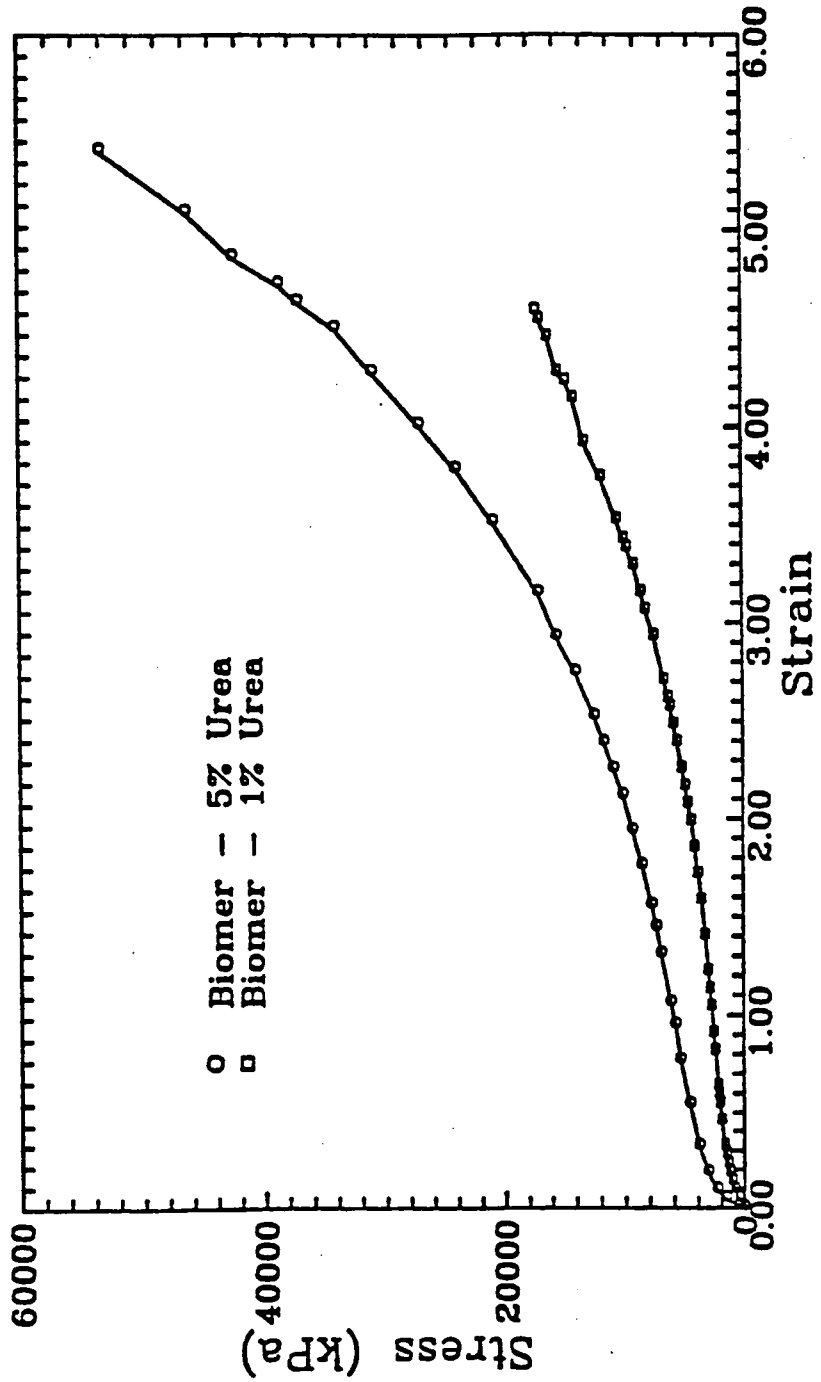

Figure 8: Tensile stress-strain curves for Biomer blended with urea.[14]

formation of crazes in highly stretched (550% strain) polyurethane elastomers. Using microscopy, they observed that stress whitening of polyurethanes in the highly stretched state are due to the formation of crazes. Their density measurements indicated that a microporous structure of crazed material was located near the crack tip. They also observed that the crazed state could be kept stable for several weeks except at elevated temperatures where stress relaxation is accelerated. In the same study, wide angle x-ray diffraction confirmed an increase in the degree of crystallinity with increasing strain and a decreasing crystallinity of the craze with increasing temperature. The disappearance of crazing at higher temperatures was attributed to stress relaxation and a loss of orientation. The study concluded that the craze in polyurethane elastomers were best characterized by the Kambour model[61] of an open cellular foam consisting of a network of highly extended material with microvoids. The transition from craze to crack became the final step in the fracture process.

2.3. Mechanical Properties of Elastomers

The disordered structure of rubbery polymers leads to a mechanical behavior which differs from that of a predominantly crystalline material. The mechanical properties of rubber are based primarily on the reduction in entropy accompanying deformation. The concept of an

ideal rubber is based on a "quasi-molecular", thermodynamic analysis of this type of system.

2.3.1. Ideal Rubber Elasticity

Elasticity is defined in terms of a theoretical element which displays three types of behavior:

1. The element has full recovery from deformation,

2. an instantaneous force leads to an instantaneous reaction with no delay, and

3. there is a direct relationship between force and deformation.

A linear elastic material has proportional deformation per unit of applied force; this is demonstrated by the ideal Hookean spring. A nonlinear elastic material satisfies the first two properties and does not have a straight line force-deformation curve.

An ideal rubber is a material in which there is no enthalpy change upon deformation at constant temperature and pressure, at large strains.[62,63] The retractive force is attributed entirely to a change in entropy. The change in free energy, A, is also due solely to an entropy decrease upon stretching. These conditions are given by:

$$(\partial U/\partial l)_{T,P} = 0 \quad \text{and} \quad (\partial V/\partial l)_{T,P} = 0 \qquad (2.3.1.1)$$

where l = sample length U = internal energy
V = volume
T = temperature
P = pressure

It follows that:

$$(\partial U/\partial l)_{T,V} = (\partial H/\partial l)_{T,P} = 0 \qquad (2.3.1.2)$$

Substituting these equations into the general expressions for free energy, the following equations are determined for the material:

$$f = -T\ (\partial S/\partial l)_{T,P} = -T\ (\partial S/\partial l)_{T,V} \qquad (2.3.1.3)$$

where f = the retractive force.

The free energy of the crosslinked network is determined through a Gaussian statistical analysis of the conformational energy of a chain constrained to span two fixed crosslinks. The result of the analysis is:

$$A' = \frac{k\ T\ \nu\ \{R^2\}_o}{2\ \langle R^2 \rangle_o} (\alpha_x^2 + \alpha_y^2 + \alpha_z^2) \qquad (2.3.1.4)$$

where A' is the deformation-dependent part of the free energy (which is entirely entropic), k is the Boltzmann constant, ν is the total number of chains in the network, $\{R^2\}_o$ is the average square end-to-end distance of the chain in a fixed crosslink network (non-temperature dependent), $\langle R^2 \rangle_o$ is the average square end-to-end distance of a free chain (highly temperature dependent), α_i is extension ratio in the i direction.

Applying the relation:

$$f = (\partial A/\partial l)_{T,V} \qquad (2.3.1.5)$$

and assuming uniaxial tension (where $\alpha = \alpha_x = 1/l_o$ and $\alpha_y = \alpha_z = 1/\alpha^{\frac{1}{2}}$), and constant volume ($\alpha_x\alpha_y\alpha_z = 1$):

$$A' = \frac{k\,T\,\nu\,\{R^2\}_o}{2\,\langle R^2\rangle_o}\,(\alpha^2 + (2/\alpha)) \qquad (2.3.1.6)$$

$$f = \frac{k\,T}{l_o}\,\frac{\{R^2\}_o}{2\,\langle R^2\rangle_o}\,(\alpha - (1/\alpha^2)) \qquad (2.3.1.7)$$

For engineering stress, $\sigma = f/\ l_y^\circ\ l_z^\circ$:

$$\sigma = \frac{R\,T\,\upsilon\,\{R^2\}_o}{\langle R^2\rangle_o}\,(\alpha - (1/\alpha^2)) \qquad (2.3.1.8)$$

where $\upsilon = \nu/V$ in units of [moles/volume]

The ratio $\{R^2\}_o/\langle R^2\rangle_o$ initially was a subject of discussion. Flory[62] contended that $\{R^2\}_o/\langle R^2\rangle_o$ should have a value of unity; that is, the probability of a network segment being created should be the same as for a free chain segment of the same number of bonds. This was later disproved by James and Guth[65] in an analysis of network elasticity which found $\{R^2\}_o/\langle R^2\rangle_o = 1/2$. The form of the engineering stress-strain curve is not affected by the constant. For the sake of simplicity in this discussion, $\{R^2\}_o/\langle R^2\rangle_o = 1$ is used. The mechanical model for an ideal rubber elastic network is given by:

$$\sigma = G_o\,(\alpha - (1/\alpha^2)) \qquad (2.3.1.9)$$

where G_o = the shear modulus

Note that if ϵ = strain, $\alpha = 1 + \epsilon$ may be substituted to arrive at a stress-strain form.

2.3.2. Load-Extension Behavior

The theoretical stress-strain curve was compared to the experimental results for natural rubber by Treloar[65] and is shown in Figure 9. The agreement is good for α less than 1.5 but is poor at high extensions where the Gaussian assumption fails. Furthermore, at high extensions, strain induced crystallization causes larger stresses than are accounted for by the ideal theory. Crystallization eliminates the assumption of freely rotating chains in a network, causing large deviations from ideality.

The theoretical treatment and experimental data on rubber display a large deviation from linear elastic behavior. It is apparent that linear elastic theories of mechanical behavior are not directly applicable to rubber except at small strains. A nonlinear elastic model is particularly useful to observe the properties of a complex network structure such as polyurethane. In practice, the nonlinear elastic model should reduce to a linear elastic model for small deformations. Furthermore, ideal rubber elasticity must be a special case of a general nonlinear elastic theory in order to be acceptable.

In real systems, the assumption of pure elasticity (linear or nonlinear) is inadequate to describe load-extension behavior. Most polymers demonstrate time dependent behavior which violates the second elasticity

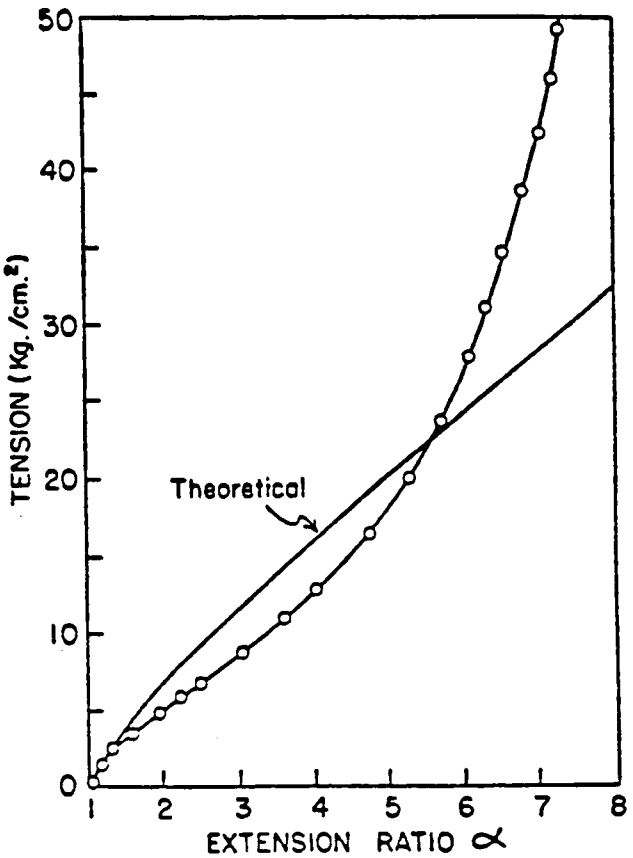

Figure 9: Theoretical and experimental stress-strain curves for simple elongation of gum-vulcanized rubber from Treloar.[65]

criteria. To model time dependent behavior, the elastic element is modified to include a viscous element. The resulting viscoelastic element causes the developed stresses to be partly dependent on the rate of strain and the strain itself to change with time.

Viscoelasticity in polymers gives rise to mechanical behavior which is time and temperature dependent. The different forms of mechanical failure were summarized by Ward[85] and are shown in Figure 10 for a series of load-extension curves for a typical polymer. Curve (a) is an example of brittle fracture in which stresses do not have sufficient time to relax prior to crack propagation. Failure occurs at a maximum load which is reached at relatively low strains. Curve (b) depicts ductile failure where the development of a yield point and a small neck occurs shortly before failure. Curve (c) is an example of necking and cold-drawing during which a stable neck forms. Curve (d) is an example of homogeneous deformation or quasi-rubber-like behavior. Note that for small extensions, the material displays ideal rubber elastic behavior.[66]

As temperature increases or strain rate decreases, the load-extension curves approach more ductile behavior. The condition at which the material goes from brittle to ductile behavior is referred to as the brittle-ductile transition. It is particularly difficult to define this

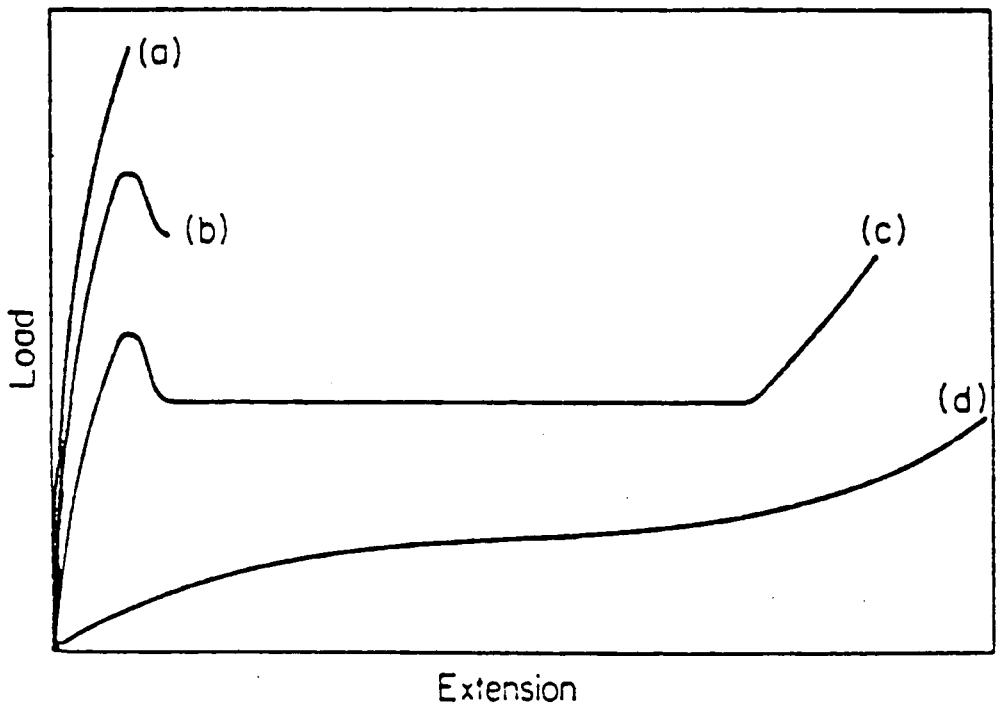

Figure 10: Load-extension curves for a typical polymer tested at four temperatures showing different regions of mechanical behavior. (a) Brittle fracture, (b) ductile failure, (c) necking and cold-drawing, and (d) homogeneous deformation (quasi-rubber-like behavior). From Ward.[66]

point because of the four distinct types of behavior.[66] Qualitatively, brittle and ductile failure may be differentiated in terms of the roughness of the crack surface and the energy dissipated in fracture.

The energy dissipated to fracture can be measured by the area beneath the stress-strain curve. Because rubbers have extremely long strains to fracture, the integrated curves yield large values of fracture toughness despite the relatively low stresses which develop. A measure of fracture toughness, therefore, does not account for the shape of the stress-strain curve but the area beneath it. It is therefore possible to compare fracture toughness values of all four of the different types of load-extension behavior. The load extension-behavior, however, must be correlated with crack growth. Details of these type of measurements are reviewed in section 2.4.

Polymer molecules under tensile stresses tend to orient in the direction of the applied stress. The excess energy of the system is dissipated in the form of a reduction in entropy. Increasing stresses cause the polymer chains to form a tightly packed crystalline structure. When the most ordered state is reached and further energy dissipation by reductions in entropy are not possible, the polymer chains rapidly break or slide past each other. The type of failure depends on the free

volume and entanglements between chains, molecular weight, and the strain rate.

The physically crosslinked polyurethane molecules display a form of non-ideal rubber elasticity which contribute to their ultimate mechanical properties. The non-ideality arises from the possibility of strain induced crystallization of the soft segment and the possibility of hard segment domain disruption (i.e. disruption of crosslinks). Both phenomena typically are observed at high strain as in the case of cracks, flaws, or stress risers in the polymer.

Mechanical properties, in general, depend on the rate of energy input. A polymer under low strain rates can have more molecules store strain energy in the form of molecular orientation. In systems where strain is applied rapidly, the formation of cracks is the most efficient method for storing strain energy. High strain rates do not allow for slow orientation processes. Instead, the polymer interatomic bonds tend to break before they can transmit the stress energy to other parts of the system. This is consistent with the concept of crack propagation. When a mechanical stress is applied to a polymer, cracking and crazing are two surface forming responses which are observed when the material can not store energy elastically.

2.3.3. Structure of the Crack Tip

As a crack propagates through a material, the highest stresses are in the vicinity of the crack tip. This can be understood qualitatively by considering material properties varying throughout a cracked tensile specimen. During testing, material deformation (and therefore, stresses) must be largest in the specimen where the material has exceeded the breaking stress. Analytical solutions which describe the stress distribution will be discussed in detail in a later section. The high stresses ahead of the crack tip cause deformations which produce structural changes in polymers.

Microscopic investigations of cracks in both elastomers and glassy polymers revealed the presence of a thin wedge of porous material in the vicinity of the crack tip which can support tensile loads.[61,67-69] This region of the sample is referred to as a craze and is shown in Figure 11. In an early study of crazes, Kambour[61] first observed that the refractive indices of crazes are less than the refractive indices for the bulk sample. The reduction of the refractive index was attributed to an increase in void volume in the porous region.[67] Donald and Kramer[68] later showed that crazes in glassy polymers can have a fibrillar structure oriented in the direction of the applied stress. It was also shown that crazes propagated by the formation of fibrils. Donald and

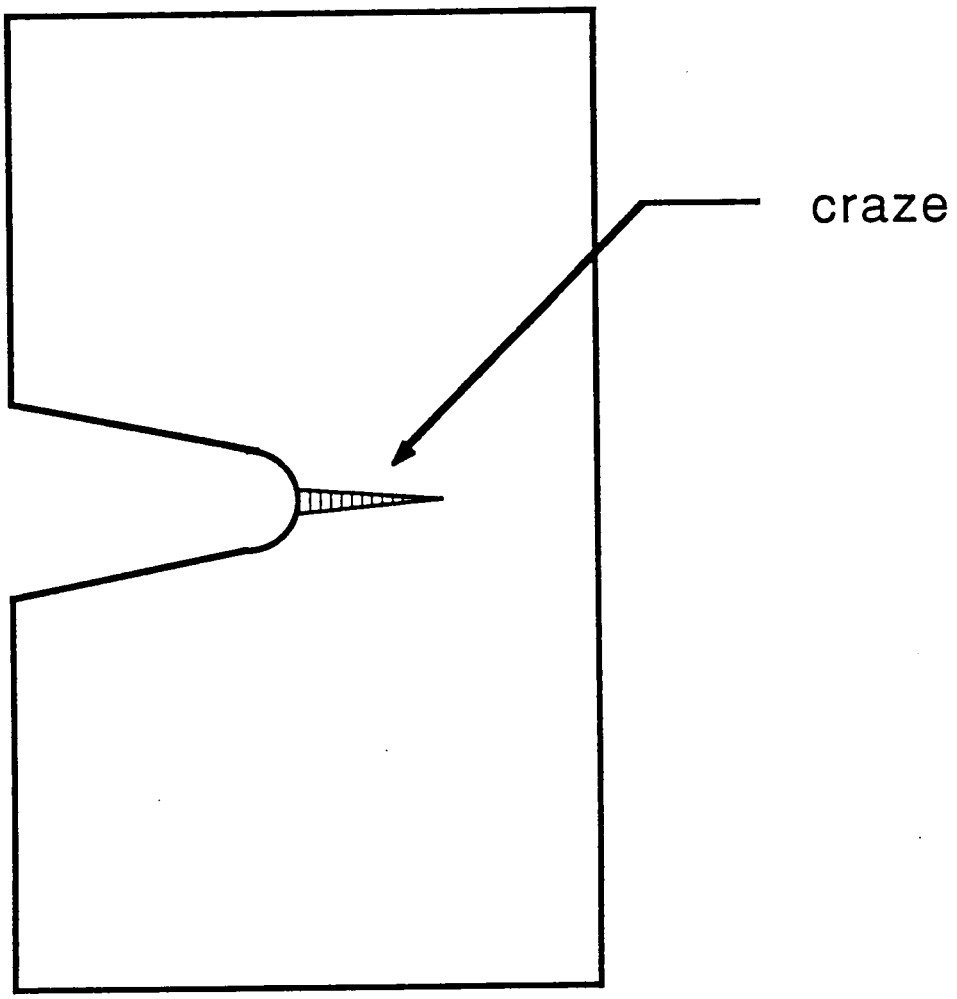

Figure 11: Blunted crack tip with craze.

Kramer[70] showed that plastic deformation is restricted to the vicinity of the craze tip in the bulk with no evidence of large scale yielding or nucleation of voids found.

Brown and Bhattacharya[71] drew several important conclusions in kinetic studies of the fracture of linear polyethylene. They showed that crack growth in pre-notched polyethylene involves instantaneous deformation followed by constant velocity growth in the deformation zone. The velocity of the cracked zone accelerated when fibrils at the root of the notch began to fracture. The tip of the deformation zone consisted of microcracks which became fibrillar toward the root of the notch. Their examination of the thinning fibrils showed that creep was the underlying mechanism that controlled both crack growth and the initiation time for crack growth. It was further noted that the Dugdale model predicted the length of the deformation zone implying that a linear elastic fracture mechanics approach was acceptable for modeling in this case.

2.3.4. Environmental Effects and Fracture Properties

An inherent assumption in most fracture experiments is that the test is conducted in the environment in which the material is to be used. This is not often the case, particularly when one considers complex loading geometries and various chemical and biological environments. The fracture test, therefore, should be considered in the

context of a material property upon which predictions can be made for applications.

In the case of this study, an experiment which completely emulates the human physiological environment was practically impossible to conduct because each patient can present a significantly different physiological environment, particularly in the case of blood contact. The experiments can be simplified by examining blood components which are common to all individuals. The components usually include water, proteins, and inorganic components. Each may be capable of accelerating stress crack growth in polyurethane; this study was limited to an aqueous calcium chloride solution. Given the complexity of the problem, a qualitative discussion of the energetics of crack surface formation is useful to understand material aspects of corrosion.

The formation of the crack surfaces may also be viewed as the formation of a new interface between the material and its environment. It does not suffice to consider a generic "surface energy"; the fluid environment (blood, air, etc.) in which the crack propagates must also be specified. Figure 12 shows a material which has a smaller interfacial free energy (per unit area) in a fluid will require a greater interfacial area to store the same strain energy. (In this case it is assumed that strain is perpendicular to the direction of crack propagation). The

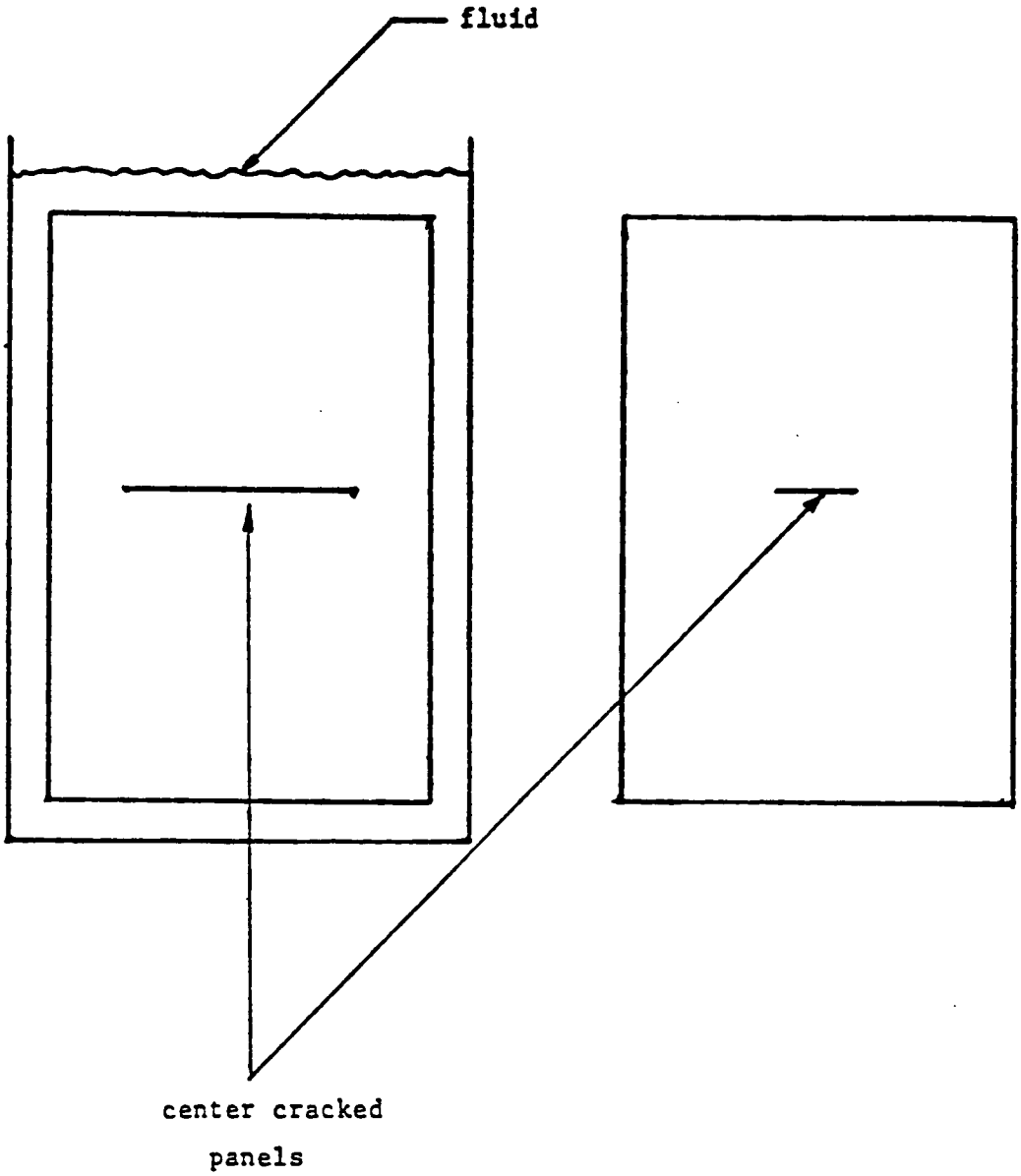

Figure 12: Effects of environment on crack propagation. (a) Sample immersed in stabilizing fluid requiring greater crack growth to store same energy as (b) sample in atmosphere.

increased interfacial area results in the form of a larger crack. The rate of crack propagation under increasing load, therefore is greater for the system with a lower interfacial energy per unit area. The surrounding environment (for example, a physiological environment) may similarly accelerate crack propagation because of the lower interfacial energy. Conversely, a material-fluid system with a high interfacial energy per unit area will propagate cracks slowly. The type of fluid is determined by the interfacial free energy of the crack surfaces.[72-74]

An aqueous solution of calcium ions may lower the interfacial free energy of surfaces, increasing the crack size required to store the same strain energy. This implies that crack propagation will be facilitated by the presence of this fluid. It should be noted that the blood environment is much more severe and will tend to lower the interfacial free energy to a much greater extent. Although testing will, by necessity be conducted in the laboratory environment, it is believed that exposure to the aqueous salt solution will produce significant energetic effects affecting crack growth.

2.4. Theory of Fracture

Historically, catastrophic failures of engineered structures has motivated research into understanding material defect propagation. As a result of these fundamental studies, engineers have developed fracture

mechanics testing methods to test materials. Their belief is that knowledge of the tendency of a material to propagate a crack can be used during the materials selection process of design.

Defects propagate with the conversion of elastic energy to crack surface energy. As stated earlier, when energy cannot be dissipated quickly enough by a reduction in the system entropy, (orientation, stress relaxation processes, etc.), the creation of a crack surface is more energetically efficient for the storage of excess strain energy. Prediction of the point at which cracks propagate continues to be the functional motive of fracture mechanics.

In a structure under load there are variations in stress due to shape and mode of loading. The distribution of the stresses determines the location of failure. The presence of holes, sharp angles, notches, grooves and other sudden discontinuities alter the stress distribution; they are referred to as stress risers. Stress risers can cause stresses to concentrate to two to four times what would normally be present. Because failure occurs at the point where the failure stress is reached first, stress risers greatly weaken the strength of a structure by causing stress to reach critical values at lower loads.

Stress concentrations can be visualized in terms of fluid flow lines. This is depicted in Figure 13. The presence of an inclusion in the path of otherwise straight flow lines leads to a velocity and pressure concentration. The disruption of flow leads to the formation of eddy currents and other complex flow patterns. By analogy, a stress field of a uniform structure may be plotted in terms of isobars rather than flow lines. In the presence of a stress riser (inclusion) the isobars are forced closer together with deviations from linearity.

One may also consider that a structure supporting a load has a continuum of stress. The presence of a flaw requires the stress to change from maximum to zero over a small distance. Stresses reorganize to bypass this zero stress area by the formation of concentrations. Ductile materials are more likely to minimize stress intensifications by deforming to reduce the stress gradients.

Within a test specimen, the flaw with the greatest stress intensification will propagate most rapidly, leading to even greater stress intensification and propagation. This results in a single crack dominating the fracture process rather than equal growth by a group of random flaws. Analyses of stress distribution by linear and nonlinear elasticity theories led to models which approximated the positions of these stresses with

Stress Intensification at a crack

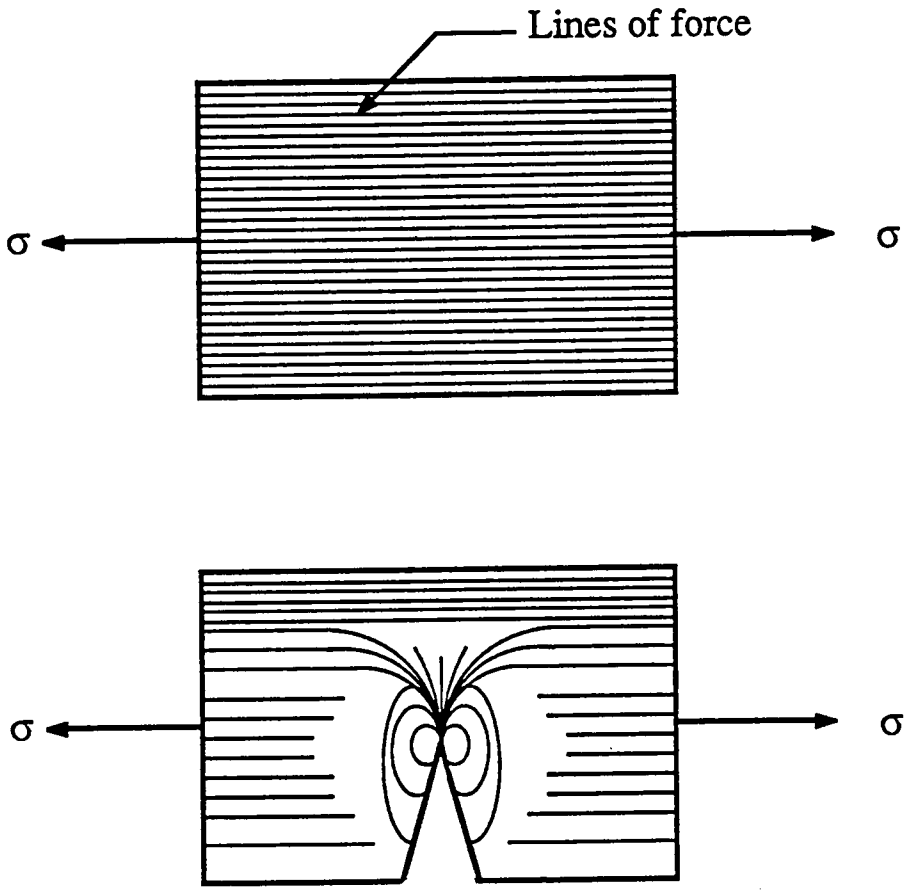

Figure 13: Stress concentration distributions visualized in terms of lines of force (similar to fluid flow about an obstacle).

respect to the crack tip. As expected, they showed that the magnitude of the stresses decreased with distance from the crack tip but the shape of the iso-stress contours were highly dependent on the elastic behavior of the material. The distribution of the stresses with position is commonly referred to as the crack tip stress field.

The shape of the crack tip stress field depends on the geometry of the flaw, the elastic properties of the material, and the applied mechanical tractions. Each of these factors is affected by a number of variables which may be accounted for, assumed negligible, or modeled with simplifying assumptions.

To simplify the problem, the flaw geometry is often modeled with a known geometry. Typically, the geometry is elliptical, circular, notched, or slit like. The choice of a specific flaw geometry simplifies mathematical analysis and is useful for the determination of material properties in the laboratory. In this study, a slit geometry will be assumed.

The elastic properties may be linear elastic or nonlinear elastic. The type of elastic behavior depends on material microstructure, processing, environmental conditions, temperature, or other variables. Nonlinear elastic fracture models have been shown to be applicable to rubber elastic and elastic-plastic mechanical properties in the following literature review. Linear

elastic fracture theory is a special case of nonlinear elastic fracture theory with the proper simplifying assumptions.

Fracture stresses can be in shear, tension or a combination of the two. (Because many biomedical applications of polyurethanes require knowledge of the tensile properties, this study was limited to uniaxial tensile properties.) The applied stresses are modeled at large distances from the crack; that is, the crack length is negligible compared to its distance from the clamps.

Mechanical failure due to the propagation of crack surfaces was first described by the Griffith energy balance.[116,117] Griffith proposed that the energy required for the formation of a new surface was balanced by a decrease in elastically stored energy. The elastically stored energy was not uniformly distributed but was concentrated in the vicinity of small cracks. He theorized that at a critical value, the applied stress caused a crack to propagate catastrophically. The critical stress was calculated for a center-cracked panel by Griffith in his classic analysis.

2.4.1. Linear Elastic Fracture

The Griffith critical stress, σ_{cr}, derived for an elliptical crack using the Inglis[75] strain energy solution

was:

$$\sigma_{cr} = (2E\gamma_s/\pi a)^{1/2} \qquad (2.4.1.1)$$

where γ_s is the crack surface energy of the material, E is the elastic modulus, and a is half the crack length of the center notched panel shown in Figure 14. The model is restricted to linearly elastic materials at absolute zero temperature. It does not account for the decrease of elastic moduli at higher stresses, nor the possible influence of other cracks in the specimen. At the time, these limitations were acceptable for many brittle materials and glasses where the mechanical behavior of the material at the use temperature is similar to its behavior at extremely low temperatures (approaching absolute zero).

Bartenev and Zuyev[76] also noted that the time dependence of the mechanical properties of the material is not taken into account because of the temperature restriction. They pointed out a further shortcoming was that the definition of the critical stress was based on an energy balance which occurs only at equilibrium when the speed of the crack propagation is zero. It was noted that during crack growth, a large dissipation of energy occurs in the form of heat. On a more practical level, surface energy and other energy measurements were difficult to determine and

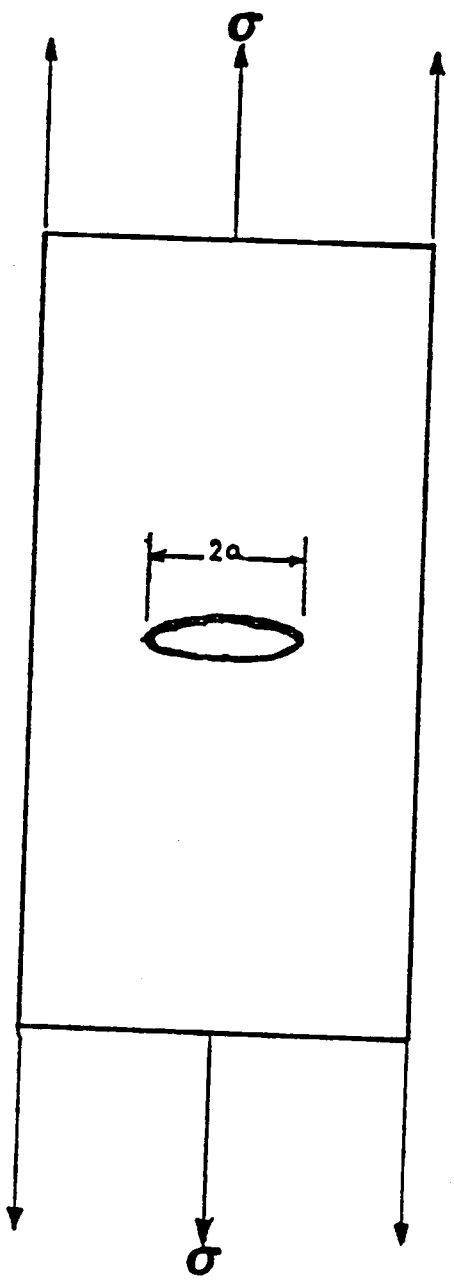

Figure 14: Center cracked notch panel under uniaxial load.[80]

of little practical use. Although there were limitations to the Griffith criteria, the energy model served as a basis for further studies in fracture mechanics using the stress field approach.

One of the more limiting disadvantages of the linear elastic analysis was that the model predicts infinite stresses at the crack tip when, in fact, plastic deformation occurs when the yield stress is exceeded. The plastic deformation precedes fracture and is a highly nonlinear elastic type behavior. To correct the linear elastic model, Orowan[77] modified the Griffith criteria to account for the energy associated with plastic deformation. The result was:

$$\sigma_c = [2E\ (\gamma_s + \gamma_p)/\pi a]^{1/2} \qquad (2.4.1.2)$$

where γ_p is the plastic deformation energy term and

$\gamma_p >> \gamma_s$.

In an independent study of the thermodynamics of fracture, Irwin[78] calculated a similar expression:

$$\sigma = (EG/\pi a)^{1/2} \qquad (2.4.1.3)$$

where G is the strain energy release rate dU/da. The value of G is therefore related to the plastic energy and the surface energy by $G = 2\ (\gamma_s + \gamma_p)$. In both studies, linear elastic energy balance models were modified to account for crack tip plasticity.

Although the energy balance models were theoretically correct, their applicability to design and engineering

problems was limited. The studies did not lead to an understanding of material properties because they required a specific knowledge of flaw geometry and how stresses were applied to the flaw. Furthermore, it was difficult to measure and calculate surface energies and strain energy release rates during the design process if the location of flaws could be anywhere on the structure.

To address these shortcomings, it was desirable to develop a material parameter which could describe the fracture properties of a material in various loading configurations. The analysis of the crack tip stresses lead to the material parameter, K, the stress intensity factor.

To determine the stress field about a crack tip, Irwin substituted a Westergaard[79] stress function into equations of equilibrium for planar conditions. The model for this case is shown in Figure 15. The model determines stresses in two dimensions (x,y) with respect to an origin at the crack tip (r,θ). The results of the substitution are given by Broek:[80]

$$\sigma_y = \frac{K}{(2\pi r)^{1/2}} \cos(\theta/2) \, [1 + \sin(\theta/2) \sin(3\theta/2)] \qquad (2.4.1.4)$$

$$\sigma_x = \frac{K}{(2\pi r)^{1/2}} \cos(\theta/2) \, [1 - \sin(\theta/2) \sin(3\theta/2)] \qquad (2.4.1.5)$$

$$\tau_{xy} = \frac{K}{(2\pi r)^{1/2}} \cos(\theta/2) \sin(\theta/2) \cos(3\theta/2) \qquad (2.4.1.6)$$

$$\tau_{xz} = \tau_{yz} = 0$$

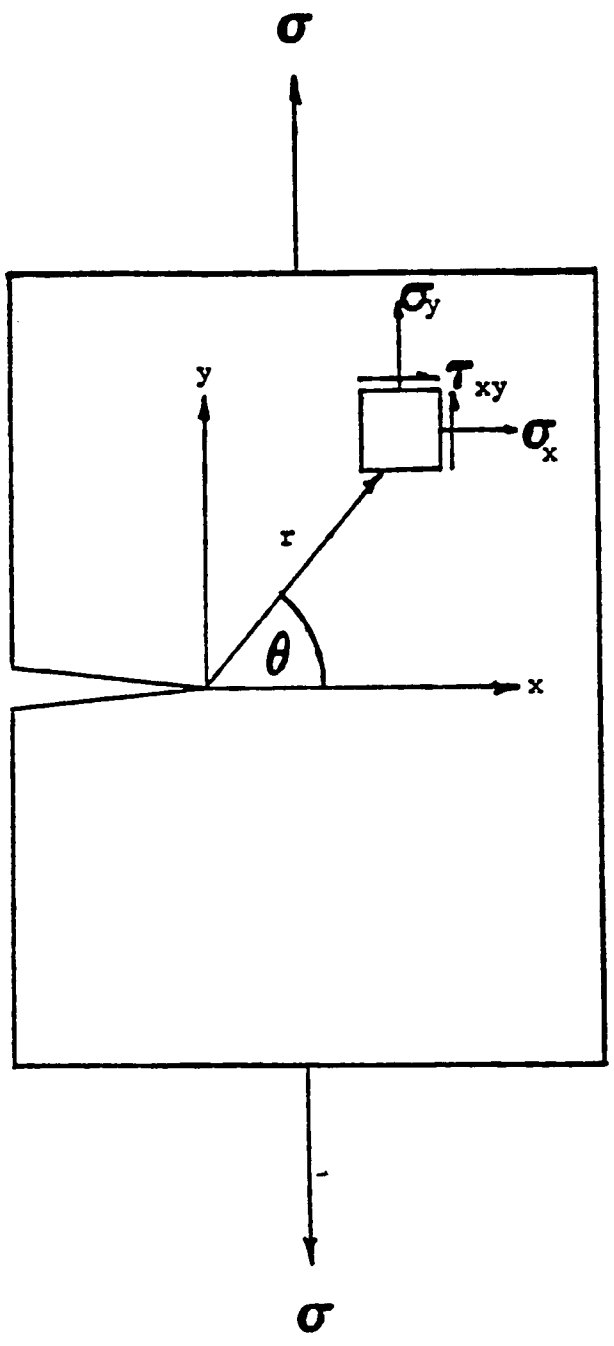

Figure 15: Planar conditions to determine for stress distribution about a crack tip.[80]

$\sigma_z \approx \nu (\sigma_y + \sigma_x)$ (plane strain)

$\sigma_z \approx 0$ (plane stress)

where ν is Poisson's ratio and K is the stress intensity factor which is a material parameter that is a function of the applied stress and crack geometry. It is important to note in these equations that stress is proportional to a geometry term (θ) and inversely proportional to $r^{1/2}$, thus the singularity at the crack tip is still present. This model is applicable to materials which display linearly elastic behavior under test conditions. This is often true of glassy polymers.

The critical stress intensity factor, K_{Ic}, is the minimum value of K which will cause a crack to propagate to failure instantaneously under normal stresses. The subscript I refers to a mode I type fracture which is a tensile loading; the subscript c denotes that K is at a critical value. It is given by:

$$K_{Ic} = \sigma_{cr} f(a) \qquad (2.4.1.7)$$

where σ_{cr} is the critical stress for crack propagation. Values of K_{Ic} are parameters which are unique for a material and specific crack geometry. K_{Ic} is commonly used as a fracture criterion.

2.4.2. Nonlinear Elastic Fracture

The $r^{1/2}$ dependence of the linear elastic model implies that the use of K for determining critical phenomena assumes a negligible zone of plastic deformation

surrounding the crack tip. The assumption is reasonable in studies of glassy polymers where plastic deformation is predominantly restricted to the vicinity of the crack tip. In this case, one also assumes that the energy release rate, G is not affected by the crack tip plastic zone. If the size of the plastic zone is of the same order as the sample specimen itself, G is affected on a large scale and linear elastic fracture mechanics does not accurately predict the critical phenomena. This is the case for elastomeric materials such as polyurethanes. Linear elastic fracture mechanics is not valid, typically, for large strains or when the stress-strain curves are nonlinear. In these cases, general nonlinear elastic fracture mechanics techniques must be applied.

In an attempt to generalize the Griffith criterion, Rivlin and Thomas[81] studied the tearing of rubbers extensively. Recognizing the shortcomings of the Griffith theory, they proposed an energy formulation which would account for surface energy, energy dissipated in plastic flow processes, and energy dissipated irreversibly in viscoelastic flow processes. Their model was given by:

$$T = -[\partial U/\partial a]_l \qquad (2.4.2.1)$$

where T is a characteristic tearing energy per unit thickness of the specimen and the partial derivative is the change in the internal energy, U with crack length, a, and constant elongation, l. This equation is the

fundamental definition of tearing, fracture energy in nonlinear elastic fracture. The measurement of the derivative term, however, has been accomplished by different methods and included different assumptions in measurement. Rivlin and Thomas tested their specimens in a trouser tear experiment or in Mode III fracture mechanics, thus requiring an extremely long initial crack length. In other words, the trouser leg inseam must be long so that the complex stresses developed at the crack are independent of the depth of the tear. Rivlin and Thomas further proposed that for a crack extension Δa, under force, F, the work done is given by:

$$W = 2F\Delta a \qquad (2.4.2.2)$$

This ignores any changes in extension of the material between the tip of the tear and the legs. The tearing energy is given by:

$$T = \partial W/\partial a$$

$$= 2F \qquad (2.4.2.3)$$

Ward[66] noted that the Rivlin-Thomas tearing energy does not relate directly to tensile strength. It is possible to have two different rubbers, one having a high tensile strength with a low elongation to fracture and low viscous losses, and another with a low tensile strength but a high elongation to fracture with high viscous losses. Despite a low tensile strength, the second rubber has a high tearing energy. The partial derivative formulation is

correct and is still used, however, the test method for determining T required some refinement.

The trouser test was sensitive to deformations very close to the crack tip but ignored deformations in the material away from the crack tip. To ignore that deformation was not acceptable in cases where material deformations far from the crack tip were quite large. Although it held for glasses, brittle polymers, and noncrystallizing rubbers, Andrews[83] noted that it failed to account for strain crystallizing elastomers.

At about the same point in time, a similar problem in fracture mechanics was a concern of the nuclear power industry. In many cases, it was found that certain steels and other materials at high temperatures were not adequately modeled by linear elasticity. Linear elastic fracture measurements (K_{Ic}) were underestimating fracture toughness as the crack tip plastic zone became large compared to the size of the test specimen. To address the problem of nonlinearity, Rice[114] introduced an energy balance based on the concept of a path independent integral, J, for the approximate analysis of strain concentration at cracks. The model is shown in Figure 16. The two dimensional form of the integral is written as:

$$J = \int_{\Gamma} W dy - \int_{\Gamma} T_i \frac{\partial u_i}{\partial x} ds \qquad (2.4.2.4)$$

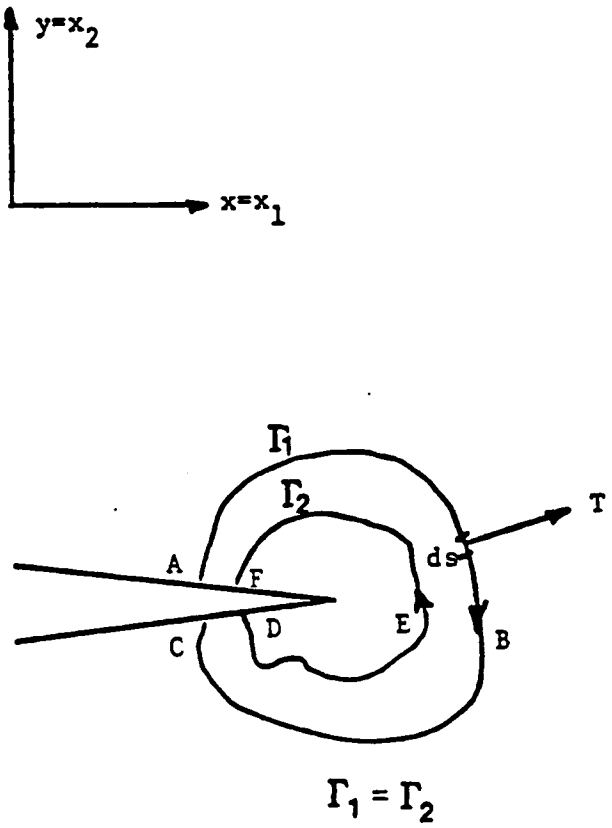

Figure 16: Definition of the J integral along path ABCDEF, where T is the traction on path segment, ds.[114]

where Γ is the counter clockwise contour line for the integral, $T_i = \sigma_{ij} n_j$ is the stress vector, ds is an increment on Γ and W is the strain energy density given by:

$$W = W(x,y) = W(\epsilon) = \int \sigma_{ij}\, d\epsilon_{ij} \qquad (2.4.2.5)$$

W may be obtained by a standard uncracked tensile measurement and a numerical integration of the data for a specific strain. The path independence of the integral allows evaluation of J from stress analysis (such as finite element analysis) using stress and strain results where they are more accurately known away from the crack tip region. Paris[17] observed that the path independence implied J was also a crack tip parameter.

Although path independence was of academic interest, Paris commented that a further physical definition was desired. His classic interpretation is depicted in Figure 17. If one considers a J system along a contour, Γ, where crack extension, da, occurs, each term of equation (2.4.2.4) is multiplied by da. Thus the individual terms become:

$\int_\Gamma$ Wdyda = the strain energy gained (and lost) by moving to new contour,

$\int_\Gamma T_i \frac{\partial u_i}{\partial x} \, ds\,da$ = the work done by tractions on the contour in moving.

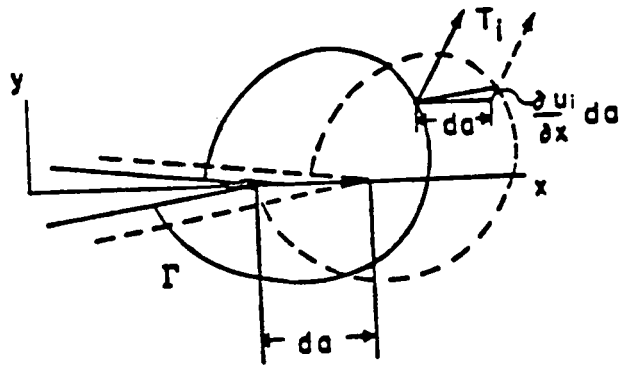

Figure 17: J contour around contour Γ at a crack tip. From Paris.[17]

Jda, therefore, is the total energy passing through the contour for a crack extension, da. This is the same quantity of energy for all contours down to one just surrounding the crack tip, because of the path independence of J.[17] As a result, for nonlinear or linear elastic materials, J is the energy being made available at the crack tip per unit increase in crack length (or crack surface area if normalized by sample thickness) or J is the Griffith energy, G. For the special case of linear elasticity:

$$J = G = K^2/E \qquad (2.4.2.6)$$

The J integral is therefore a measure of the total energy released through the contour for an incremental crack extension, Δa, hence, Rice showed that J was similar to the Rivlin-Thomas tearing energy, T if one ignores the energy for non-crack growth deformations. As a further consequence, in nonlinear elastic fracture mechanics, J is a measure of the strength of the crack tip singularity, as K is the strength of the crack tip singularity in linear elastic fracture mechanics. By analogy, J_{Ic} is the critical value of J at which a crack will propagate in nonlinear elastic fracture. Hutchinson[19] , Rice and Rosengren[18] combined with the work of McClintock[83] to show that the crack tip stress and strain singularities can be expressed in terms of J for materials obeying a power law

type behavior. They are referred to as the HRR stress singularities:

$$\sigma_{ij}(r,\theta) = \sigma_1 \left[\frac{J}{\sigma_1 I_n}\right]^{n/(n+1)} \frac{1}{r^{n/(n+1)}} f_{ij}(\theta) \qquad (2.4.2.7)$$

$$\epsilon_{ij}(r,\theta) = \left[\frac{J}{\sigma_1 I_n}\right]^{n/(n+1)} \frac{1}{r^{1/(n+1)}} g_{ij}(\theta) \qquad (2.4.2.8)$$

where n is the strain hardening exponent in the Ramberg-Osgood relation between equivalent stress, σ_1, and equivalent plastic strain, ϵ_p:

$$\sigma = \sigma_1 (\epsilon_p)^n \qquad (2.4.2.9)$$

The term I_n is a function of n and the mode of crack opening, but is generally close to a value of 5.0.[19] Qualitatively, the stress and strain at each r and θ depends on three factors: material properties, the distance from the crack tip, r, and a function of the angle $f_{ij}(\theta)$ or $g_{ij}(\theta)$. The first bracket is a scalar which represents the material's ability to resist crack growth; if this term is large, the material requires more energy for crack growth which will lead to higher stresses. The bracket is large if J (fracture toughness) is large or the power law exponent is large.

The last two terms determine the shape of the stress and strain distribution. The linear elastic, singular dependence of $r^{1/2}$ has been replaced by a function of the

power law hardening exponent, n, to account for nonlinearity.

The functions $f_{ij}(\theta)$ and $g_{ij}(\theta)$ depend on the individual stresses or strains of interest (the values of i and j). The functions are not independent and must be chosen to satisfy the stress-strain relationship. Rice and Rosengren[18] assumed plane stress and plane strain in a two dimensional analysis so the nine components of the stress tensor may be reduced to three independent stresses and strains: : σ_{rr}, $\sigma_{\theta\theta}$, and $\tau_{r\theta}$ and ϵ_{rr}, $\epsilon_{\theta\theta}$, and $\epsilon_{r\theta}$. Their solution for the functions $f(\theta)$ and $g(\theta)$ were generated numerically from the solution of a fourth order differential equation. For details of the solution, the reader is referred to the work of Rice and Rosengren.[18] The shape of the HRR stress fields are shown in Figure 18. Each curve represents the calculated boundary between regions of elastic and plastic deformation for varying power law exponents. It should be noted that stress whitening is commonly observed near the crack tip in a similar geometry.

Andrews[84] employed a microscopic, photoelastic technique to investigate the principal stress and strain distributions around a crack in natural rubber. His results are shown in Figure 19. The stress distribution in Andrews' study appears to be narrower perpendicular to the crack axis because of blunting of the crack tip. The

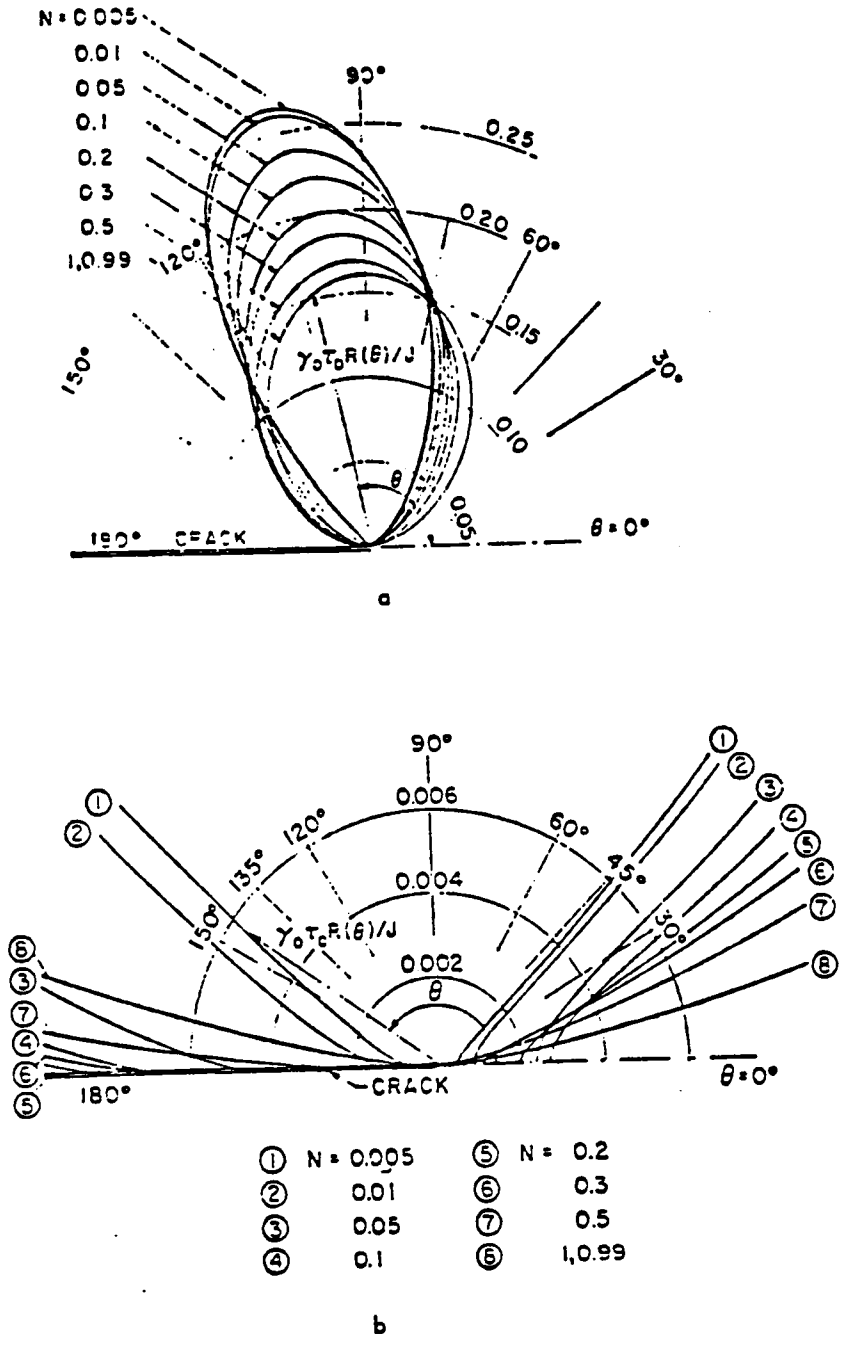

Figure 18: Calculated non-linear elastic crack tip stress model (a) Approximate location of yield boundary and geometrical shape of constant stress near the crack tip. (b) Yield boundary; detail very near the crack tip. From Rice and Rosengren.[18]

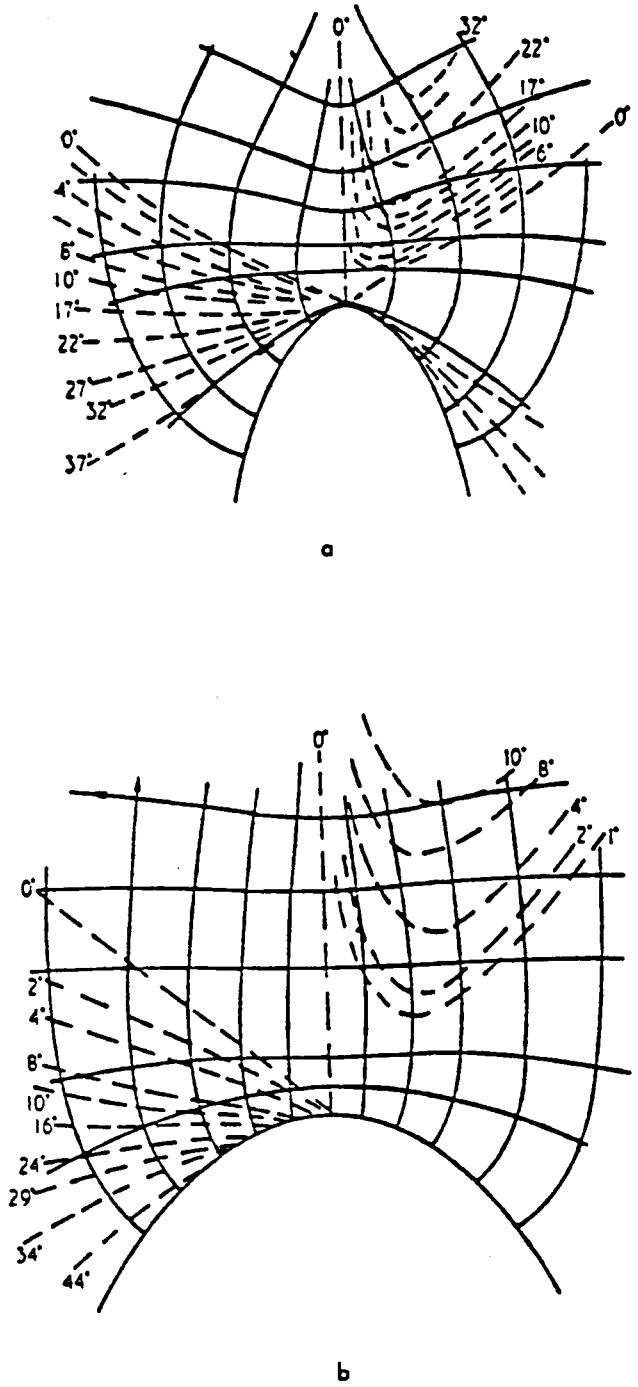

Figure 19: Experimental principal stress map (isoclinics shown as broken lines) at (a) T = 0.16 kg/cm and (b) T = 0.65 kg/cm. From Andrews.[82]

geometric shape of the stress field appears to be consistent with the HRR fields. In preliminary studies, stress whitening has been observed to follow the same geometric distribution around a slit shaped crack in Pellethane.

Begley and Landes[85] showed that J values could be used as a fracture criterion as K is used in linear elastic fracture. J was the same as Rivlin and Thomas' tearing energy, T, if it is redefined to include far field tensile energy dissipation. This is described mathematically by:

$$J = T = -[\partial U/\partial a]_1 \qquad (2.4.2.10)$$

where U is the potential energy and a is the crack length. The potential energy per unit thickness of a two dimensional elastic body of area A is given by:

$$U = \iint_A W dx dy - \int_{S_T} T\,(uds) \qquad (2.4.2.11)$$

where W is the strain energy density and S_T is the portion of the boundary over which the tractions T are applied. Differentiating with respect to the crack length, a, one obtains an expression for J (or T).

Although it was not the aim of this research to derive a constitutive model of viscoelastic fracture, it was desirable to attempt to understand the nature of the specific energy contributions to the measurement of J. To

understand the physical interpretation of J measurements of polymers, models have been proposed which relate the form of the stress-strain behavior to energy release with crack growth. The J integral has been modeled as a two component system; a term which accounts for linear elastic behavior and a term which accounts for nonlinear behavior. This is analogous to the simple Voigt model where stress energies are modeled as a spring (linear elastic) and a dashpot (nonlinear elastic, viscous):

$$J = J_{elastic} + J_{non\text{-}elastic} \qquad (2.4.2.12)$$

where $J_{elastic} = K^2 / E$
$= $ the J integral due to linear elastic deformation

and $J_{non\text{-}elastic}$ = the J integral due to deviations from linear elastic deformation.

Physically, the nonlinear term approaches zero for materials with purely linear elastic behavior. By analogy to the linear elastic case, J_{IC} is the critical value of J at which a crack will propagate. Recent developments in J_{IC} testing assume the model is correct and measure the contributions to the two terms through mechanical hysteresis unloading. (The pure elastic contribution is obtained from the area under the unloading curve.) The application of the J integral to materials testing was also proposed by Paris[17] and demonstrated by Landes and Begley[86]. It is reviewed in the following section.

During the same period of time, Andrews and Kinloch[121-122] investigated the mechanics of rubber adhesive failure. In the first paper, they confirmed an earlier work of Gent and Kinloch[123] that a characteristic amount of energy, θ, per unit area of interface was required to cause separation of the joint. The characteristic energy was a sum of two components; the energy dissipated viscoelastically, ψ and the intrinsic adhesive failure energy, θ_o or the energy required for crack propagation in the absence of viscoelastic energy losses in the rubbery adhesive. ψ was shown to be dependent on the rate of crack propagation and temperature; lower rates of crack propagation and higher temperatures led to smaller values of ψ. ψ was the dominant component in the rubbery material and was shown to be proportional to θ_o. In the second study, Andrews and Kinloch showed that θ_o was approximately equal to W_A, the thermodynamic work of adhesion, when joint failure is wholly interfacial. This was the case for low strength joints. When cohesive failure occurred during joint separation, θ_o was much greater than W_A. In this case the joint was of a much higher strength. In the absence of unsaturated bonds joint failure was interfacial. In the presence of unsaturated groups, the instrinsic strength of the interface was enhanced, thus favoring cohesive failure.

The work of Andrews and Kinloch laid the groundwork for a generalized theory of fracture mechanics which Andrews[124] published in 1974. The theory made no restrictions on the elastic behavior of the material, similar to the earlier work of Begley and Landes.[86] The Andrews theory showed a relationship between surface work and true surface energy. It also was shown to account for unloading situations as well. At the time, Andrews questioned the validity of the Rice[114] J integral approach, although later studies showed that the two theories were directly related.

In a more recent paper, Andrews[115] proposed that J could be expressed by two terms:

$$J = J_o \Phi(T,a,\epsilon) \qquad (2.4.2.13)$$

where J_o, represents the energy available for creation of the crack surface, Φ is a loss function which depends on temperature, crack growth rate and strain intensity. J_o is the energy for cleavage fracture which is equivalent to the Griffith's surface energy. The value of Φ varies from 1 (perfect elasticity) to infinity (crack does not propagate in a fluid). The function is also determined by the energy density distribution in the specimen, the limits of loading and unloading stress fields as the crack propagates, and the mechanical hysteresis ratio of the material.

Andrews further suggests that the craze energy may be determined for J_o by taking advantage of the path independence of the J integral. His hypothesis is shown in Figure 20. The craze energy may be measured by determining J for a path following the contours of the crack tip and a path along the craze tip region. The difference between the two will be the energy which contributed to forming the craze. This simplifies the analysis of crazes which usually lack sufficient information of the complex strain energy distribution. J_o is thus the energy required to form and break the craze. In cleavage fracture, J_o becomes the energy required to break atomic bonds along the fracture plane.

There could be a large number of methods for modeling energy contributions to the J integral if one were to attempt to apply each of the numerous viscoelastic models. To further complicate each model, the time-temperature dependence of viscoelastic properties would have to be considered.

Because each material has a different stress-strain behavior depending on temperature and strain rate, it becomes difficult to compare materials with radically different mechanical behavior. The best method is to compare the areas beneath the stress-strain curves to determine which material dissipated the most energy prior to fracture. This is the basis of measurements of the J

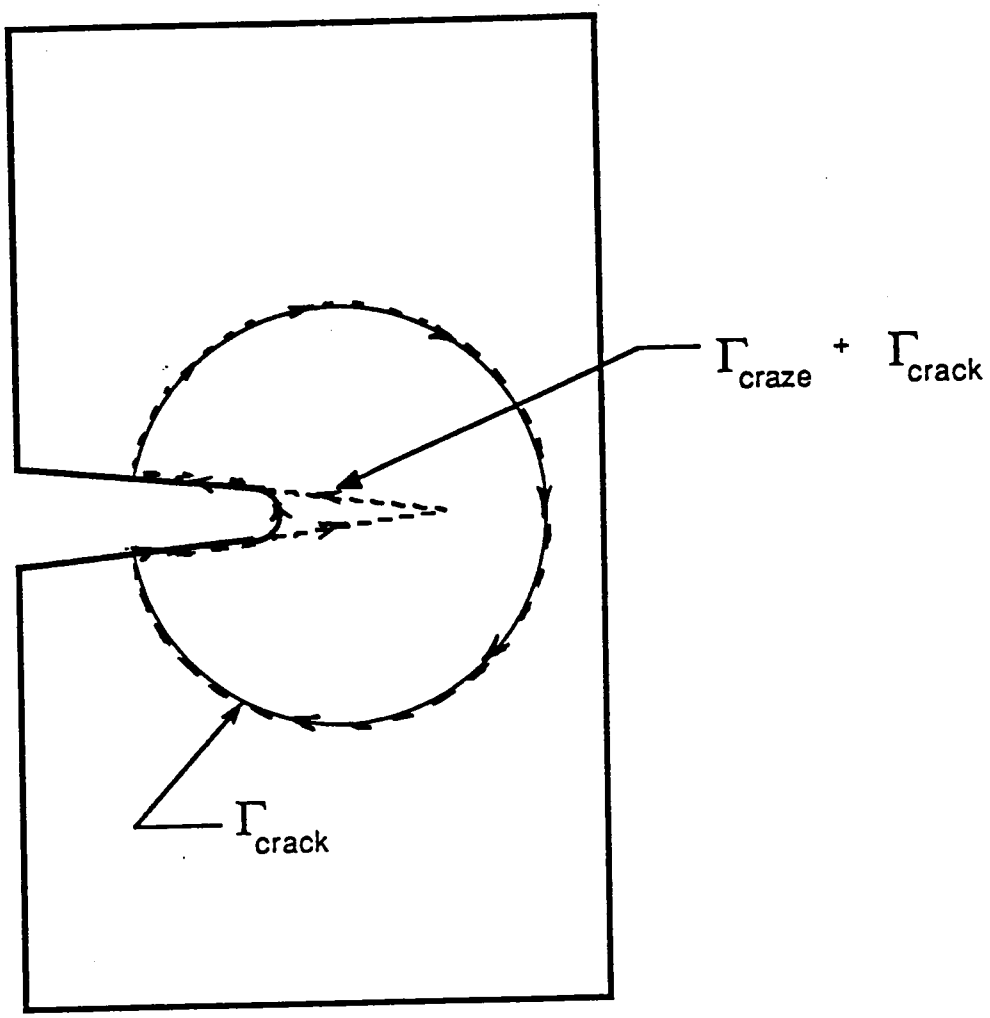

$$\Gamma_{crack} = \frac{\Gamma_{crack}}{\Gamma_{craze} + \Gamma_{crack}}$$

Figure 20: Andrews' proposed method for measuring craze energy.[115]

integral as a fracture criterion. By examining the total stress energy to fracture, the problem of modeling contributions of viscous and elastic contributions are avoided. The measurement is not concerned with the shape of the stress-strain curve (although it is significant in other studies) but the area beneath it and consequently, the energy expended. The only requirements are that measurements be made at the same temperature, strain rate, and geometry. The details for measurement of fracture properties are discussed in the following section.

2.4.2.1. Experimental Determination of J for Polymers. An early refinement to the trouser test for determination of tearing energy was also proposed by Rivlin and Thomas[110] and known as the total energy drop method. In an independent study for ductile metals, Landes and Begley proposed a similar method for determining the J integral[86]. The total energy drop accounted for the energy losses far from the crack tip. The experiments directly determine the derivative in equation (2.4.2.4) by obtaining data of load-elongation from identical specimens with different crack lengths, a. This is known as compliance calibration. As defined in section 2.4.2., the area, U, under each curve at a specific elongation is the mechanical energy applied to the specimen to obtain that elongation. A plot of U as a function of a was constructed followed by a graphical

determination of $-[\partial U/\partial a]_l$. The method is illustrated in Figure 21. The shortcomings of the compliance calibration method involve the need to test many identical specimens and the inaccuracy involved in curve fitting and graphical differentiation. These problems are easily overcome, however, by the use of computers.

The specifics of the method described above were first proposed by Begley and Landes[85], and were a standard designated by ASTM E813-81. The multiple specimen J integral method is summarized as follows:

To begin, one specimen is completely fractured to determine the ultimate displacement. The remaining test specimens are loaded to different displacements to obtain different values of crack growth. J is calculated from the area under each tensile curve. Crack growth is measured from the surface for each J-specimen. A plot of J as a function of crack extension can be constructed. J_{Ic} is the intersection of this curve and a blunting line:

$$J = 2\sigma_y \sqrt{a} \qquad (2.4.2.1.1)$$

The applications of ASTM E813-81 to polymers will be reviewed in the next section. It should be noted that the standard was modified in 1987 to ASTM E813-87 which allows for an optional single specimen method. The single specimen method uses a compliance calibration method which calculates the elastic contribution from hysteresis effects; the linear elastic and nonlinear elastic energy

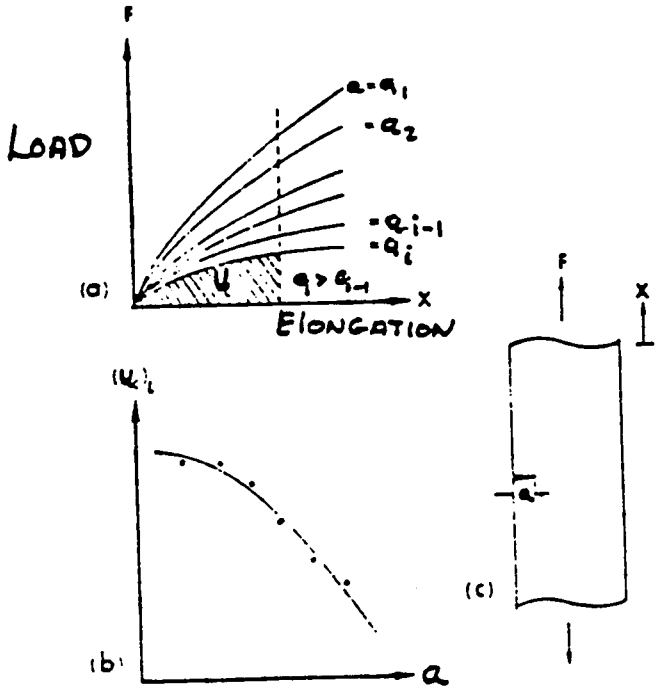

Figure 21: (a) Load-displacement curves of cracked specimens having various crack lengths. (b) stored strain energy versus crack length for a given displacement 1, and (c) notation used in (a) and (b). From Landes and Begley.[86]

contributions are calculated by the difference in area under the loading and unloading curves. The complexity of polymer relaxation and hysteresis effects is overlooked by the single specimen method, hence, a multiple specimen technique may be necessary for this study.

A second method, known as the crack-surface displacement method was developed by Lake[87] and Lindley.[88] Their method examines deformations occurring near the crack tip and evaluates the energy required to close the crack. The energy to close the crack was equated with the energy drop due to the crack opening to estimate the fracture energy. It was believed that measurements very close to the crack tip were more sensitive than the far field total energy drop method. Although experimentally the crack-surface displacement method appeared consistent with the total energy drop method, it required the assumption of linear elasticity. Furthermore, it had a larger experimental error because of the inaccuracies in measuring deformations in a small region.

A third method suggested by Oh[89], applied a direct interpretation of the J integral to rubber. The path independence of the method retained the sensitivity of the near crack tip strain field but computed the fracture energy based on far field deformations. Most importantly, the method required only a single specimen. To experimentally determine the strain energy density, W of

equation (2.4.2.3), it is necessary to measure the local strain along the path chosen. Oh[89] printed a circular grid on a nicked rubber strip to measure local deformations in terms of the change in circle diameter. The circles of diameter, d, deform into ellipses of diameter d_{max} and d_{min}. The corresponding local strains may be computed:

$$\epsilon_{xx} = (d_{max} - d)/d \qquad (2.4.2.1.2)$$

$$\epsilon_{yy} = (d_{min} - d)/d \qquad (2.4.2.1.3)$$

The corresponding values of W are obtained by equation (2.4.2.5). J is then evaluated according to equation (2.4.2.4). Wang[90], Chang[91], and Knowles et al.[92] showed that the infinitesimal deformations of the J integral also held for finite deformations and were acceptable measurements.

To implement the path independent line integral, deformations are measured along a single path chosen for convenience. The path is shown in Figure 22 for a thin nicked, rectangular strip. By symmetry, it is necessary to only measure path ABCD and double the result to obtain J. A path parallel to the x axis forces the first term of the integral to zero, while a path along a stress free boundary (T=0) or along a clamped boundary parallel to the x axis forces the second term to zero. Referring to

Figure 22, the J measurement reduces to:

$$J = 2\left[\int_{AB} Wdy + \int_{CD} Wdy\right]$$

$$= 2\left[\int_{AB} Wdy + \int_{DC} Wdy\right] \qquad (2.4.2.1.4)$$

Along the two edges, the rubber is under simple tension so that only edge strain needs to be calculated. Along edge AB, deformation is in uniform extension while along edge DC, strain is zero at the crack plane but rises to the same level as at AB. From the strain measurements, values of W are obtained, from which J may be calculated, assuming that the finite summations approximate the infinitesimal deformations of the line integral.

A multiple specimen, total energy drop method similar to that described by ASTM E813-81 was used with certain modifications. Although there is a requirement of multiple specimens, individual measurements can be checked for reproducibility and precision. The test is performed by a series of simple tensile measurements with basic instrumentation. Furthermore, the method has been well established in the engineering design community and has been applied successfully to a variety of polymers. These applications are discussed in the following section.

2.4.2.2. Measurements of J for Polymers. The development of the J integral in the last ten years has led to a substantial body of literature on the fracture

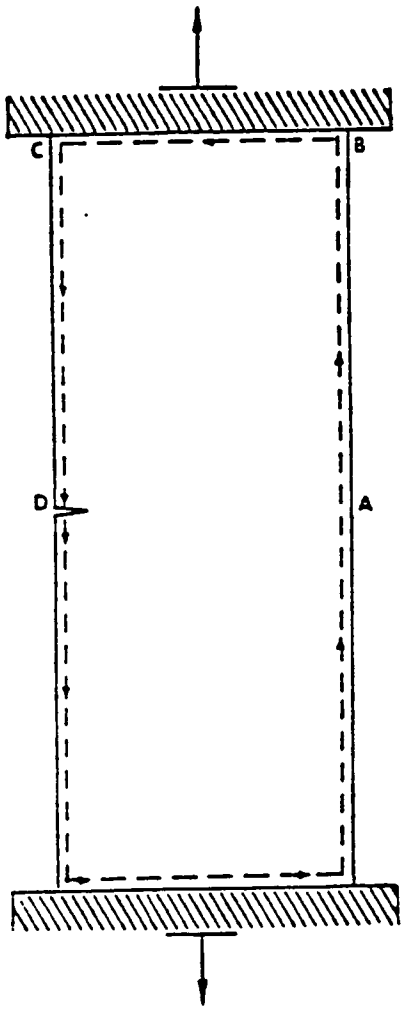

Figure 22: Simple extension specimen with a cut in one edge. Dotted line shows the integration path chosen to evaluate the J-integral. From Oh.[89]

properties of polymers. Most studies implemented the multiple specimen total energy drop method or a modified ASTM E813-81 test to determine J (or T). Much of the polymer data has been published within the last four years, although the J integral technique was first demonstrated for steel in 1972 by Landes and Begley.[86] A review of the polymer applications of this technique follows.

Hashemi and Williams[93] used the J integral method to examine temperature effects on the fracture toughness of low density (LDPE) and linear low density polyethylenes (LLDPE). Noting the failure of K measurements because of high toughness values, they proposed a method which followed ASTM E813-81. Their results are shown in Figure 23. Noting that considerable crack tip blunting preceded cracking, Hashemi and Williams showed that LDPE had low toughness and high ductility as a consequence of the low yield stress. LLDPE behaved qualitatively the same with higher fracture toughness values.

In another study, Hashemi and Williams[94] used the J method to characterize poly(vinyl chloride) (PVC), high density polyethylene (HDPE), rubber toughened PVC (r-PVC), acrylonitrile-butadiene-styrene (ABS), and an unspecified nylon. All these materials have a high toughness and low yield stress which disqualified the use of the ASTM test method E399 to determine the linear elastic K_{Ic}. The

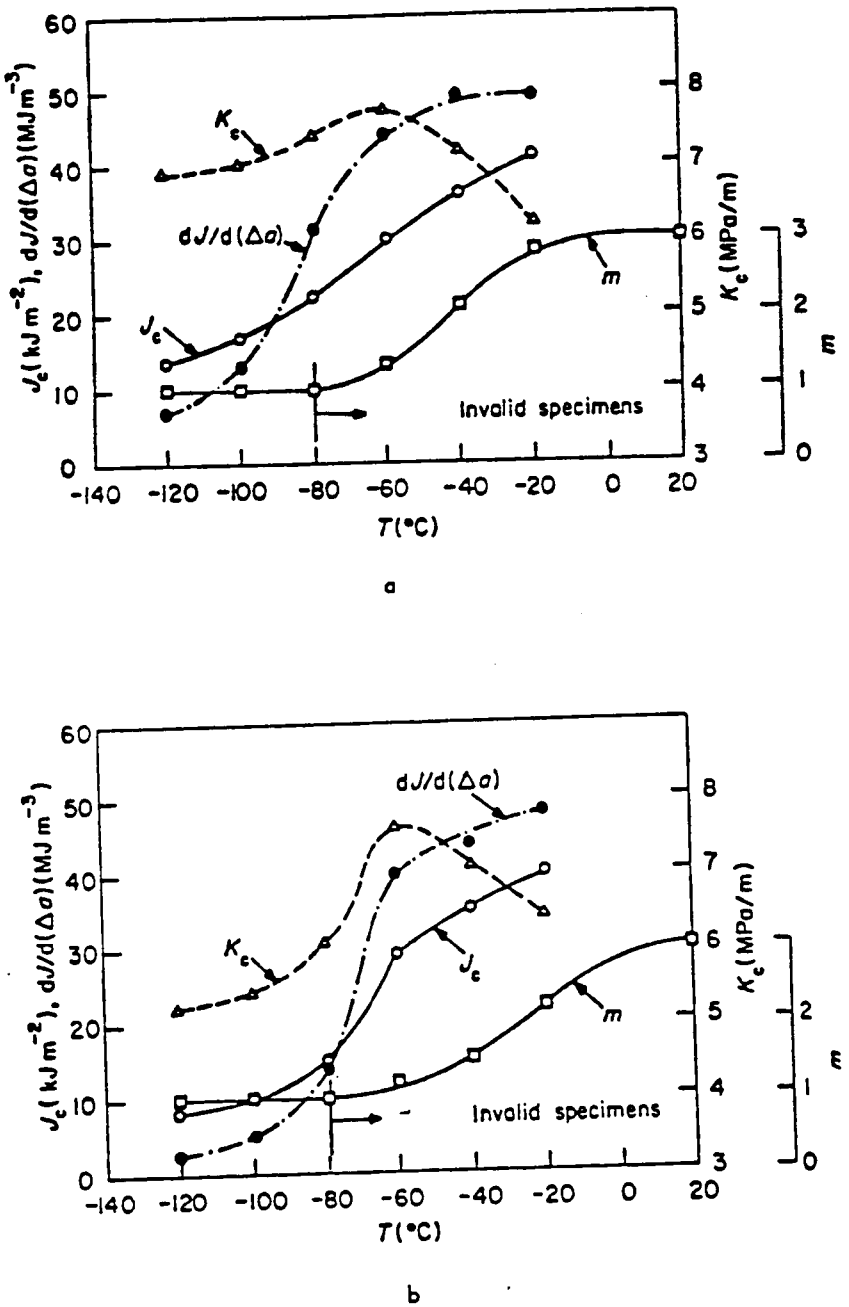

Figure 23: (a) Effect of temperature on Jc, Kc, dJ/d(Δa) and m for LDPE. (b) Effect of temperature on Jc, Kc, dJ/d(Δa) and m for LLDPE. From Hashemi and Williams.[93]

results are shown in Table I. PVC and HDPE displayed low J_c and $dJ/d\Delta a$ values. The polymers with a rubbery phase (r-PVC and ABS) had relatively small J_c values but were able to reach high $dJ/d\Delta a$ values leading to more stable crack growth and a lower tendency toward unstable failure. Nylon and polypropylene (PP) tended toward high toughness and high $dJ/d\Delta a$ values.

Huang and Williams[95] applied a modified ASTM E813-81 J method to measure the fracture toughness of three toughened nylons at room temperature and varying strain rates. The modifications corrected restrictions which were developed for metals and were not applicable to polymers. They included: limits on the span to depth ratio of test specimens, crack growth measurement techniques, crack resistance curve fitting, loading rates, pre-cracking methods, and yield stress definition according to Ward[85] rather than the 0.2% offset yield stress. Each correction tended to result in a more conservative estimation of J.

The three nylons used have the DuPont trade name Zytel. They were rubber-toughened semicrystalline nylon 66 (A), rubber-toughened amorphous nylon 66 (B), and moderately toughened semicrystalline nylon 66 (C). Huang and Williams showed that nylons A and C had a higher fracture toughness than the amorphous nylon. Although they used a uniform processing method, they did not

Table I. Comparison of Properties at 20°C.

Material	J_c (kJ/m^2)	$dJ/d(\Delta a)$ (MJ/m^3)	σ_y (MPa)	E (GPa)
PVC	1.7	0.33	60	3.6
HDPE	0.78	0.07	27	1.85
PVC-R	3.0	23.1	50	2.80
ABS	3.0	8.4	40	2.10
nylon	10.0	15.4	80	2.40
PP	15.5	25.0	30	1.40

Source: Hashemi, S.; Williams, J.G. Polymer **1986**, 27, 384.

account for processing variables in their sample preparation which may differ in real applications, nor did they examine the effects of processing on the crystallinity of their samples.

Modifications to the ASTM J integral method for use with polymers must be conducted with care. In a recent study of a copolyester/elastomer blend, Moskala and Tant[96] satisfied the J_{IC} specimen thickness requirement by lowering the temperature at which their test was conducted. As one might expect, they observed a loss in fracture toughness as the temperature was lowered to as low as -73 C. Although Moskala and Tant have made an interesting contribution to the properties of polymers at lower temperatures, in their desire to satisfy the ASTM validity test they changed the properties which they were trying to measure. The work of Moskala and Tant should be viewed, therefore, as a study of polymers at low temperatures and not represented as an attempt to demonstrate the applicability of ASTM E813. Future versions of ASTM E813 should specify the testing temperature to avoid confusion.

The studies cited have demonstrated the applicability of the J integral as a fracture criterion for polymers. They have shown that general, nonlinear elastic fracture mechanics may be used as a tool for materials characterization. Perhaps the most significant result is

that the fracture toughness of non-brittle polymers may be directly compared with the fracture toughness of rubbers without correction for different mechanical nonlinearities. Because the J integral is defined for any stress-strain curve, the same general fracture test for glassy polymers may be applied to rubbers.

2.5. Infrared Spectroscopy

Infrared spectroscopy (IR) is a tool used to examine several effects. In this study, IR is used primarily to characterize metal ion complexation of polyurethanes and calcium ions with time. As noted earlier, calcium ion complexation has produced spectral shifts of both the polyether and urethane bands of these polymers. It is believed that the molecular mobility of the polyurethane is restricted by the metal ion which leads to shifts in the vibrational spectrum.

An application of infrared dichroism was to examine molecular orientation in the fracture process using a microscope attachment. It was believed that the complex stress fields surrounding the crack tip led to molecular orientation which could be detected by infrared dichroism. It was therefore of interest to characterize the oriented state of a material prior to fracture and observe the trends leading to the propagation of a crack.

This review is divided into two subsections. The first reviews the theory of infrared absorption and the

information which may be obtained from a spectrum. The second discusses infrared dichroism and determining orientation functions.

2.5.1. Interpretation of Infrared Spectra

Infrared spectroscopy is a measure of the absorption of infrared light energy as a function of wavelength or frequency. Absorption of infrared radiation (IR) occurs when both of the following conditions are satisfied:

(1) The vibrational frequency of interatomic bonds matches the frequency of the incident radiation.

(2) There is an associated change in the dipole moment of the bond.

Both phenomena are shown schematically in Figure 24. Because the vibrational frequency of each bond depends on the atomic weights of the participating atoms and the electronic structure (ionic, covalent, etc.), ideally, the absorption frequency is unique for each bond. Deviations from ideality occur as intermolecular forces lead to distributions of frequencies of absorption, hence an infrared spectrum is composed of frequency bands and not frequency spikes.

Infrared spectrometers measure the absorption of infrared radiation as a function of the light frequency. The frequency at which radiation is absorbed is determined by the vibrational modes of intramolecular bonds. The vibrations which are commonly observed are shown in

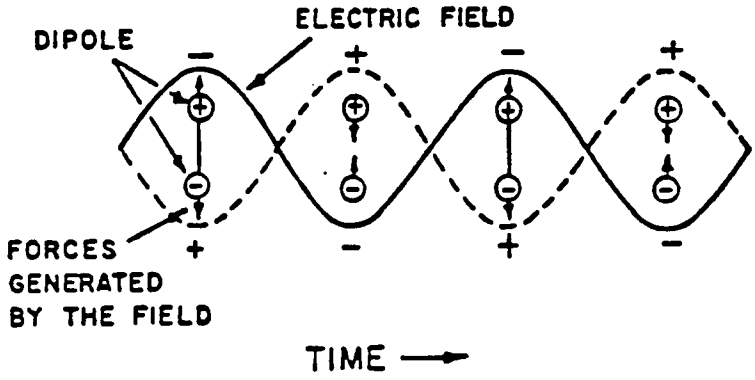

Figure 24: Diagram of the interaction of an oscillating electric field (light) with a vibrating dipole. From Koenig.[118]

Figure 25. They include bending, stretching, out of plane vibrations, wagging, rocking, and harmonics of these motions. The type and frequency of the vibration is unique for a combination of atomic bonds; some vibrational modes will be more strongly absorbing than others since certain molecular motions may occur more readily. Changes in these vibrational modes often are indicated by shifts in peak absorbance to higher or lower frequencies. Changes in the vibrational modes are often caused by physical or chemical forces such as hydrogen bonding, free volume changes, or chemical reactions. These changes may reflect the effects of processing variables as well.

Classically, the infrared spectrometer had a polychromatic source and gratings or slits which allowed a single frequency to pass to the sample for transmission measurements. The instrument had to have a slit program which attenuated the beam to allow for varying source power at different frequencies. A single scan of the mid-IR region commonly required several minutes for a relatively low resolution measurement. The weak power of the source required that thin sample films be used.

The modern Fourier transform infrared spectrometer (FTIR) is based on the Michelson interferometer having a highly efficient light source. A silicon carbide source provides a much higher intensity signal than older instruments, allowing the study of thicker samples. The

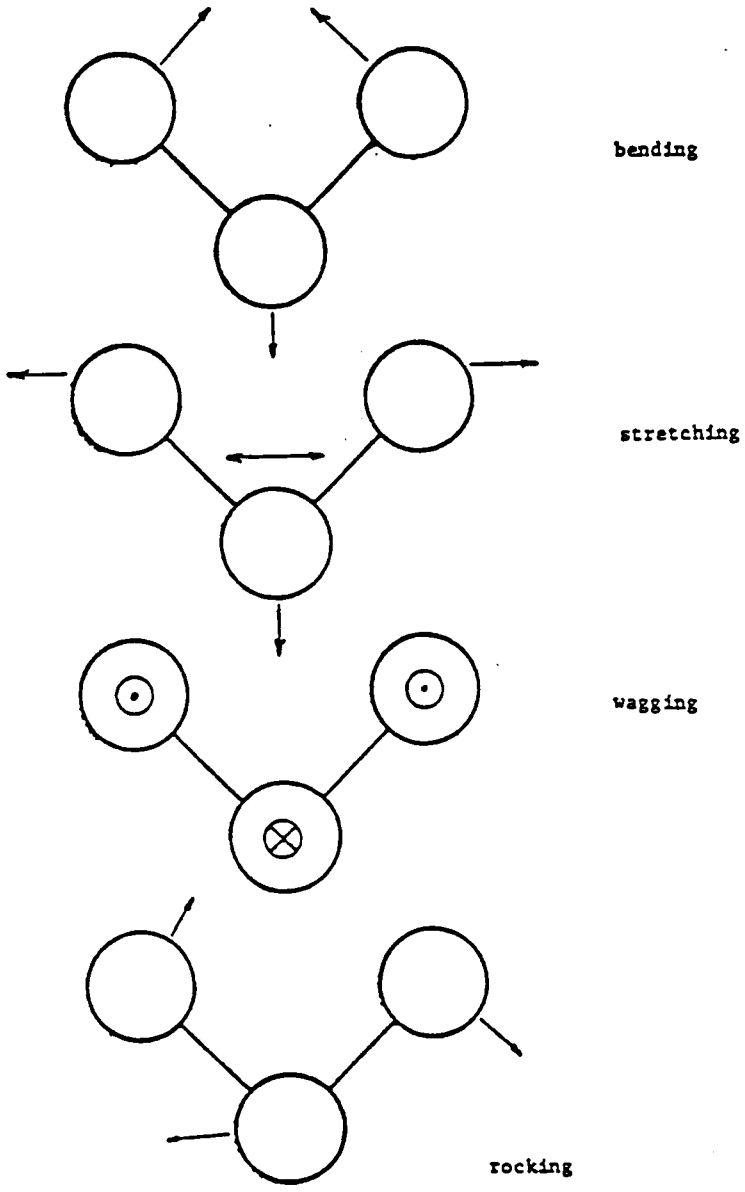

Figure 25: Commonly observed infrared vibrations.

Michelson interferometer has a moving mirror and a fixed mirror which are used in conjunction with a beam splitter to produce an interference pattern. In an FTIR, the Michelson interferometer produces an interference pattern of polychromatic infrared radiation which is detected by an infrared detector after transmission through a sample. All frequencies are passed and detected simultaneously resulting in a more efficient use of the infrared source radiation with higher energy throughput. Because the interference pattern will vary according to the absorption at each frequency, it is possible to perform a Fourier transform on the interferogram to resolve the absorbance of each frequency. The instrument takes advantage of the high speed computing abilities of the microcomputer for control, detection and calculation of the infrared spectrum. For the design advantages and shortcomings of FTIR spectroscopy, the reader is referred to other sources which cover the subject more thoroughly.[97]

The major advantages of FTIR spectrometers over grating instruments are:

(1) The resulting spectra have higher signal to noise ratios,

(2) the spectra are obtained more rapidly and

(3) the spectra have a stronger energy throughput. Because of the higher energy throughput, it is possible to focus or attenuate the beam for specialty applications

such as infrared microscopy, reflectance, attenuated total internal reflectance (ATR), diffuse reflectance (DRIFTS), and photoacoustic spectroscopy (PAS). For polymers, ATR (surface-depth studies), PAS (powders, pellets, and carbon filled samples) and infrared microscopy (microscopic structures, spherulites, impurities, trace amounts of sample) are commonly used in addition to transmission spectroscopy.[97]

2.5.2. Infrared Dichroism and Orientation Functions

The selectivity and absorptivity of interatomic bond vibrations can be used as a tool to measure molecular orientation. Using polarized infrared light to collect spectra, one may make comparisons of the absorbances in each polarization direction to determine the direction atomic bonds tend to favor. This is known as infrared dichroism. Fraser[98,99] was the first to quantitatively described the infrared dichroism phenomena in a study of globular proteins.

More specifically, infrared dichroism is a method for measuring the orientation of the transition moment of a bond, not the bond itself. Because the transition moment direction is usually within 2 to 3 degrees of the bond direction, the errors from this assumption are quite small.

In an oriented polymer sample, the molecular bonds and transition moments are preferentially oriented in

accordance with the processing or stresses applied in each direction. Using plane polarized infrared radiation, it is possible to determine the degree of orientation by comparing the absorbance for light polarized parallel to and perpendicular to the direction of stretch for a particular frequency. This model is shown in Figure 26. The ratio of the absorbances of the plane polarized in the parallel and perpendicular directions is the dichroic ratio:

$$D_{ij} = A_i/A_j \qquad (2.5.2.1)$$

where D_{ij} is the dichroic ratio with respect to the i and j directions, and A is the absorbance with light polarized in the specified direction. The orientation functions can be specified for both uniaxial and biaxial orientations with the measurement of appropriate dichroic ratios.

Uniaxial orientation functions from infrared dichroism were derived by Fraser.[98,99] The dichroic ratio was related to the Hermans' orientation function by:

$$f_H = \frac{A_1 - A_2}{A_1 + 2A_2} \quad \frac{A_1^\circ + 2A_2^\circ}{A_1^\circ - A_2^\circ} \qquad (2.5.2.2)$$

where A_j is the absorbance in the j principal directions and A_j° is the absorbance of a perfectly oriented sample. The orientation may also be expressed by:

$$f_H = \frac{D_{12} - 1}{D_{12} + 2} \quad \frac{D_{12}^\circ + 2}{D_{12}^\circ - 1} \qquad (2.5.2.3)$$

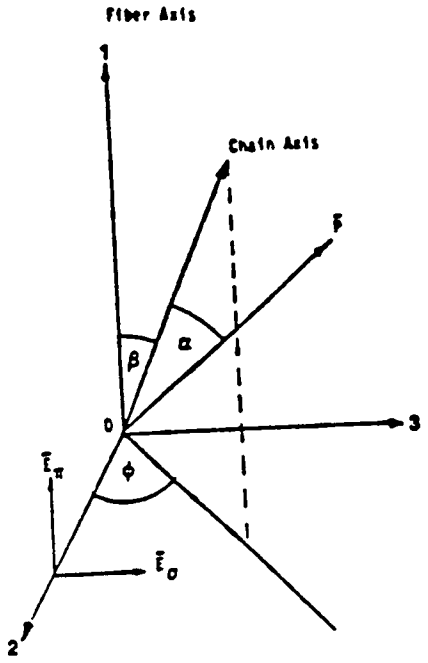

$\bar{E}$ = The electric vector of the incident polarized radiation. (The subscripts π and σ indicate the direction of the mutually perpendicular vectors.)

$\bar{P}$ = A vector representing the transition moment of a bond.

α = The angle between the transition moment direction and the chain axis.

β = The angle between the chain axis and the fiber axis.

ϕ = The angle between the 1 axis and the projection of the chain axis onto the 2-3 plane.

Figure 26: Model for infrared dichroism for uniaxially oriented systems.[98,99]

where $D_{12} = A_1/A_2$ and $D_{12}^{\circ} = A_1^{\circ}/A_2^{\circ}$. D_{12}° is the dichroic ratio for a perfectly oriented sample. If α is the angle between the transition moment and the polymer chain backbone, D_{12}° is given by:

$$D_{12}^{\circ} = 2\cot^2\alpha \qquad (2.5.2.4)$$

The advent of the modern FTIR has made measurements of infrared dichroism simpler because of it's high energy throughput. Early measurements of infrared dichroism by Read and Stein[100] and Stein, et al.[101] using grating infrared spectrometers demonstrated the applicability of the technique in orientation measurements of polyethylene and ethylene copolymers. Using wide angle x-ray diffraction, birefringence and infrared dichroism, Stein and his coworkers correlated measurements of orientation of crystalline and amorphous regions for a variety of polymers. Because infrared dichroism measures chemical bond vibration orientation, one may examine the orientation of particular vibration modes. Hence, Stein showed that it was possible to assign the gauche conformation vibrations primarily to the amorphous state and examine the orientation of that vibration.[100] The chemical dissimilarity of the hard segment urethane group and the soft segment polyether in this study, however, alleviates the complexity of Stein's interpretation.

Polyurethane orientation is easily determined by infrared dichroism because the crystalline domains are

predominantly urethane groups, while the amorphous matrix will be predominantly polyethers because of the chemical incompatibility of the copolymer segments. Previous studies of polyurethanes using infrared dichroism attempted to characterize the domain-matrix structure of the material. Early studies observed the change in orientation of the polyurethane hard and soft segments with stretching.[102-106] Laptij et al.[107] observed that linear crystallizable polyurethanes demonstrate an inversion of the N-H band dichroism on stretching with no inversion of the CH_2 group dichroism. Upon drawing, the N-H bond orients perpendicularly to the draw direction (and the main chain backbone), causing the denominator (perpendicular polarized absorbance) of the dichroic ratio to become large compared to the numerator. The CH_2 groups which are predominantly in the polyether segment tended to orient in the draw direction, hence, the lack of inversion or the dichroic ratio or change in orientation.

In a study of a polyurethane homopolymer, Wong[108] showed that dichroic ratios could be used to observe orientation. By examining a polyurethane with a short ethylene glycol "chain extender" as opposed to a polyether, the orientation effects of the soft segment could be minimized. Furthermore, the pure hard segment polymer reduced the effects of the associated phase separation. The results of the study identified a series

of bands which could be used to observe molecular orientation. The calculation of dichroic ratio is shown schematically in Figure 27. Infrared spectra were collected with the beam polarized parallel and perpendicular to the draw direction. After baseline correction, the parallel polarized spectrum was divided by the parallel polarized spectrum to yield a dichroic ratio spectrum. Table II lists polyurethane bands and their frequencies. The major bands for dichroic measurements were the hydrogen bonded N-H stretch band at 3320 $cm.^{-1}$, the free N-H band at 3450 $cm.^{-1}$, the Amide I band between 1750 and 1675 $cm.^{-1}$, the Amide III band for 1200 $cm.^{-1}$, and the methylene rocking band between 850 and 835 $cm.^{-1}$. This study demonstrated that infrared dichroism could be used to measure the orientation of polyurethane segments.

Young[109] reported the first application of microscopic infrared dichroism in a recent paper. Using polarized infrared microscopy, he measured the molecular orientation of a series of polyaramide fibers. As expected, Young observed that hydrogen bonding of these fibers approached a perpendicular orientation to the draw direction with increasing modulus. He concluded that because infrared dichroism was sensitive to both the crystalline and amorphous orientation, the technique was able to detect differences which were too small to be

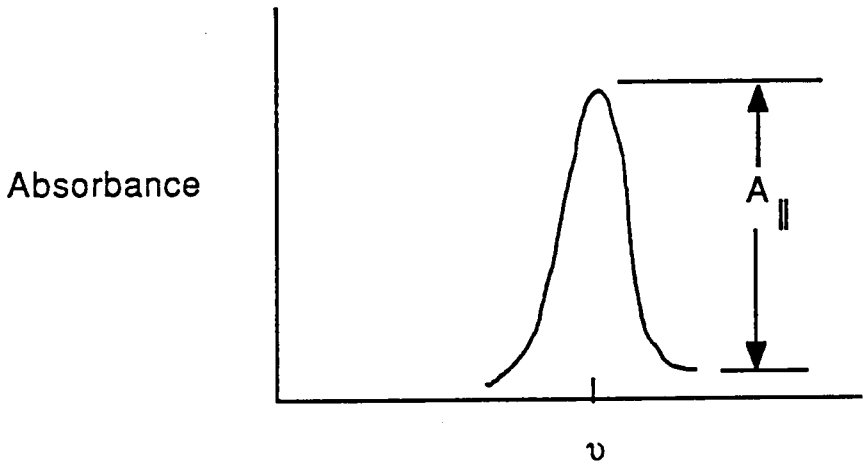

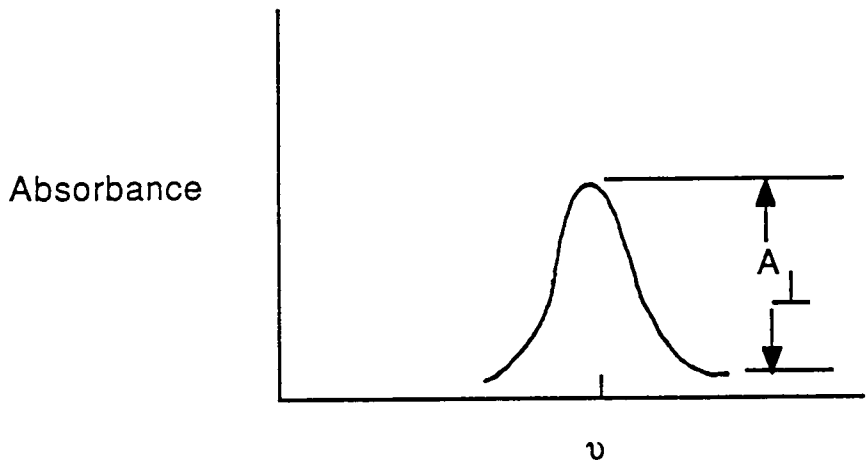

$$D = \frac{A_{\parallel}}{A_{\perp}}$$

Figure 27: Calculation of dichroic ratio, D, from infrared absorbance spectrum.

Table II. Infrared Band Assignments for Polyurethane.

Band $_{-1}$ (cm.	Bond Assignment
3335	N-H Stretch H-Bond
3190	N-H Stretch Cis/Trans Isomer H-Bond
3120	Amide II Overtone
3100-3000	C-H Stretch Aromatic Ring (3035)
2950	C-H Asym.
2910	C-H Stretch Sym.
1730	C=O Urethane Amide I H - Bond
1610	C=C Aromatic Ring Breathing
1595	C=C Aromatic Ring Breathing
1527	C-N Stretch, N-H Bend Urethane Amide II
1510	C=C Aromatic Ring Breathing
1480-1440	C-H Bend CH_2 (1455) C-H Bend Asym. C-H Aromatic Ring Breathing
1405	C=C Aromatic Ring Breathing
1382	C-H Bend Sym. CH_2 Wag $-OCH_2$
1325-1320	C-N Stretch Aromatic Ring CH_2 Twist (Shoulder)
1300	CH_2 Wag
1250-1200	C-N Stretch N-H Bend Urethane Amide III O=C-O Stretch Asym.
1205	C-H In Plane Bend Aromatic Ring
1182	C-H In Plane Bend Aromatic Ring (Shoulder)
1112	C-H In Plane Bend Aromatic Ring
1090-1072	O=C-O Stretch Sym. (Split)
1020	C-H In Plane Bend Aromatic Ring
980-960	C-H In Plane Bend Aromatic Ring, C-C-C- Stretch
912-900	C-H In Plane Bend Aromatic Ring, C-C-C Stretch
852	CH_2 Rock
820-800	C-H Out of Plane Bend Aromatic Ring

Source: Wong, R.P. MS Thesis, University of Utah, 1986.

observed by wide angle x-ray diffraction which only examines the crystalline orientation.

Infrared dichroism for the measurement of molecular orientation has been shown to be a most useful tool. The advent of high throughput infrared spectrometers has made it possible to perform experiments in a variety of configurations which were previously not possible. Molecular orientation can now be measured for microscopic samples, surfaces and thick samples through the use of reflectance and transmission techniques. These high throughput sources are also leading to developments in remote sensing through fiber optics. Although still in the developmental stages, remote sensing will become a major tool for on-line quality control in the chemical process and control field.

2.6. Literature Conclusions

The primary objective of this research was to explore polyurethane calcification and and the resulting mechanical properties. The resulting mechanical properties were shown to be associated with molecular structure and orientation as well as disruption of the microstructure of the polyurethanes. A secondary objectives included the development of instrumentation which could correlate stress, strain and orientation using rapid infrared dichroism measurements.

Because of the breadth of the subject, it was necessary to review the literature on biomedical polymer interactions, polyurethane material properties, polyurethane structure-property relationships, mechanical properties of elastomers, and polymer fracture. This study attempts to merge the currently unrelated fields of soft tissue biomedical polymers with engineering fracture analysis, hence, both fields can not be completely addressed. Specifically, this study did not involve any animal (in vivo) degradation testing, nor were blood components other than calcium salts examined. Omission of animal testing reduced the complexities of the genetic/biological interactions. To simplify the degradation effects, an in vitro model of an aqueous salt solution was used to test the polyurethanes.

In addition, no new fracture theories were advanced in this study, however, fracture energy measurements were used as a tool for comparing material properties. It is believed that an understanding of biomedical polyurethanes and fracture mechanics can be brought together as working tools of the material scientist.

3. EXPERIMENTAL

3.1. Materials

In this study, samples of the medical grade polyurethanes Biomer (Ethicon, Inc.) and medical grade Pellethane 2363 (Dow Chemical Co.) were examined. (Biomer is a medical grade version of the polyurethane introduced by DuPont in fiber form under the trade name Lycra.[2]) The samples were graciously donated by their manufacturers exclusively for this study. Both are copolymers synthesized from the end capping of polytetramethylene ether diol with 4-4'-methylenediphenyl diisocyanate (MDI). In the synthesis of Pellethane, the isocyanate end groups were then reacted with 1,4- butanediol to form a poly(ether urethane). In the case of Biomer, the remaining isocyanate end groups were reacted with ethylene diamine to form a poly(ether urethane urea). The chemical structures are shown in Figure 28. Biomer was received in a solution of dimethyl acetamide; Pellethane 2363 was in pellet form.

Thin films of Biomer and Pellethane were cast from 20 wt% solutions of dimethyl acetamide (DMAc). Films were also prepared from solutions with calcium chloride blended in 1, 5, and 10% by weight. All films were cast on clean glass plates using a casting knife. The solvents were driven off in a forced air oven at 80°C for 20 minutes.

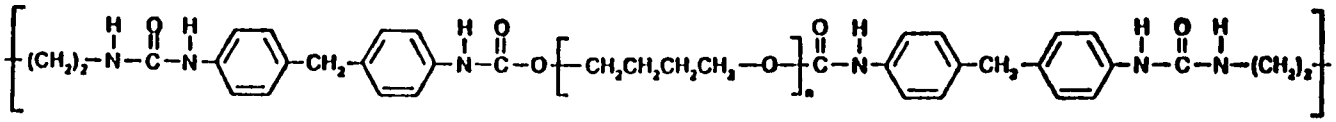

Biomer (Ethicon)

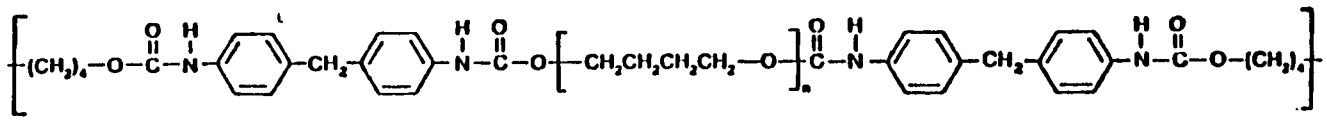

Pellethane (Dow)

Figure 28: Chemical structure of polyurethane elastomers used in this study.

3.2. Instrumentation and Equipment

An important goal of this study was to develop new instrumentation for analyzing the problem of stress-strain induced orientation effects on calcification. The extensive hardware and software development also provided tools for analysis of orientation and mechanical properties of other common synthetic polymers.

3.2.1. The Fourier Transform Infrared Spectrometer

A Digilab FTS-40 FTIR equipped with a UMA-300 infrared microscope was used to collect infrared spectra. The optical bench is based on the Michelson interferometer with a KBr beamsplitter. The detector in the main sample compartment is a pyroelectric bolometer type, deuterated triglycine sulfate (DTGS) detector. The microscope detector is a liquid nitrogen cooled, quantum type, mercury cadmium telluride (MCT) detector. The thermal TGS detector measures temperature changes with infrared radiation, while the quantum MCT detector measures changes in semiconductor properties with IR. As a result, the MCT type is a significantly faster detector. An infrared polarizer for the microscope attachment was directly mounted in the path of the infrared beam.

The microcomputer which controls the optical bench is based on the Motorola 68000 microprocessor and is operated by the Whitesmith's IDRIS (UNIX-like) operating system.

Bio-Rad DIGILAB software controlled the scanning and spectral data analysis.

The flexibility of the IDRIS operating system allows the user to write lists of commands which are executed sequentially. These lists of commands (not programs) are commonly referred to as macros. Macros can be written for any common operating system, however, the UNIX type environment allows for much greater control without resorting to programming in a language such as C or Pascal. Macros are particularly useful for repetitive tasks and maintaining reproducibility. Software macros were written to simplify the collection of spectral data. They are listed and described in Appendix A.

3.2.2. Tensile Mechanical Testing Instrument

A separate microcomputer based tensile tester was constructed to mount a film sample in the path of the infrared beam. The device was designed to allow for infrared dichroism measurements on the focal plane of the infrared microscope stage. The triggering mechanism was manually operated to coincide with collection of the infrared spectrum.

3.2.2.1. Hardware. Two JASTA Pulse Power (PP150-06) step motor driven linear actuators (drawing in opposite directions) were used to draw the films so that the samples remained centered under the microscope field. A schematic diagram of the equipment is shown in Figure 29.

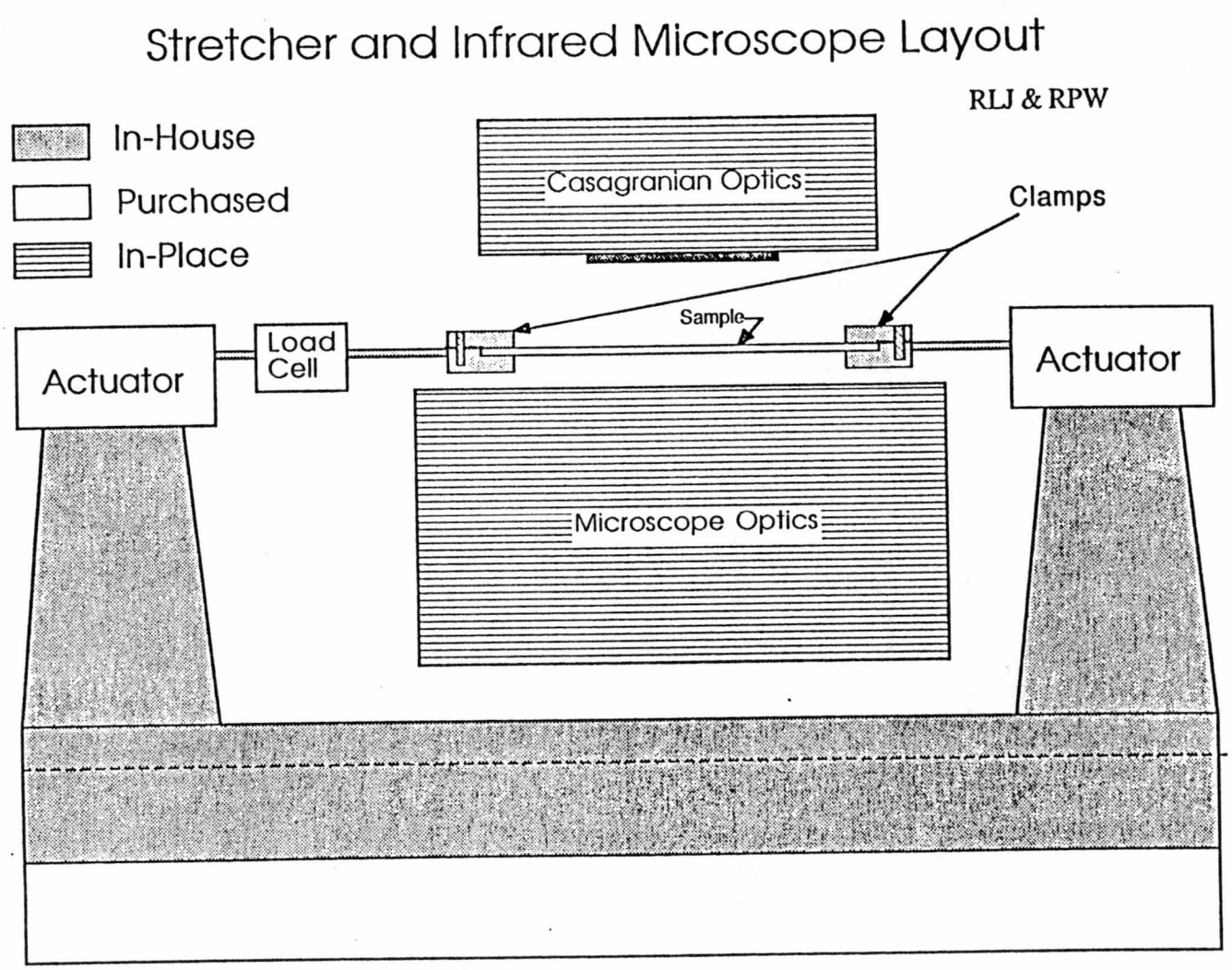

Figure 29: Layout of infrared microscope and tensile testing equipment.

The actuators were mounted on columns which move the motors vertically. This allows the user to focus the sample under the microinfrared attachment of the FTIR. Flat film self adjusting clamps were attached to the heads of the linear actuators. The clamps were designed to allow measurements of wide film samples which are used to measure crack growth of up to 8 cm. The mechanical drawings used in the machining of the equipment are in Appendix C.

The actuators were capable of applying a maximum of 89 N (20 pounds) of thrust while achieving stroke speeds of 12.7 cm/sec. (5 inches/sec.). At slower speeds, each actuator can apply up to 800 N (180 pounds) of thrust. Each actuator was precisely positioned by steps of 6.35×10^{-6} meters; with two actuators acting in concert, the positioning precision was 12.7×10^{-6} meters.

The actuators were controlled by a Step Pak motor controller Model MCU-2 and power supply Model PSU-2. The power supply was used to control the maximum work which could be done by each actuator. This was accomplished using potentiometers which limited current and voltage through the power supply. The motor controller acted as both a manual control for jog and slew functions as well as a controller which received control instructions from a serial communications port (9600 baud, no parity).

A Sensotec Model 450D load cell was attached to the left actuator to measure loads up to 222.4 N (50 pounds). The load cell was zeroed and calibrated using a digital display supplied by the manufacturer. A more rapid and precise Data Translation DT2821 A/D-D/A circuit board was also used to zero, calibrate, and collect load data.

Both the motor controller and the ADC board were connected to a Dell System 200 microcomputer. The microcomputer is based on the Intel 80286 microprocessor (IBM-PC AT compatible). This setup allowed for nearly simultaneous sampling of position and load for later calculation of stress versus strain curves.

For each of the hardware instrumentation components, appropriate software was written to precisely control the stretching experiments.

3.2.2.2. Software. To insure reproducibility and precision, a series of computer programs were written to collect sample data and store it in a format which could be recalled later for analysis. The software had the further requirement that it support and maintain compatibility with the hardware described in section 3.2.2.1.

All control software for the Dell System 200 was written in Borland Turbo Pascal version 5.5. The load cell (A/D) readings were obtained using Data Translation ATLAB software device drivers written in Turbo Pascal.

The motor control and position readings were measured directly from the motor controller. Each simultaneous measurement of position and force was timed using the internal clock of the Dell microcomputer. Each load cell measurement (A/D conversion) was the average of 100 data samplings which were accomplished in less than 0.2 of a second. For most tensile measurements, this rate is acceptable.

Three programs were written. The first program, CONTROL.PAS allows the user to manually send strings of commands to the motor controller (serial port) to acquaint one with the command syntax. The second program, MYATLEX.PAS, continuously displays the load cell reading for zeroing and calibration. A batch file was used to set the serial communications port and execute CONTROL and MYATLEX in sequence. The third program, STRETCH.PAS, controls tensile experiments.

The computer logic for STRETCH.PAS (the tensile experiment) is shown in the form of a flow chart in Figure 30. After initiation of the computer display, the program prompts the user for information regarding the sample, including the sample identification and dimensions. Next, the user is prompted for information about the nature of the tensile test including the strain rate (calculated from the dimensions of the sample), the maximum strains and/or stresses. If the input maximum values exceed the

Film Stretcher Control Based on Control Loop Diagram

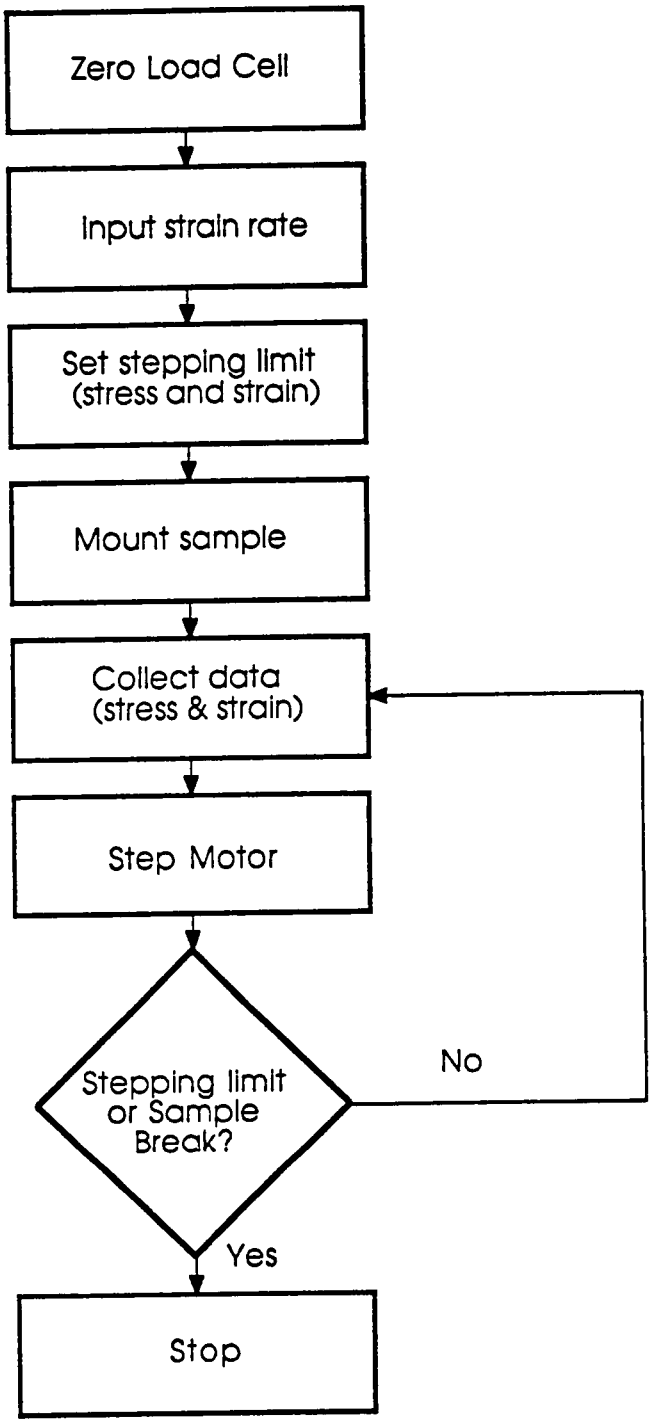

Figure 30: Flow diagram of software written for tensile test control.

hardware limits of the instrument, the program overrides the user input and sets maximum stress and strain values which prevent damage to the load cell and the step motors. The user is then given a chance to correct any input errors prior to initiation of the experiment.

The program was optimized for data collection at extremely low loads, particularly in the case of fracture of thin films. Although the load cell was capable of loads up to 200 N (45 pounds on a 50 pound maximum load cell), it was desirable to maximize the sensitivity for loads in the range of 0-5 N (or about one pound). At such low loads, however, random electrical background noise becomes a contributing factor in the measurements. It was therefore necessary to average 100 A/D conversions to reduce the effects of random noise by a factor of 10. The time required for the 100 conversions was typically 0.1 sec and was considered well below the allowable measurement time.

Stress was calculated based on the area of the film's uncracked dimensions:

σ = Force/Area = Force/(width x thickness)

After the stretching experiment began, each calculated stress-strain data pair is checked to insure that none of the maximum values has been exceeded; if it has been exceeded, the program terminates data collection and returns the clamps to their initial positions.

Furthermore, if any stress value is less than 20% of the maximum stress, the program terminates the experiment; the assumption in this case, is that the sample has broken. (The program was slightly modified to accept data for stress relaxation experiments as well.) The program may also be terminated by the user at any point by pressing any key on the computer keyboard.

After the data is collected, plots of stress versus strain are displayed on the computer screen using Pascal software units supplied in the Borland Turbo Pascal Graphix Toolbox version 4.0.

The source code of each program is listed in Appendix B.

3.3. Data Reduction and Analysis

3.3.1. Infrared Spectroscopy

Infrared spectroscopy was used in two related studies. An analysis of peak shape and position of the N-H stretch band was used to determine the nature of calcium salt interaction with the domain.

The second study examined molecular orientation surrounding the crack tip by infrared dichroism. The details of infrared dichroism are discussed in section 2.5.2. The dichroic ratio in uniaxial orientation is measured by the ratio of absorbed light polarized parallel and perpendicular to the draw direction.

The spectral data was analyzed first using the standard spectral software of the Digilab 3240-SPC data station.[110] This included the pkpick program which located peaks by absorbance strength. The search sensitivity selected by the user determined the peaks which were labeled. This program removes the subjective method of identifying the significance of absorbance peaks. It was possible, therefore, to use only the spectral data which met the sensitivity criterion, while ignoring spectral data which could be attributed to trace impurities, random noise, atmospheric water and carbon dioxide.

PEAKS.PAS was a program written in Turbo Pascal 5.5 to rapidly identify the peak absorbances. A flow chart of this program is shown in Figures 31 and 32. The program searches selected libraries of infrared spectral data by frequency (in cm^{-1}) for peak absorbances. The libraries are arranged by class of organic compound (e.g. amides, esters, alcohols, alkanes, etc.) for rapid identification as well as a general library containing all bands when the nature of the material is completely unknown. Currently, the library contains the major absorbance frequencies identified by Bellamy in reference 111. This program is also quite useful for the identification of unknown organic compounds and polymers.

Flow Diagram for Pascal program PEAKS.PAS

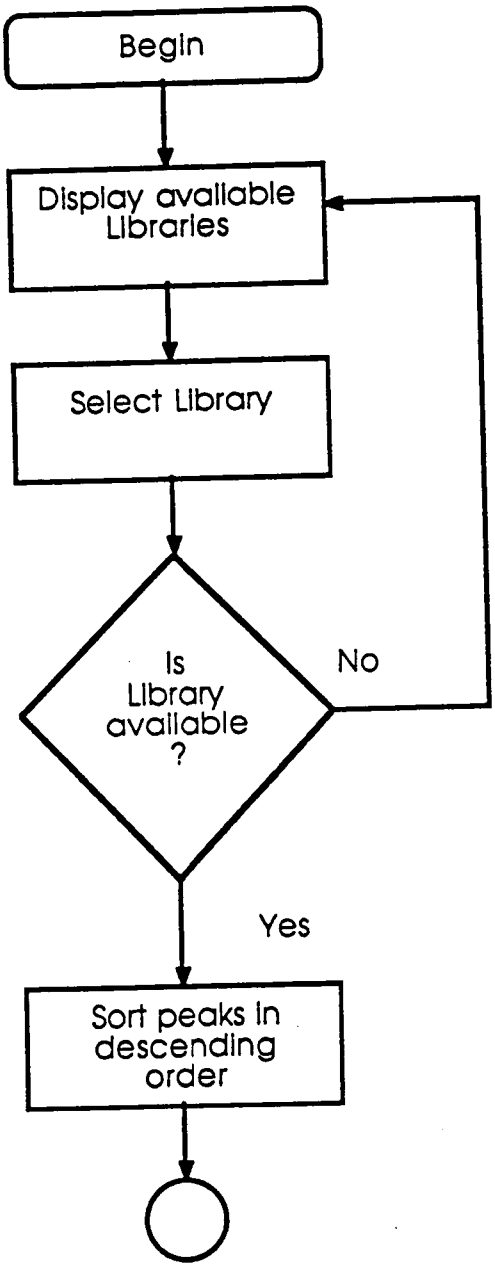

Figure 31: Flow diagram of software written for analysis of infrared spectra. Initializing the program and sort data.

Flow Diagram for PEAKS.PAS continued

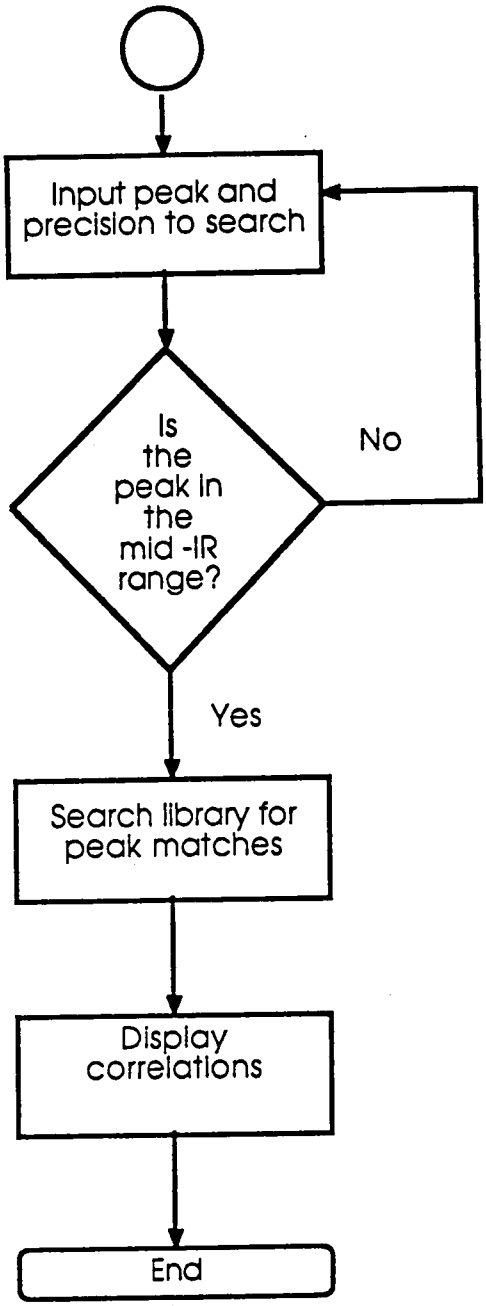

Figure 32: Flow diagram of software written for analysis of infrared spectra. Executing a comparison search and termination.

3.3.2. Fracture Property Measurements

Fracture toughness was determined using a multiple specimen method with varying initial crack lengths. The method is a variation of the total energy drop method discussed in section 2.4.2. The polyurethane sample films (in all calcium blend and uptake experiments) were cut with a razor into 3.8 cm. by 3.8 cm. samples. The film thicknesses for each sample were measured by micrometer. Initial crack lengths ranging from 0.25 to 1.0 cm were introduced into the films. The films were drawn at a strain rate of 20% per second. Low level noise in low load measurements of Pellethane was removed using a five point averaging digital low pass filter. The digital filter had a negligible effect on all subsequent calculations of strain energy.

The total change in internal elastic energy upon fracture, U, was measured as the total area under the stress versus strain curves to break for various initial crack lengths:

$$U = \int_0^{\epsilon_b} \sigma \, d\epsilon$$

U was calculated using a direct numerical integration of the data by the trapezoidal approximation.[112]

Fracture of the thin films followed two distinct patterns. The first pattern, observed for the longer initial cracks, was a rapid tearing of the material with

only a small amount of stretching prior to rapid failure. When normalized to the length of the uncracked ligament, this behavior is directly related to the J integral:

$$J = (1/B)(-dU/da)$$

where almost all the strain energy is absorbed in the form of crack propagation. For short cracks, the crack tip tended to blunt under the high elasticity of the rubber; the film absorbed a large amount of tensile energy as a result of a reduction of configurational entropy, or increasing orientation. After blunting, the crack propagated rapidly to failure.

The crack length at which these two patterns of behavior converge on the strain energy curves is the point of crack instability, a_c. The strain energy plots show this behavior as a discontinuity or deviation from a linear behavior observed for the longer cracks. Cracks longer than the instability crack length propagated rapidly to failure upon the application of a small strain energy. Cracks which were shorter than the instability length did not propagate until sufficient strain energy had been absorbed; the blunting of the crack tip was related to the elongation of the material prior to failure. The instability condition was not always clear, particularly as the strain energy curves varied with salt concentration.

3.4. Experimental Methods

3.4.1. Fracture Property Changes with Calcium Chelation

Fracture property changes with blended calcium chloride were observed by a series of fracture tests. Samples of Biomer and Pellethane blended with varying concentrations of calcium chloride were used to determine the fracture instability criteria. Instability values of toughness were determined from approximate discontinuities in total strain energy vs. crack length curves

3.4.2. Molecular Orientation of Polyurethanes

Uncracked film samples of Biomer and Pellethane blended with 0, 1, 5, and 10% wt. of calcium chloride were tested at 0, 10, 50, and 100% strain. The films initially measured 3.8 cm long by 1.3 cm wide and were of thicknesses between 0.0025 and 0.005 cm. Infrared dichroism was used to measure molecular orientation by examining bands assigned to the hard segments and soft segments as in previous studies. The crystalline domain orientation functions were calculated from dichroic ratios of the N-H stretch absorbance in the region of 3320 cm^{-1}. The soft segment polyether orientation was followed using the C-H stretch vibration in the region of 2800 cm^{-1}. The orientation functions were calculated directly from the dichroic ratios, assuming a perfect orientation condition occurs when the C-H and N-H vibrations are perpendicular to the chain axis or:

$\alpha = 90°$

$D° = 2\cot^2\alpha = 0$

$f = (D-1)(D°+2) / ((D+2)(D°-1)) = -2(D-1)/(D+2)$

where D is the measured dichroic ratio.

Plots of the change in the orientation function, Δf, with strain were calculated for each calcium chloride concentration and polyurethane.

3.4.3. Orientation of the Crack Tip Field

Calcium blended samples and untreated polyurethane samples, were subjected to measurements of orientation surrounding the crack tip. Fracture specimens of these polymers with initial crack lengths approaching the instability crack lengths were loaded to 20% strain. Because the stress intensification is greatest in the vicinity of the crack tip, a series of microinfrared dichroism experiments were conducted at positions parallel to and in front of the crack (HRR stress field regions). The positions of orientation measurement are shown in Figure 33. These regions included two positions of the highly nonlinear plastic zone at the crack tip (positions 1 and 4), and two positions of the HRR plastic zone (positions 2 and 3).

The collection of FTIR data was rapid enough to prevent significant stress relaxation effects in the measurements. (The stress relaxation was typically 1% of the maximum stress.) Preliminary benchmarks estimated

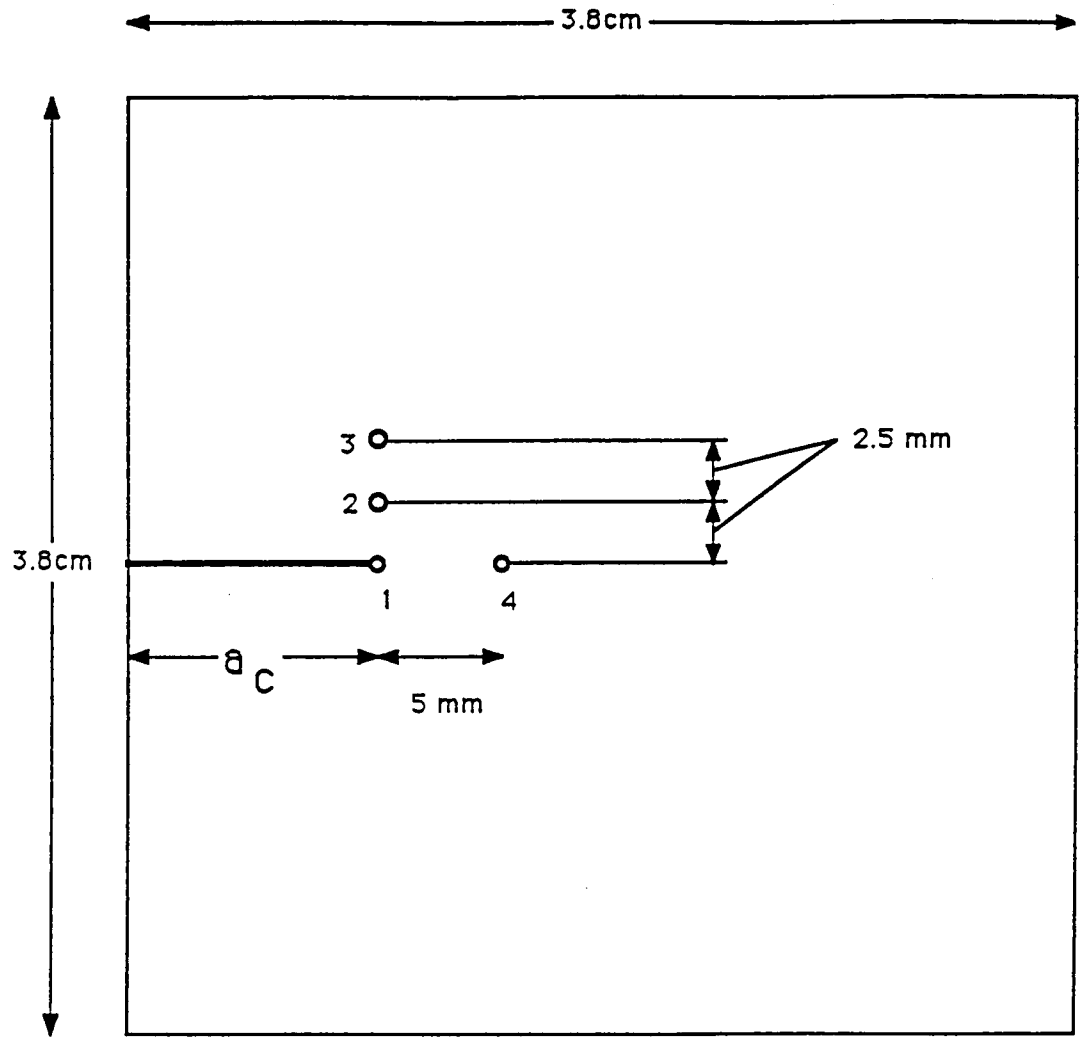

Figure 33: Map indicating positions analyzed for stress induced orientation using infrared micro-dichroism.

scanning times to be about one minute for a complete dichroic ratio measurement (two spectra) while significant stress relaxation does not occur two minutes after step loading, as discussed in section 2.2.4. Furthermore, it is believed that the remaining elasticity of the material allowed for large deformations prior to crack growth which presented measurable orientation in all regions surrounding the crack tip.

Maps of orientation surrounding the crack tip were prepared. The sample symmetry made it necessary to measure orientation on either side of the crack only. The orientation functions measured in each region as instability conditions are approached are referred to as the critical Hermanns orientation function, f_{Hc}.

3.4.4. Changes in Mechanical Properties with Calcium Uptake

The polyurethane films described in section 3.1. were immersed in a tank containing an aqueous solution of calcium chloride. The calcium salt concentration was approximately the concentration found in the body, about 11 mg/100 ml.[113] The tank was stirred continuously with a magnetic stirring bar to prevent the formation of boundary layers. The samples were withdrawn from the tank after thirty days. The samples were dried under vacuum at 40°C. Control samples of each polymer were similarly treated in deionized water without the calcium salts.

Fracture properties were measured as described in section 3.3.2. Tensile fracture tests were performed to observe mechanical property changes due to the uptake of calcium.

Calcium ion chelation was observed by FTIR spectroscopy as in the studies described in section 2.2.3. The effects of calcium chloride blended into the polyurethane films was examined to correlate with the aqueous solution uptake study.

4. RESULTS

In attempting to understand the structure and mechanical properties of the interaction between medical polyurethanes and calcium salts, this study also extended methods of examining polymer orientation and mechanical properties. A general result of this study, therefore, was an increased understanding of the calcification of polyurethanes through the development of instrumentation for the general study of polymers properties.

The experimental data and results of the experiments are presented in this chapter. Comparisons and analysis of the data are presented in the following discussion chapter.

4.1. Fracture Property Changes with Calcium Chelation

The mode 1 (tensile) mechanical fracture tests were performed on the polyurethane films blended with different calcium chloride concentrations. A second order polynomial (parabolic) curve fit was calculated with the stress versus strain data and plotted in the form of a solid line.

Figure 34 shows the stress plotted as a function of strain for pure Biomer with varying initial crack lengths. The areas under these curves representing the strain energy to failure, U, were plotted as a function of the initial crack length, a, and the crack extension to

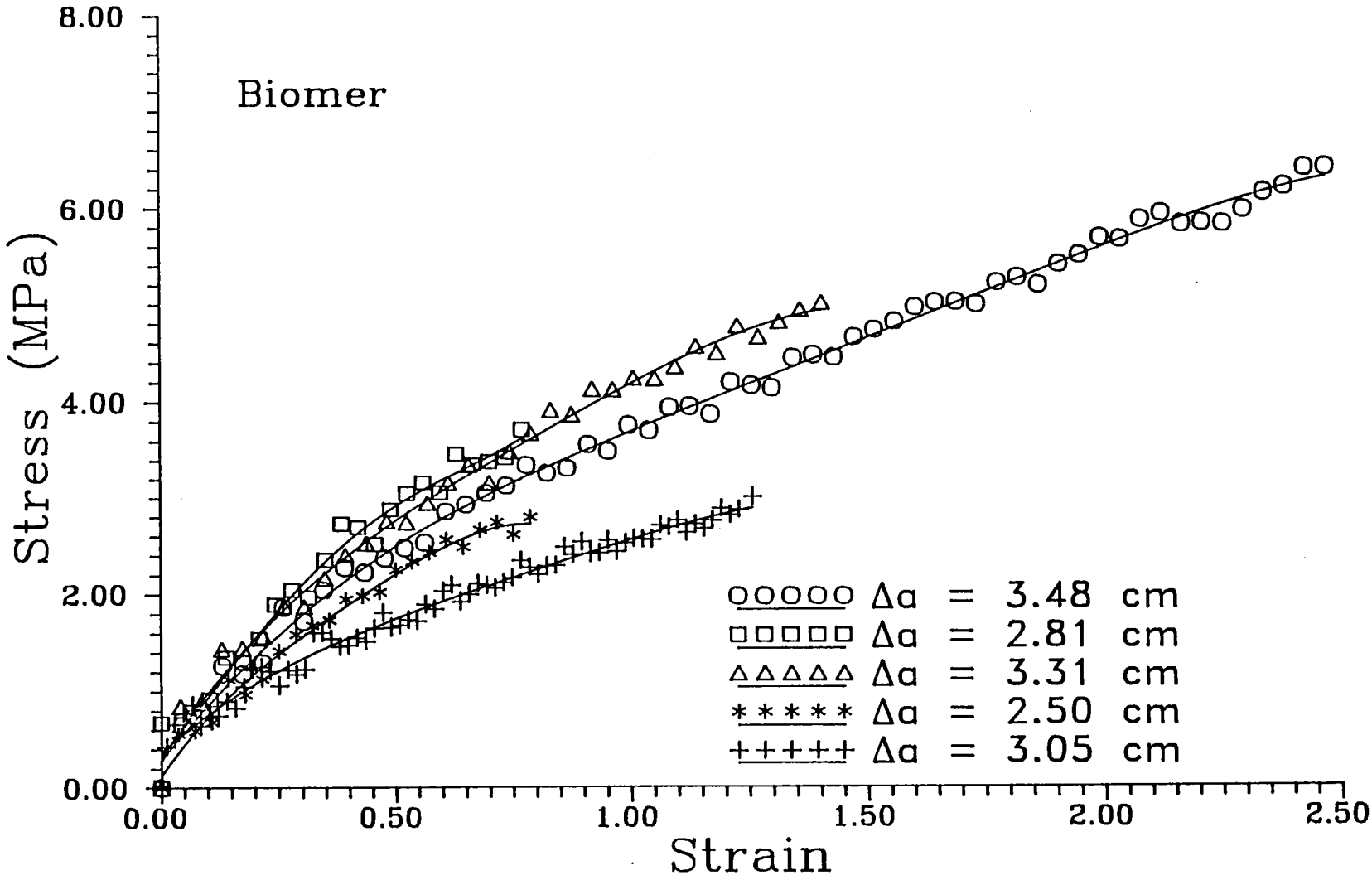

Figure 34: Stress versus strain data for pure Biomer films with varying crack growth to failure.

failure, Δa. These are presented in Figures 35 and 36, respectively.

Similar tests were conducted for Biomer blended with 1%wt. of calcium chloride. Figure 37 shows the stress plotted as a function of strain for Biomer blended with 1%wt. calcium chloride with varying initial crack lengths. Values of U were plotted as a function of a, and Δa. These are presented in Figures 38 and 39, respectively.

Figure 40 shows the stress plotted as a function of strain for Biomer blended with 5%wt. calcium chloride with varying initial crack lengths. Values of U were plotted as a function of a, and Δa. These are presented in Figures 41 and 42, respectively for the 5%wt. calcium chloride samples.

Figure 43 is a plot of the stress versus strain for Biomer blended with 10%wt. calcium chloride with varying initial crack lengths. Values of U were plotted as a function of a, and Δa. These are presented in Figures 44 and 45, respectively for the 10%wt. calcium chloride samples.

Identical fracture experiments were conducted on Pellethane 2363 and blends of Pellethane with calcium chloride. Because Pellethane does not maintain its elastic properties as well as Biomer, similar test specimens of Pellethane had lower forces and stresses. The resulting stress versus strain data has more scatter

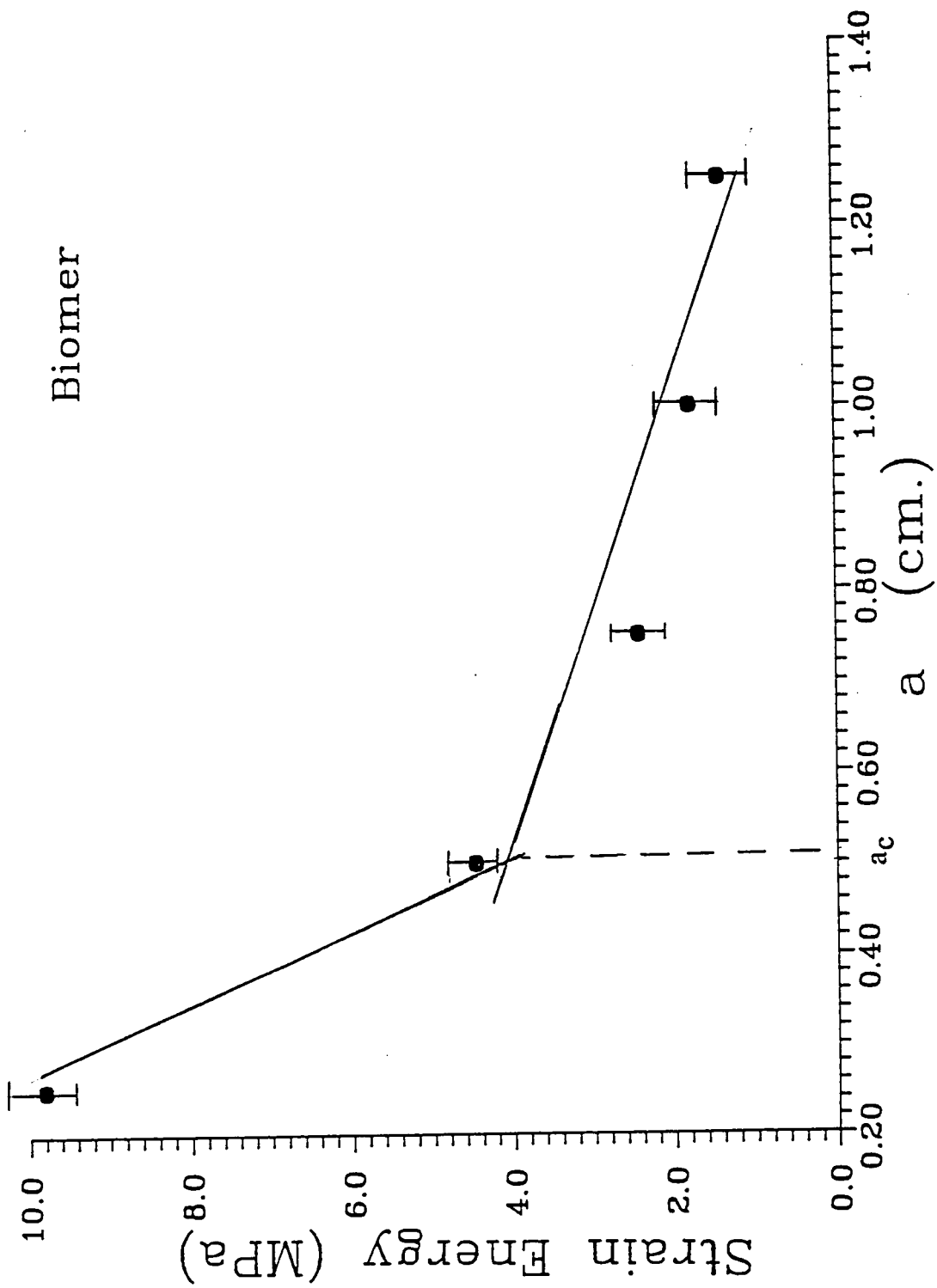

Figure 35: Strain energy to failure versus initial crack length for pure Biomer.

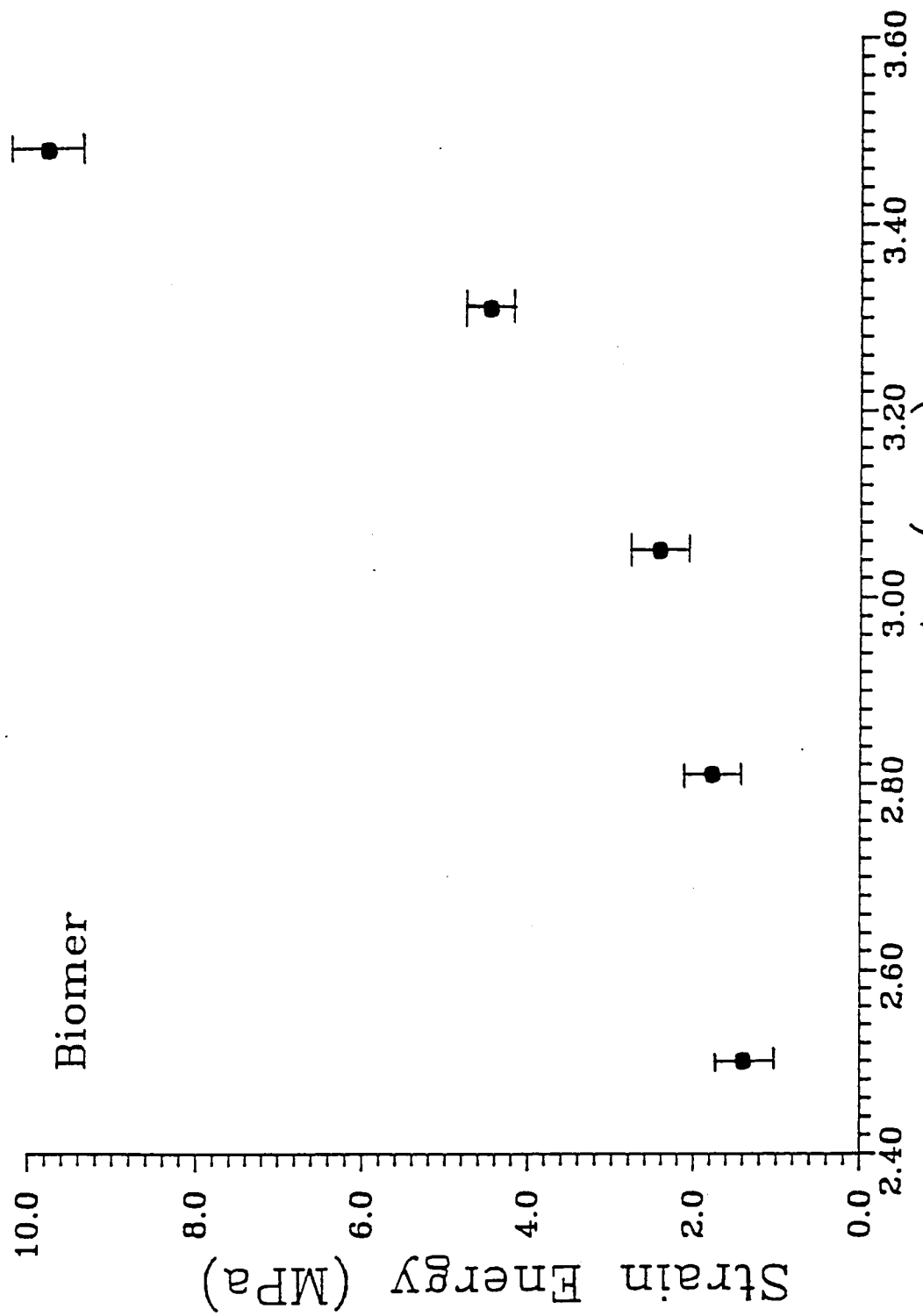

Figure 36: Strain energy to failure versus crack growth to failure for pure Biomer.

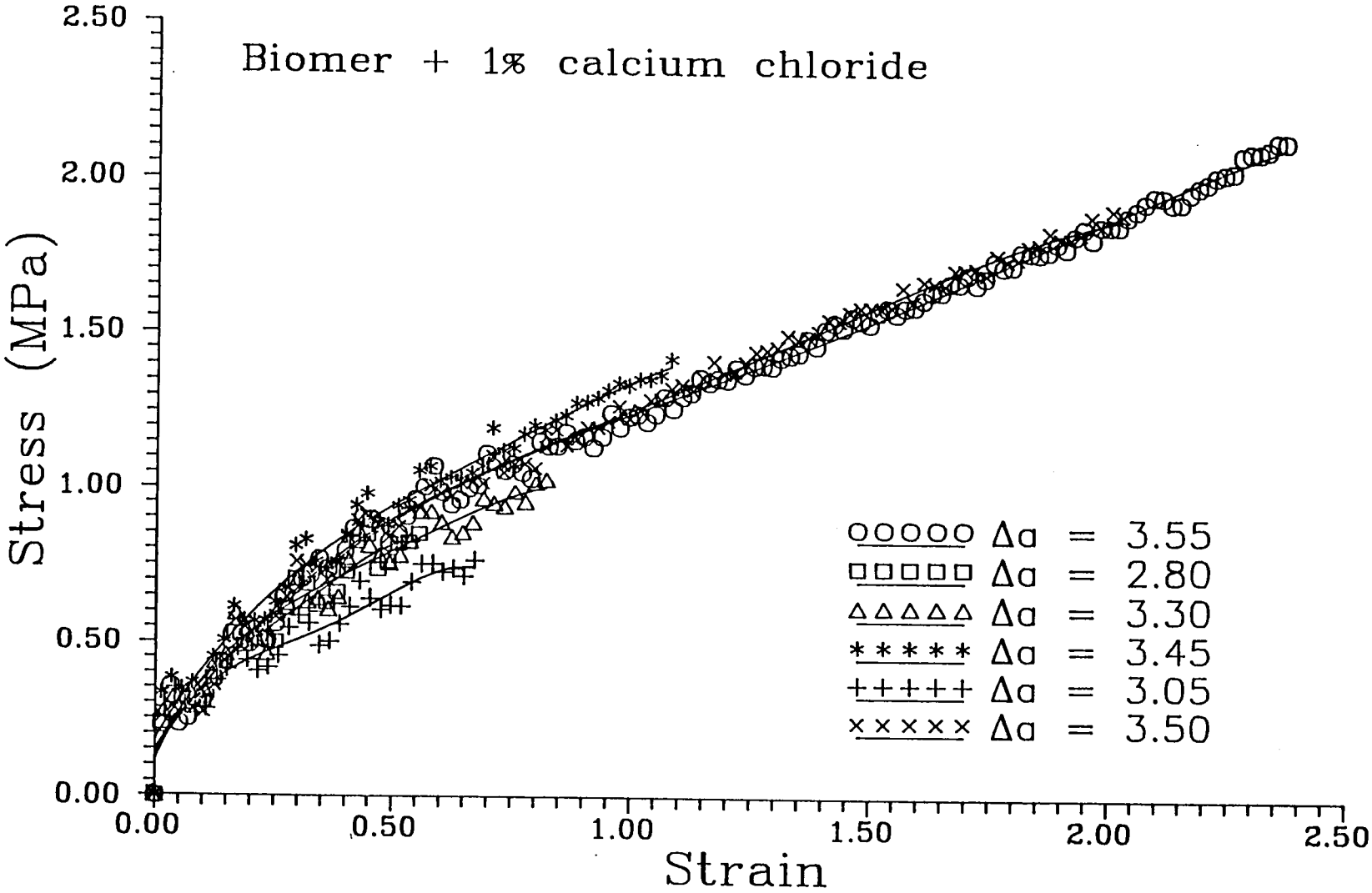

Figure 37: Stress versus strain data for Biomer blended with 1% wt. calcium chloride with varying crack growth to failure.

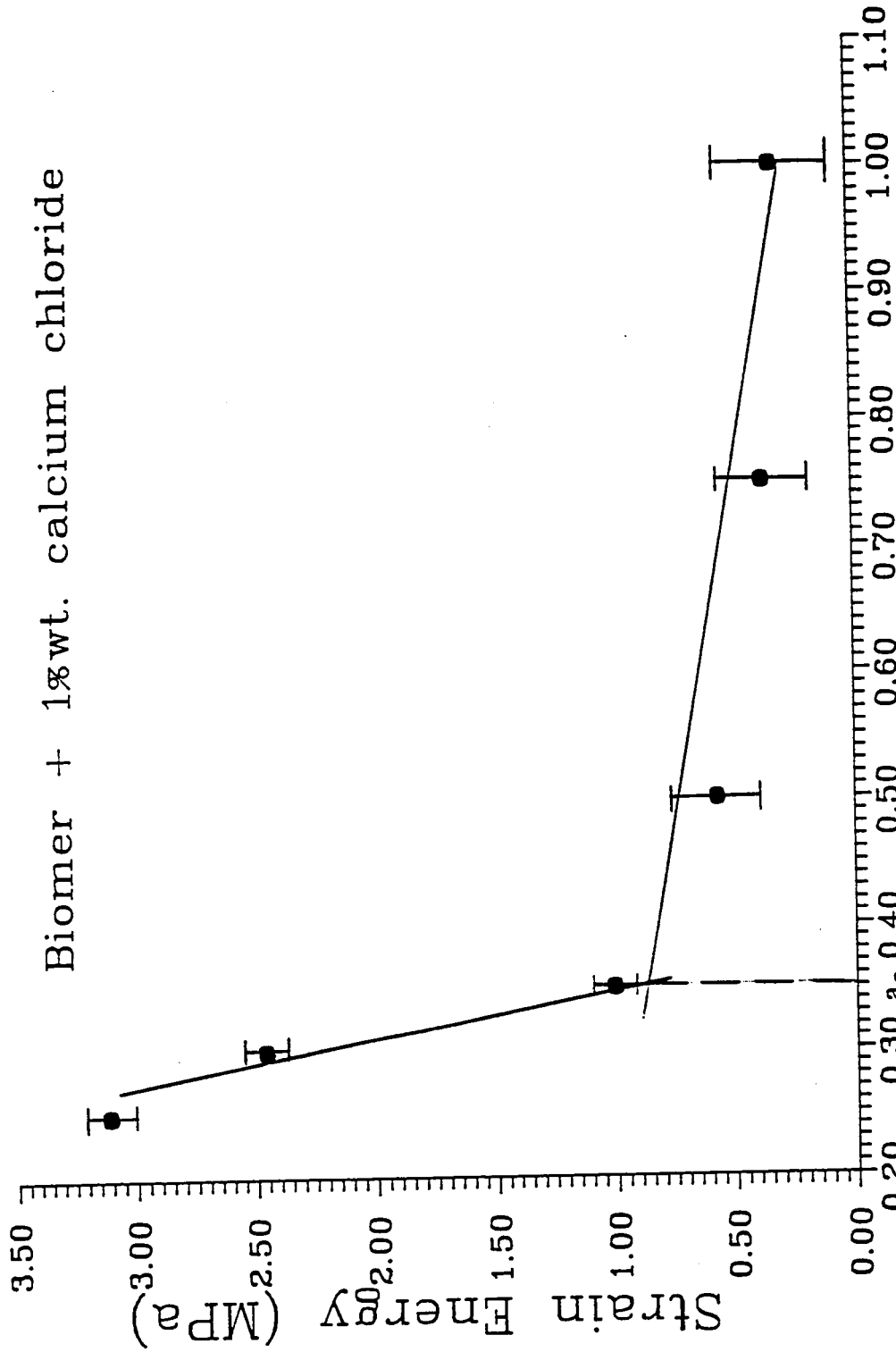

Figure 38: Strain energy to failure versus initial crack length for Biomer blended with 1% wt. calcium chloride.

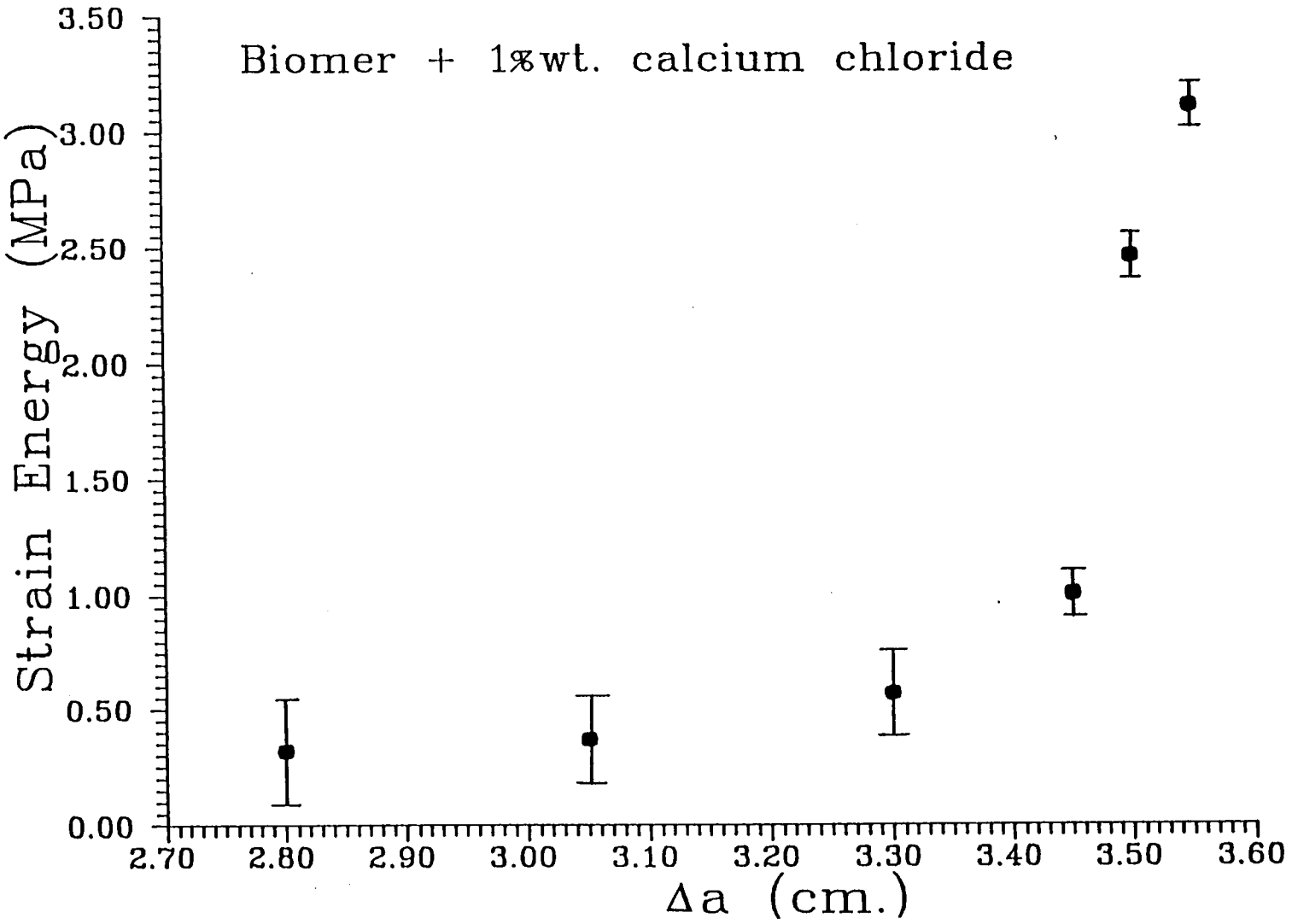

Figure 39: Strain energy to failure versus crack growth to failure for Biomer blended with 1% wt. calcium chloride.

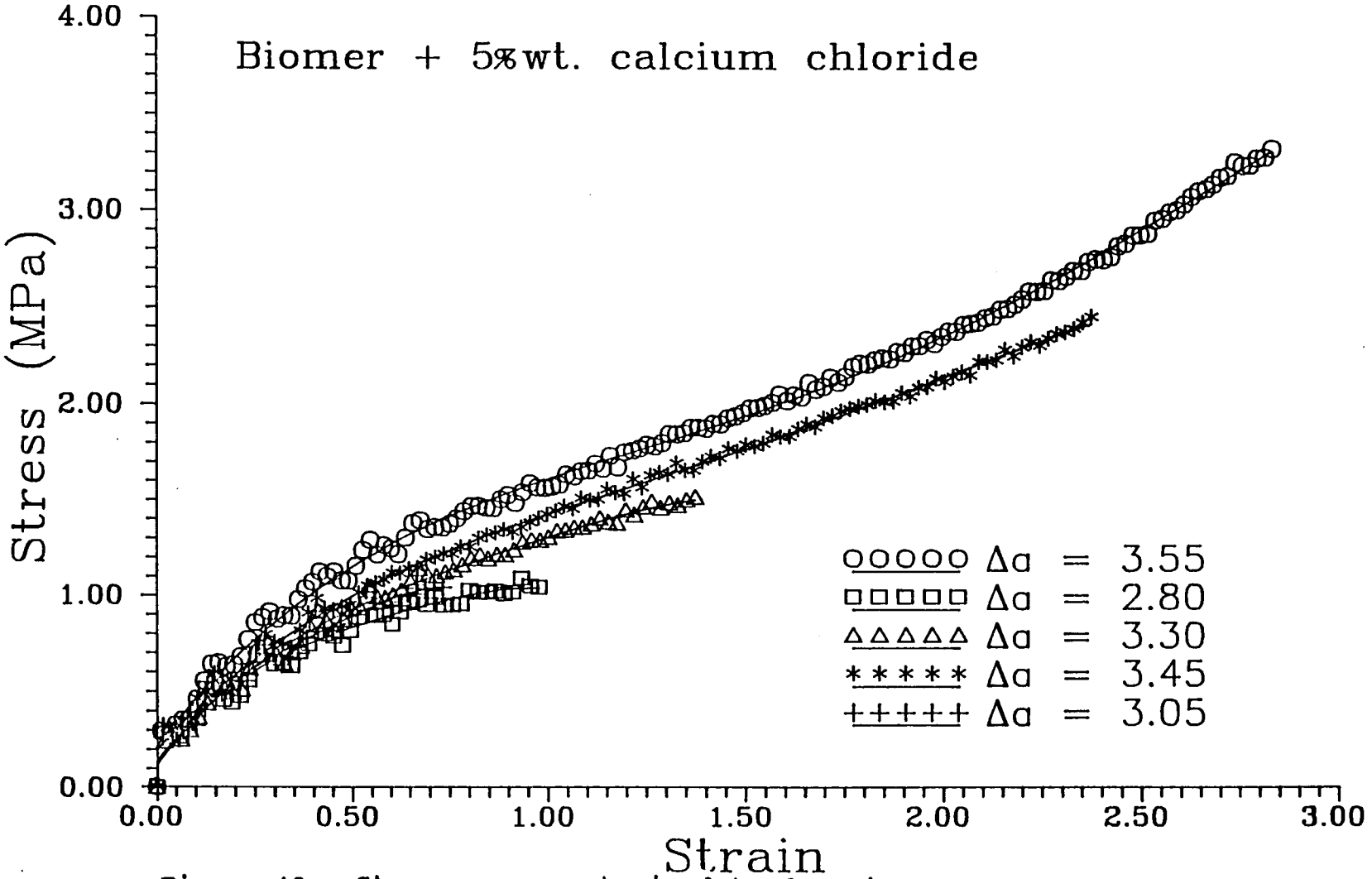

Figure 40: Stress versus strain data for Biomer blended with 5% wt. calcium chloride with varying crack growth to failure.

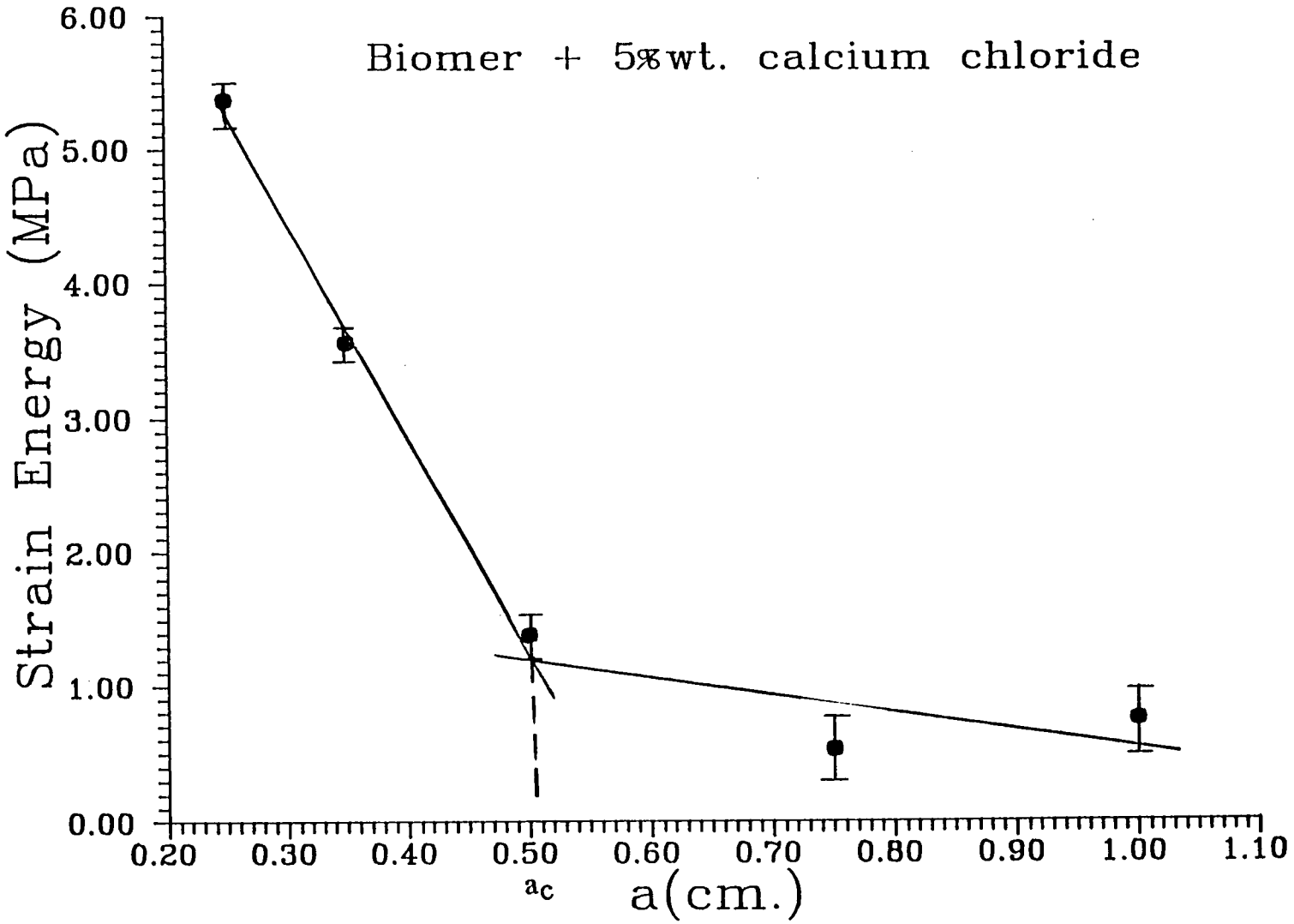

Figure 41: Strain energy to failure versus initial crack length for Biomer blended with 5% wt. calcium chloride.

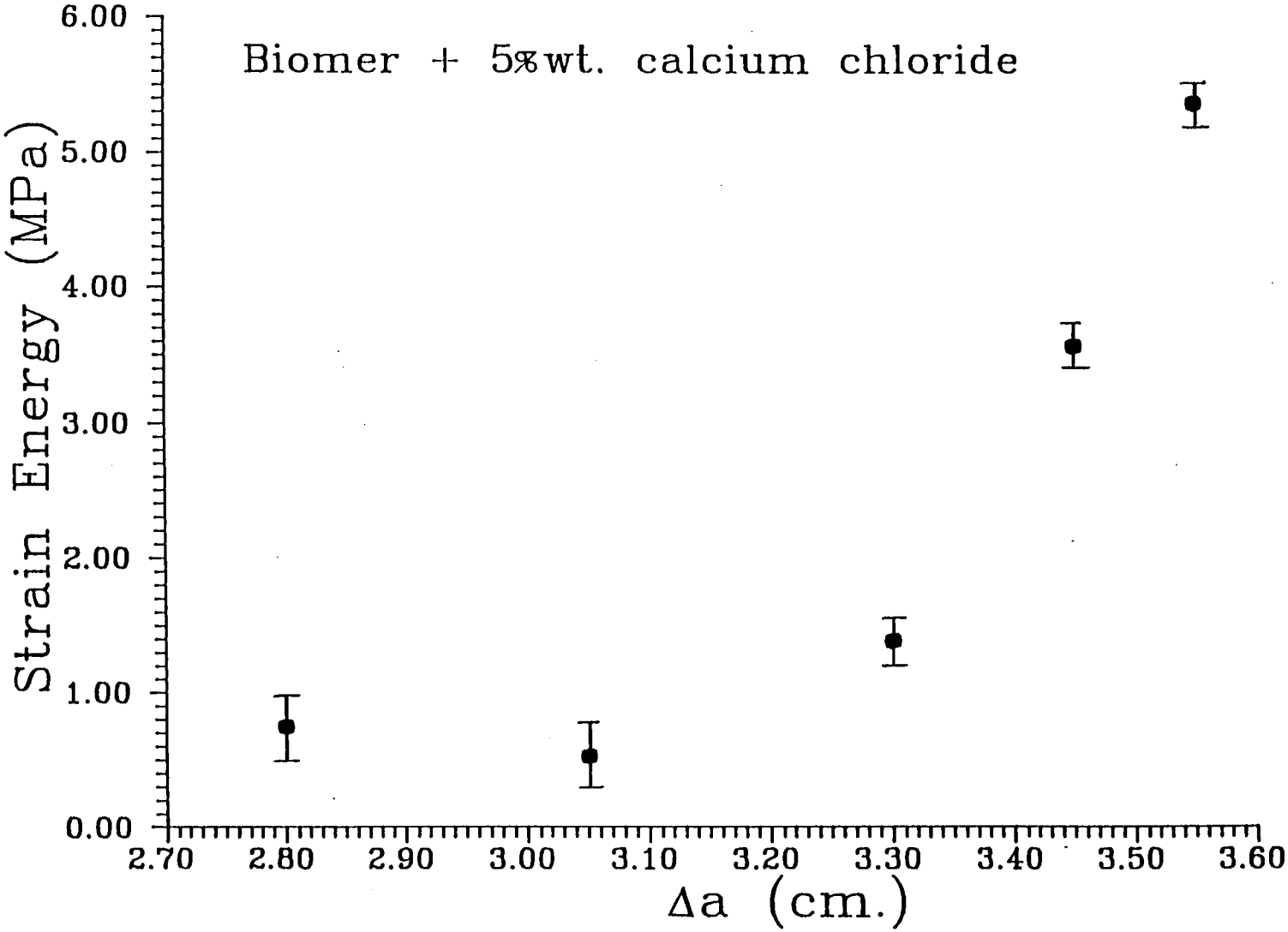

Figure 42: Strain energy to failure versus crack growth to failure for Biomer blended with 5% wt. calcium chloride.

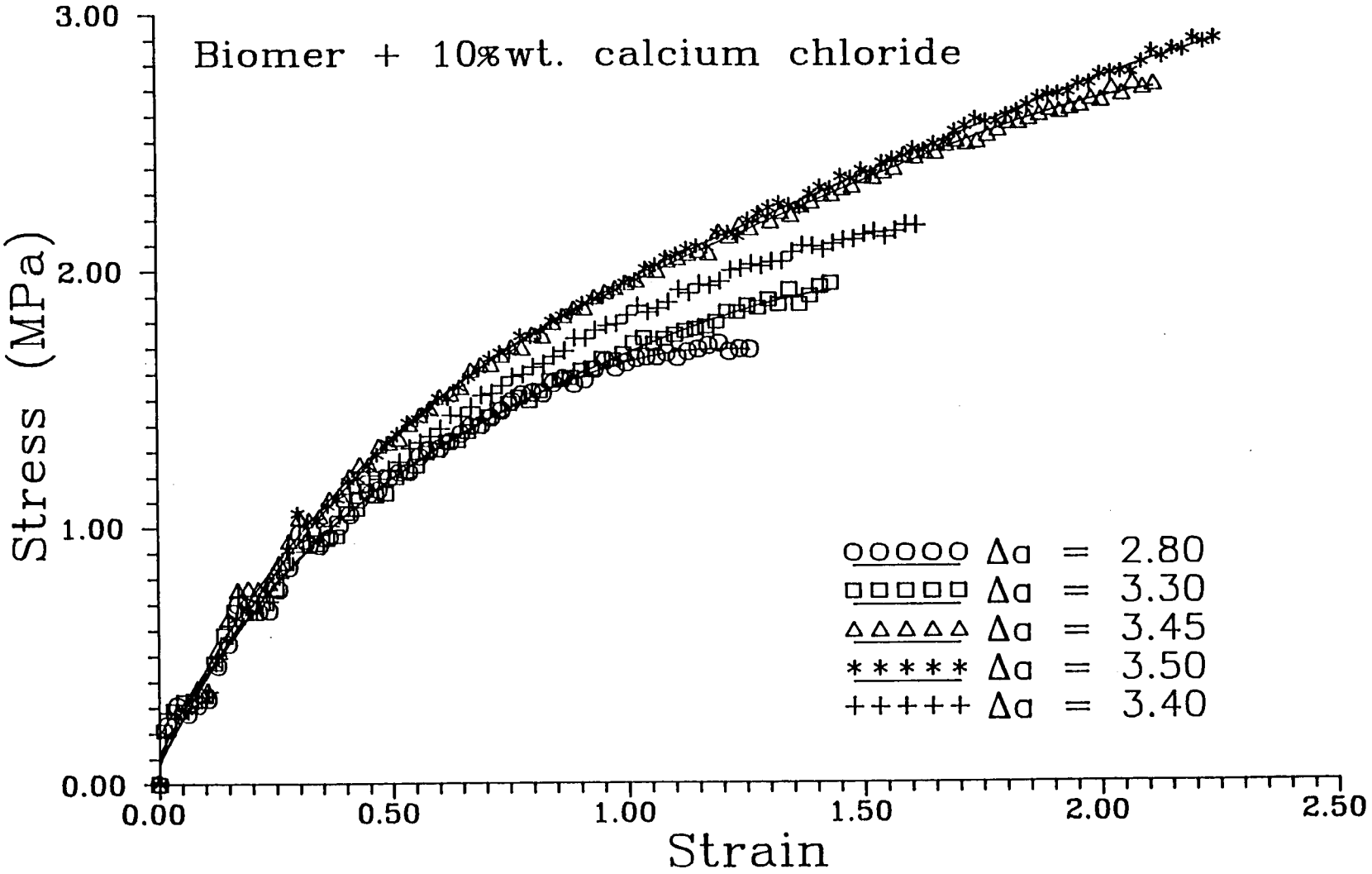

Figure 43: Stress versus strain data for Biomer blended with 10% wt. calcium chloride with varying crack growth to failure.

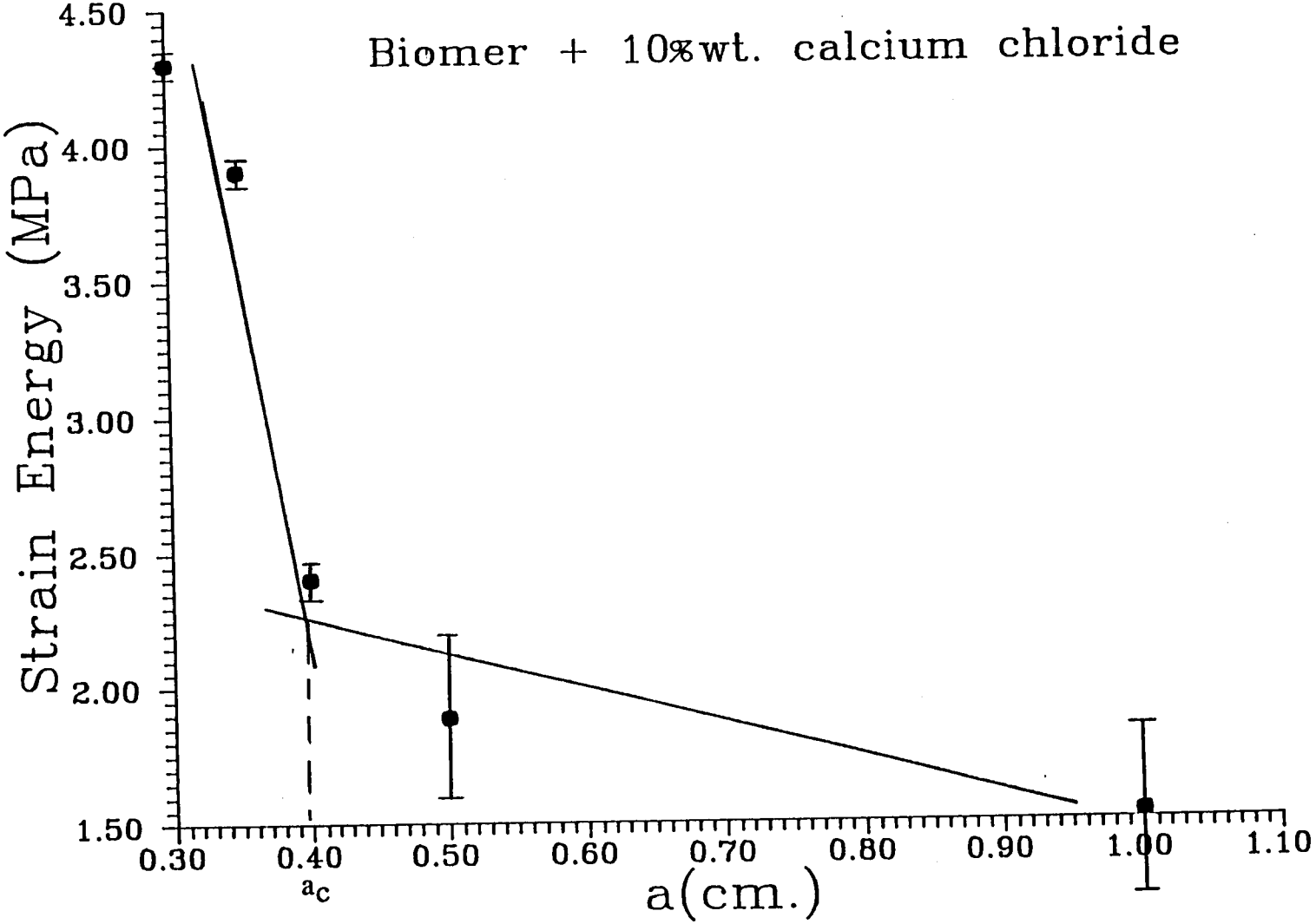

Figure 44: Strain energy to failure versus initial crack length for Biomer blended with 10% wt. calcium chloride.

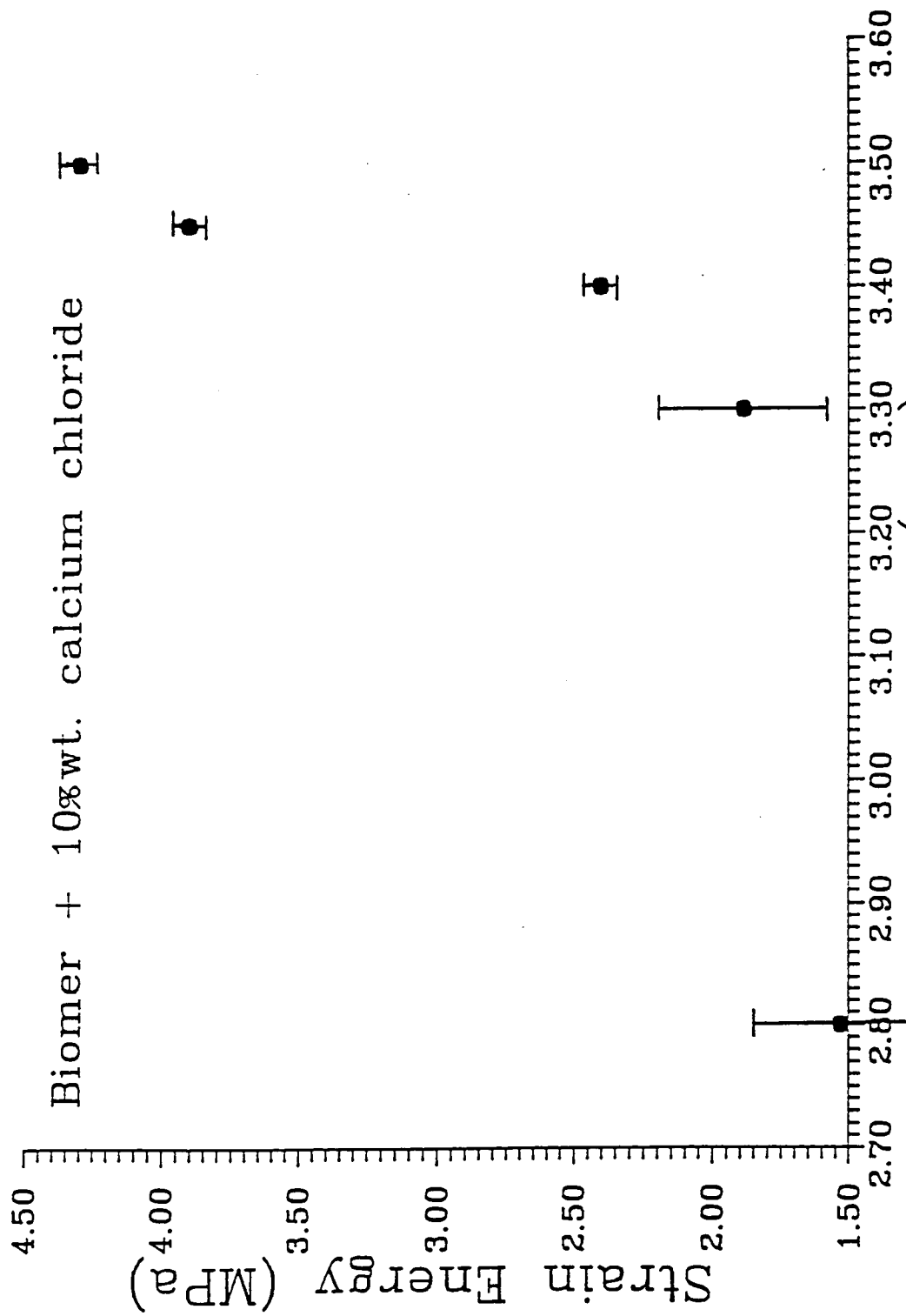

Figure 45: Strain energy to failure versus crack growth to failure for Biomer blended with 5% wt. calcium chloride.

which resulted from the electrical background noise. The 60 Hz noise, however, appeared to have a negligible effect on the calculation of U because the cyclic noise was evenly distributed above and below the expected values.

Figure 46 shows the stress plotted as a function of strain for pure Pellethane with varying initial crack lengths. Two distinct sets of curves appear in this plot because of the necessity to prepare a second film of pure Pellethane. The second film was of a slightly greater thickness, resulting in lower stress curves at the same strain. It must be noted, however, that the areas under all the curves were consistent with the initial crack lengths as predicted by fracture theory. In other words, the thicker sample increased the strain to failure but absorbed the same amount of energy per unit of crack surface area. The areas under these curves representing the strain energy to failure, U, were plotted as a function of the initial crack length, a, and the crack extension to failure, Δa. These are plotted in Figures 47 and 48, respectively.

Similar tests were conducted for Pellethane blended with 1%wt. of calcium chloride. Figure 49 shows the stress plotted as a function of strain for Pellethane blended with 1%wt. calcium chloride with varying initial crack lengths. Values of U were plotted as a function of

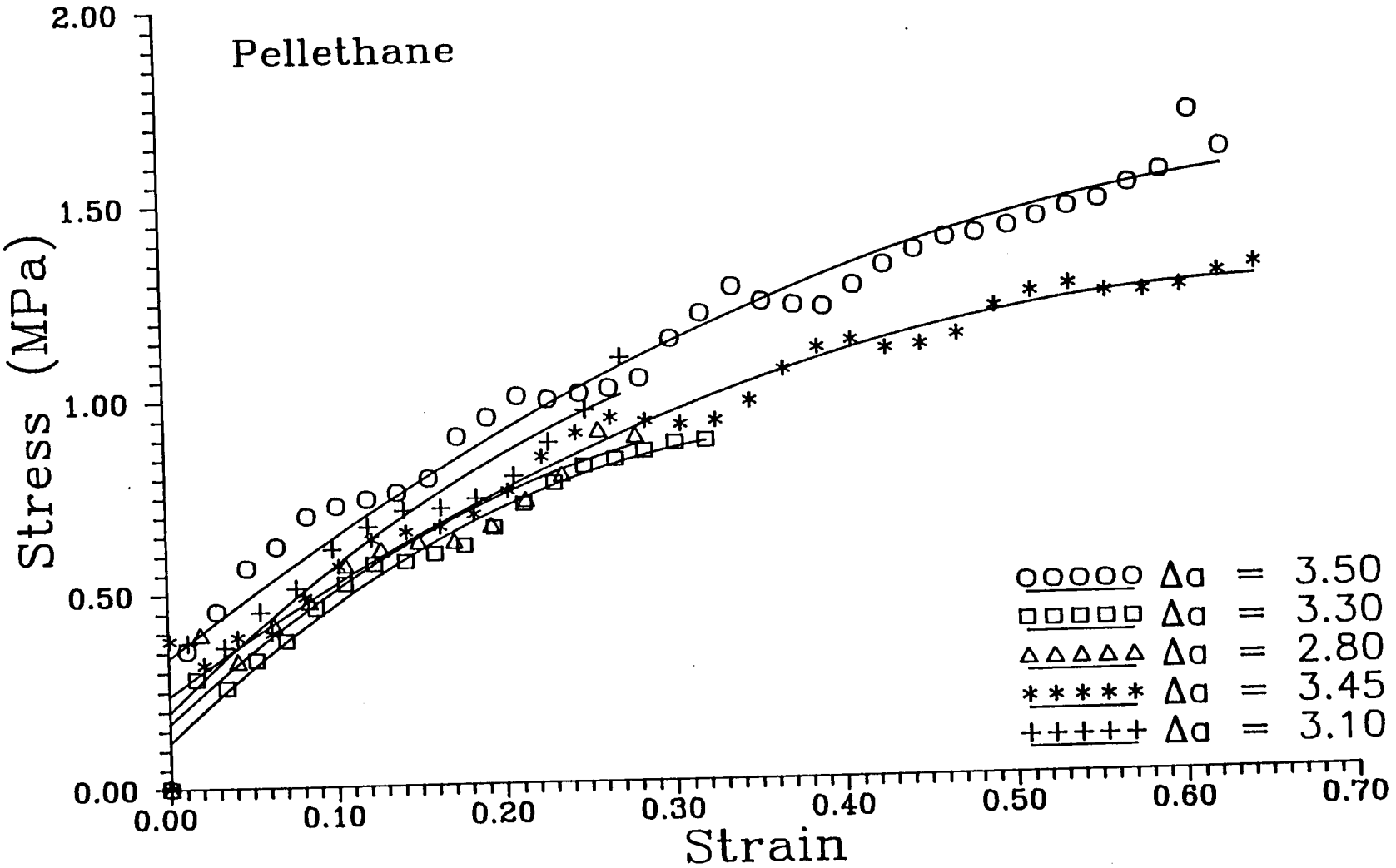

Figure 46: Stress versus strain data for pure Pellethane films with varying crack growth to failure.

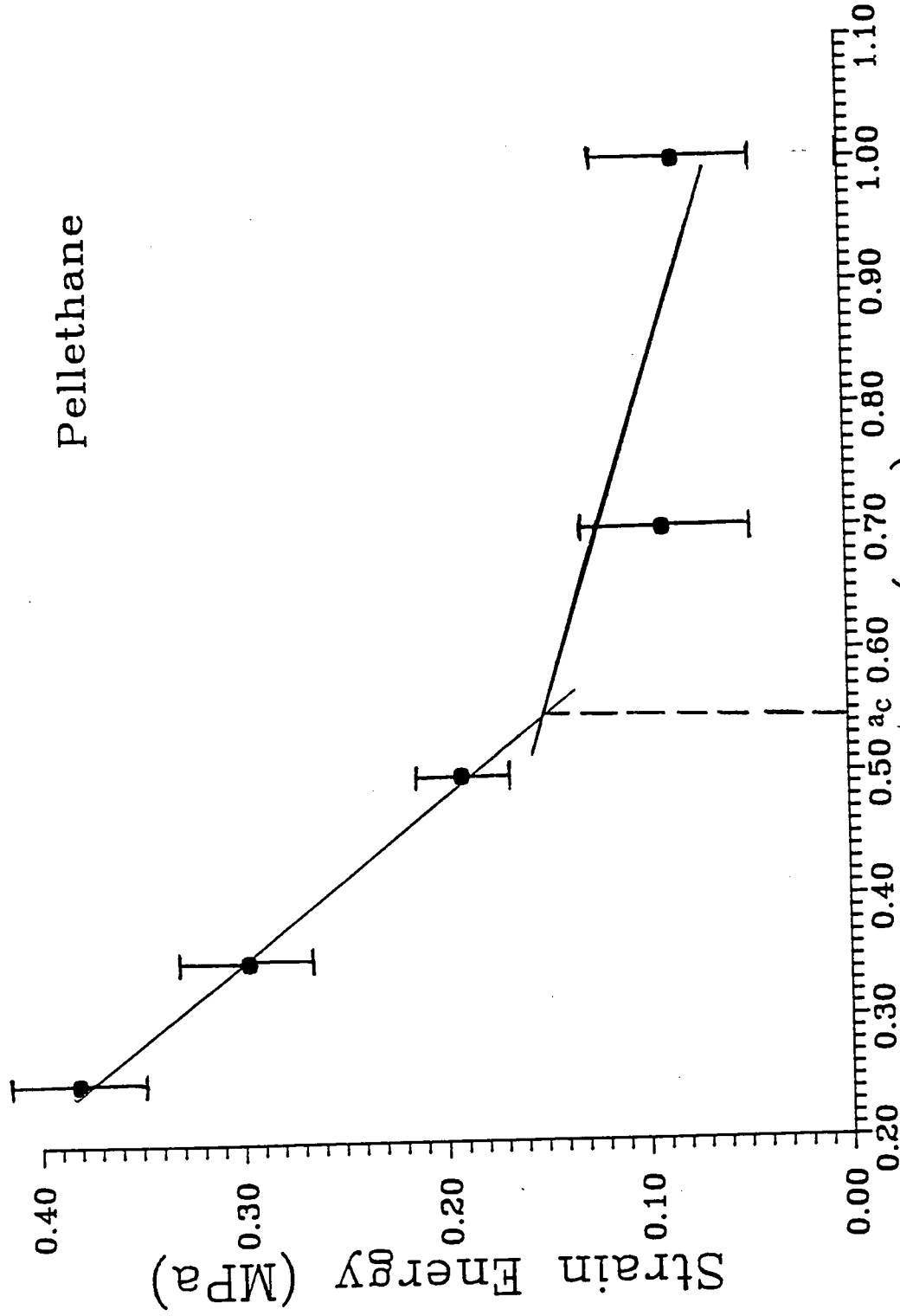

Figure 47: Strain energy to failure versus initial crack length for pure Pellethane.

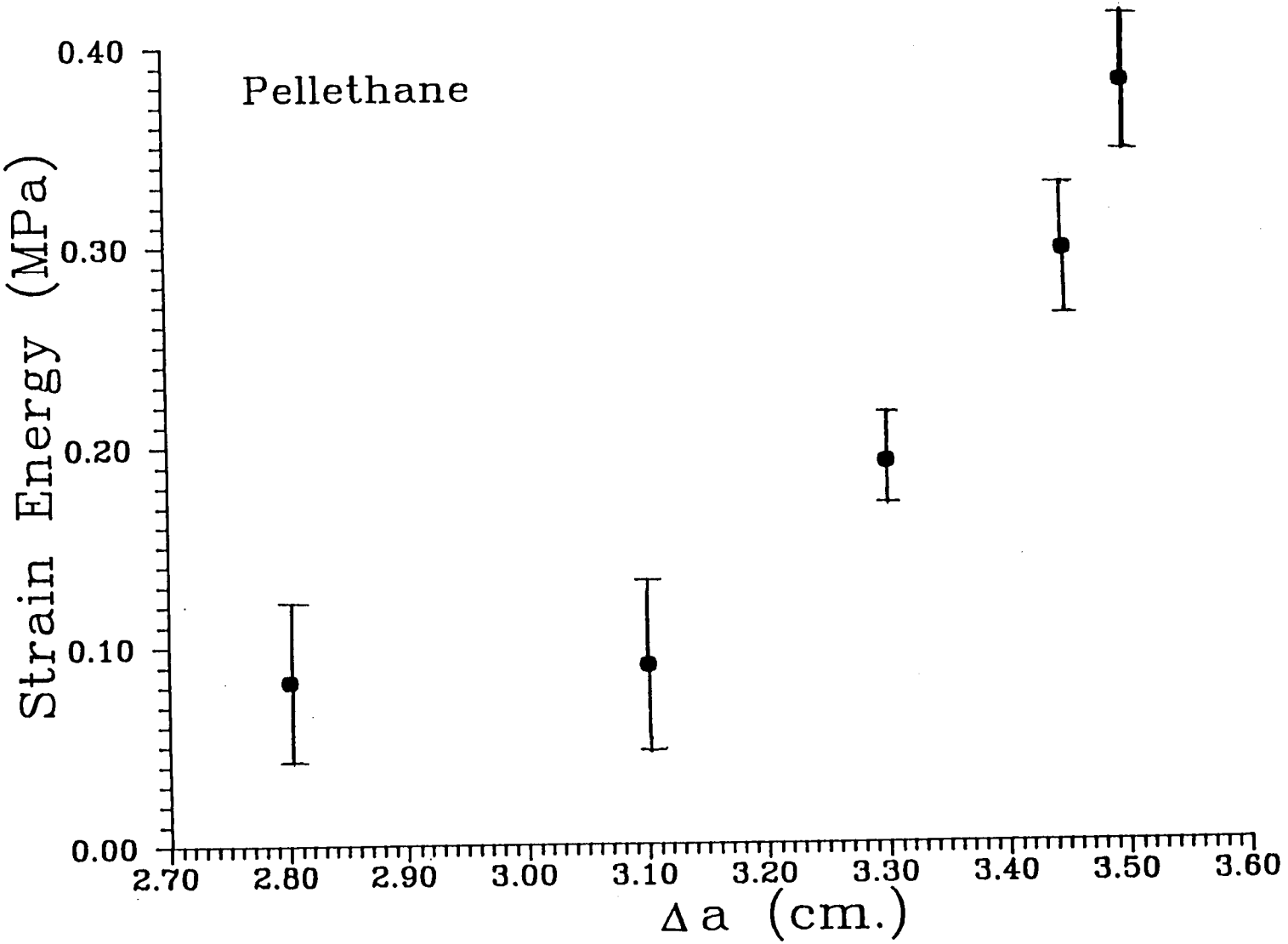

Figure 48: Strain energy to failure versus crack growth to failure for pure Pellethane.

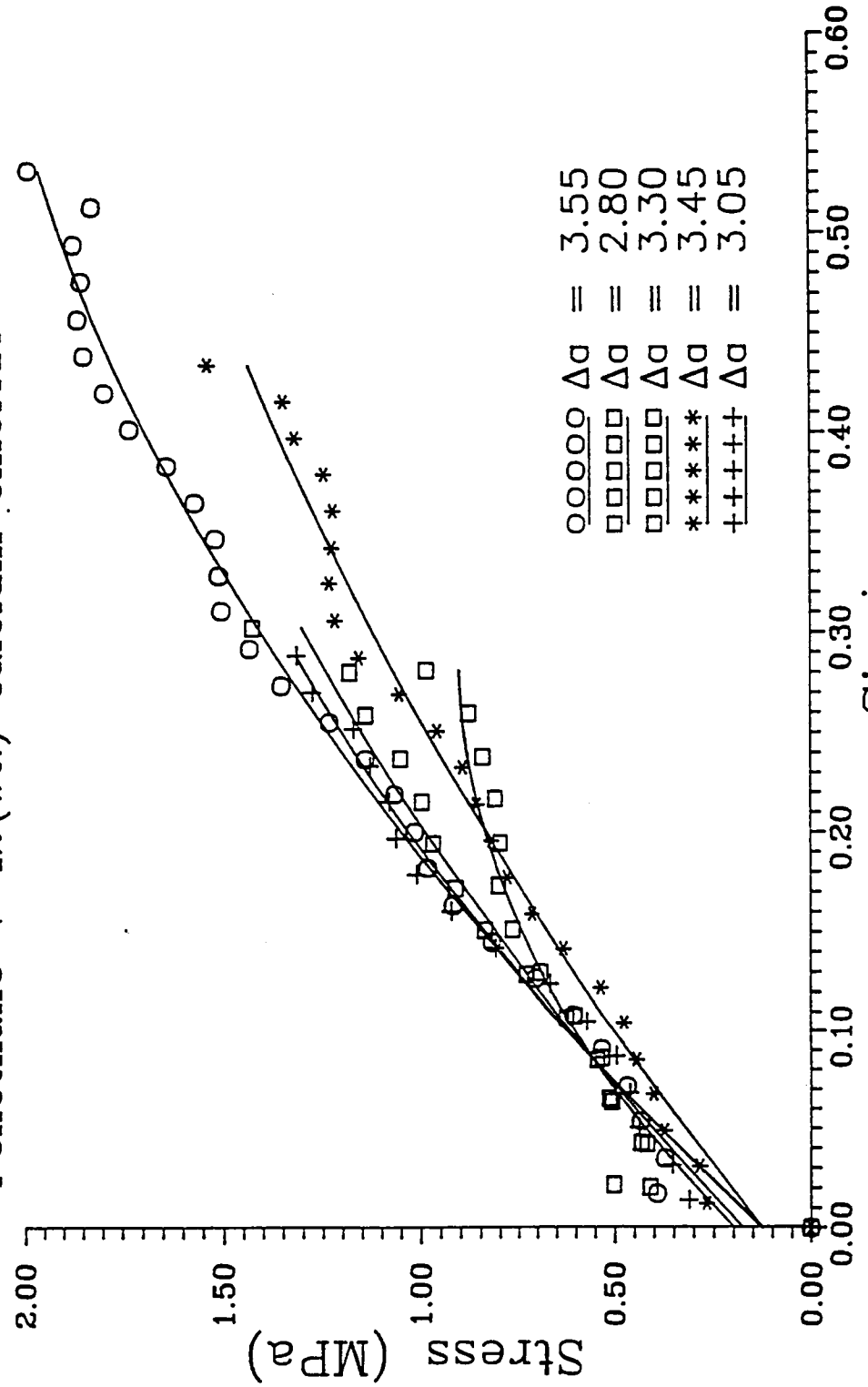

Figure 49: Stress versus strain data for Pellethane blended with 1% wt. calcium chloride with varying crack growth to failure.

a, and Δa. The results are presented in Figures 50 and 51, respectively.

Figure 52 is a plot of stress as a function of strain for Pellethane blended with 5%wt. calcium chloride with varying initial crack lengths. Values of U were pl as a function of a, and Δa. These are shown in Figures 53 and 54, respectively.

The results of the fracture tests for Pellethane at 10%wt calcium chloride concentrations are shown in Figures 55 through 57. Figure 55 is a plot of stress as a function of strain for Pellethane blended with 10%wt. calcium chloride with varying initial crack lengths. Values of U for each specimen were plotted as a function of a, and Δa. These are shown in Figures 56 and 57, respectively.

4.2. Molecular Orientation of Polyurethanes

Spectra of Biomer and Pellethane are shown in Figures 58 and 59, respectively. Band vibration assignments were made using the PEAKS.PAS program and are shown in Table III. Based on these assignments, molecular orientation measurements were made for the hard segment domains.

The hard segment orientation of Pellethane and Biomer as a function of strain was measured in uncracked samples. For both polyurethanes, the effects of calcium chloride concentration on orientation were studied.

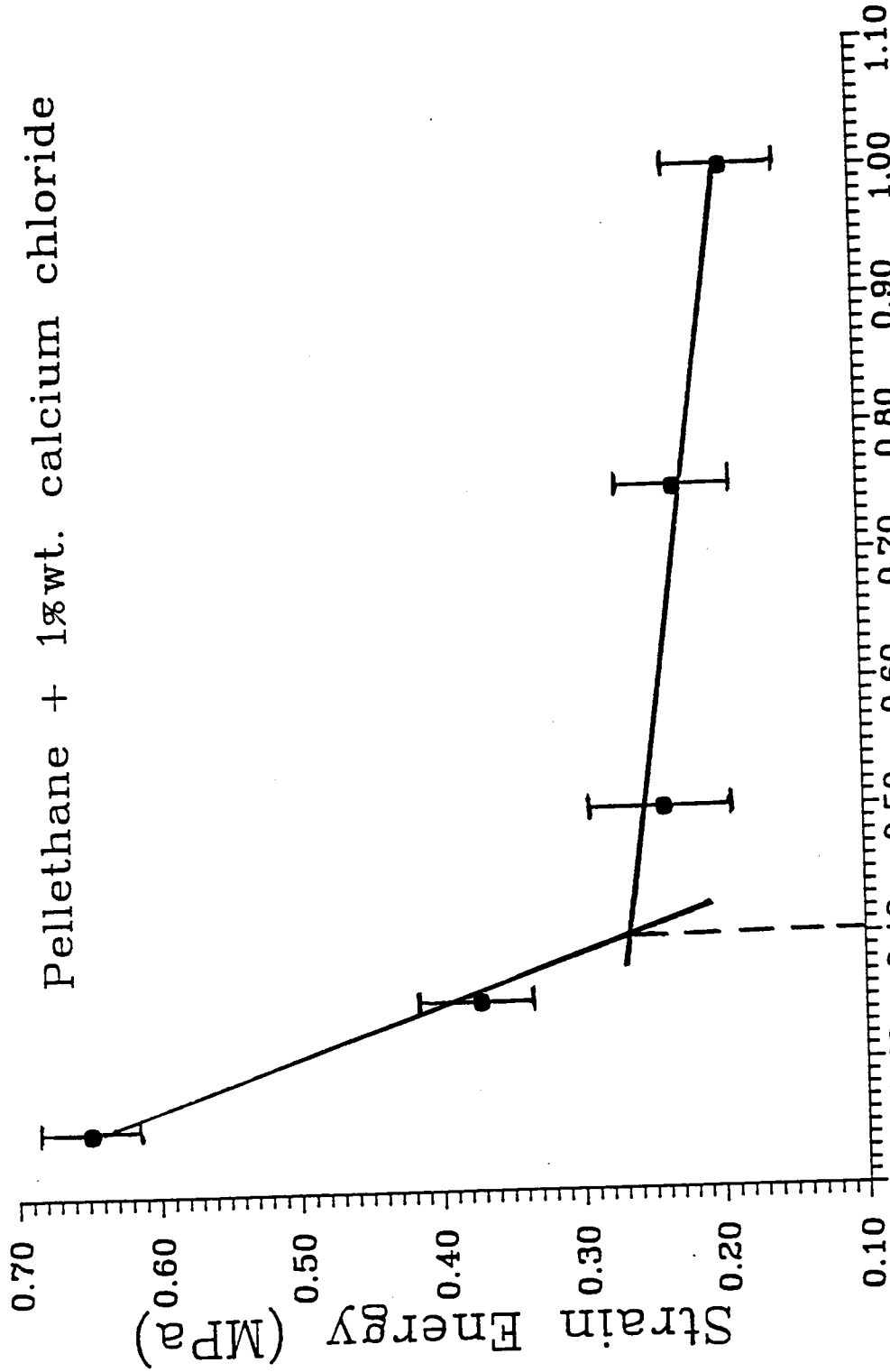

Figure 50: Strain energy to failure versus initial crack length for Pellethane blended with 1% wt. calcium chloride.

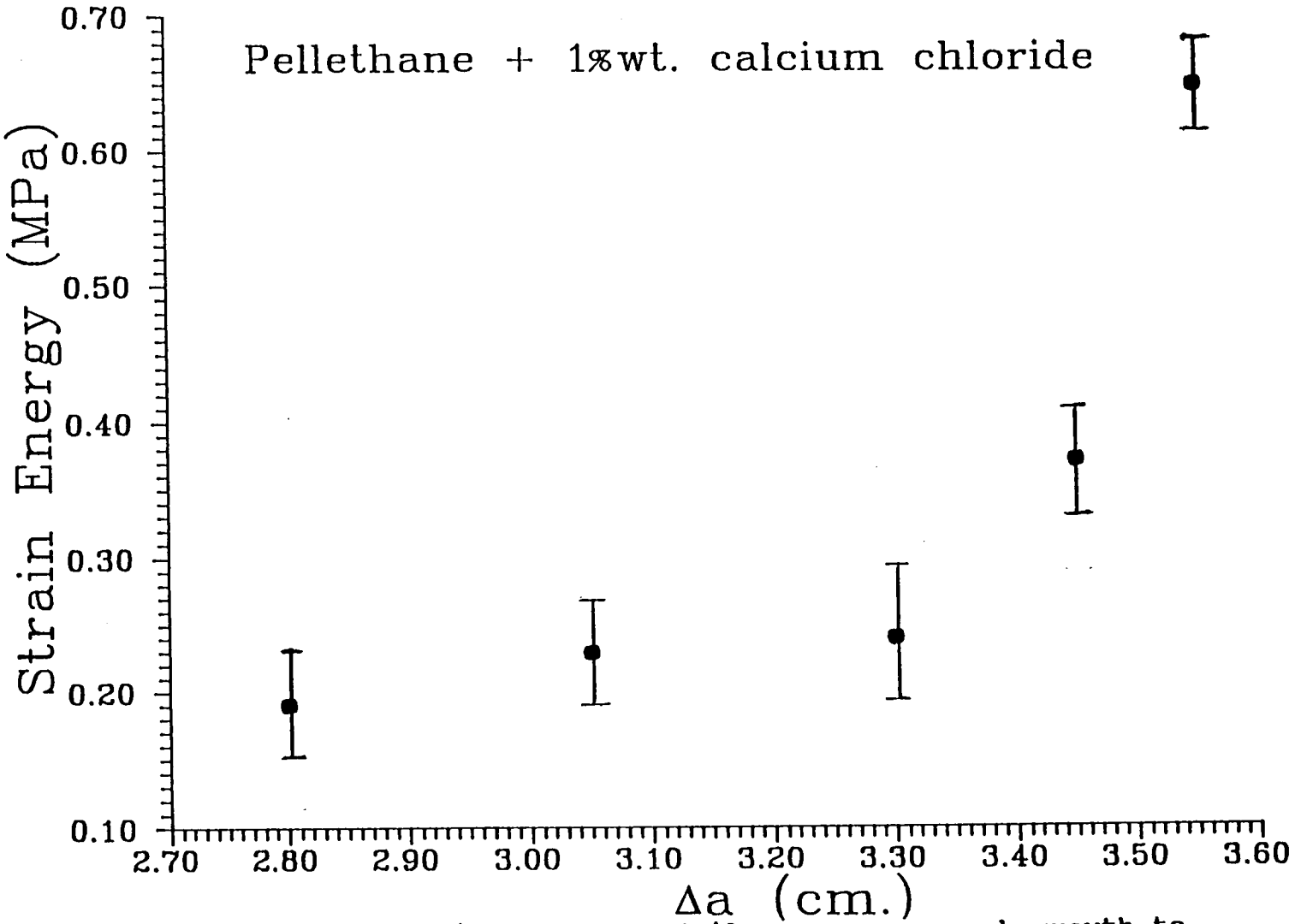

Figure 51: Strain energy to failure versus crack growth to failure for Pellethane blended with 1% wt. calcium chloride.

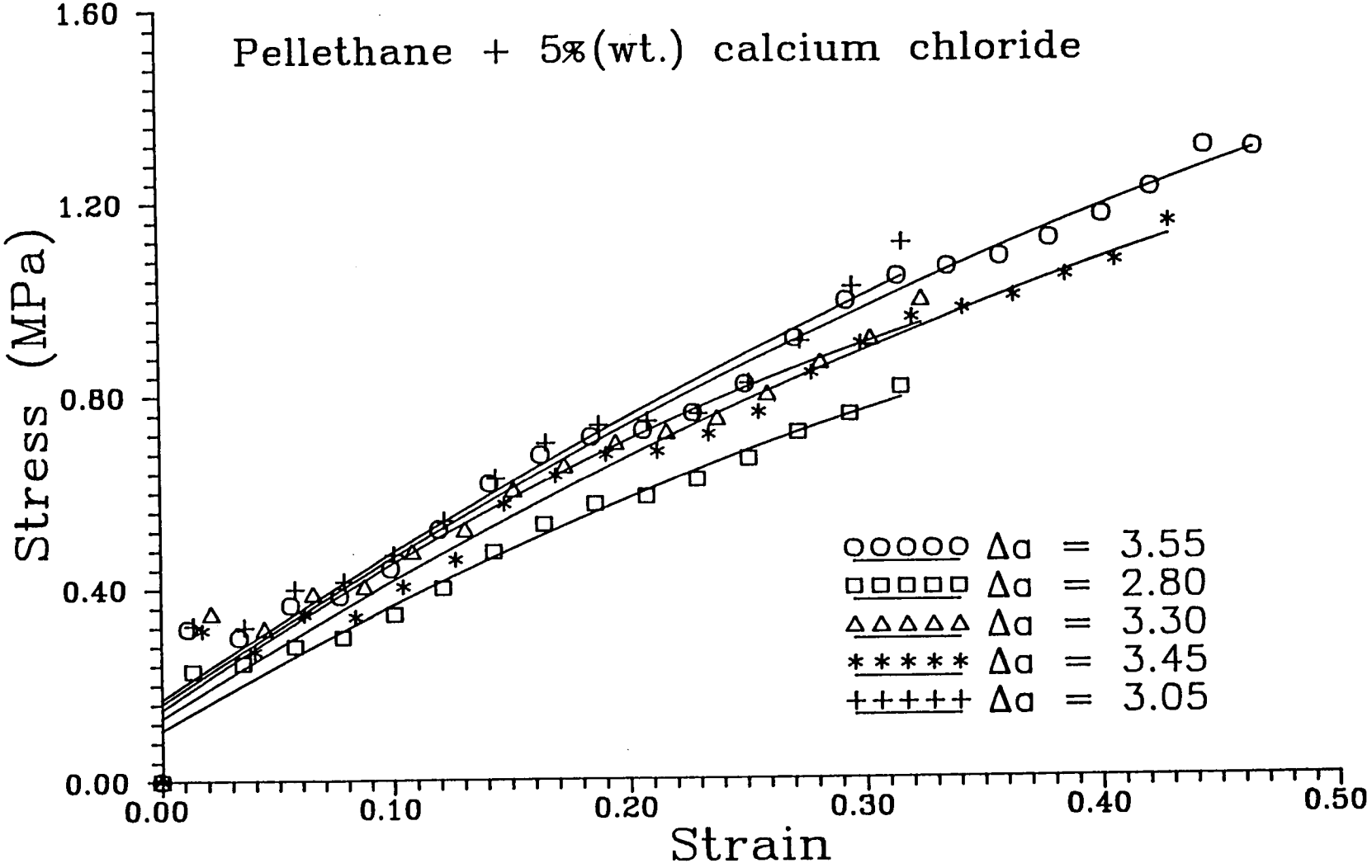

Figure 52: Stress versus strain data for Pellethane blended with 5% wt. calcium chloride with varying crack growth to failure.

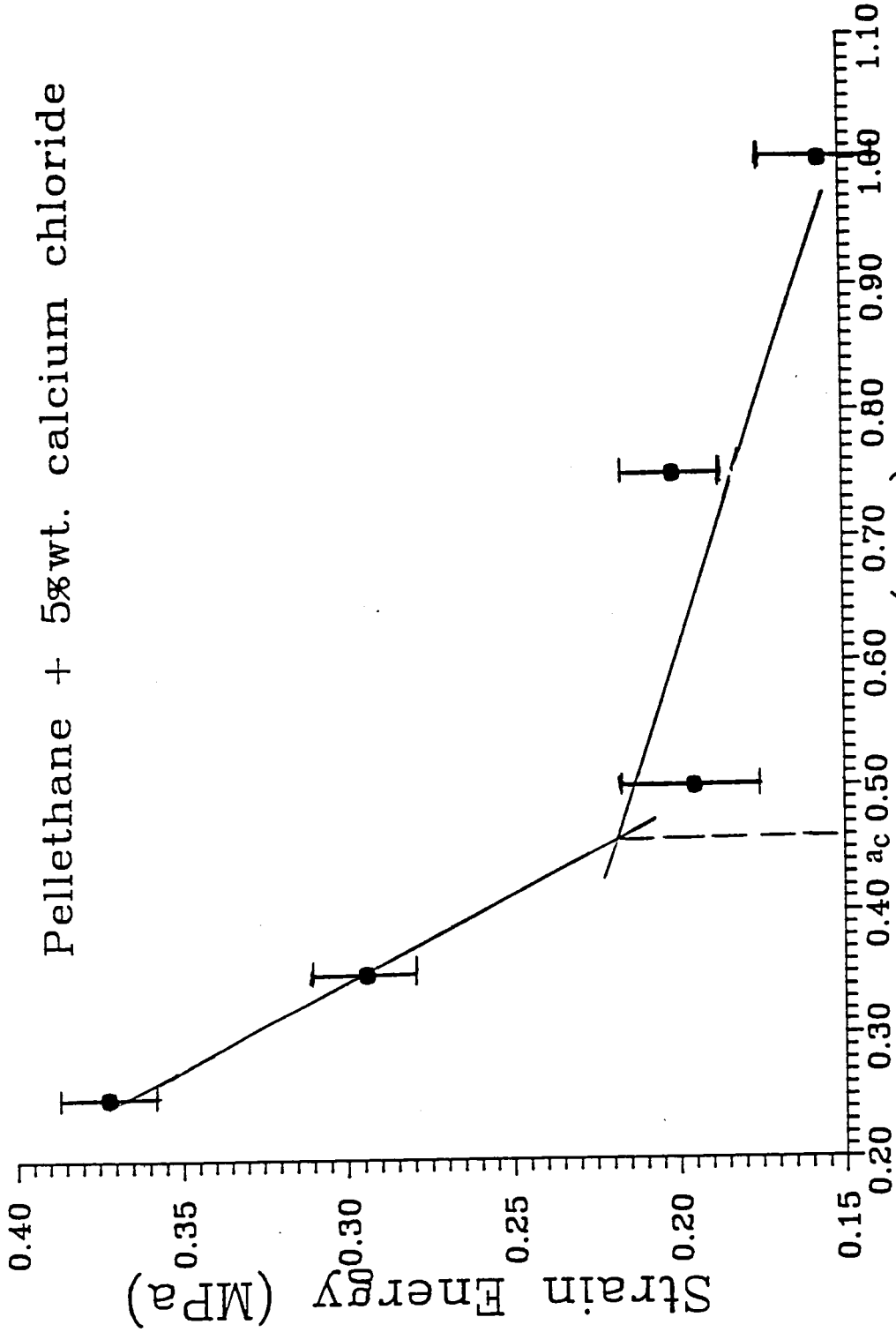

Figure 53: Strain energy to failure versus initial crack length for Pellethane blended with 5% wt. calcium chloride.

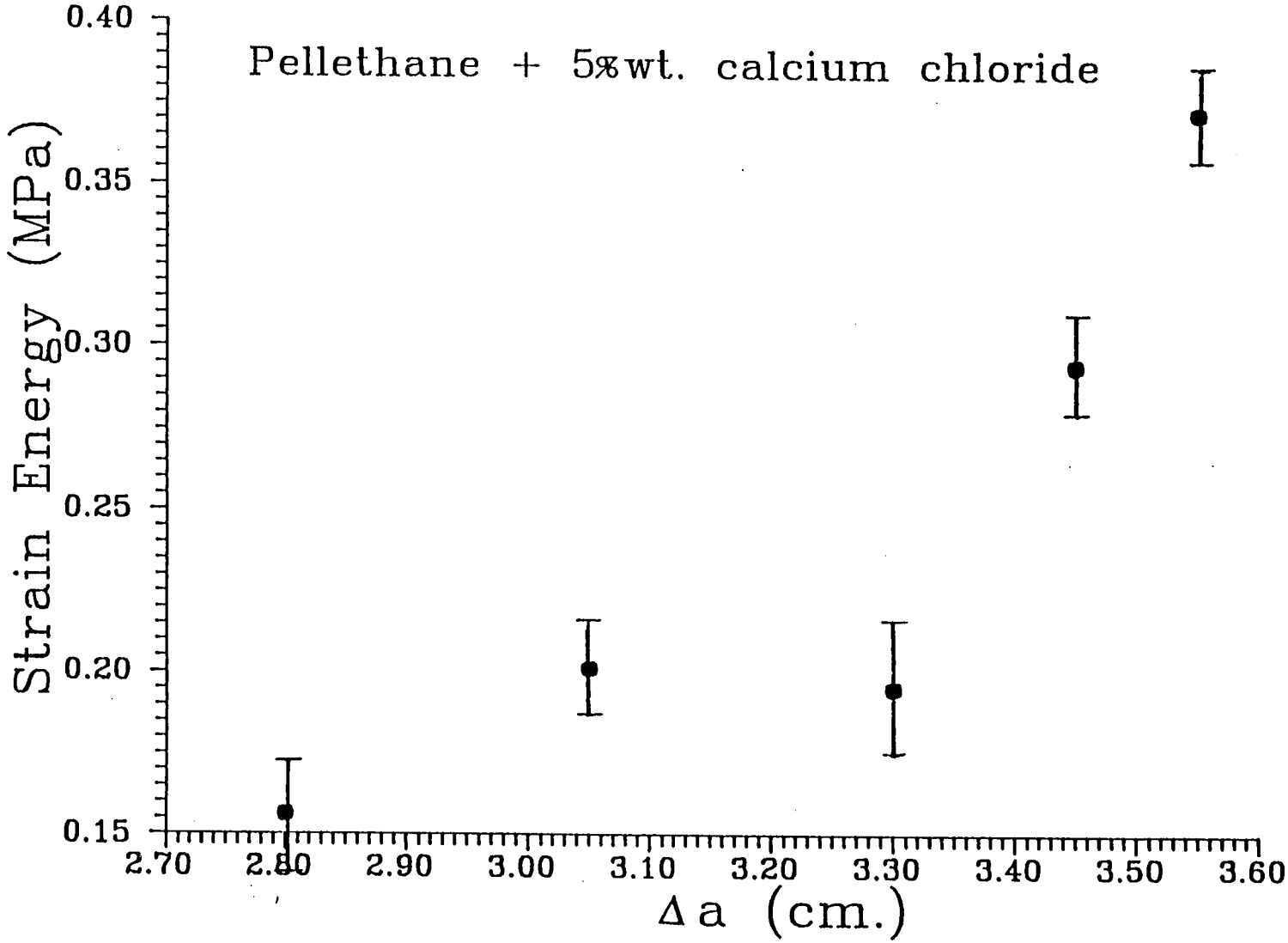

Figure 54: Strain energy to failure versus crack growth to failure for Pellethane blended with 5% wt. calcium chloride.

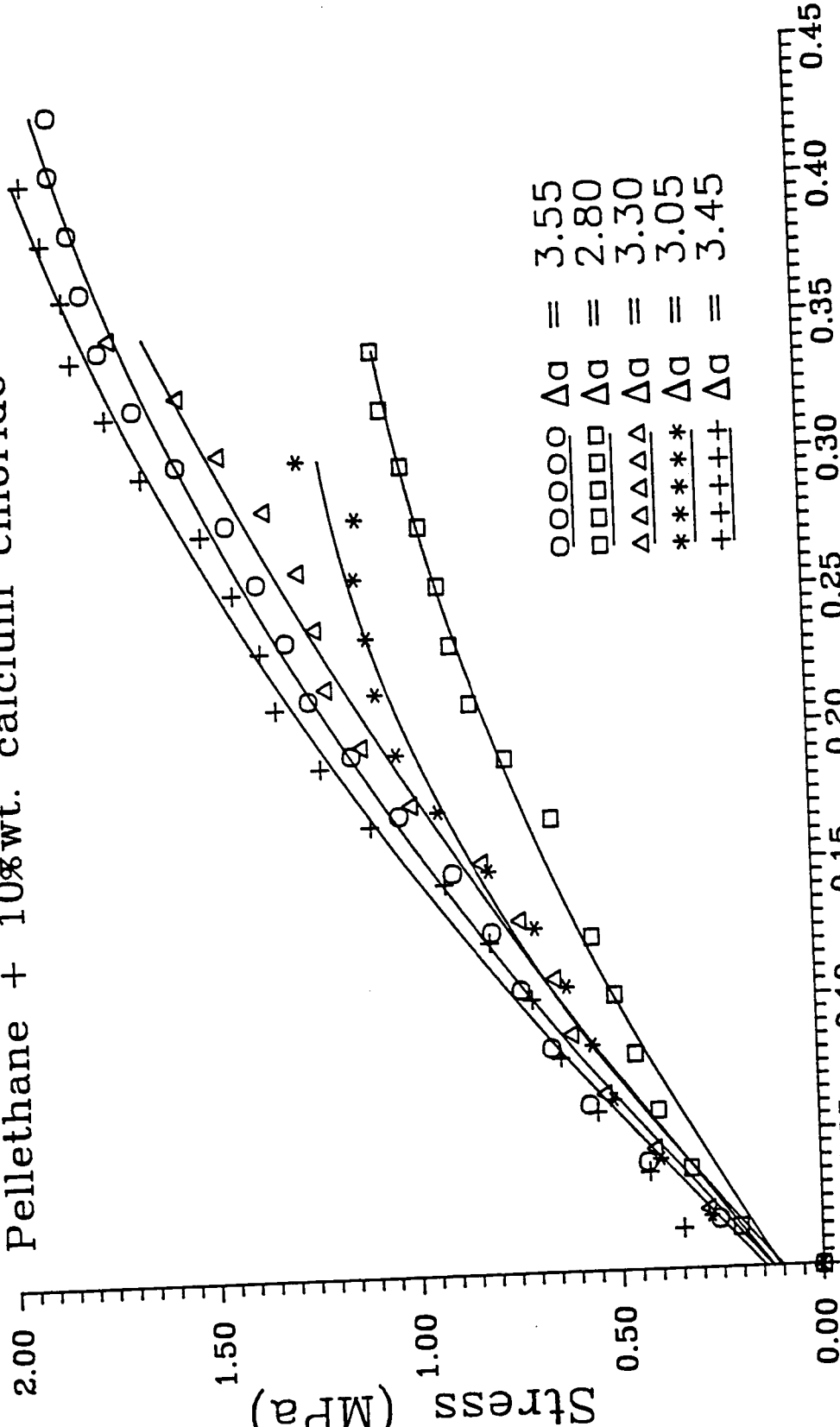

Figure 55: Stress versus strain data for Pellethane blended with 10% wt. calcium chloride with varying crack growth to failure.

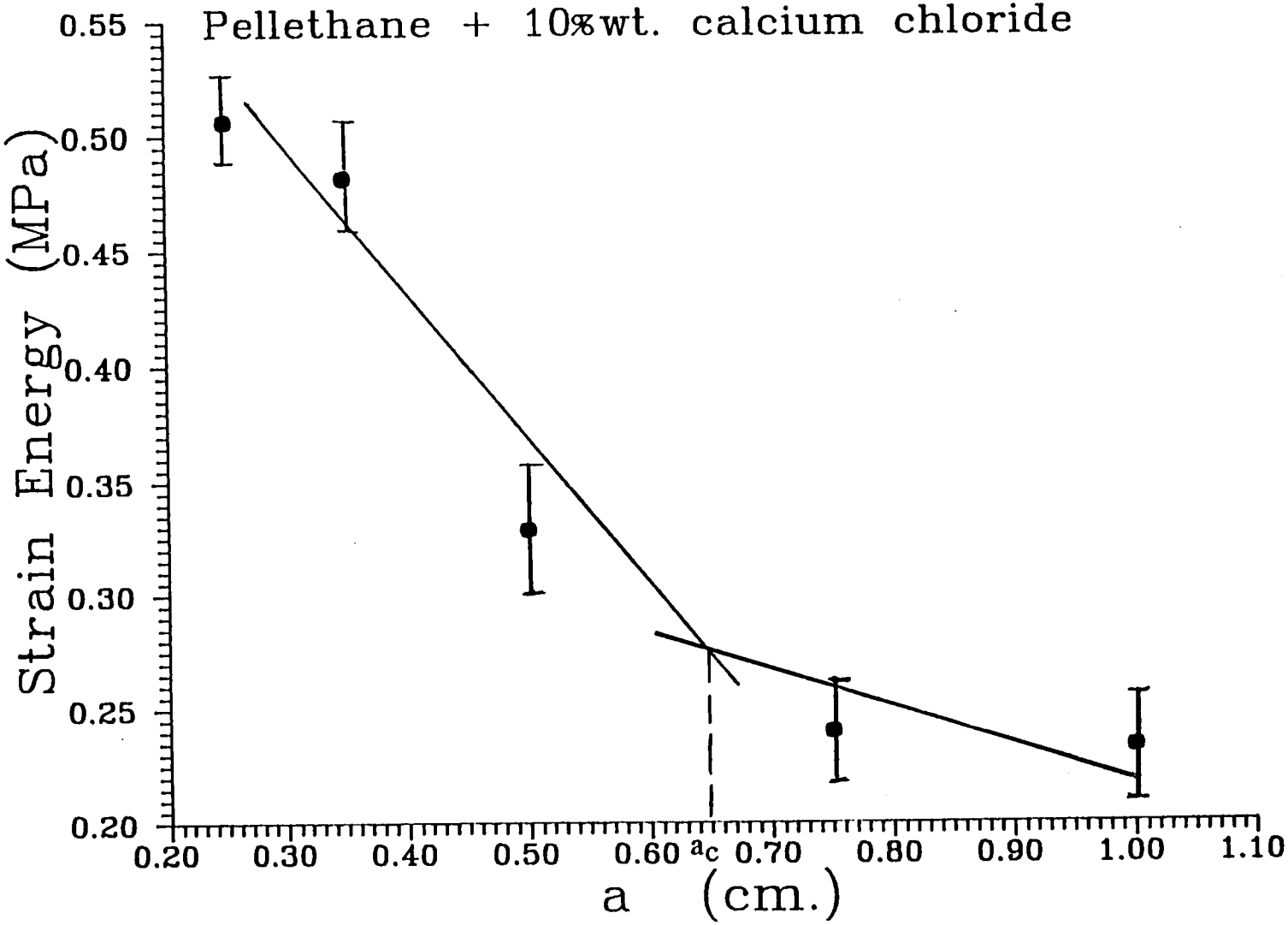

Figure 56: Strain energy to failure versus initial crack length for Pellethane blended with 10% wt. calcium chloride.

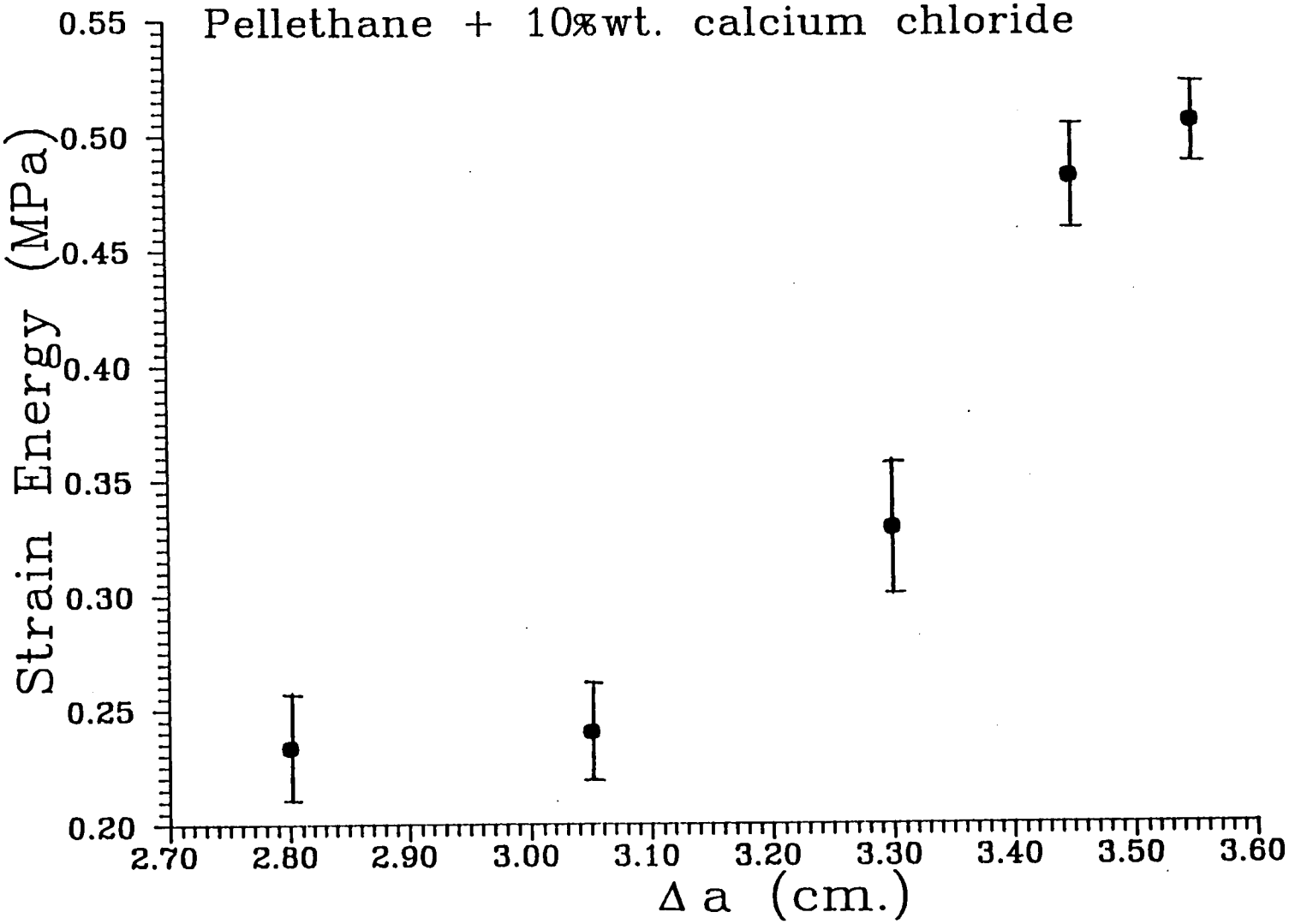

Figure 57: Strain energy to failure versus crack growth to failure for Pellethane blended with 10% wt. calcium chloride.

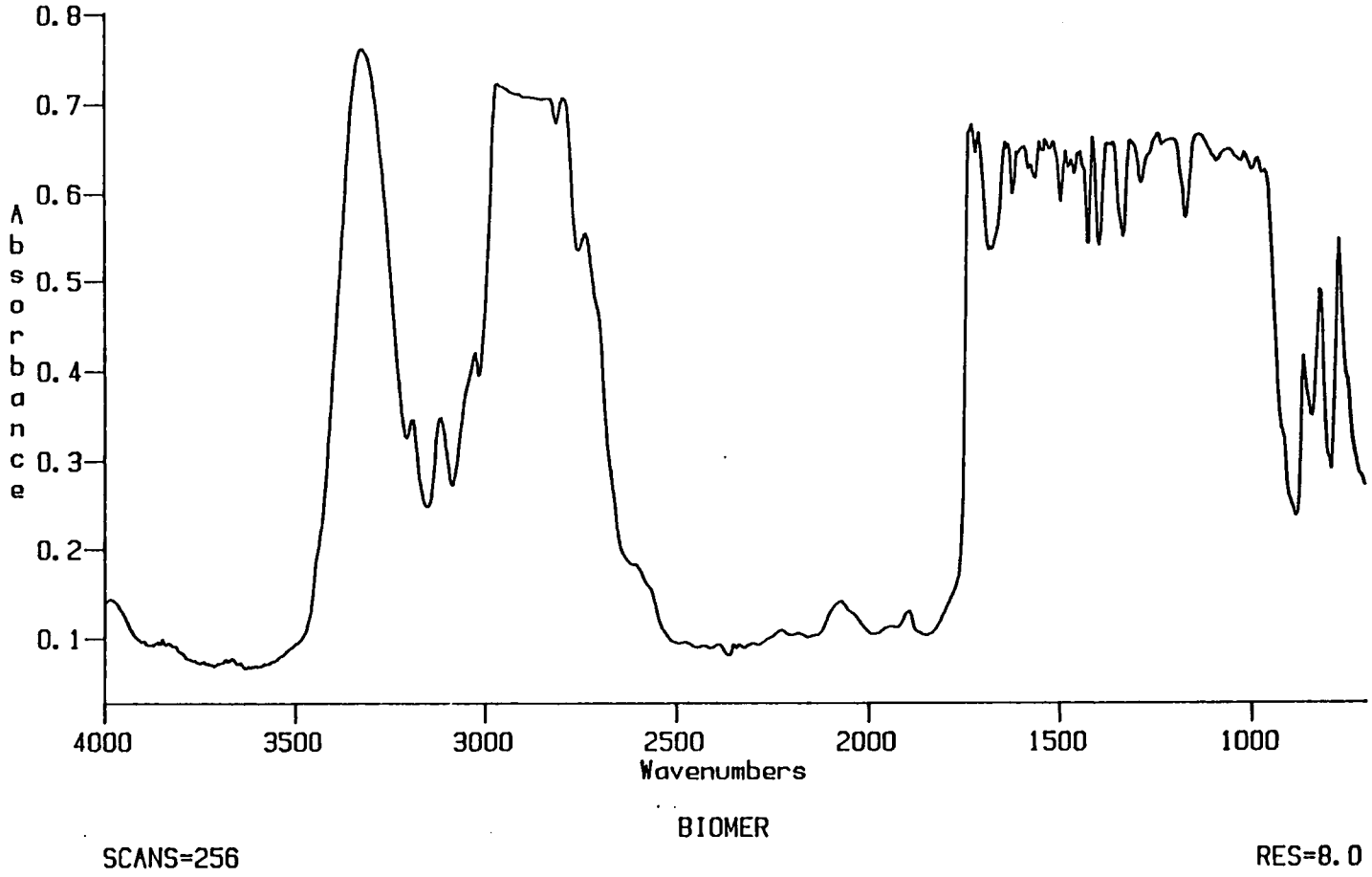

Figure 58: Mid-infrared absorbance spectrum of Biomer.

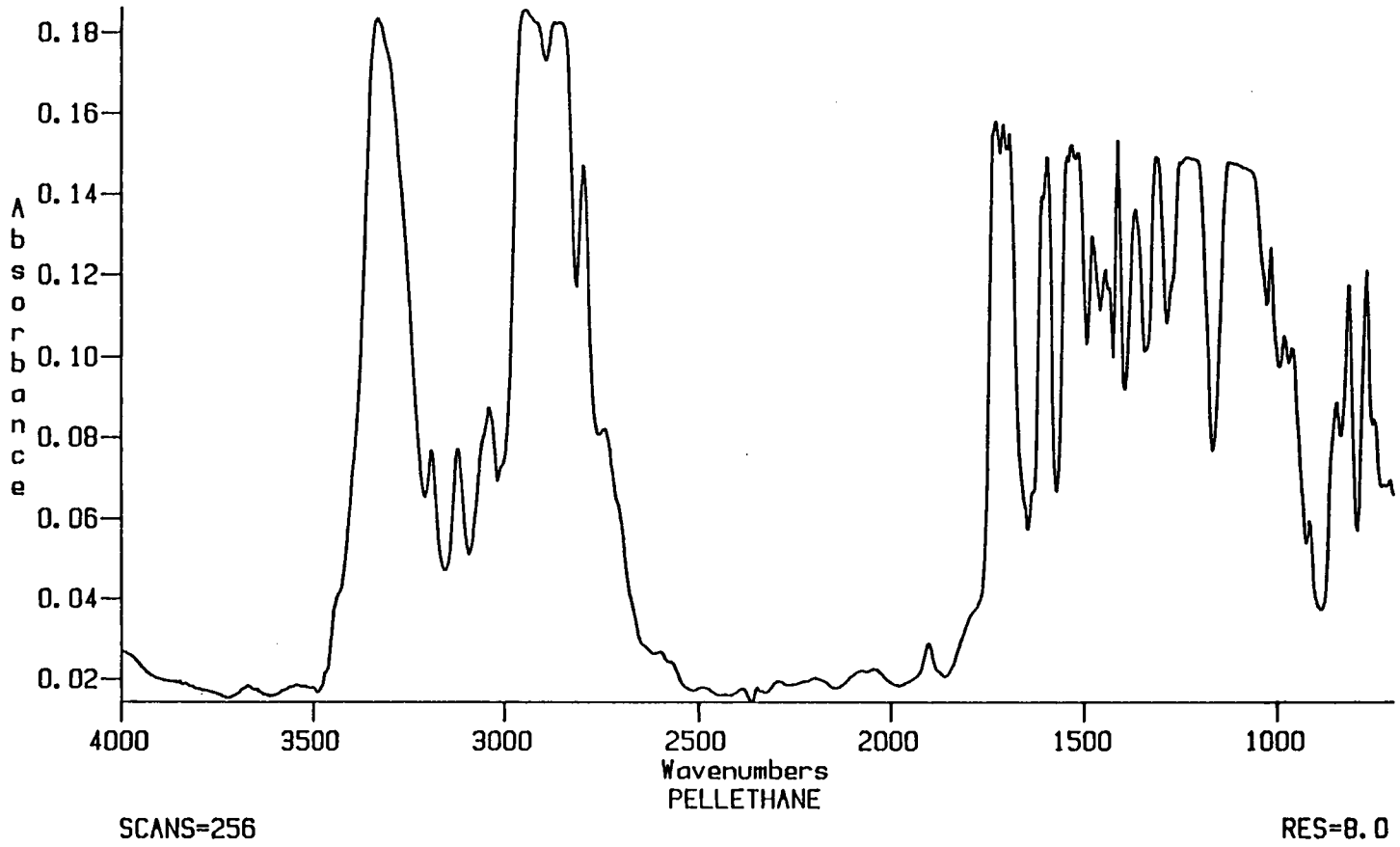

Figure 59: Mid-infrared absorbance spectrum of Pellethane.

Table III. Infrared Band Assignments for Biomer and Pellethane.

Peak (cm^{-1})	Assignment
3330	N-H stretch, H bond.
3195	N-H stretch, primary amides (bonded NH).
3124	Amide II overtone.
3037	C-H stretch aromatic ring.
2948	C-H (CH_2) stretching.
2801	C-H stretch.
2745	Overtone of 2801 cm^{-1} band.
1733	C=O stretch vibration.
1714	C=O saturated open bond.
1645	(Biomer only) 1-keto-2-hydroxy or amino aryl ketones; phenyl ring-CO, OH, or NH_2.
1635	CO Amide I stretch.
1600	C=C aromatic ring breathing.
1538	Amide II, amido acid.
1482	C-H Bend CH_2, aromatic ring breathing.
1447	Aromatic ring breathing.
1416	C=C aromatic ring breathing.
1370	C-H deformation.
1315	C-N stretch aryl amine, secondary.
1238	Amide III, C-O stretch acetates.
1124	C-O stretch; benzoates and phthalates.
1018	(Pellethane only) C-H in-plane bend aromatic ring.
984	C-H in-plane bend aromatic ring.
964	C-H in-plane bend aromatic ring.
917	OH Deformation (unreacted end groups).
863	(Biomer only) C-N stretch (alkyl and aryl).
851	(Pellethane only) C-N stretch (alkyl and aryl) or CH_2 rock.
772	C-H deformation.

The molecular orientations corresponding to 0, 10, 50 and 100% strain conditions were measured in two spectral regions for the hard and soft segments of the polyurethane. The stresses corresponding to the strains are included for each sample set. Figures 60 through 63 are plots of the N-H stretch (3400-3300 cm^{-1}) polarized absorbance spectra for varying concentrations of calcium chloride in Biomer. Figure 64 through 67 are plots of the N-H stretch spectra for varying concentrations of calcium chloride in Pellethane. Figures 68 through 71 are plots of the C-H stretch absorbances for varying concentrations of calcium chloride in Biomer. Again, the same information for the C-H stretch is plotted in Figures 72 through 75 for Pellethane.

4.3. Orientation of the Crack Tip Fields

Orientation measurements surrounding the crack tip were also measured by infrared dichroism. Critical crack lengths were approximated from the instability conditions observed in strain energy versus Δa curves. These estimated critical crack lengths were used as the initial crack lengths in fracture specimens. The crack length values are tabulated in Table IV.

Figure 76 is a plot of the stress relaxation measurements for each Biomer sample during which all polarized spectra were collected. Figure 77 presents

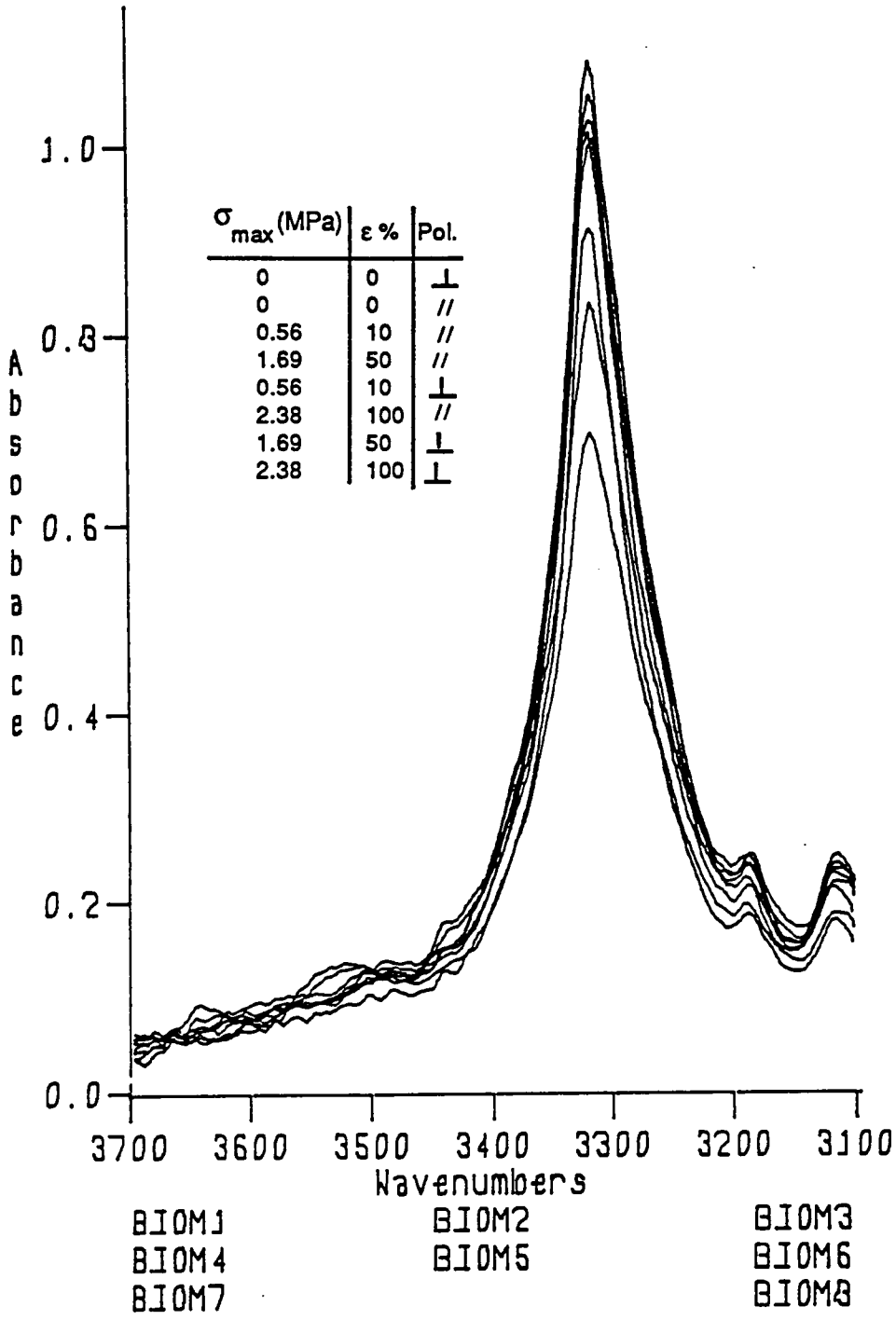

Figure 60: Polarized infrared absorbance spectra for pure Biomer at various strains; N-H stretch.

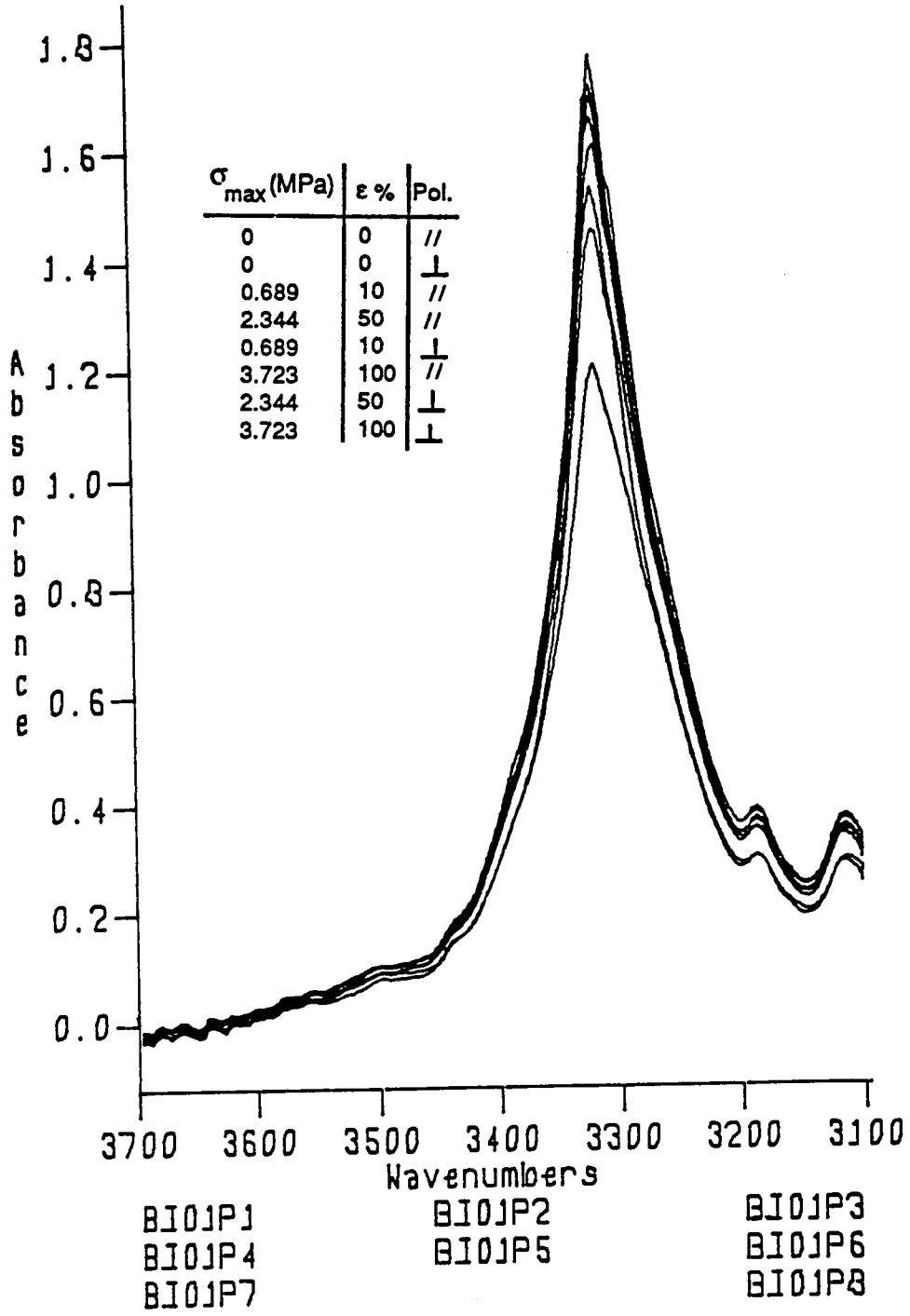

Figure 61: Polarized infrared absorbance spectra for Biomer blended with 1% calcium chloride; at various strains; N-H stretch.

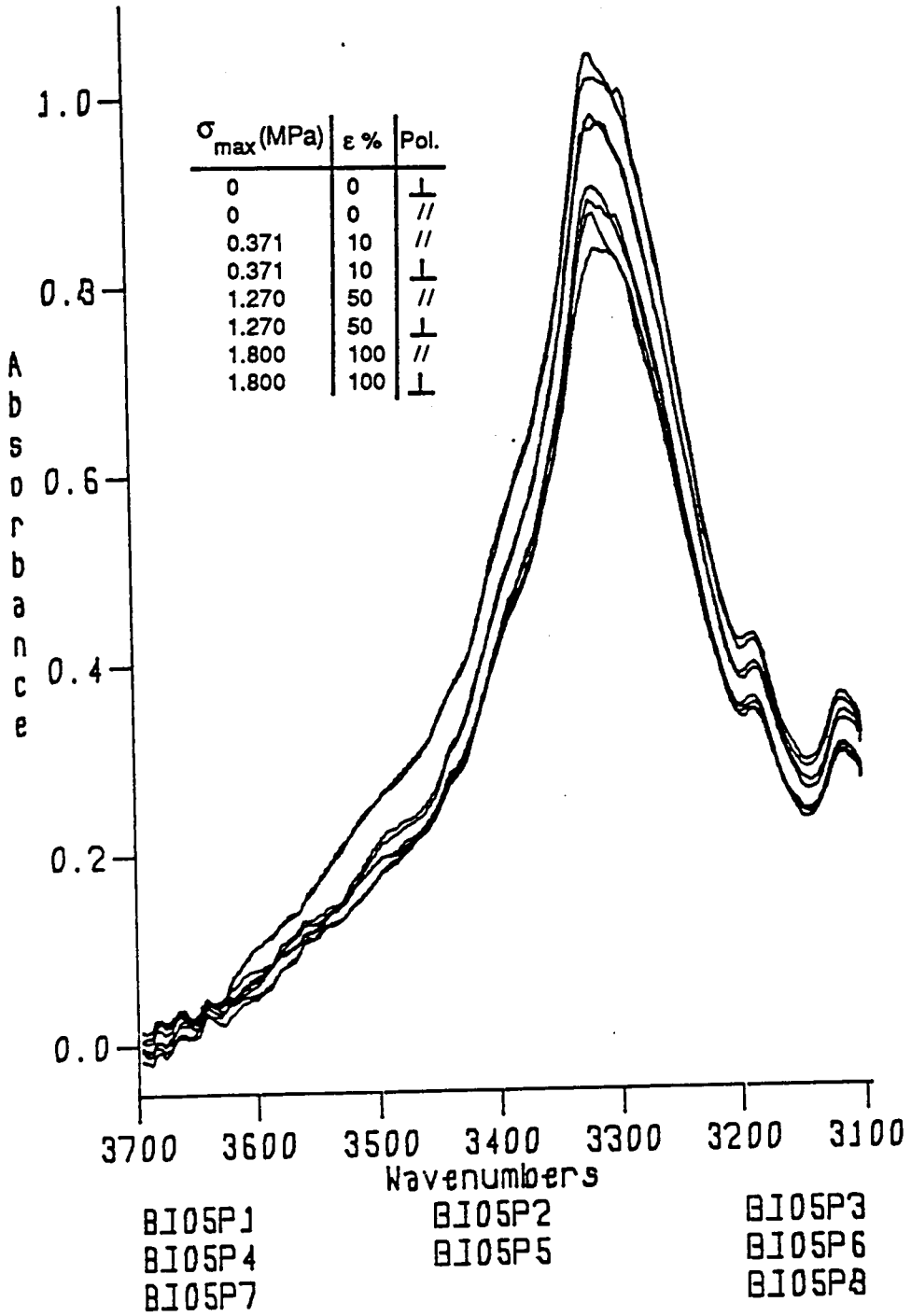

Figure 62: Polarized infrared absorbance spectra for Biomer blended with 5% calcium chloride; at various strains; N-H stretch.

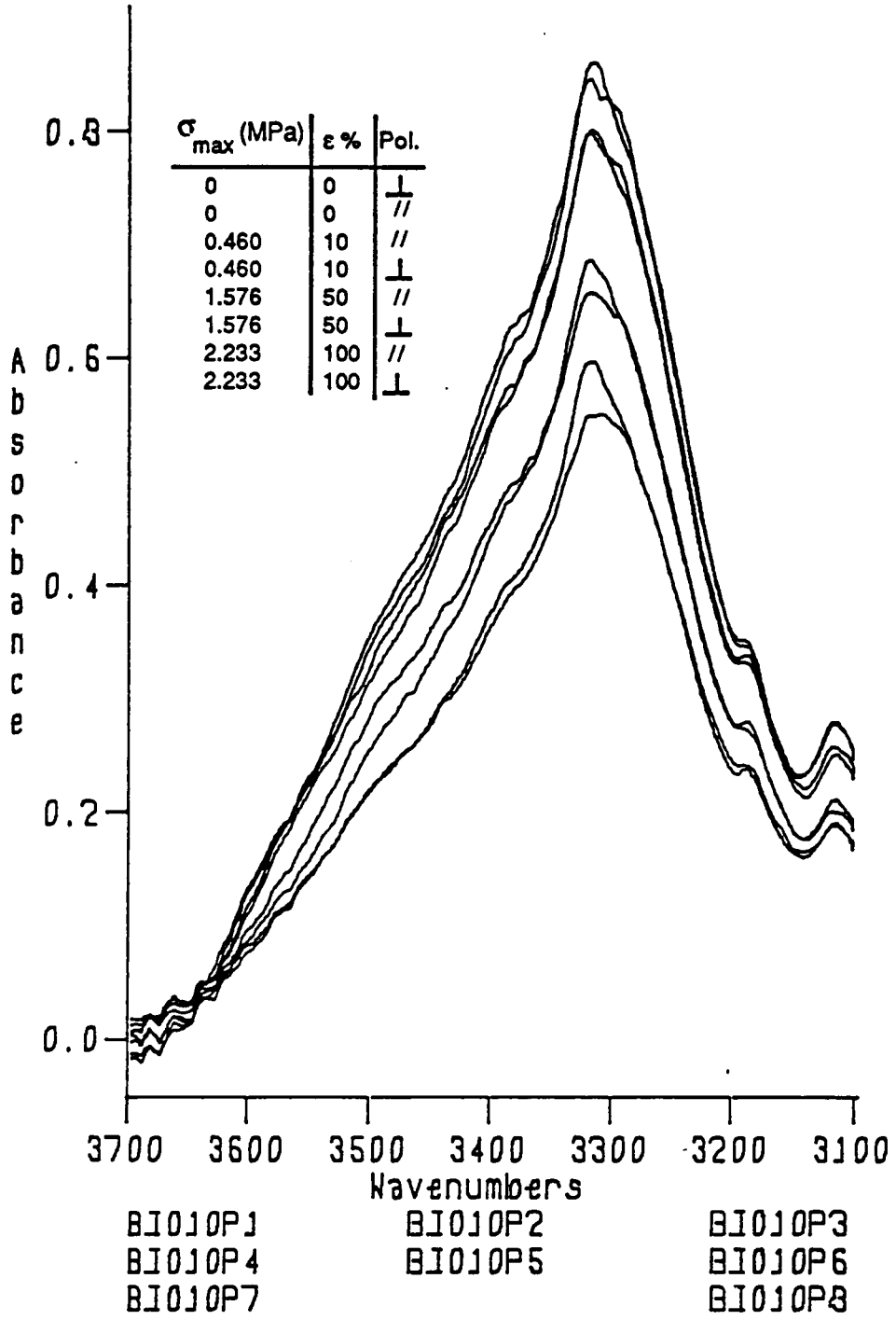

Figure 63: Polarized infrared absorbance spectra for Biomer blended with 10% calcium chloride; at various strains; N-H stretch.

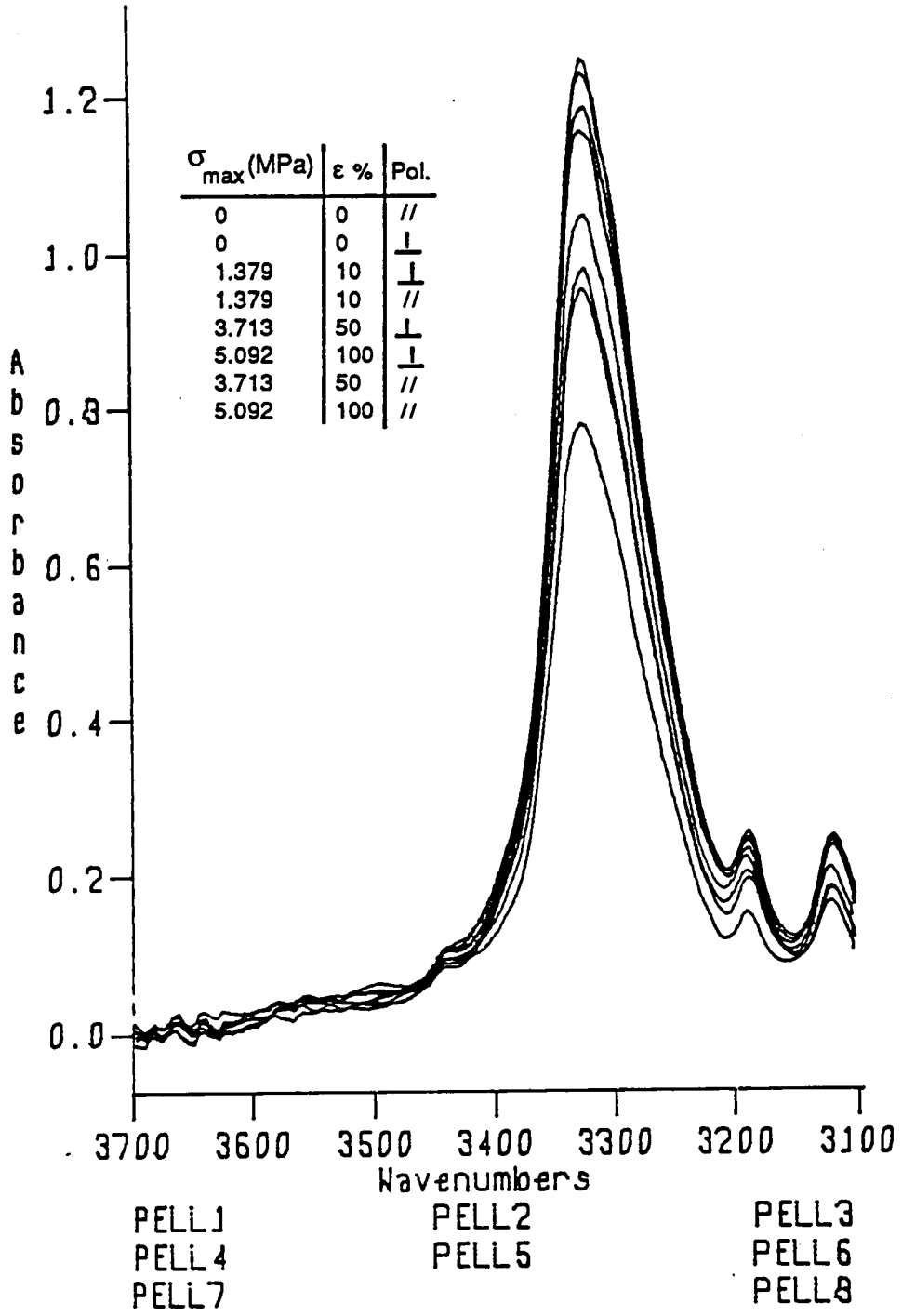

Figure 64: Polarized infrared absorbance spectra for pure Pellethane at various strains; N-H stretch.

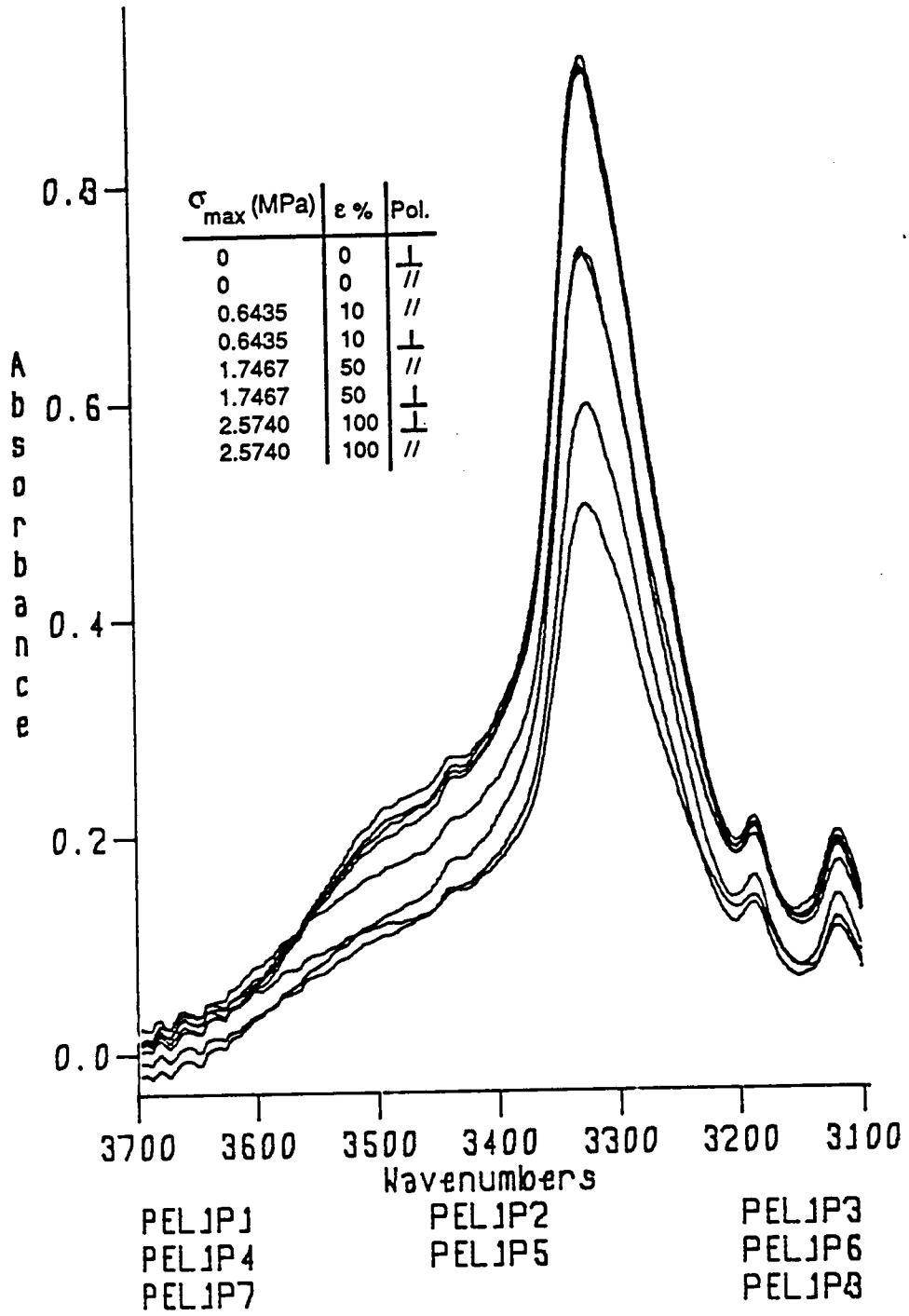

Figure 65: Polarized infrared absorbance spectra for Pellethane blended with 1% calcium chloride; at various strains; N-H stretch.

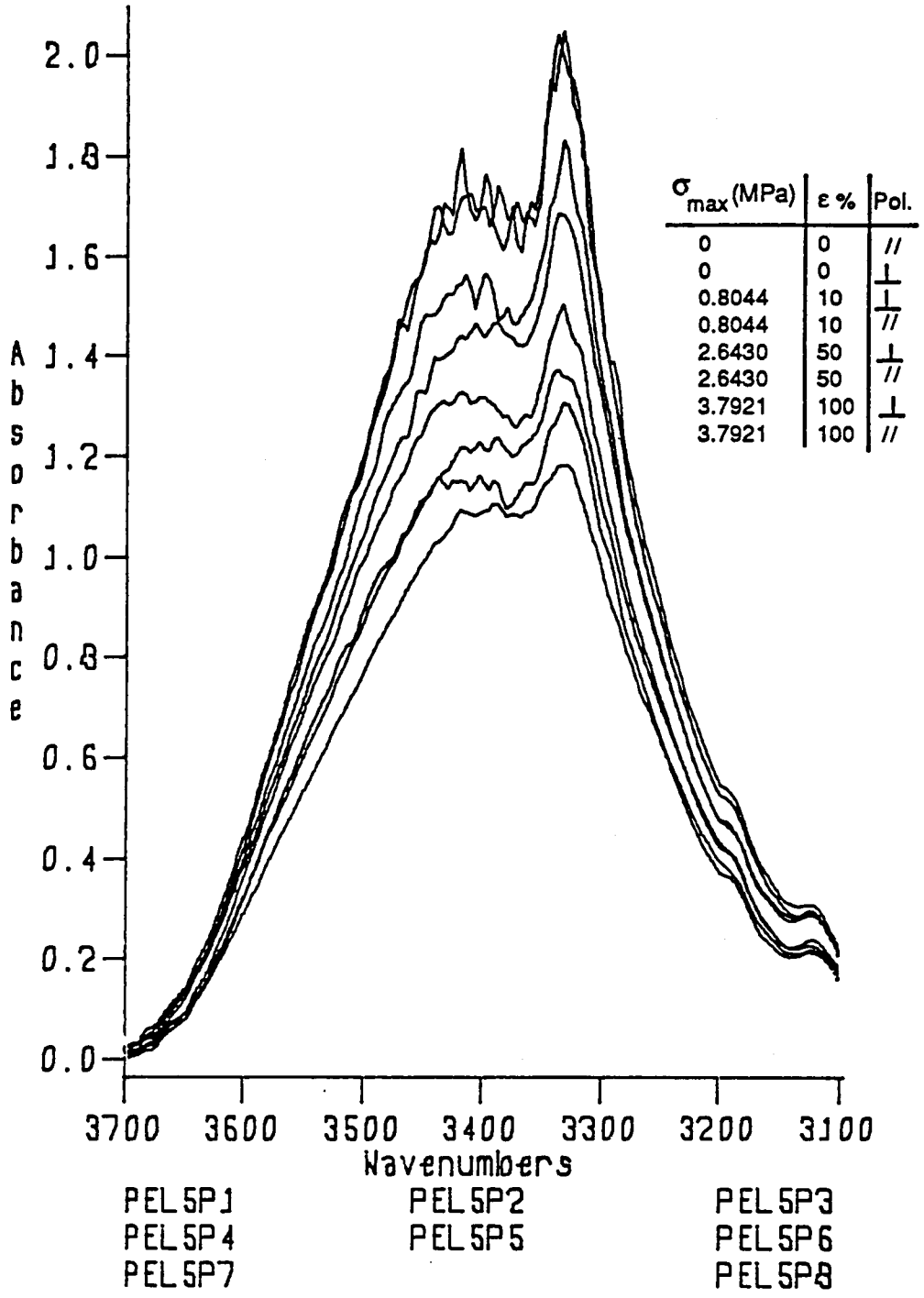

Figure 66: Polarized infrared absorbance spectra for Pellethane blended with 5% calcium chloride; at various strains; N-H stretch.

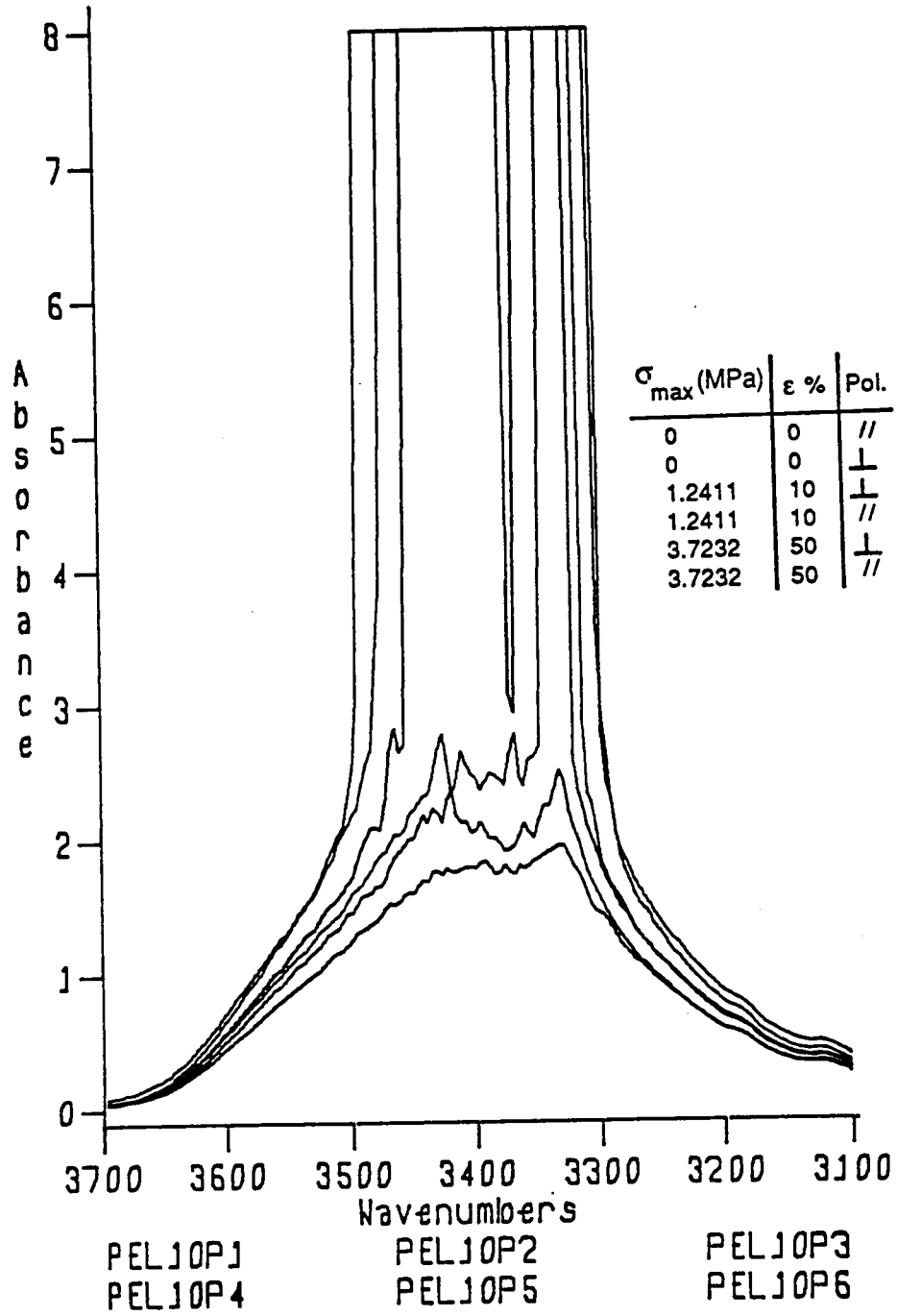

Figure 67: Polarized infrared absorbance spectra for Pellethane blended with 10% calcium chloride; at various strains; N-H stretch.

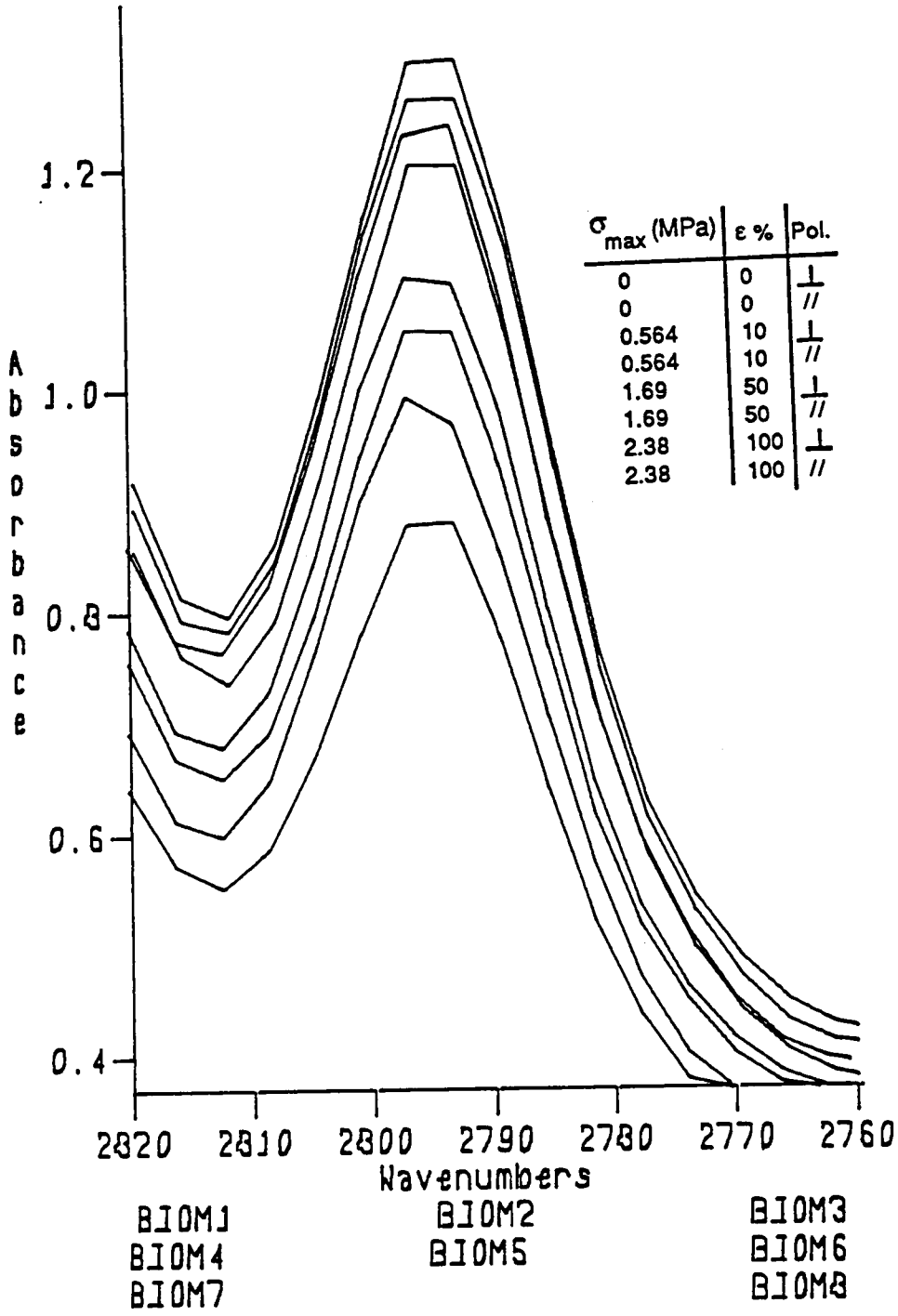

Figure 68: Polarized infrared absorbance spectra for pure Biomer at various strains; C-H stretch.

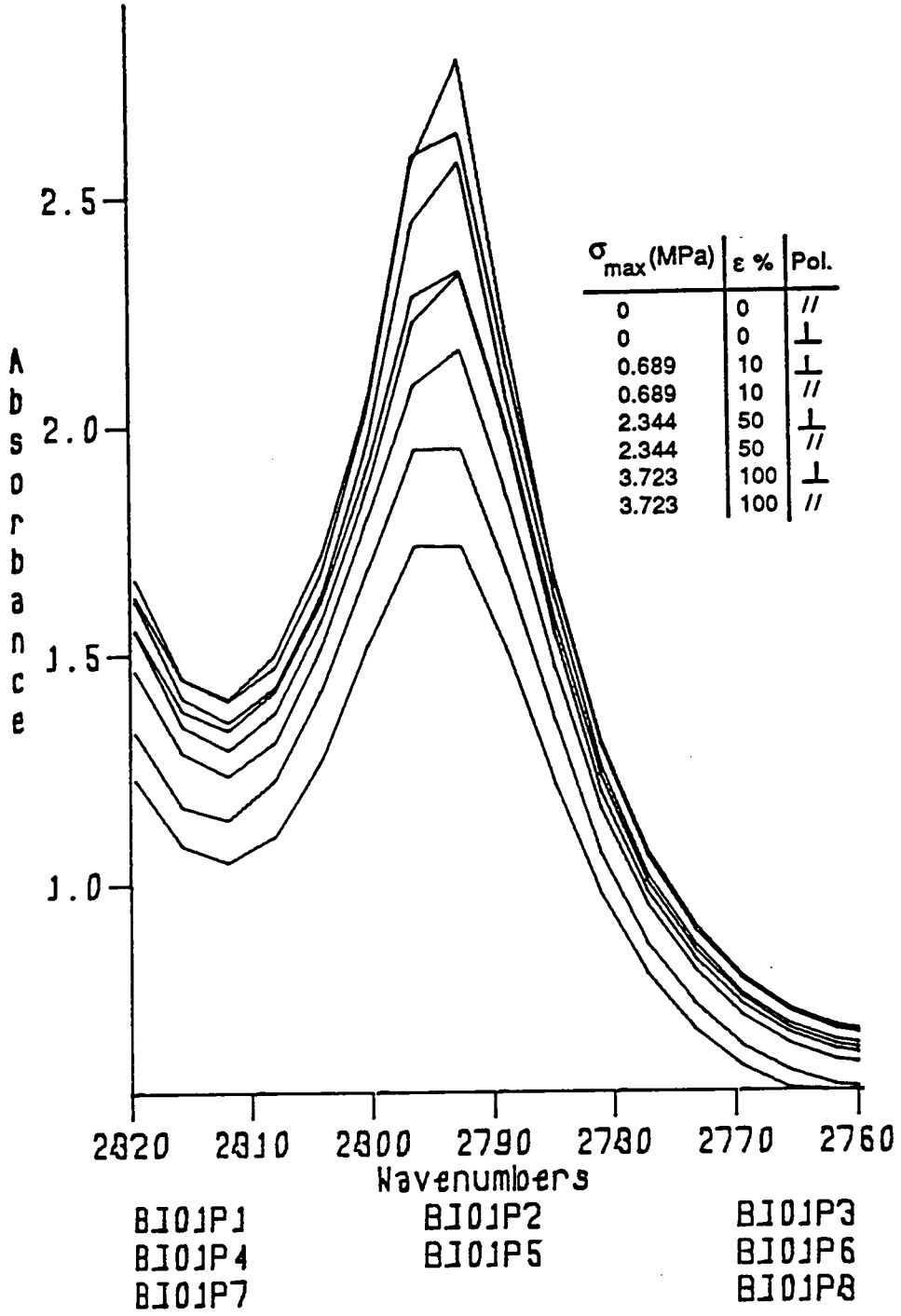

Figure 69: Polarized infrared absorbance spectra for Biomer blended with 1% calcium chloride; at various strains; C-H stretch.

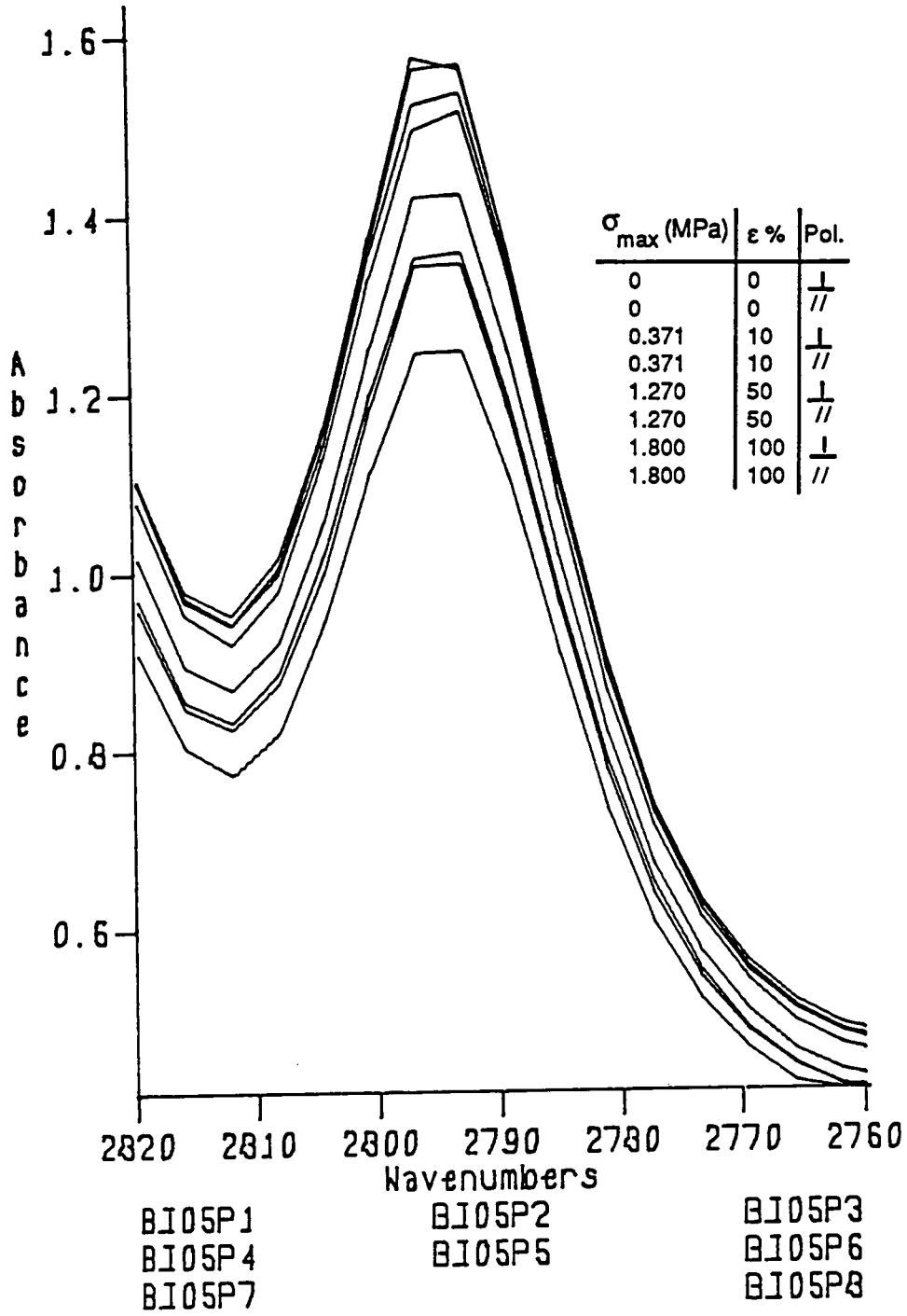

Figure 70: Polarized infrared absorbance spectra for Biomer blended with 5% calcium chloride; at various strains; C-H stretch.

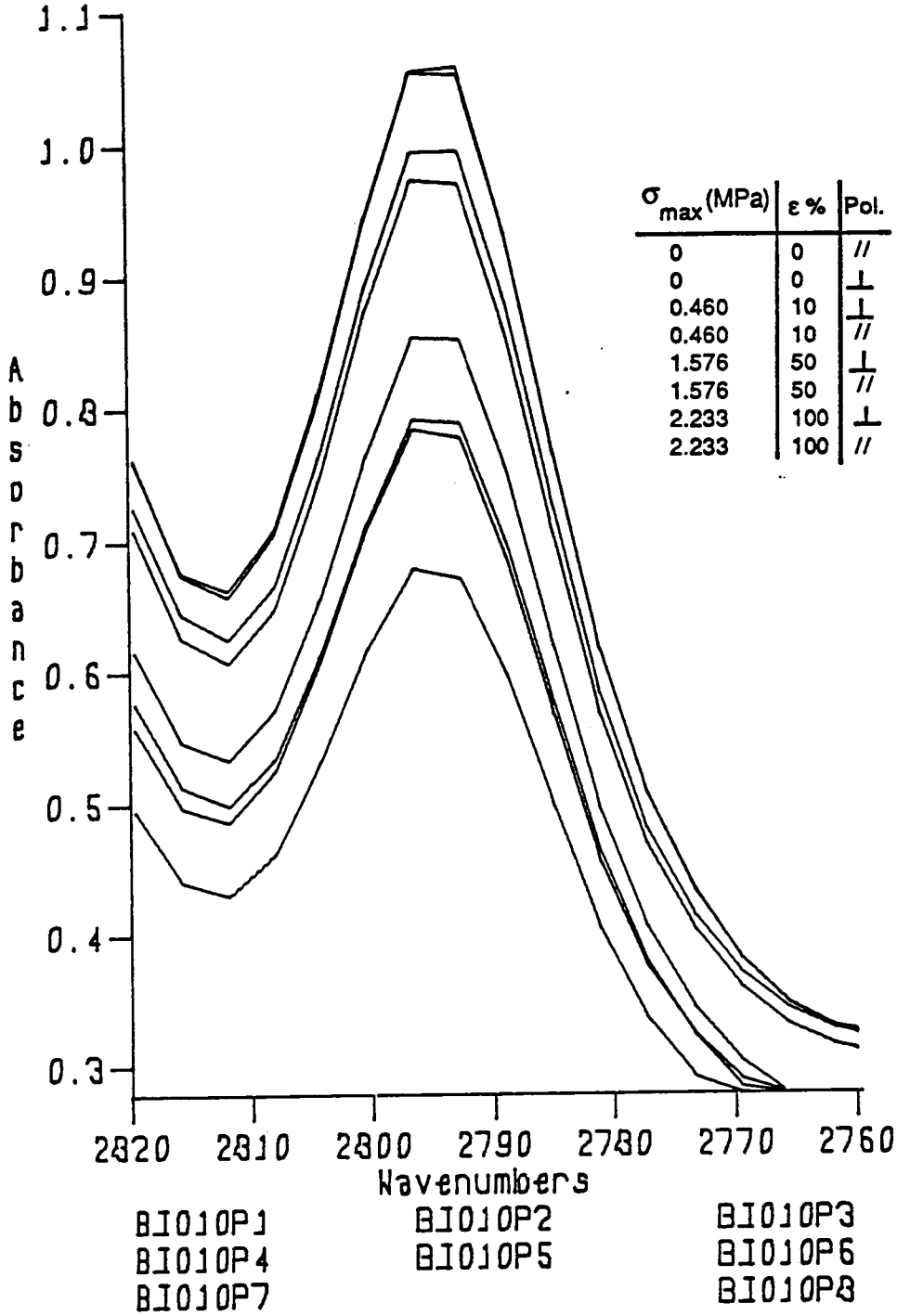

Figure 71: Polarized infrared absorbance spectra for Biomer blended with 10% calcium chloride; at various strains; C-H stretch.

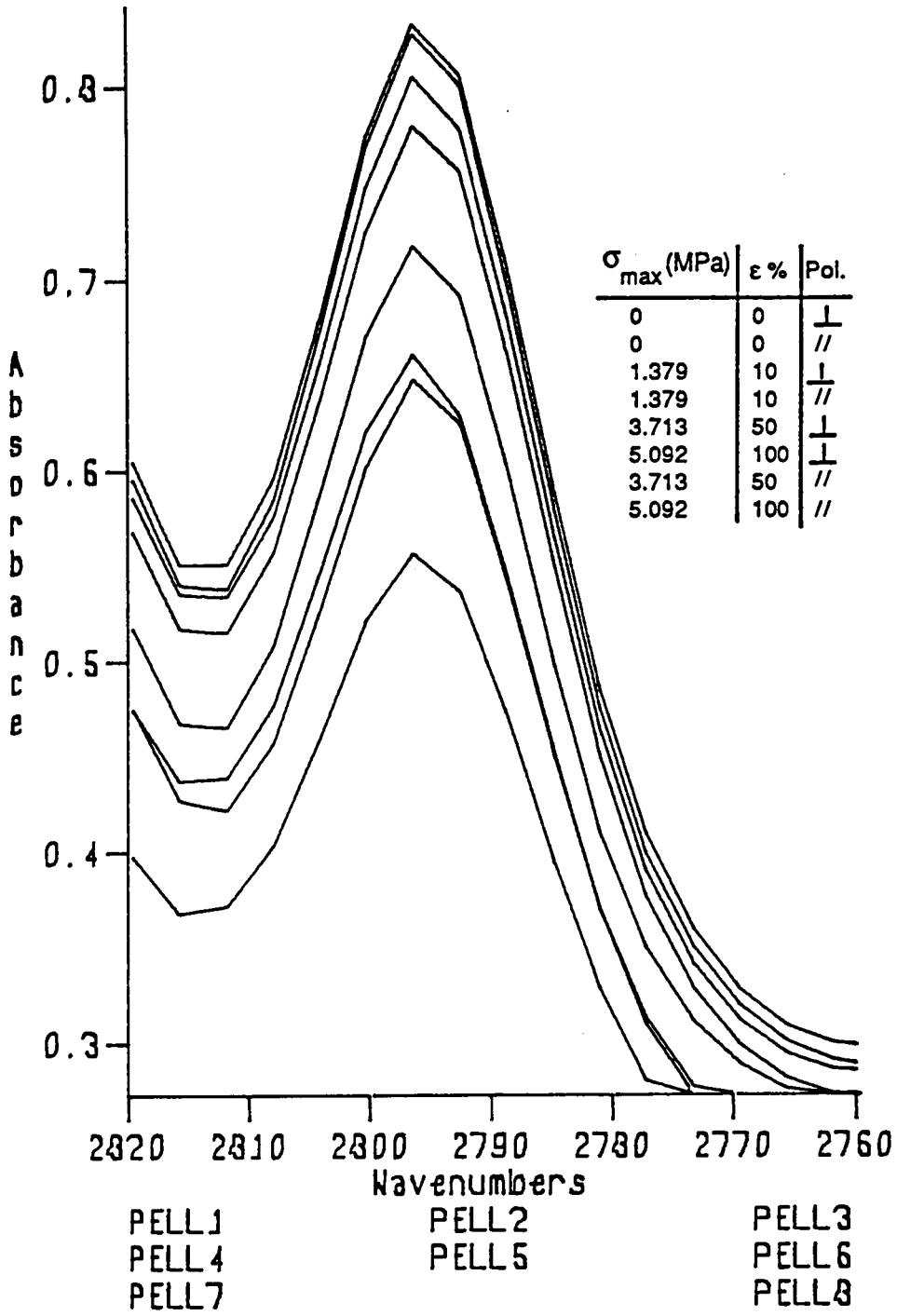

Figure 72: Polarized infrared absorbance spectra for pure Pellethane at various strains; C-H stretch.

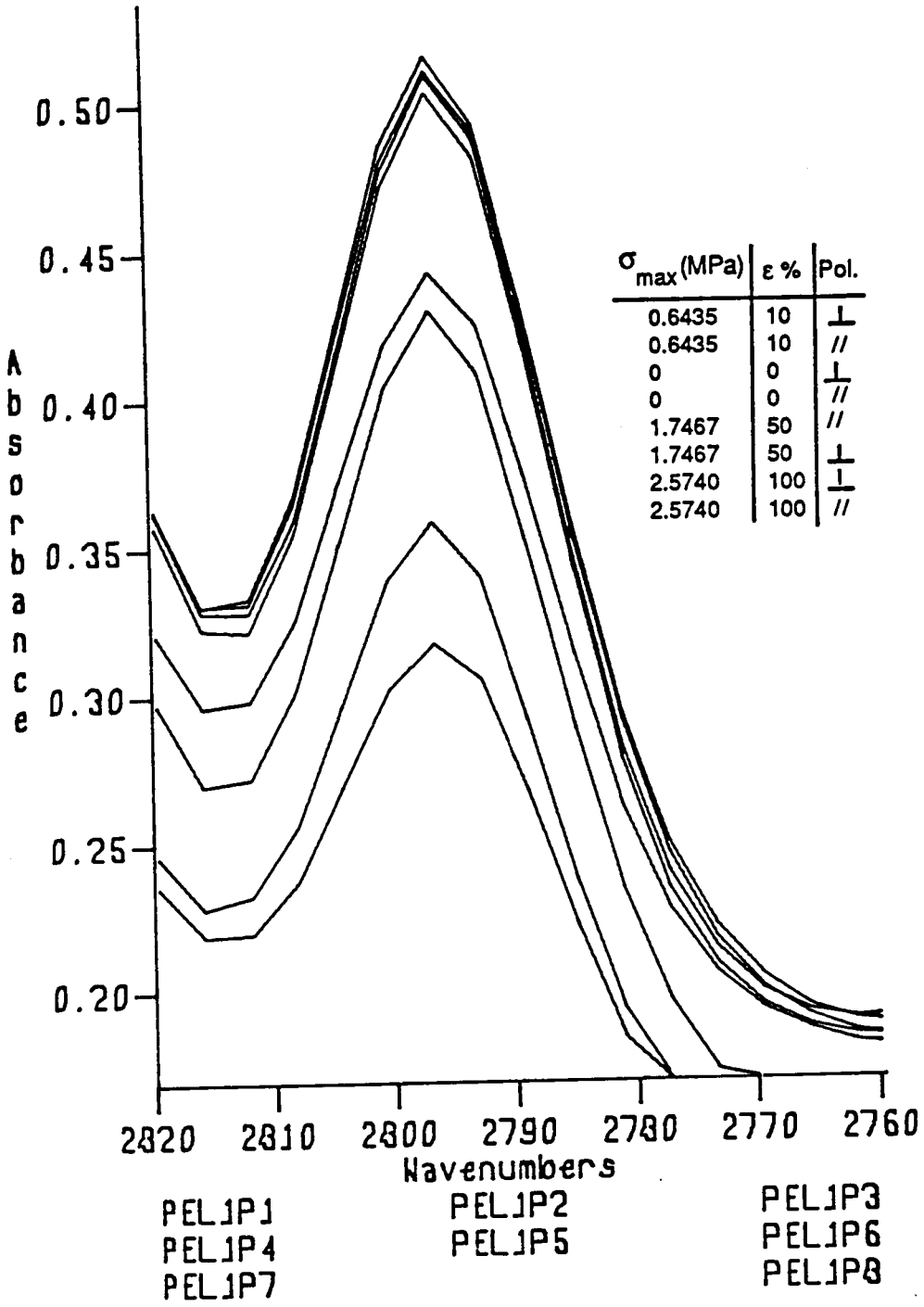

Figure 73: Polarized infrared absorbance spectra for Pellethane blended with 1% calcium chloride; at various strains; C-H stretch.

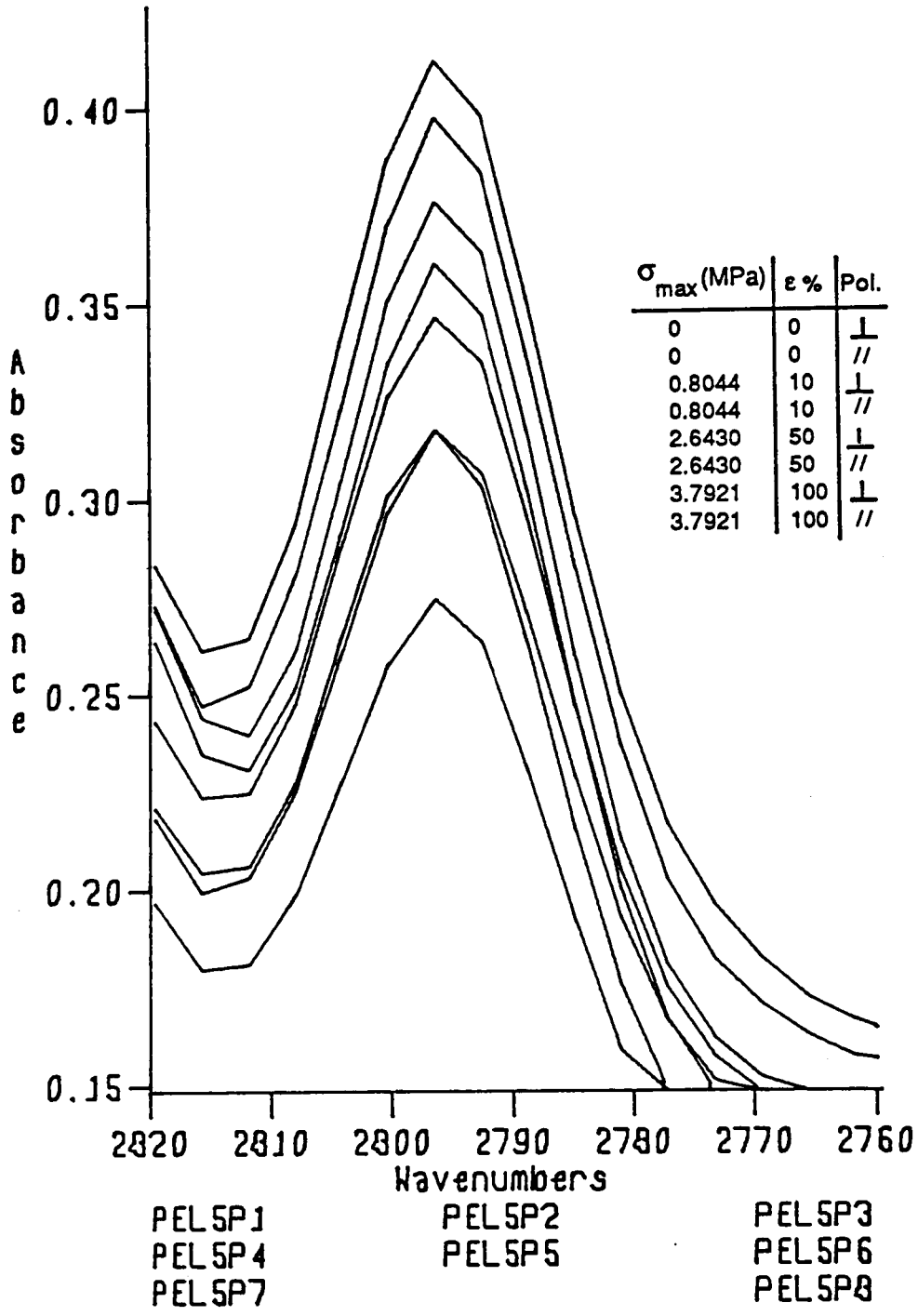

Figure 74: Polarized infrared absorbance spectra for Pellethane blended with 5% calcium chloride; at various strains; C-H stretch.

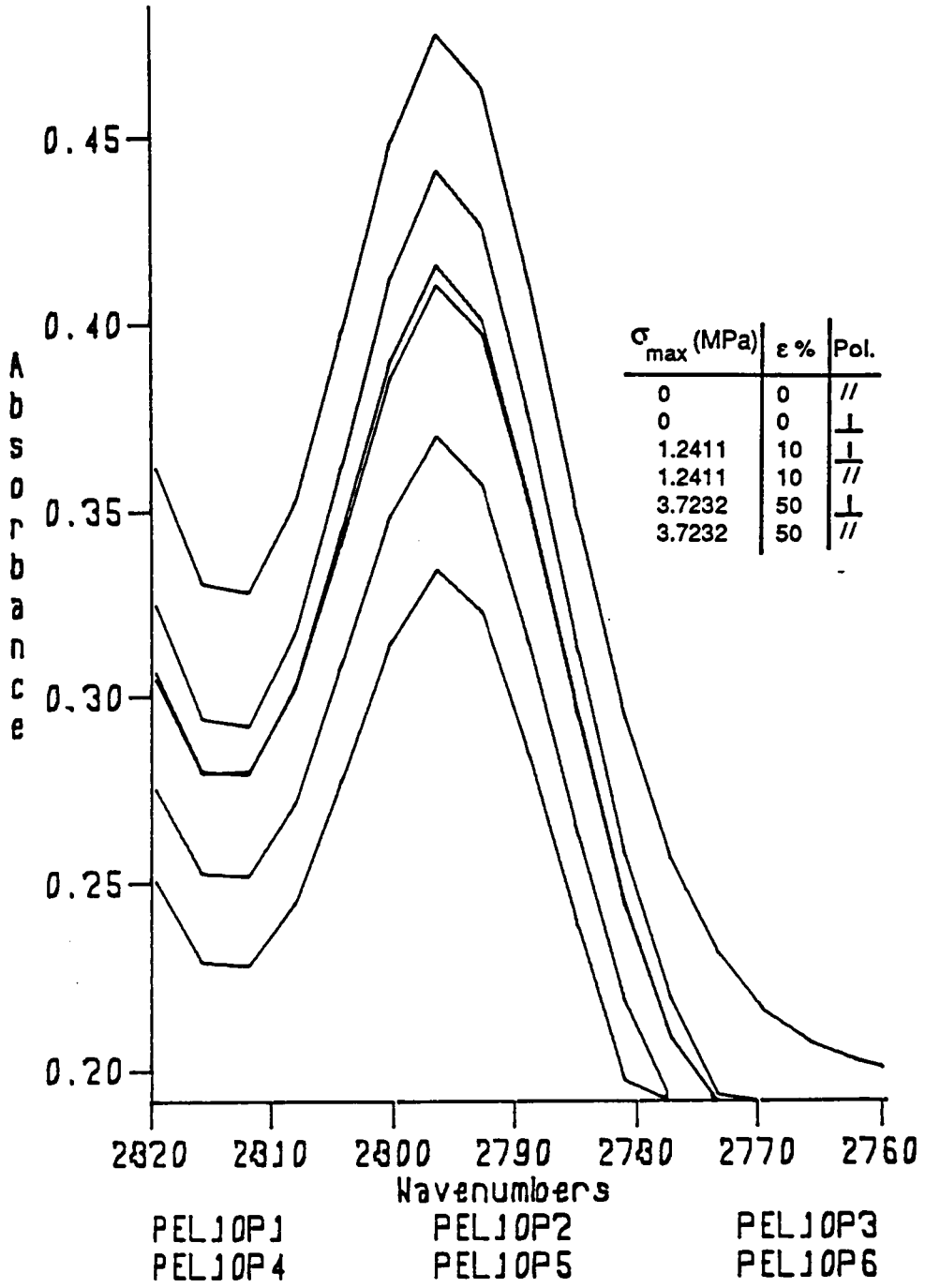

Figure 75: Polarized infrared absorbance spectra for Pellethane blended with 10% calcium chloride; at various strains; C-H stretch.

Table IV. Approximate Instability Crack Lengths.

Polyurethane	Calcium Chloride (wt.%)	a_c(mm.)
Biomer	0	5
Biomer	1	3.5
Biomer	5	5
Biomer	10	4
Pellethane	0	5.5
Pellethane	1	4
Pellethane	5	4.5
Pellethane	10	6.5

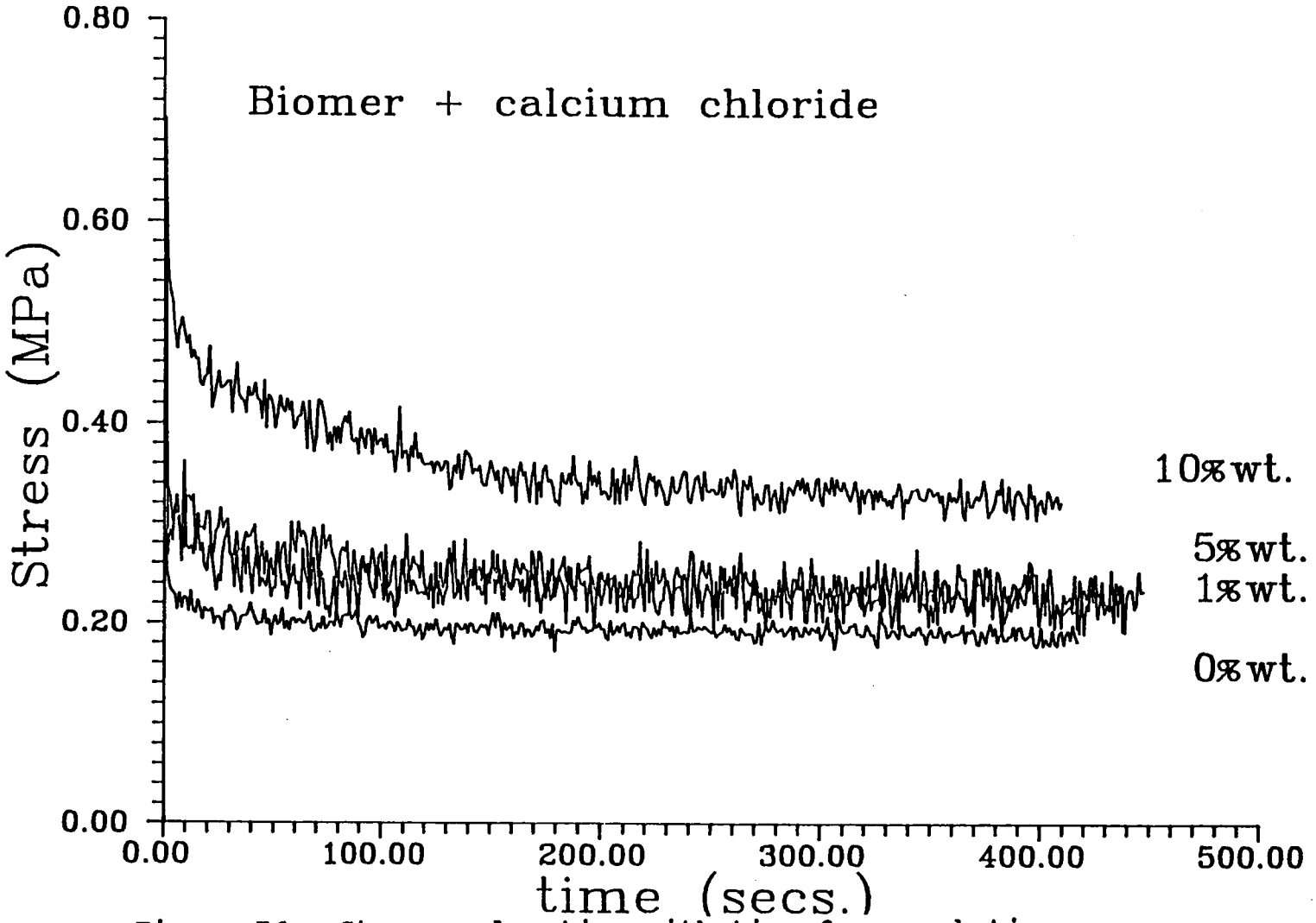

Figure 76: Stress relaxation with time for crack tip orientation studies of Biomer blended with calcium chloride.

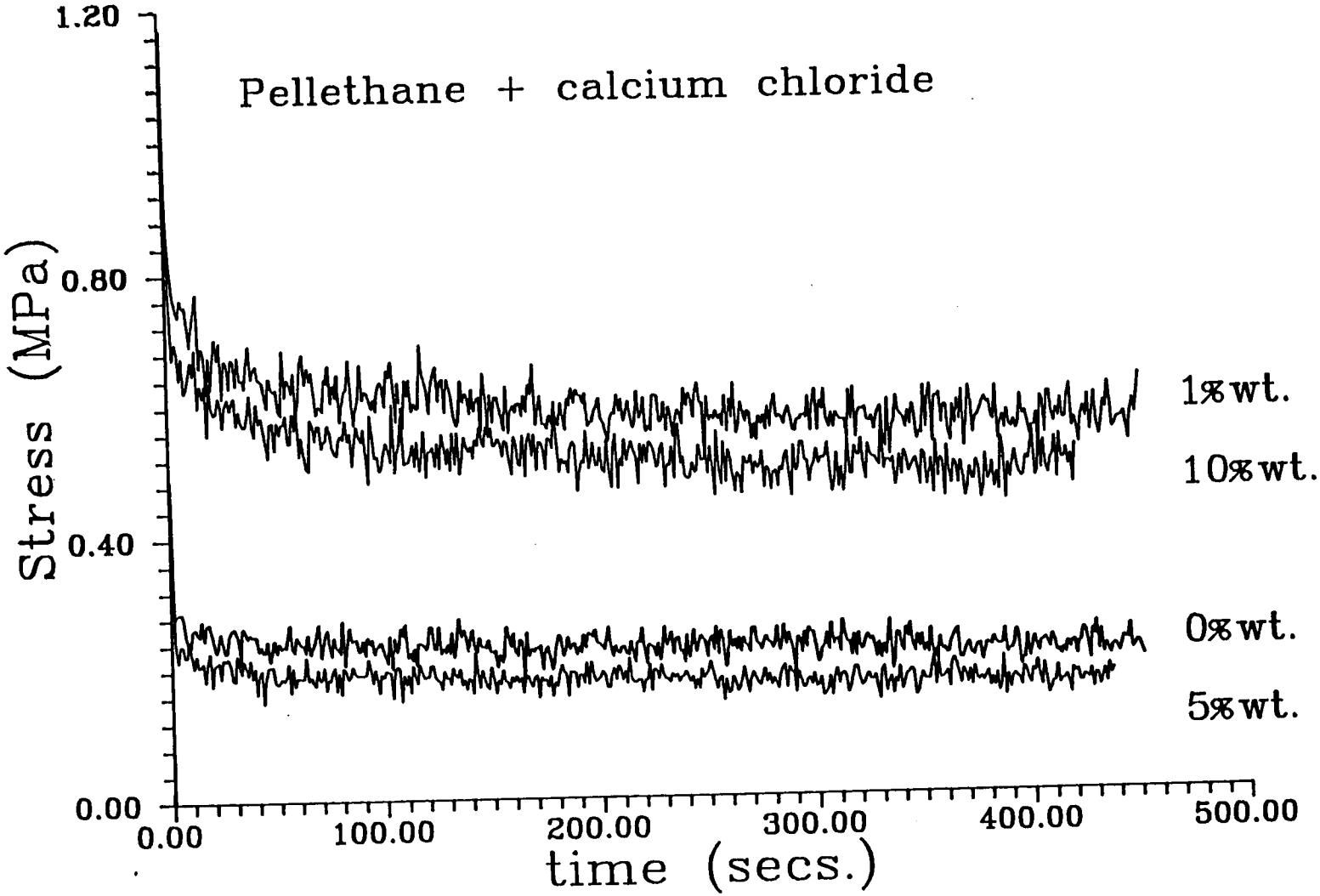

Figure 77: Stress relaxation with time for crack tip orientation studies of Pellethane blended with calcium chloride.

similar data for Pellethane and it's calcium chloride blends.

Figures 78 through 85 are plots of the polarized absorbance spectra for the hard segment domains of Biomer, Pellethane and their blends with calcium chloride collected at the positions surrounding the crack tip shown in Figure 33. Figure 78 shows the N-H stretch vibration for pure Biomer. Figure 79 shows the C=O stretch vibration for pure Biomer. Figure 80 shows the N-H stretch vibration for Biomer blended with 1% wt. calcium chloride. Figure 81 shows the C=O stretch vibration for Biomer blended with 1% wt. calcium chloride.

Figure 82 shows the N-H stretch vibration for Biomer blended with 5% wt. calcium chloride. Figure 83 shows the C=O stretch vibration for Biomer blended with 5% wt. calcium chloride. The unusual absorptions in the range of 3700 to 3550 cm^{-1} and 1730 to 1680 cm^{-1} which appear in the parallel polarized spectrum were attributed to atmospheric moisture in the background; the absorption measurements of the N-H and C=O groups were unaffected.

Figure 84 shows the N-H stretch region for Biomer blended with 10% wt. calcium chloride. Figure 85 shows the C=O stretch for Biomer blended with 10% wt. calcium chloride.

The same spectral regions are presented for Pellethane and it's blends. Figure 86 is a plot of the N-

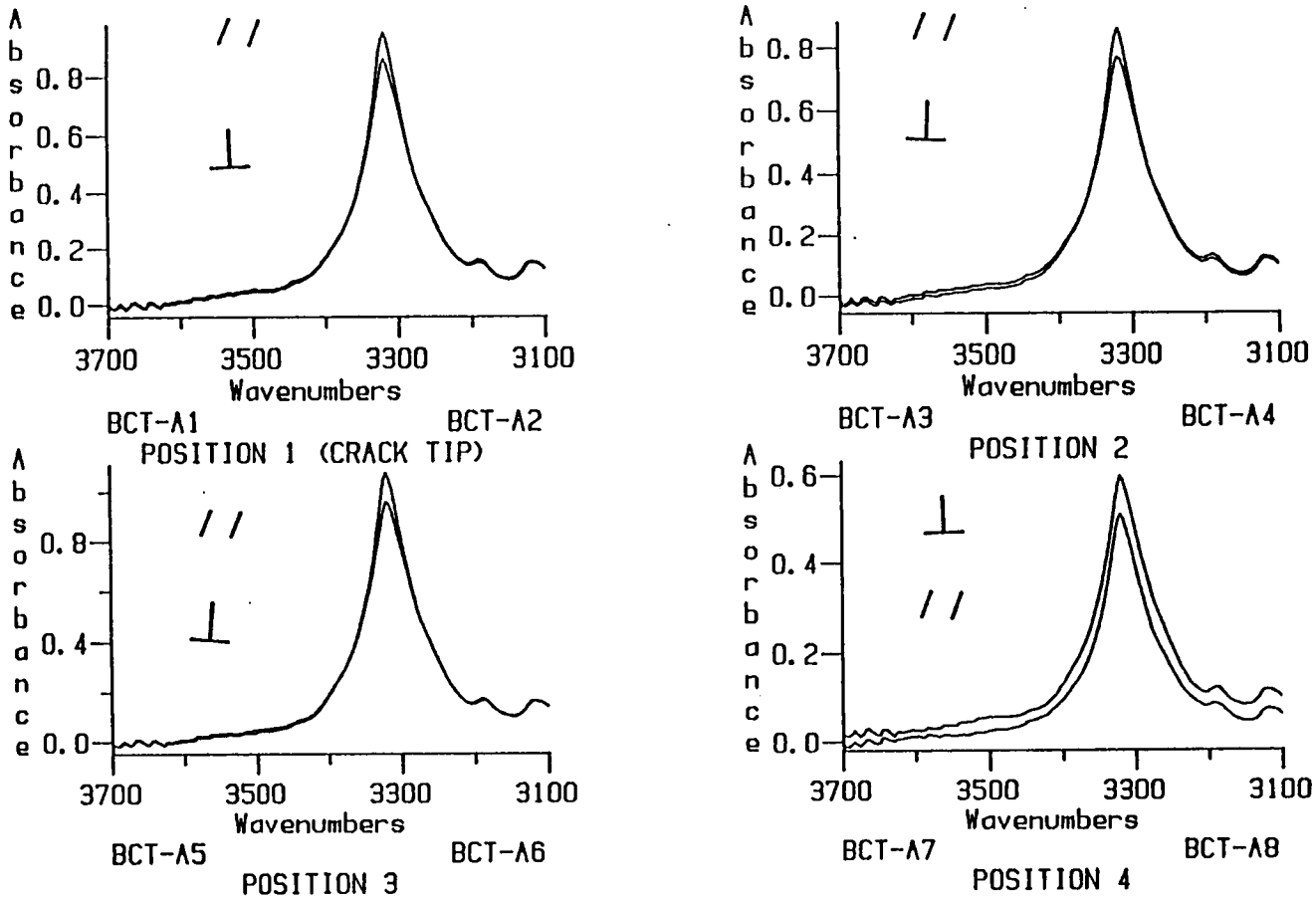

Figure 78: Polarized infrared absorbance spectra for pure Biomer surrounding the crack tip; N-H stretch.

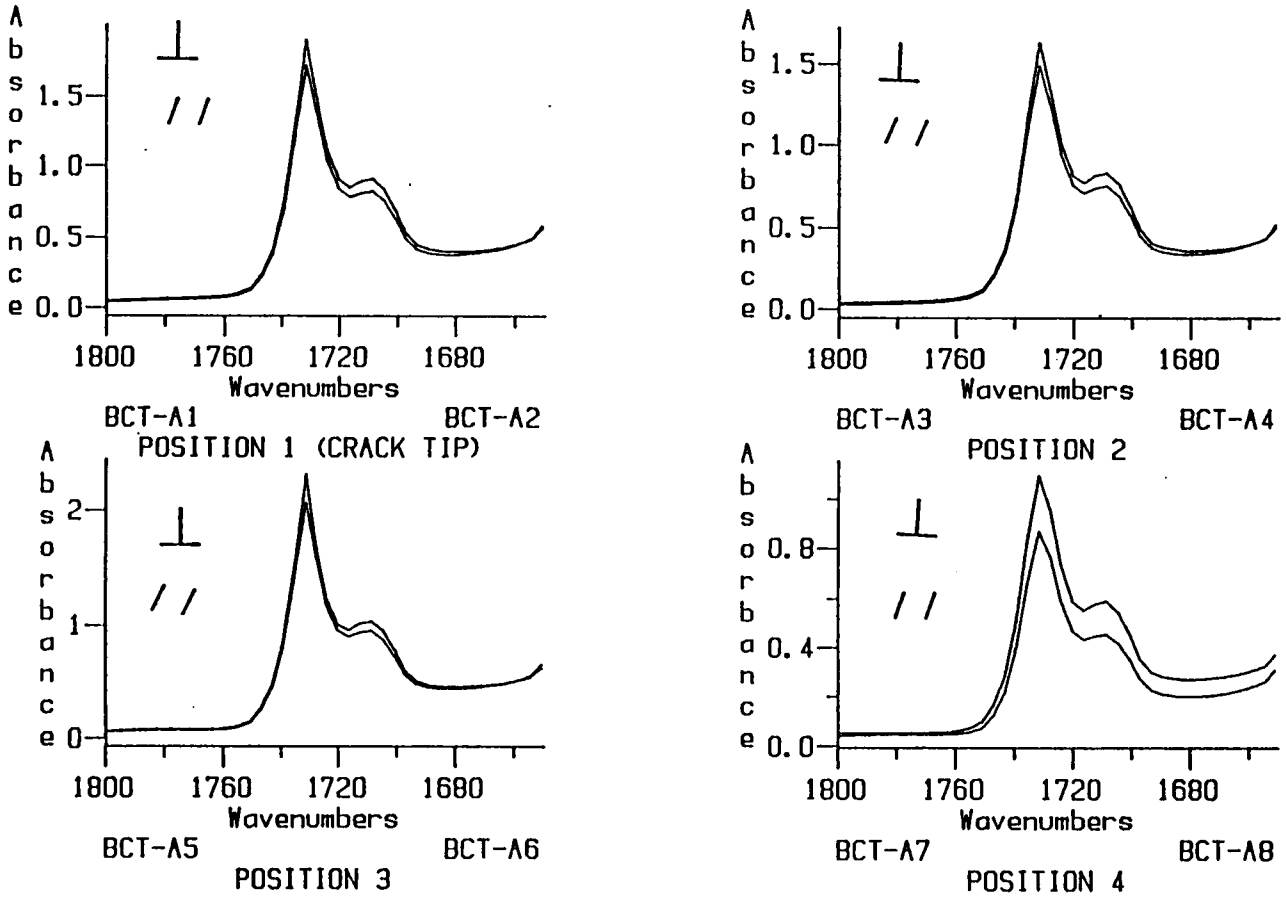

Figure 79: Polarized infrared absorbance spectra for pure Biomer surrounding the crack tip; C=O stretch.

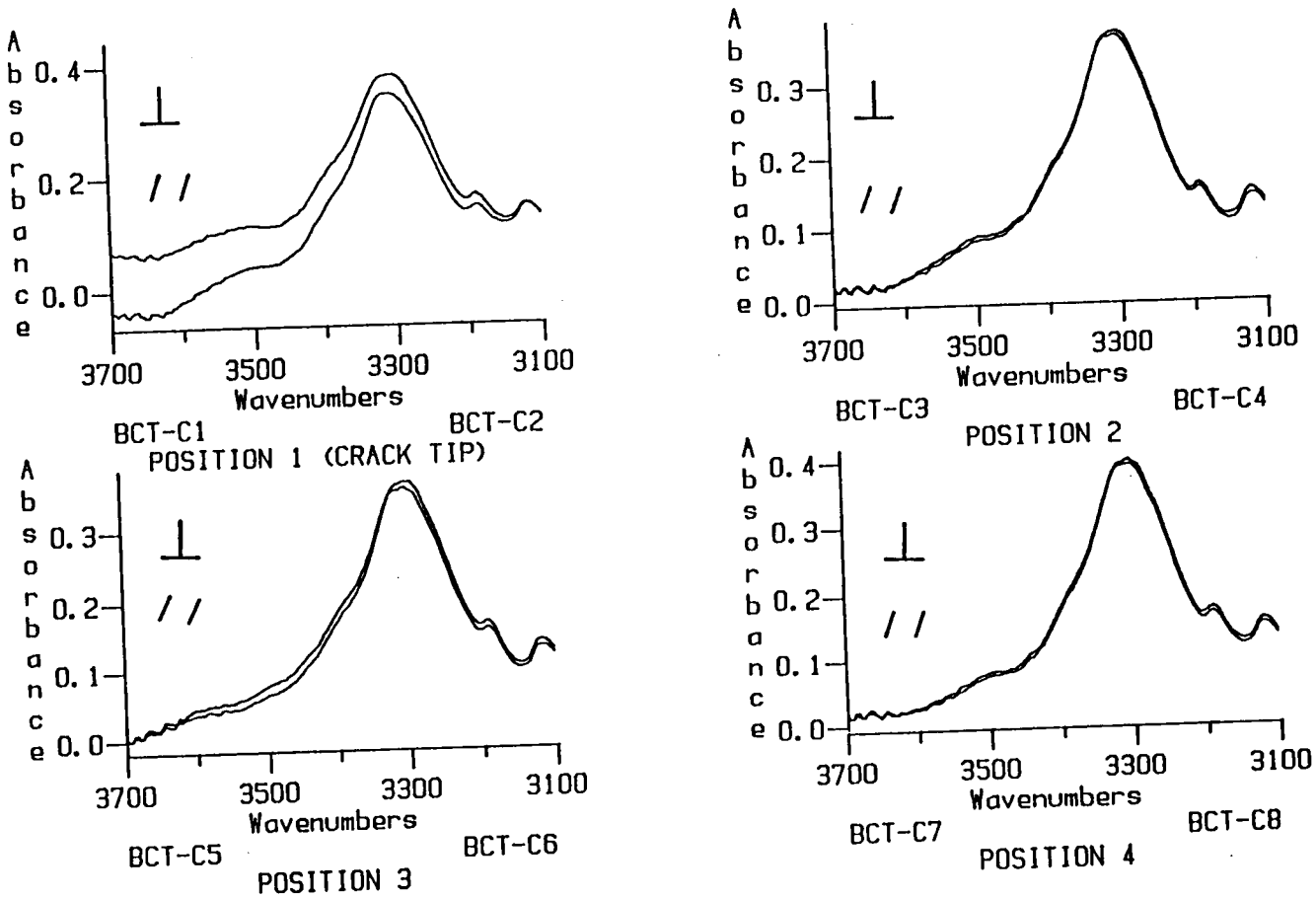

Figure 80: Polarized infrared absorbance spectra for Biomer blended with 1% wt. calcium chloride; surrounding the crack tip; N-H stretch.

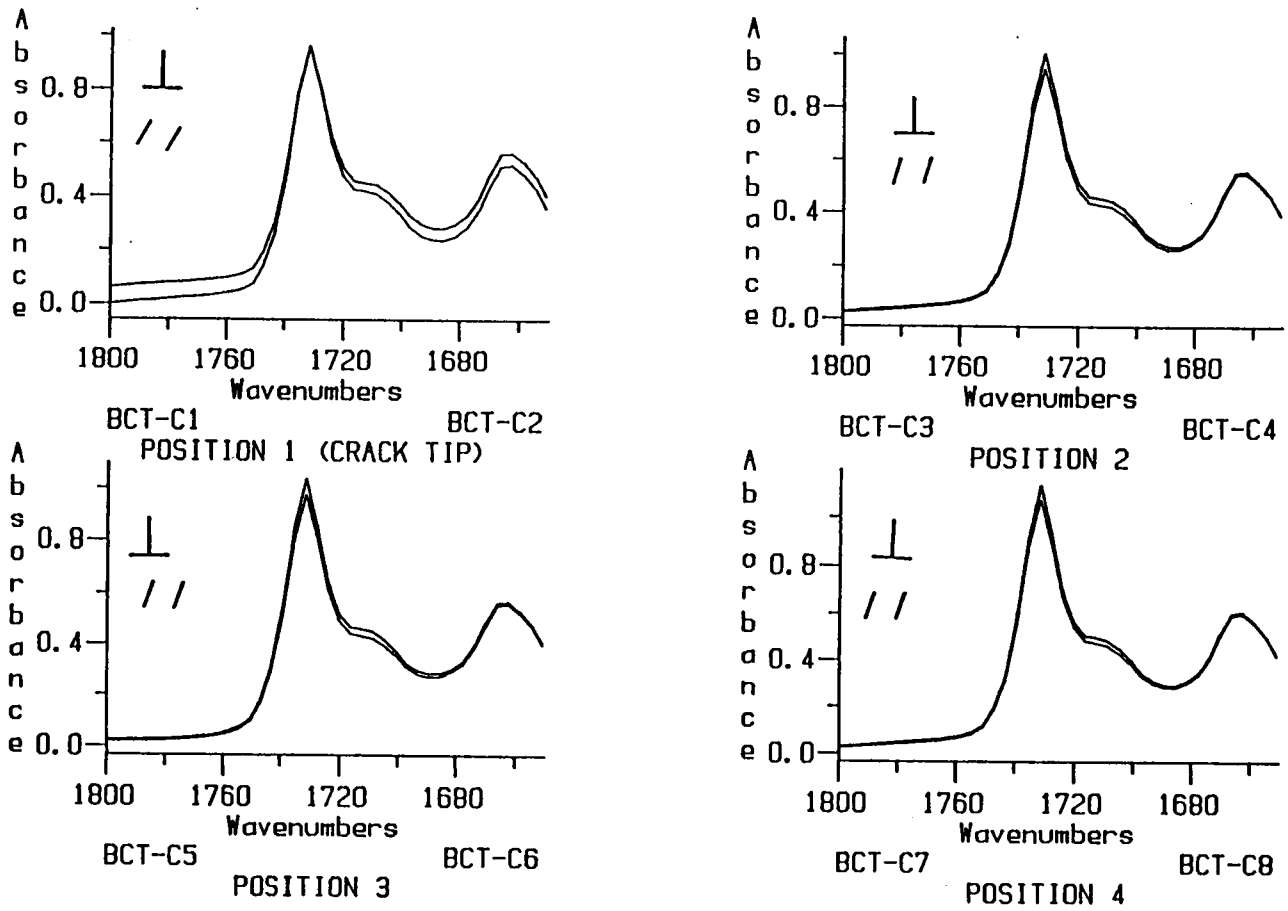

Figure 81: Polarized infrared absorbance spectra for Biomer blended with 1% wt. calcium chloride; surrounding the crack tip; C=O stretch.

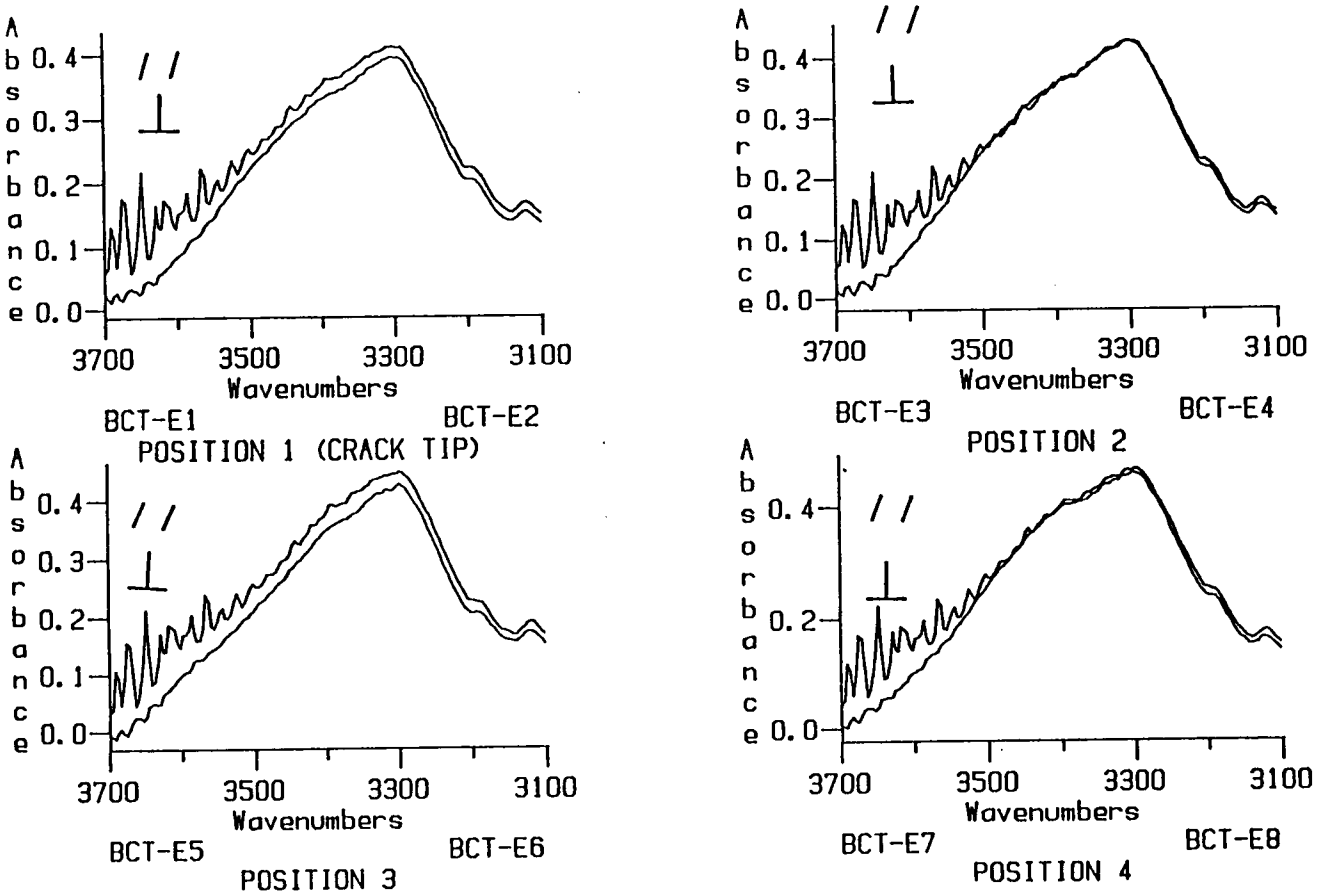

Figure 82: Polarized infrared absorbance spectra for Biomer blended with 5% wt. calcium chloride; surrounding the crack tip; N-H stretch.

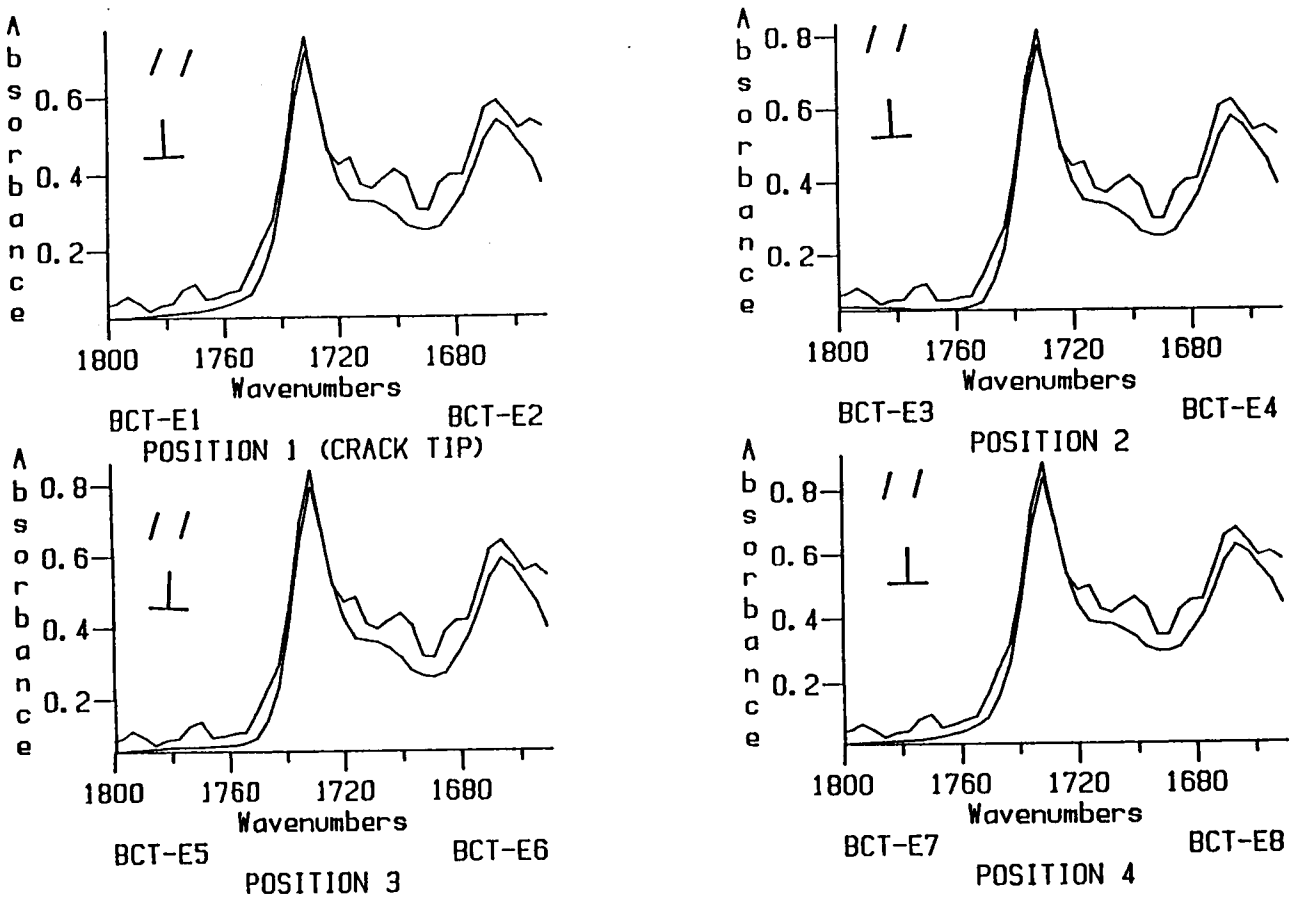

Figure 83: Polarized infrared absorbance spectra for Biomer blended with 5% wt. calcium chloride; surrounding the crack tip; C=O stretch.

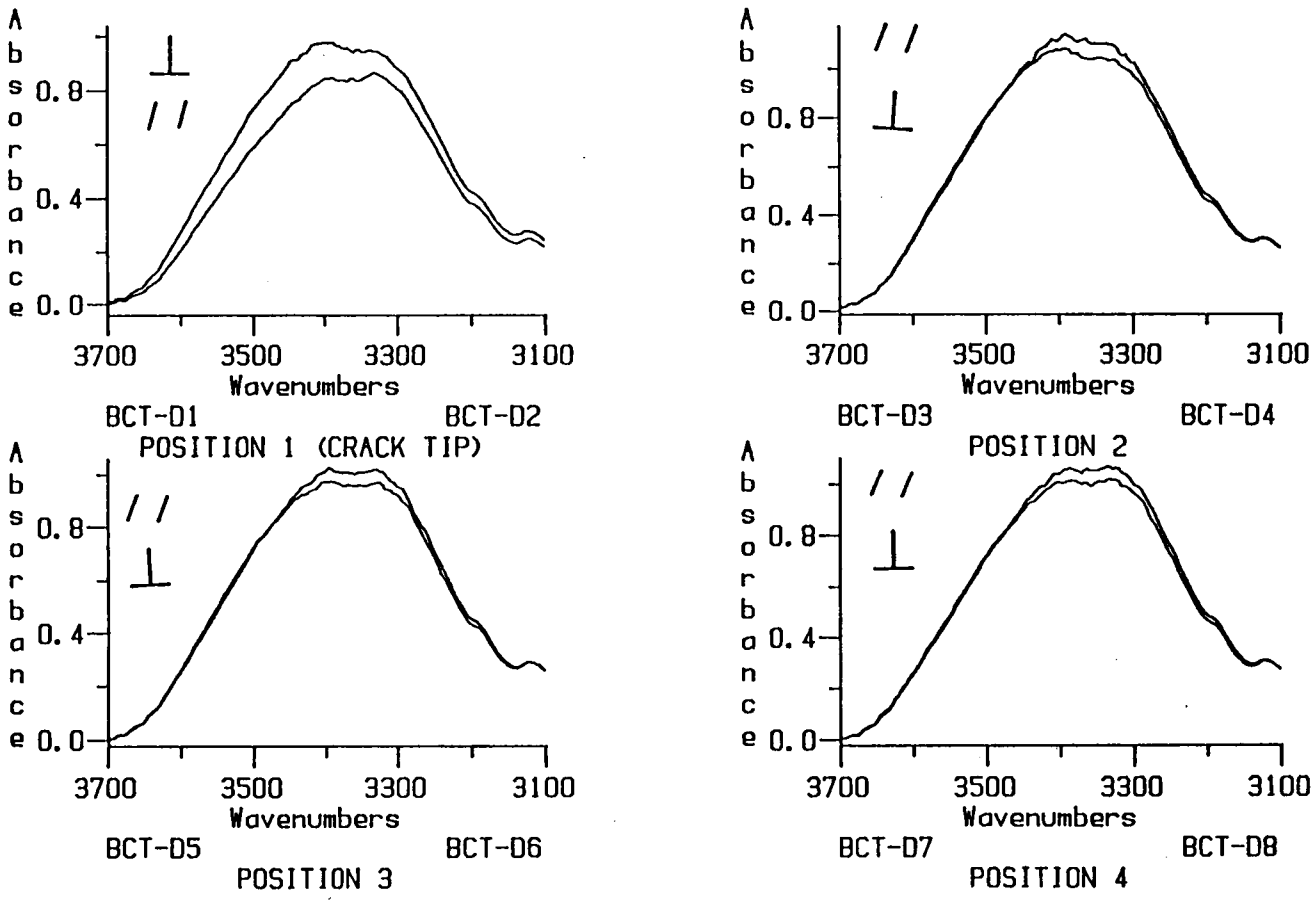

Figure 84: Polarized infrared absorbance spectra for Biomer blended with 10% wt. calcium chloride; surrounding the crack tip; N-H stretch.

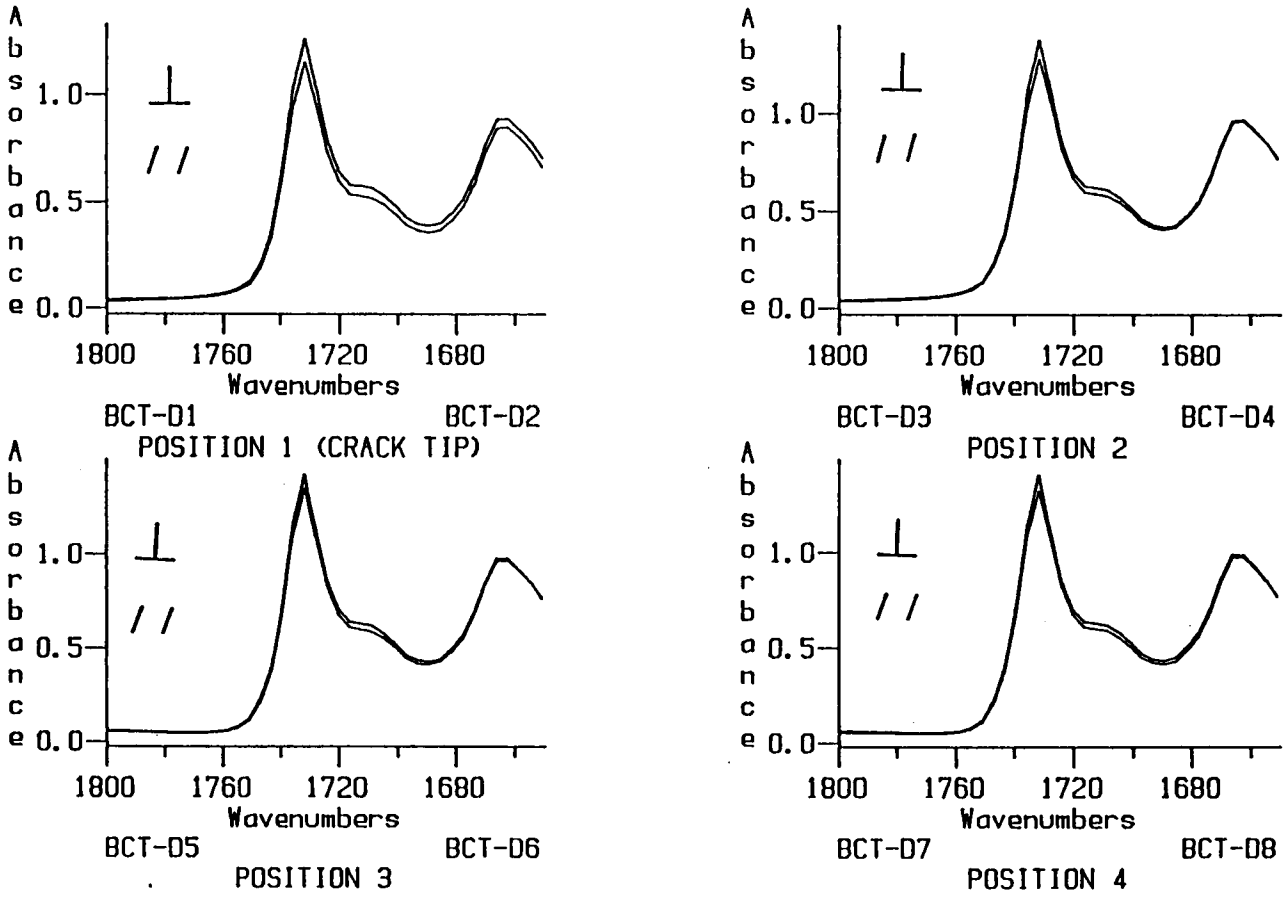

Figure 85: Polarized infrared absorbance spectra for Biomer blended with 10% wt. calcium chloride; surrounding the crack tip; C=O stretch.

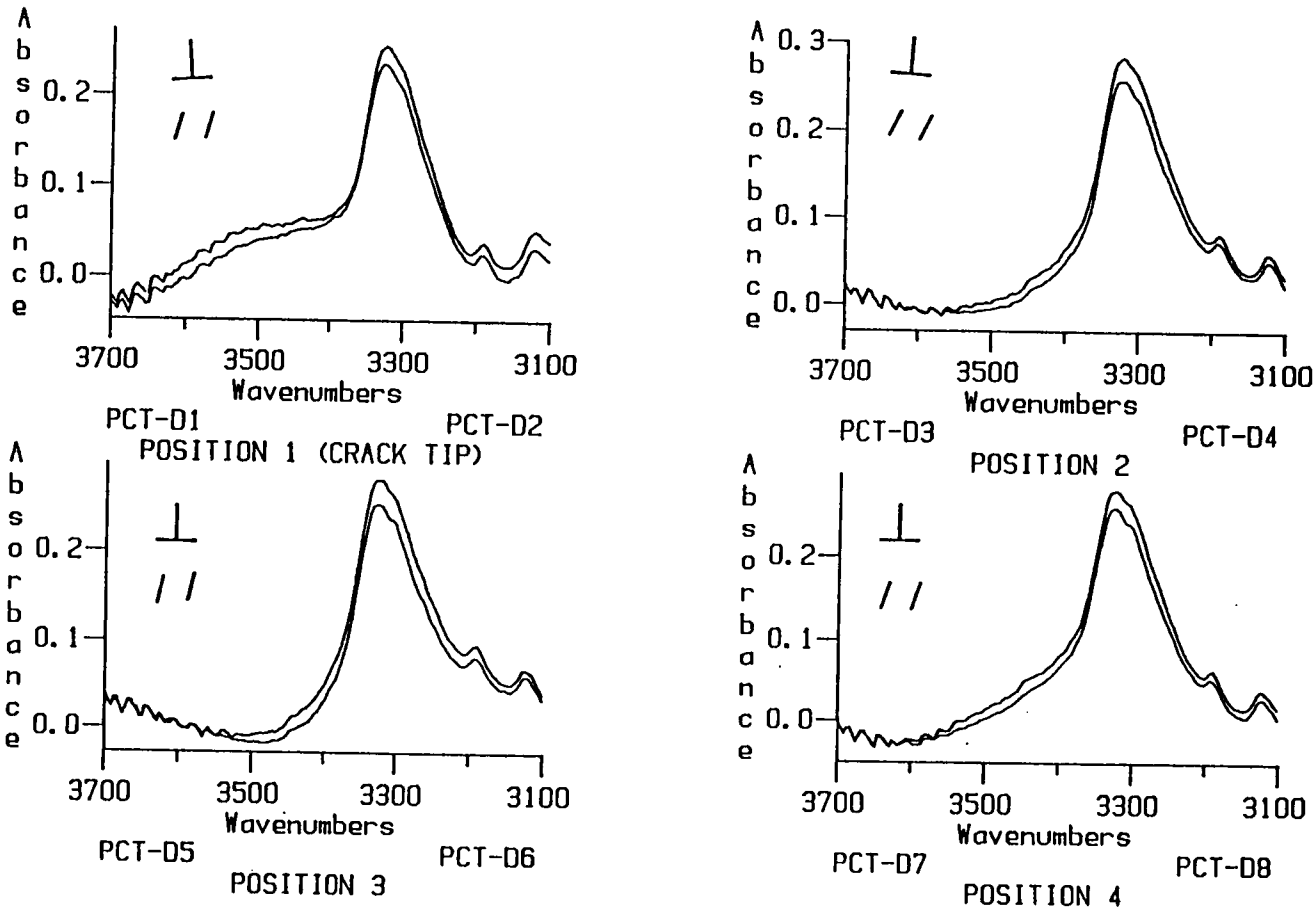

Figure 86: Polarized infrared absorbance spectra for pure Pellethane surrounding the crack tip; N-H stretch.

H stretch band for pure Pellethane. Figure 87 is a plot of the C=O stretch band for Pellethane. Figure 88 is a plot of the N-H stretch for Pellethane blended with 1% wt. calcium chloride. Figure 89 is a plot of the C=O stretch for Pellethane blended with 1% wt. calcium chloride. Figure 90 is a plot of the N-H stretch region for Pellethane blended with 5% wt. calcium chloride. Figure 91 is a plot of the C=O stretch region for Pellethane blended with 5% wt. calcium chloride. Figure 92 is a plot of the N-H stretch region for Pellethane blended with 10% wt. calcium chloride. Figure 93 is a plot of the C=O stretch region for Pellethane blended with 10% wt. calcium chloride.

To complete the analysis of orientation, the C-H stretch vibration was examined for each of the calcium chloride concentrations of Biomer and Pellethane. Although two non-aromatic C-H stretch vibrations are expected from each urethane group, the largest number of these vibrations are found for the soft segment poly(ether) group.

Figure 94 is a plot of the polarized spectra of Biomer in the C-H stretch region. Figure 95 shows the polarized spectra for Biomer blended with 1% wt of calcium chloride. Figure 96 shows the same information for the 5% wt. blend and Figure 97 shows the spectra for the 10% wt. blend with Biomer.

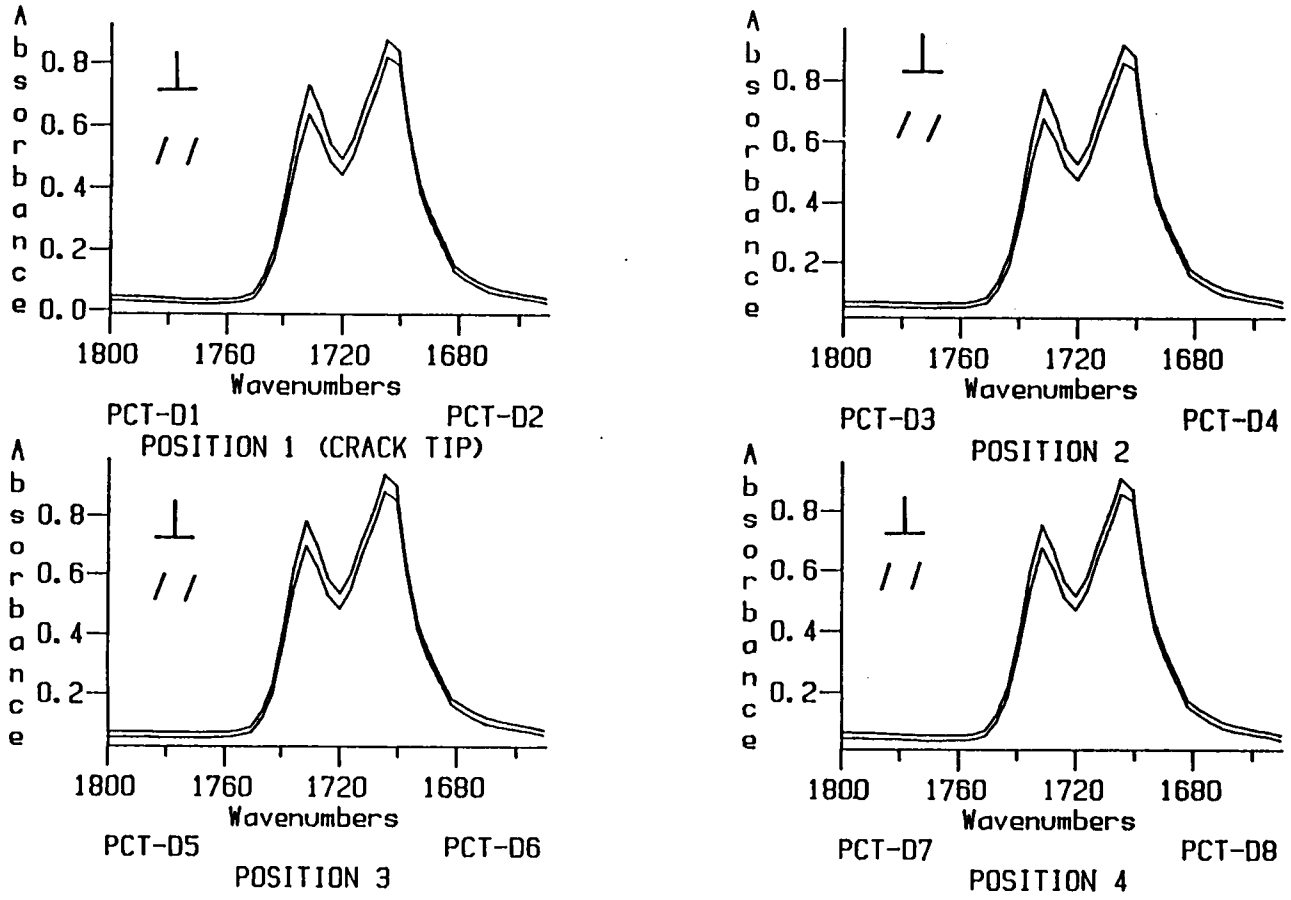

Figure 87: Polarized infrared absorbance spectra for pure Pellethane surrounding the crack tip; C=O stretch.

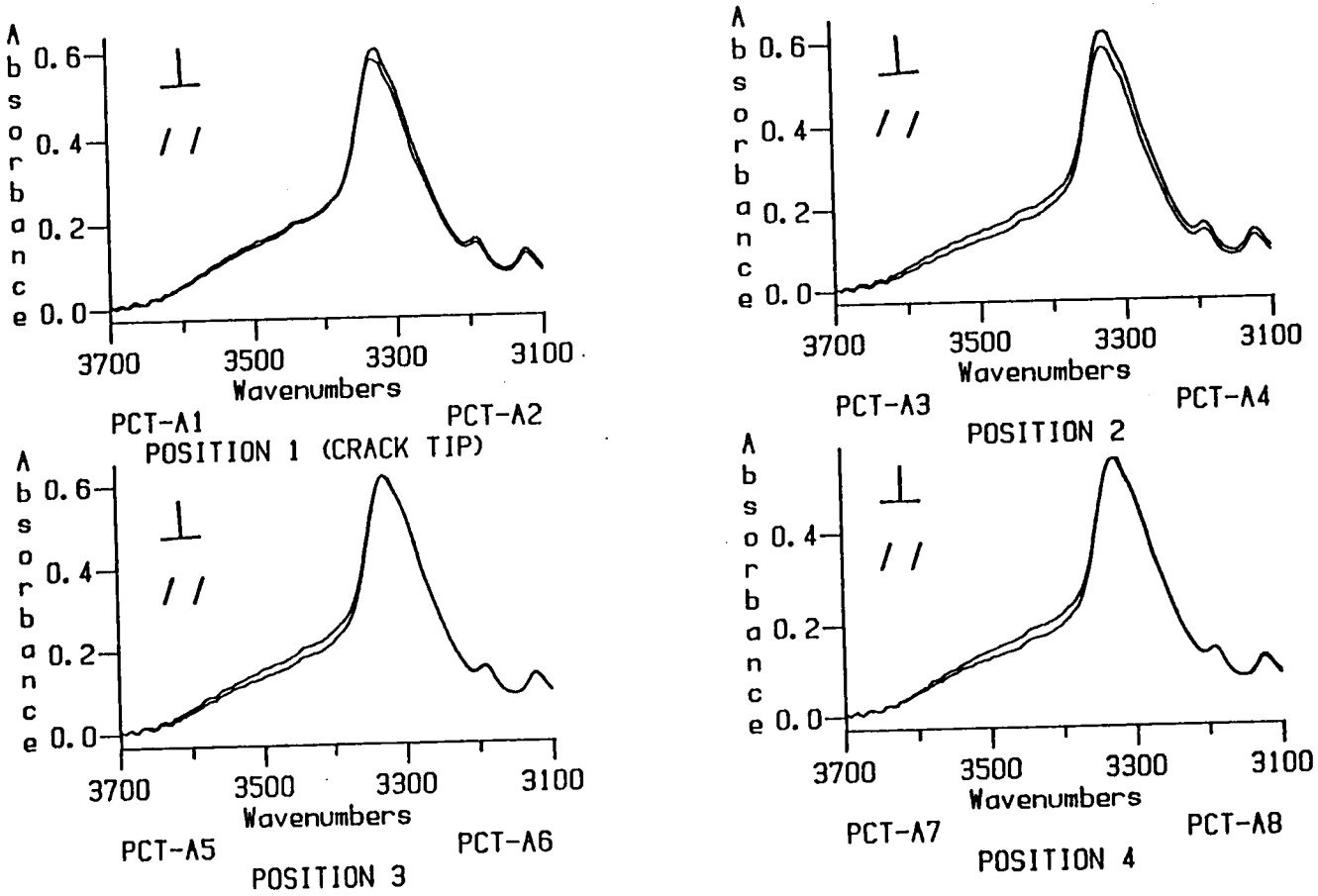

Figure 88: Polarized infrared absorbance spectra for Pellethane blended with 1% wt. calcium chloride; surrounding the crack tip; N-H stretch.

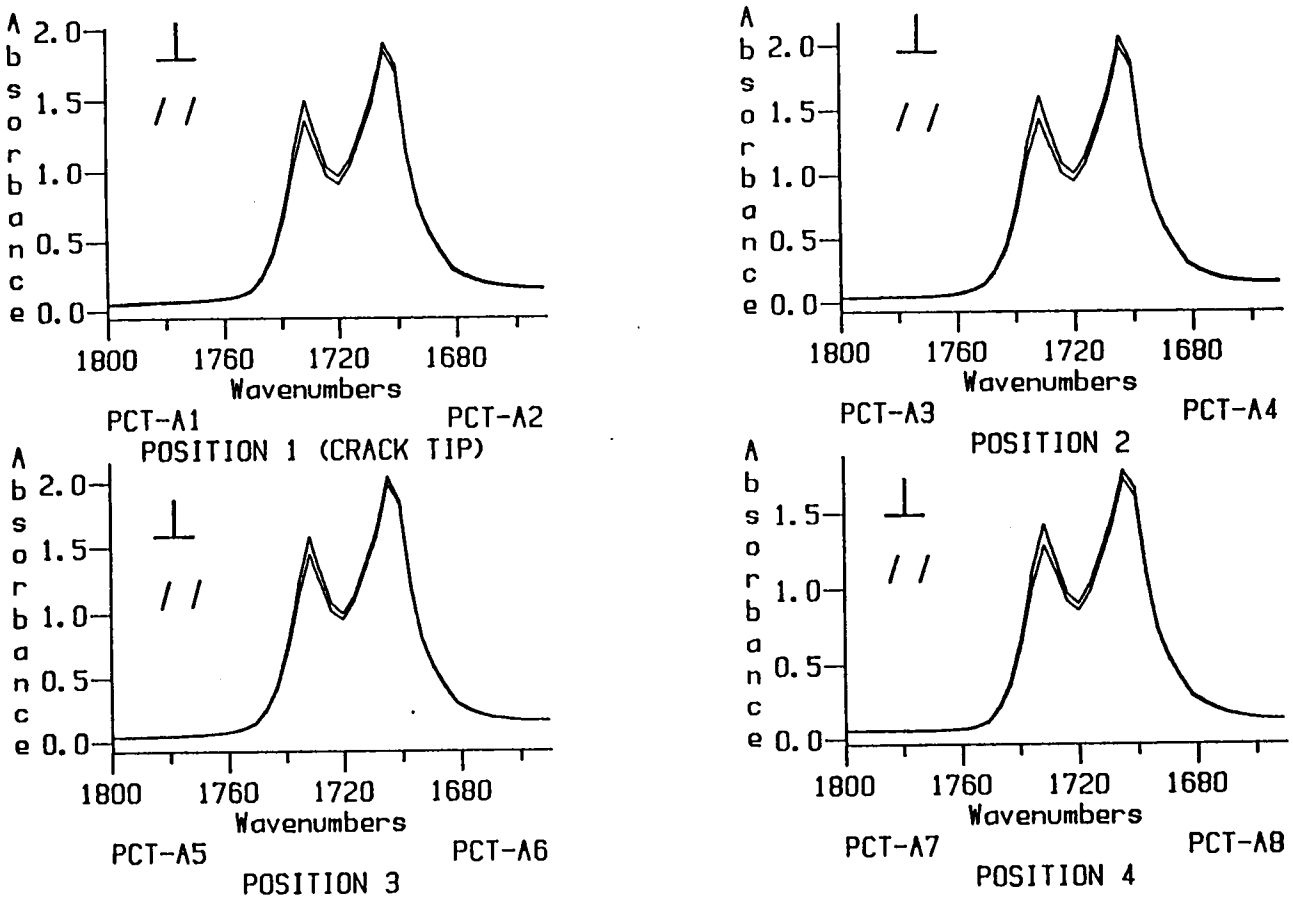

Figure 89: Polarized infrared absorbance spectra for Pellethane blended with 1% wt. calcium chloride; surrounding the crack tip; C=O stretch.

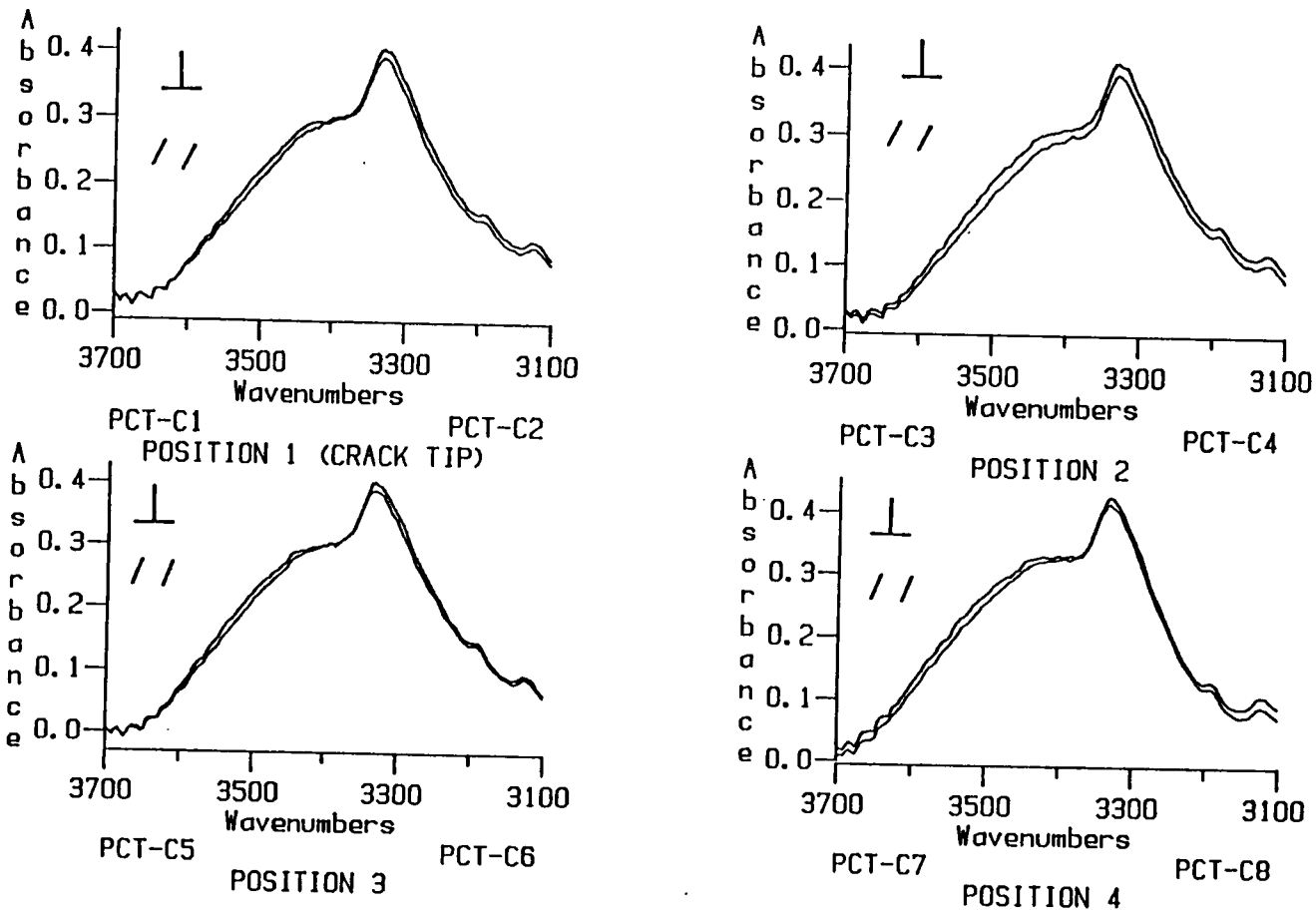

Figure 90: Polarized infrared absorbance spectra for Pellethane blended with 5% wt. calcium chloride; surrounding the crack tip; N-H stretch.

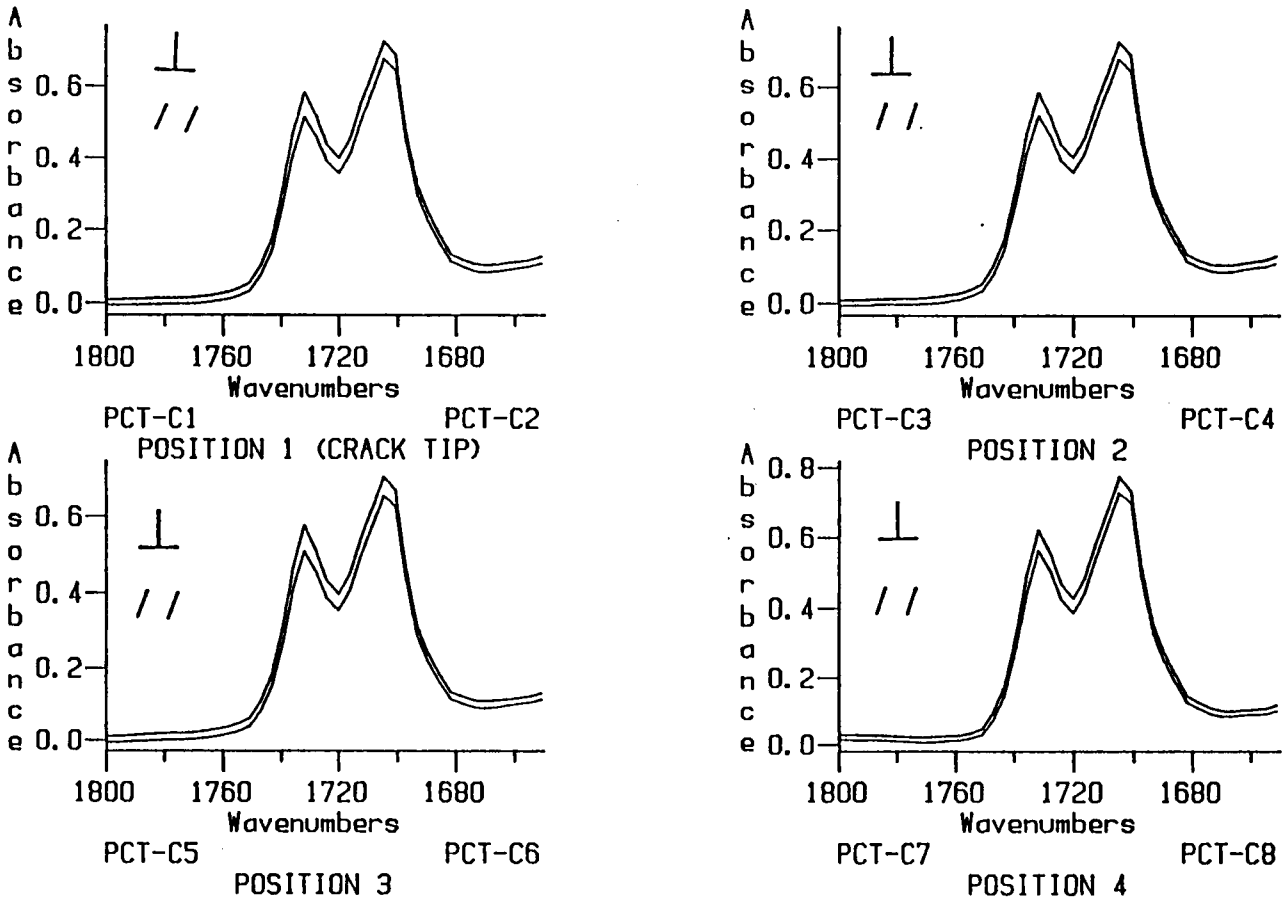

Figure 91: Polarized infrared absorbance spectra for Pellethane blended with 5% wt. calcium chloride; surrounding the crack tip; C=O stretch.

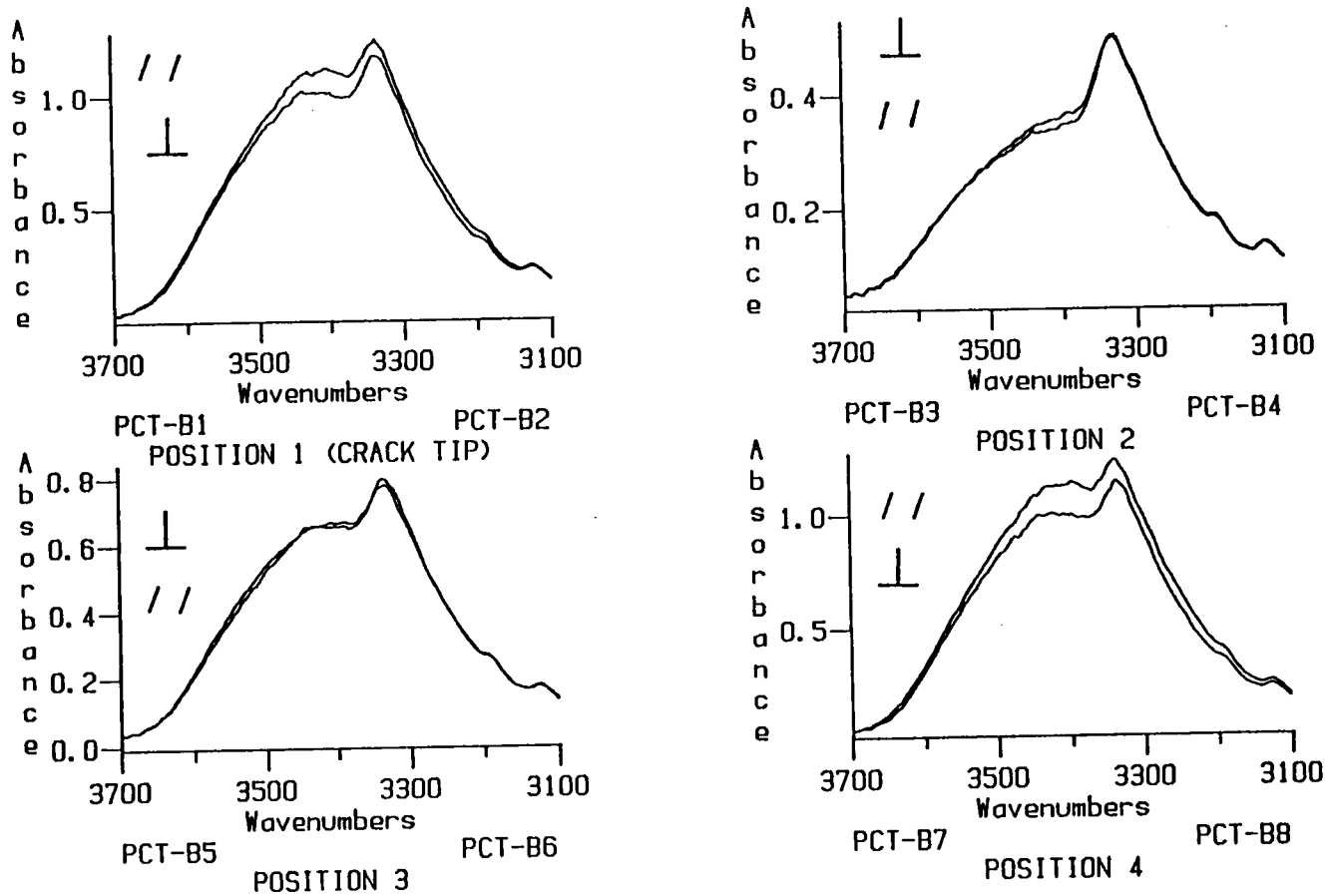

Figure 92: Polarized infrared absorbance spectra for Pellethane blended with 10% wt. calcium chloride; surrounding the crack tip; N-H stretch.

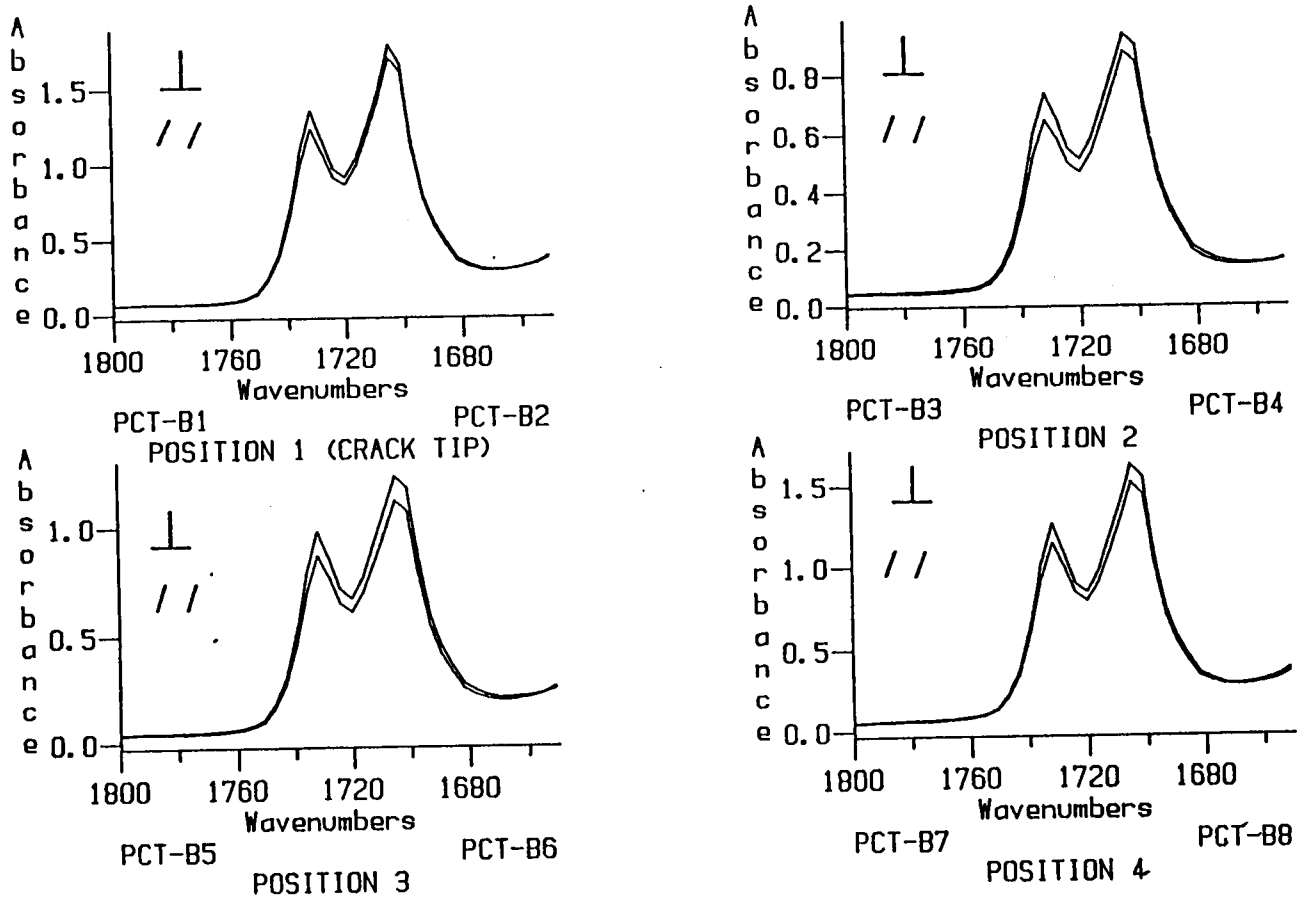

Figure 93: Polarized infrared absorbance spectra for Pellethane blended with 10% wt. calcium chloride; surrounding the crack tip; C=O stretch.

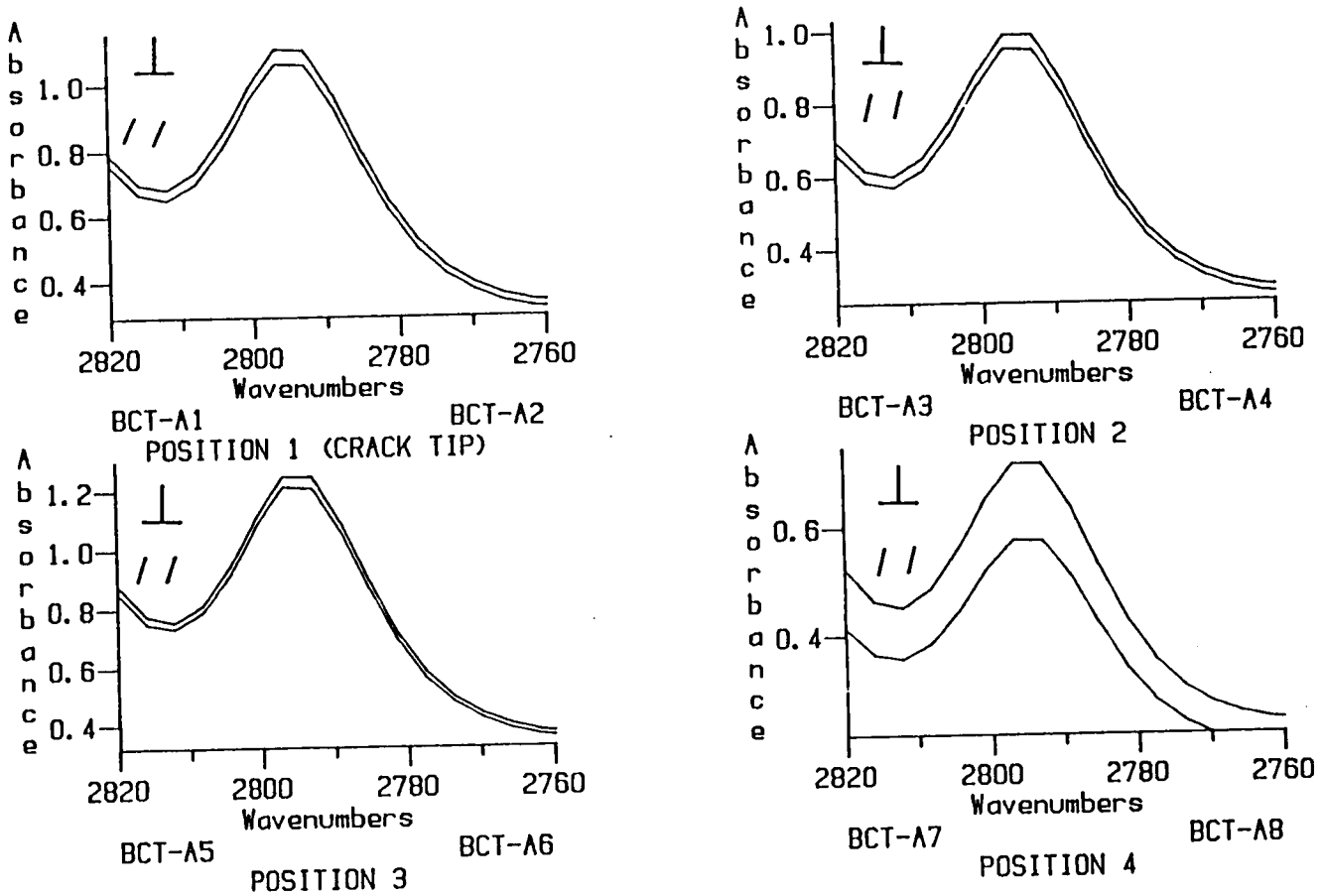

Figure 94: Polarized infrared absorbance spectra for pure Biomer surrounding the crack tip; C-H stretch.

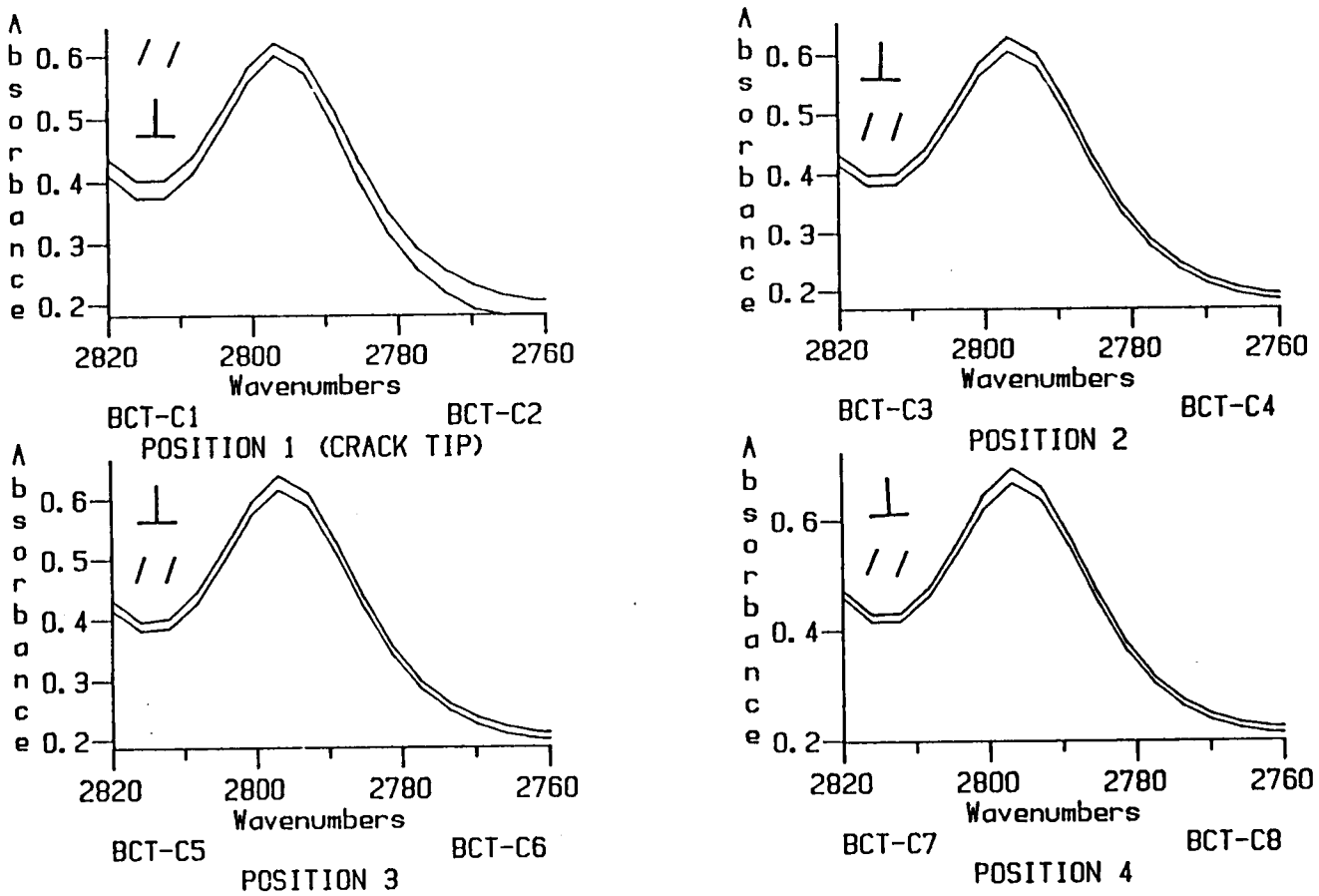

Figure 95: Polarized infrared absorbance spectra for Biomer blended with 1% wt. calcium chloride; surrounding the crack tip; C-H stretch.

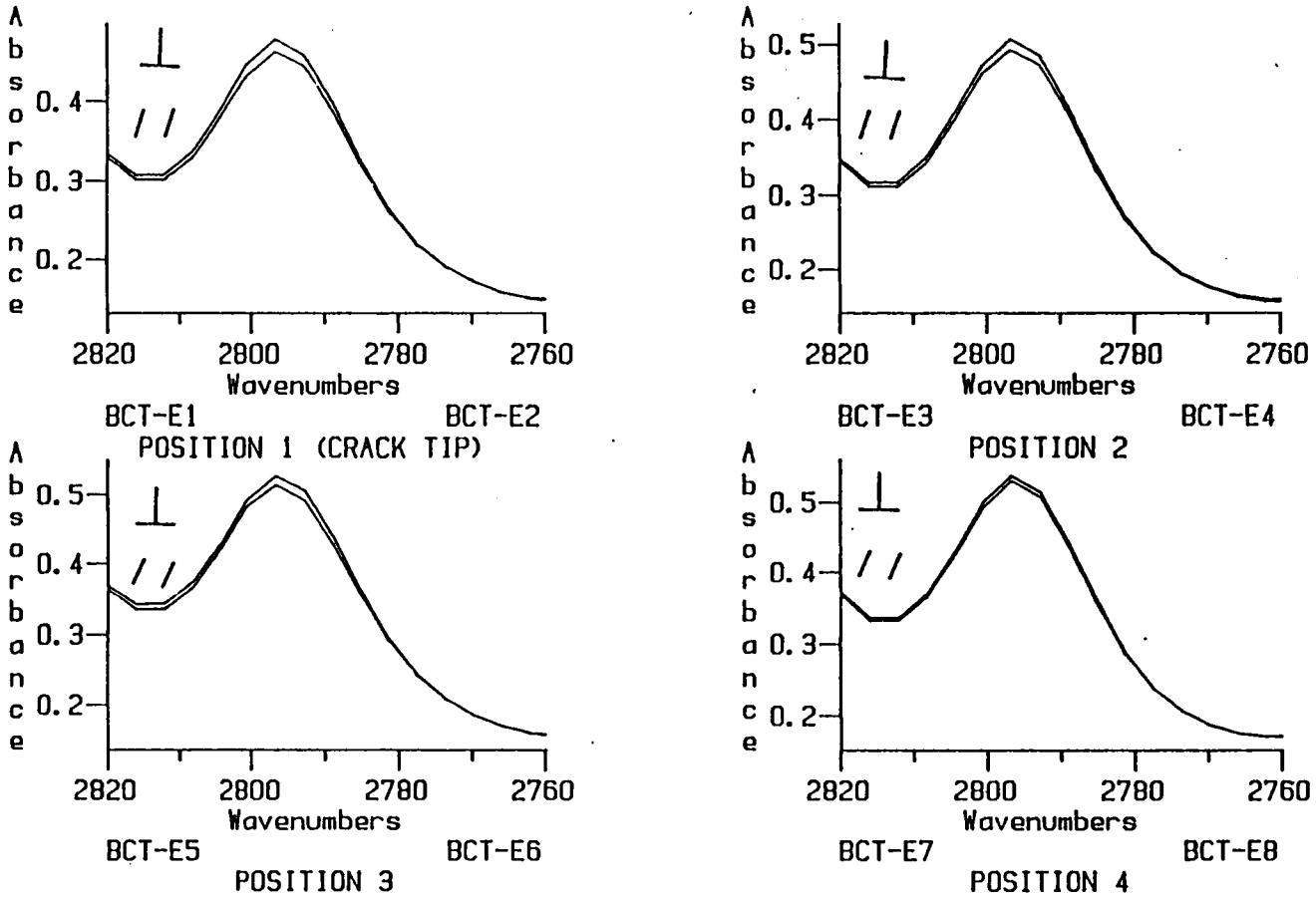

Figure 96: Polarized infrared absorbance spectra for Biomer blended with 5% wt. calcium chloride; surrounding the crack tip; C-H stretch.

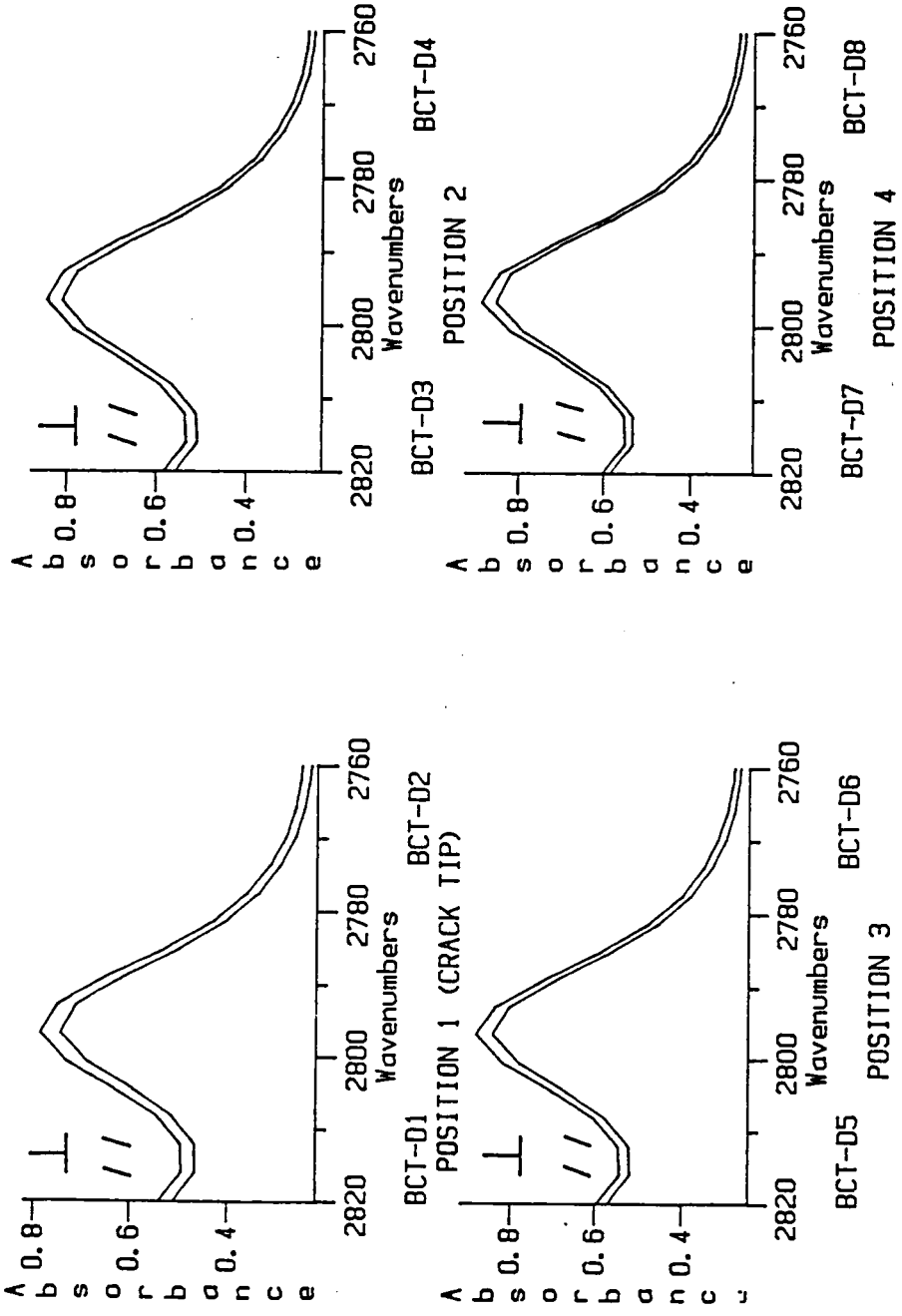

Figure 97: Polarized infrared absorbance spectra for Biomer blended with 10% wt. calcium chloride; surrounding the crack tip; C-H stretch.

Figure 98 shows the C-H polarized stretch bands for Pellethane at different positions. Figure 99 is a plot of the same spectral region for Pellethane blended with 1% calcium chloride. Figure 100 shows the same information for 5% wt. calcium chloride in Pellethane. Figure 101 is a plot of the same information for 10% wt. calcium chloride blended with Pellethane.

4.4. Changes in Mechanical Properties with Calcium Uptake

After subjecting the polyurethanes to a physiological concentration of calcium chloride solution, the polyurethanes were tested in fracture, tensile orientation and crack tip orientation measurements to observe and understand any changes in mechanical properties.

Figure 102 is a plot of the stress versus strain curves for the Biomer uptake sample for varying initial crack lengths. The areas under these curves (strain energy) are plotted in Figures 103 and 104 as a function of initial crack length, a, and initial length of the uncracked ligament, Δa, respectively.

Figure 105 shows plots of the stress versus strain curves with varying initial crack length. The strain energy for each case was plotted as a function of the initial crack length in Figure 106 and as a function of the length of the initial uncracked ligament in Figure 107.

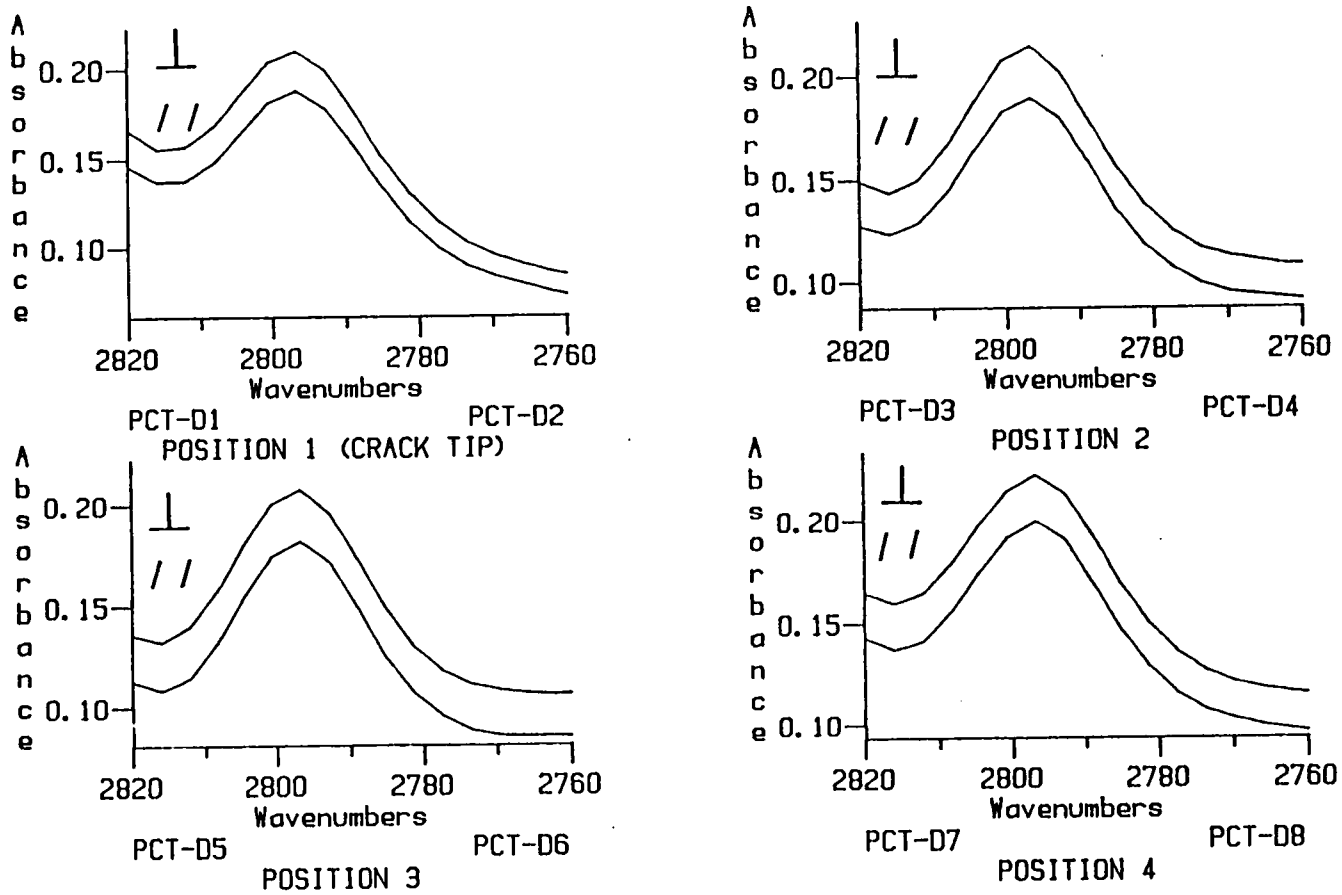

Figure 98: Polarized infrared absorbance spectra for pure Pellethane surrounding the crack tip; C-H stretch.

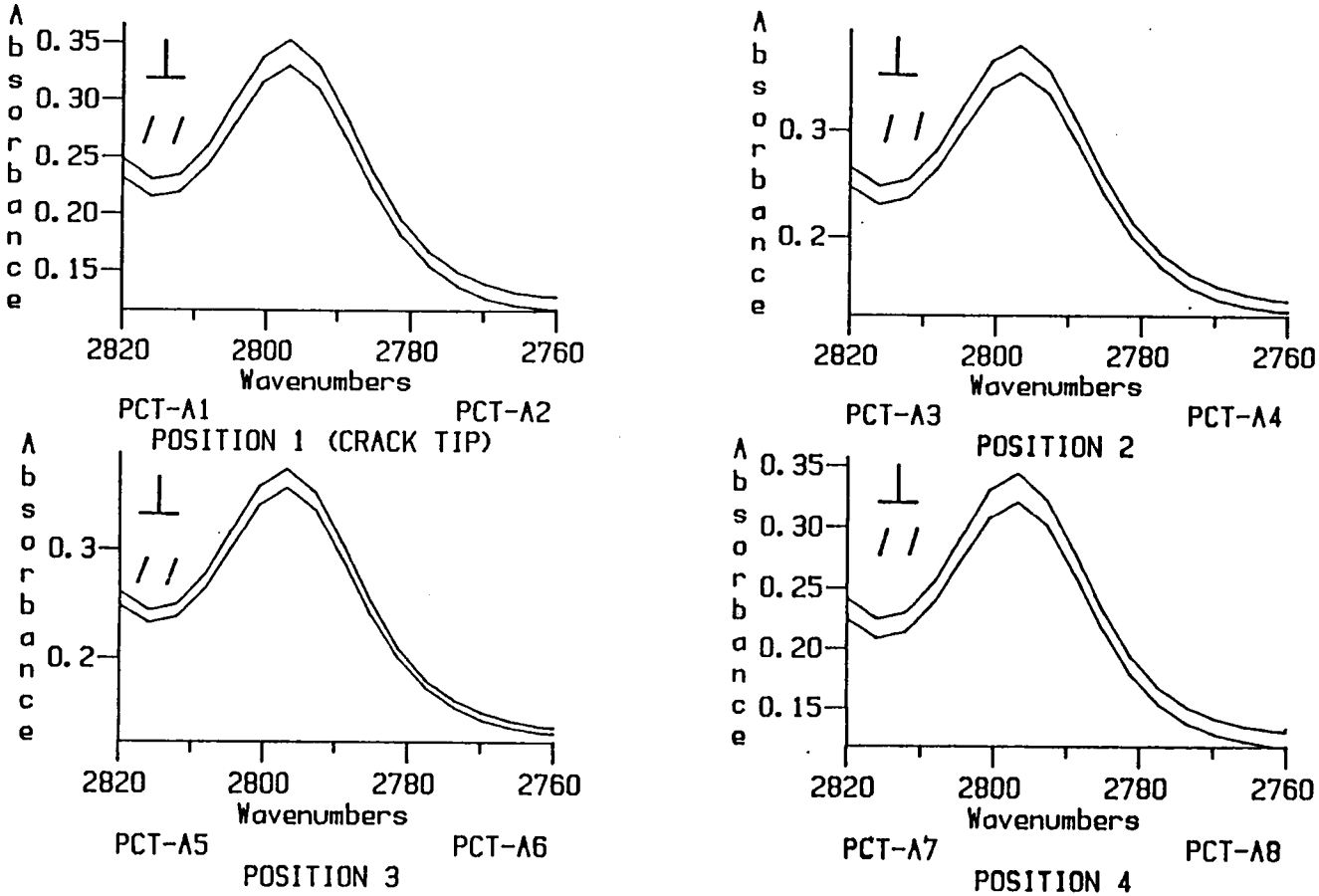

Figure 99: Polarized infrared absorbance spectra for Pellethane blended with 1% wt. calcium chloride; surrounding the crack tip; C-H stretch.

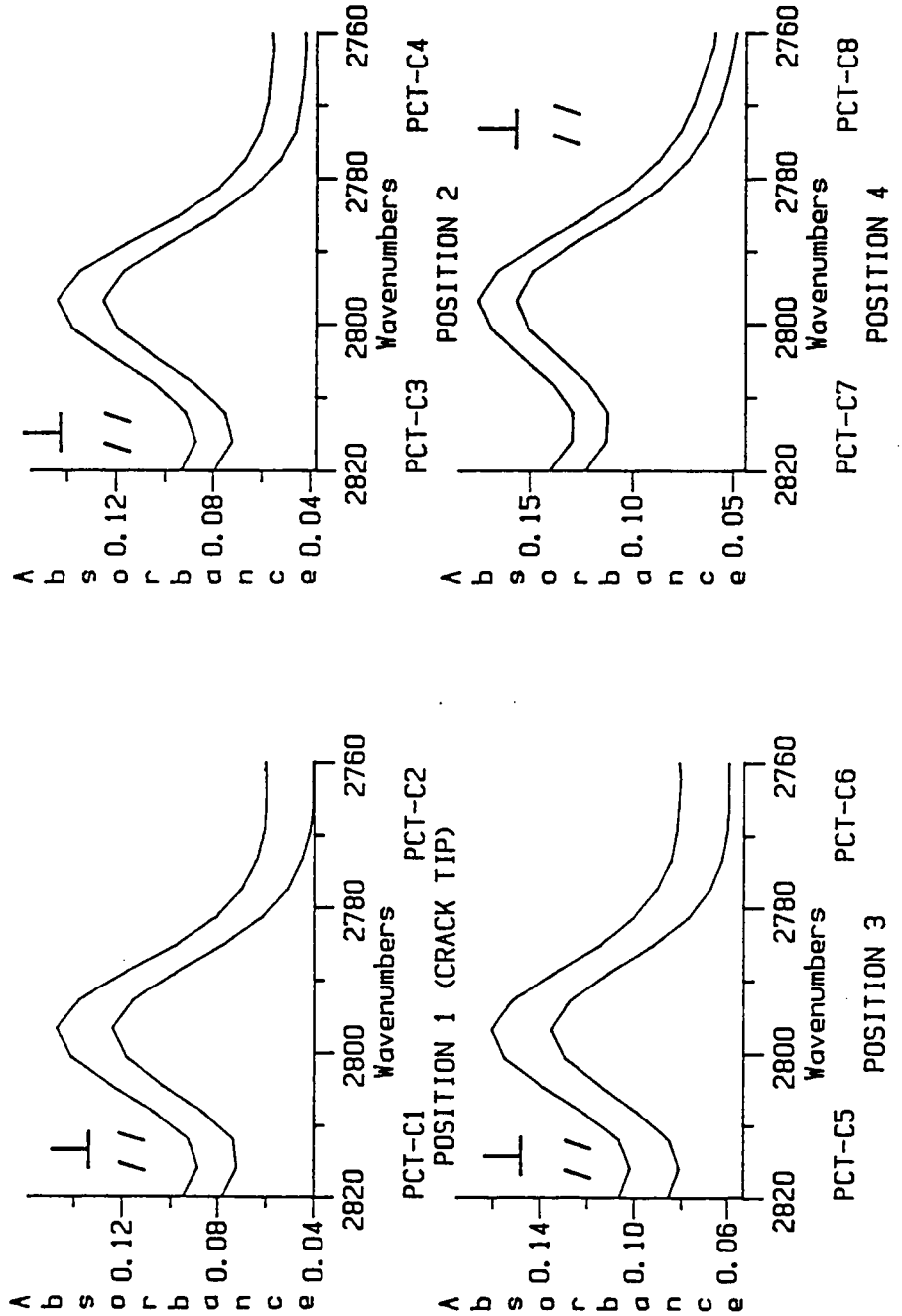

Figure 100: Polarized infrared absorbance spectra for Pellethane blended with 5% wt. calcium chloride; surrounding the crack tip; C-H stretch.

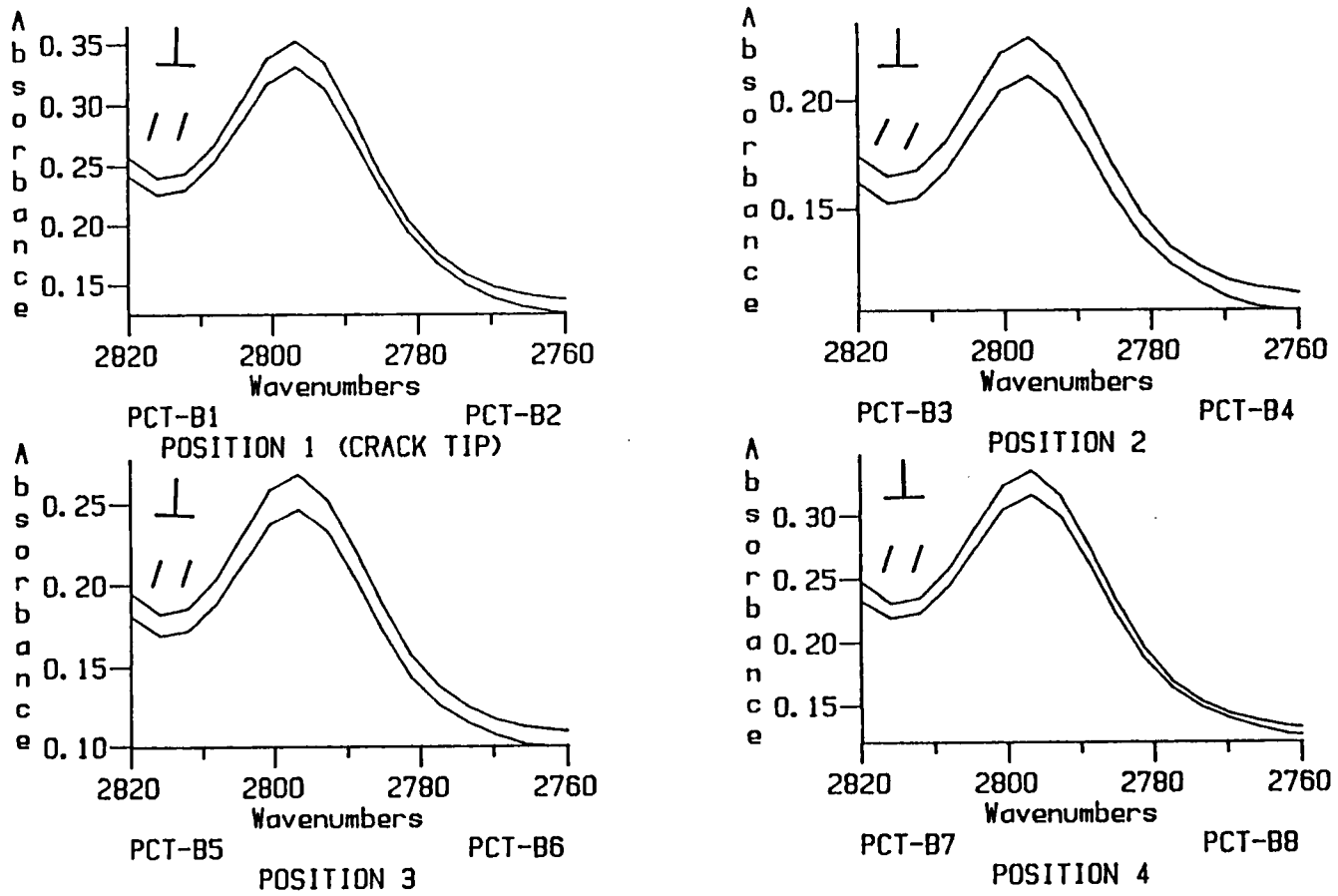

Figure 101 Polarized infrared absorbance spectra for Pellethane blended with 10% wt. calcium chloride; surrounding the crack tip; C-H stretch.

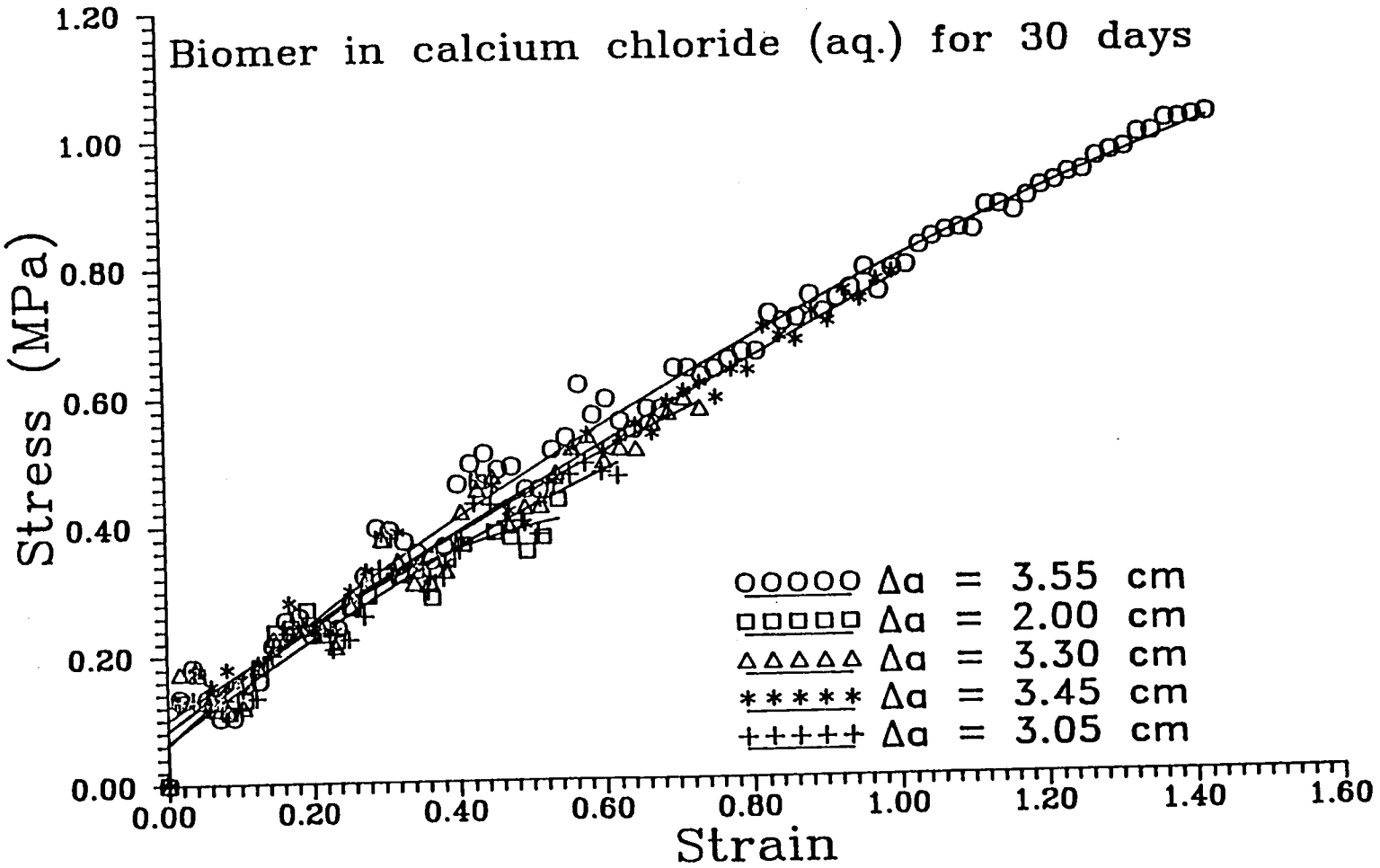

Figure 102: Stress versus strain data for Biomer after 30 days in aqueous calcium chloride solution with varying crack growth to failure.

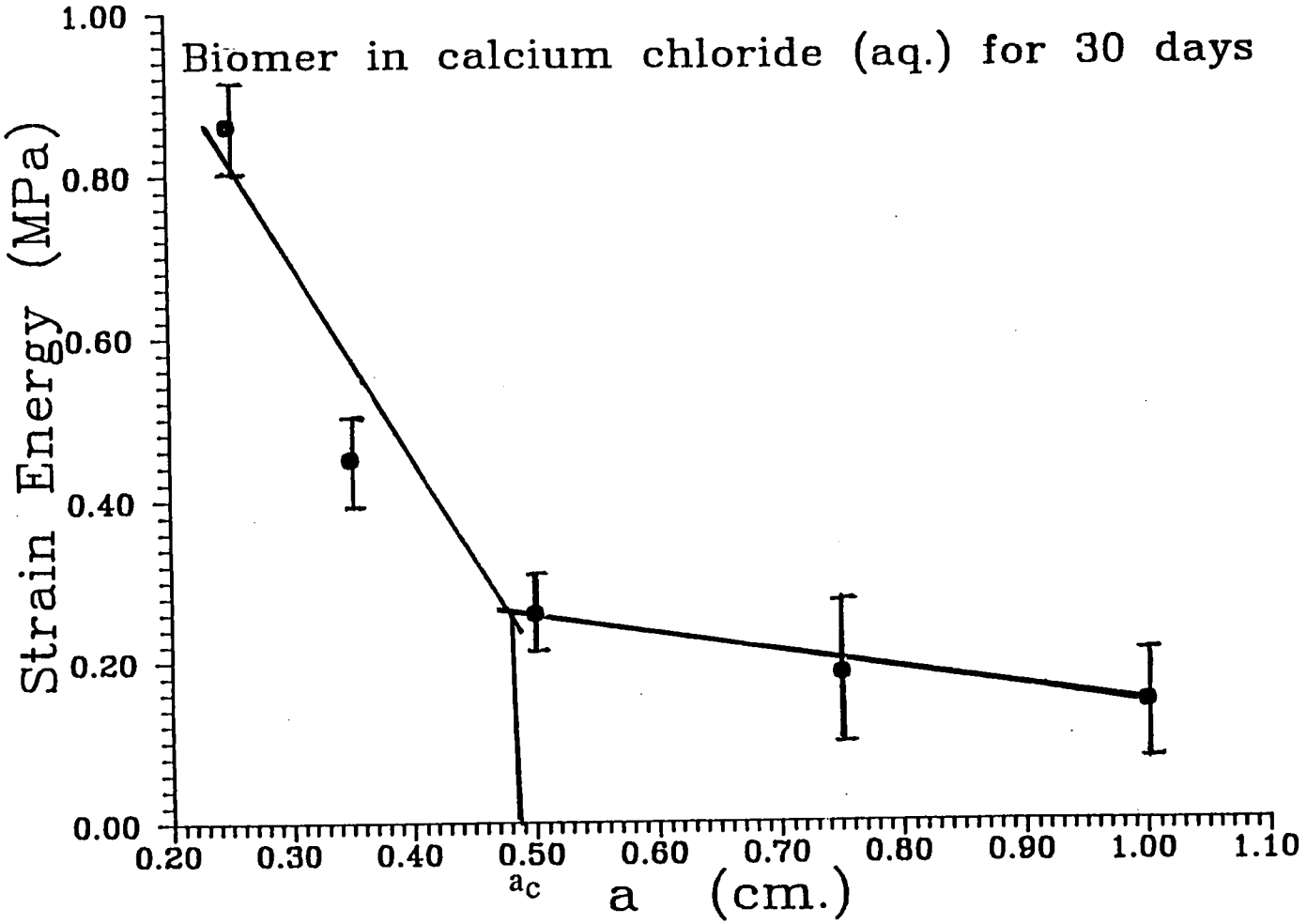

Figure 103: Strain energy to failure versus initial crack length for Biomer after 30 days in aqueous calcium chloride solution.

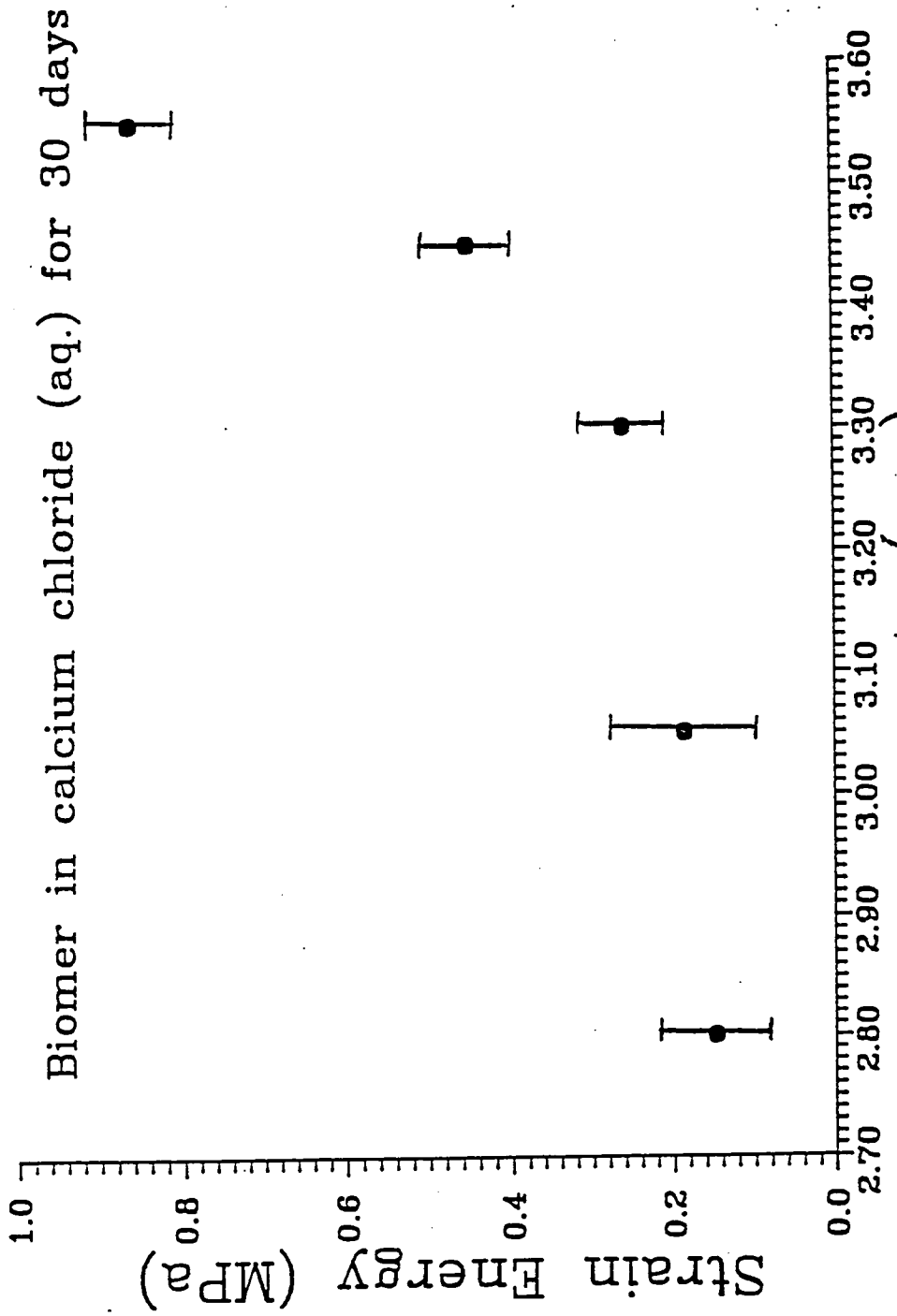

Figure 104: Strain energy to failure versus crack growth to failure for Biomer after 30 days in aqueous calcium chloride solution.

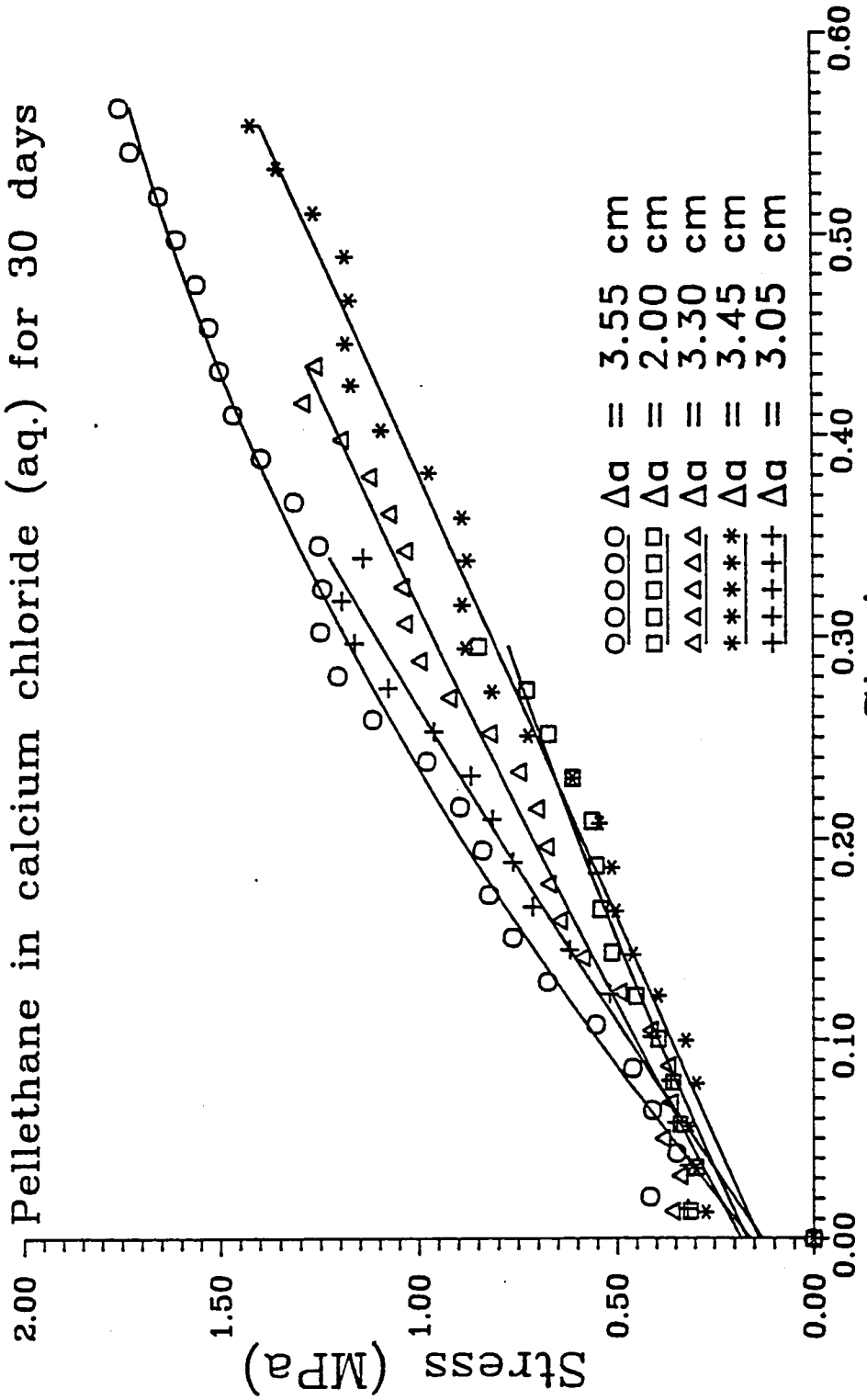

Figure 105: Stress versus strain data for Pellethane after 30 days in aqueous calcium chloride solution with varying crack growth to failure.

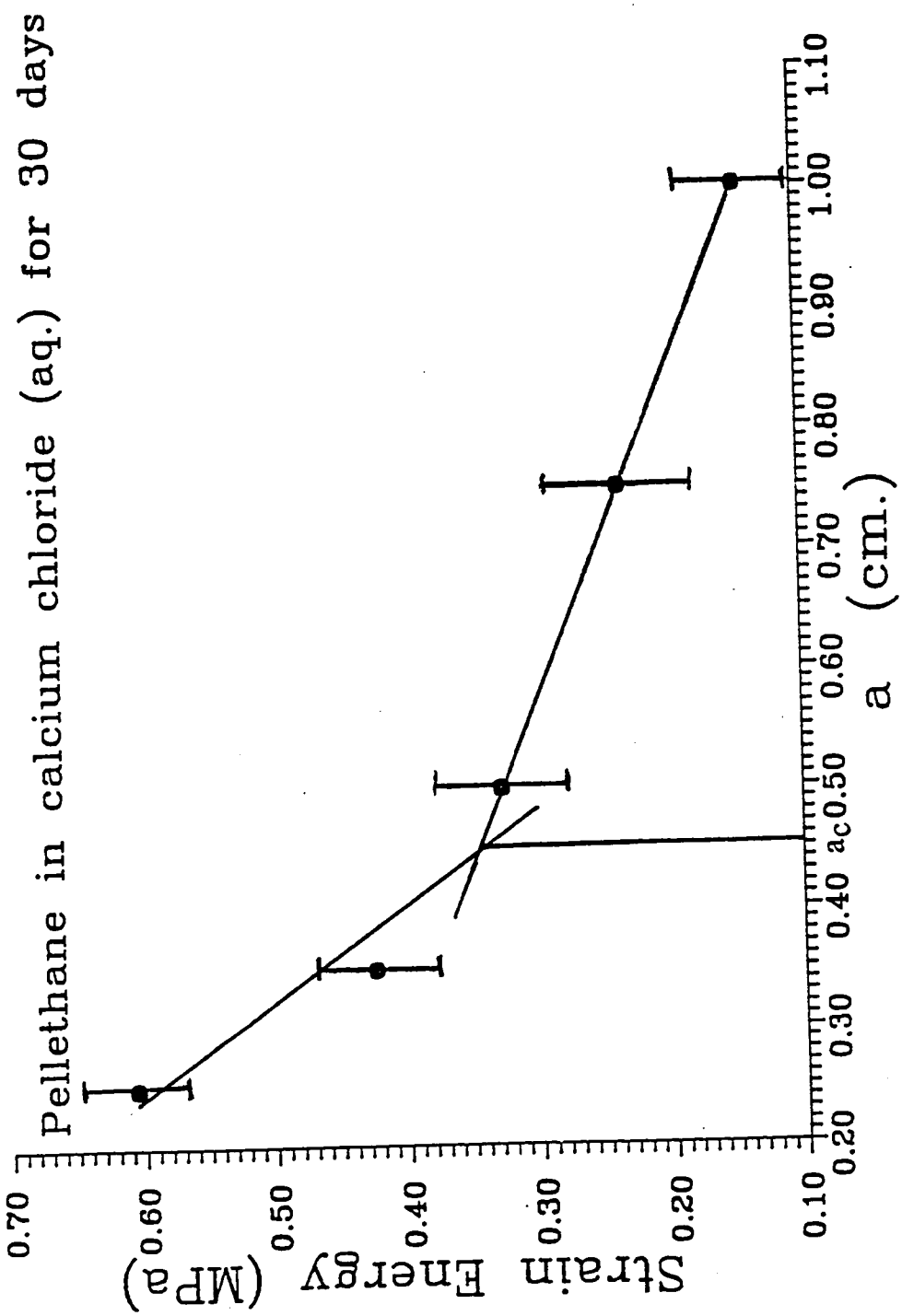

Figure 106: Strain energy to failure versus initial crack length for Pellethane after 30 days in aqueous calcium chloride solution.

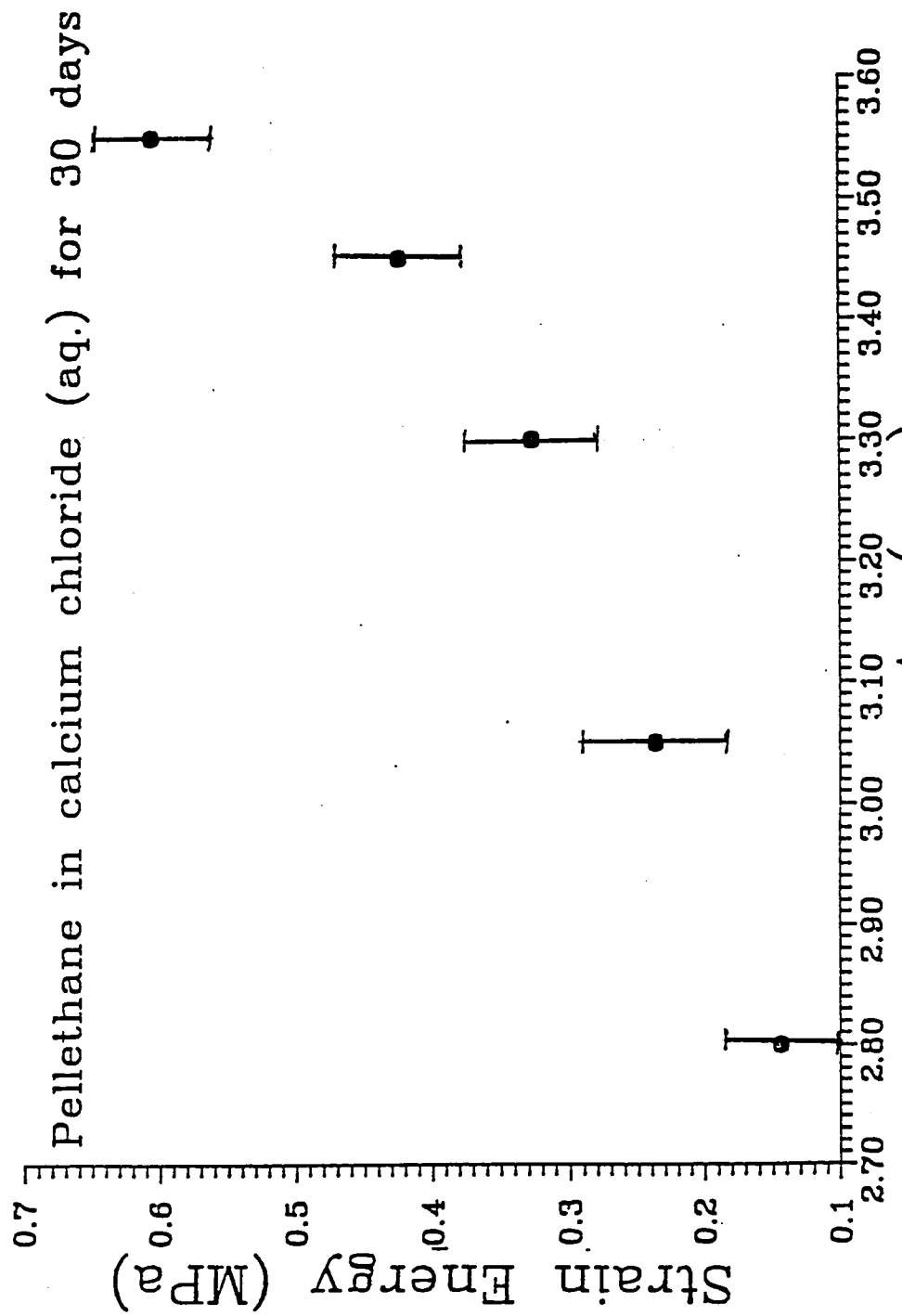

Figure 107: Strain energy to failure versus crack growth to failure for Pellethane after 30 days in aqueous calcium chloride solution.

The tensile stress-strain-orientation data is presented in Figures 108 through 111. Figure 108 is a plot of the plane polarized absorbance spectra from the N-H stretch vibration. Figure 109 is the same set of Biomer spectra, however, the C-H stretch vibration is plotted. For the Pellethane uptake, Figure 110 is a plot of the plane polarized IR spectra for the N-H stretch region at varying strains. Figure 111 shows the same spectra but in the vicinity of the C-H stretch vibration. The peak absorbance data from these spectra were used to calculate stress-strain-orientation information which is presented in the discussion chapter.

The mapping of the crack tip orientation fields was achieved by measurements presented in Figures 112 to 117. The data in Figure 112 was used to examine the N-H stretch orientation as a function of position in the Biomer uptake sample. The C=O stretch vibration indicated more dramatic differences in Figure 113. The data in Figure 114 examines the orientation by position of the N-H stretch for the Pellethane uptake study. Figure 115 shows the polarized spectra of the C=O stretch for the Pellethane uptake. (The C=O stretch is the peak on the left which did not saturate the IR source.) The soft segment orientation by position was examined in Figures 116 and 117. Figure 116 shows plot of polarized spectra of the C-

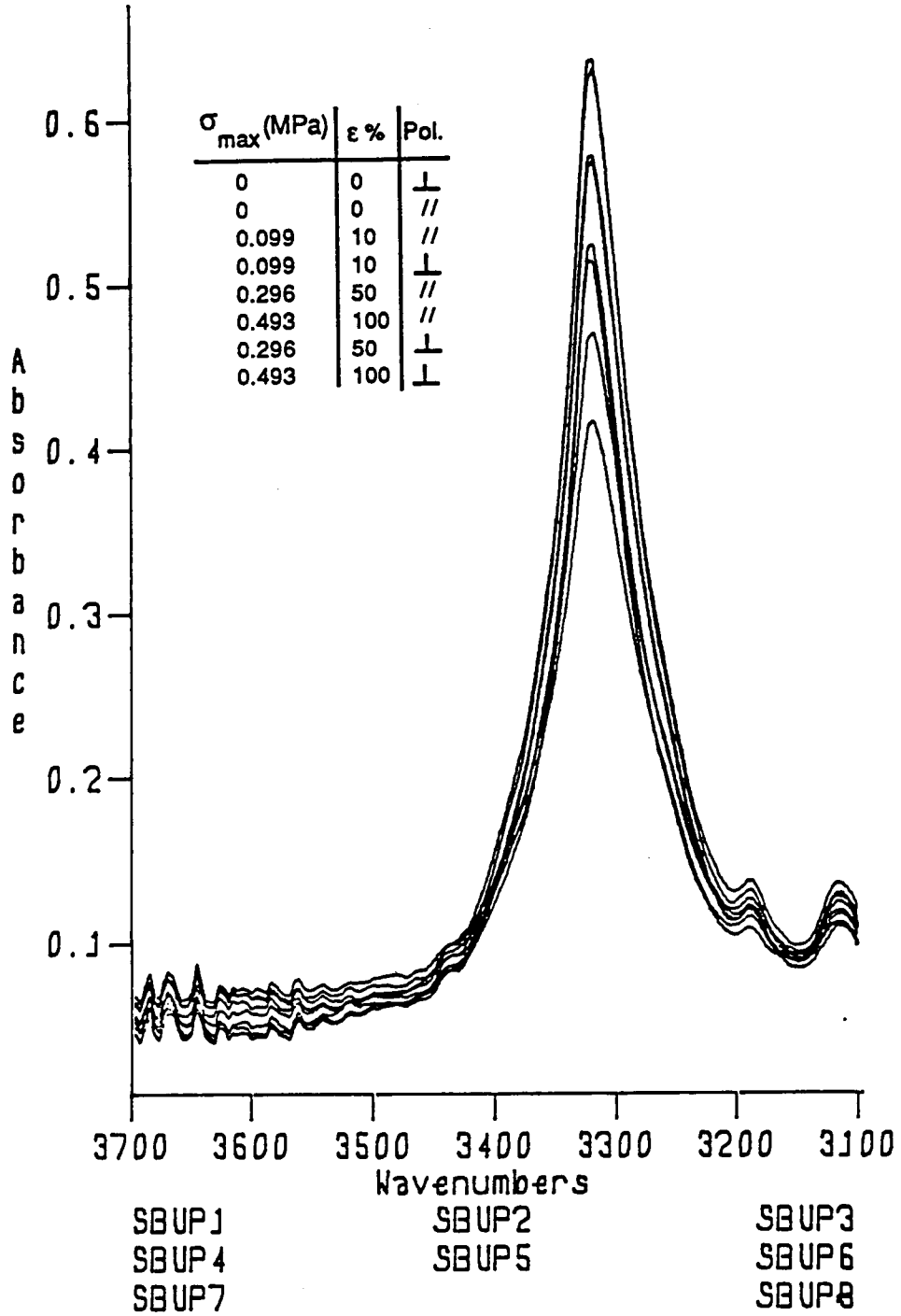

Figure 108: Polarized infrared absorbance spectra for Biomer after 30 days in aqueous calcium chloride solution, at various strains; N-H stretch.

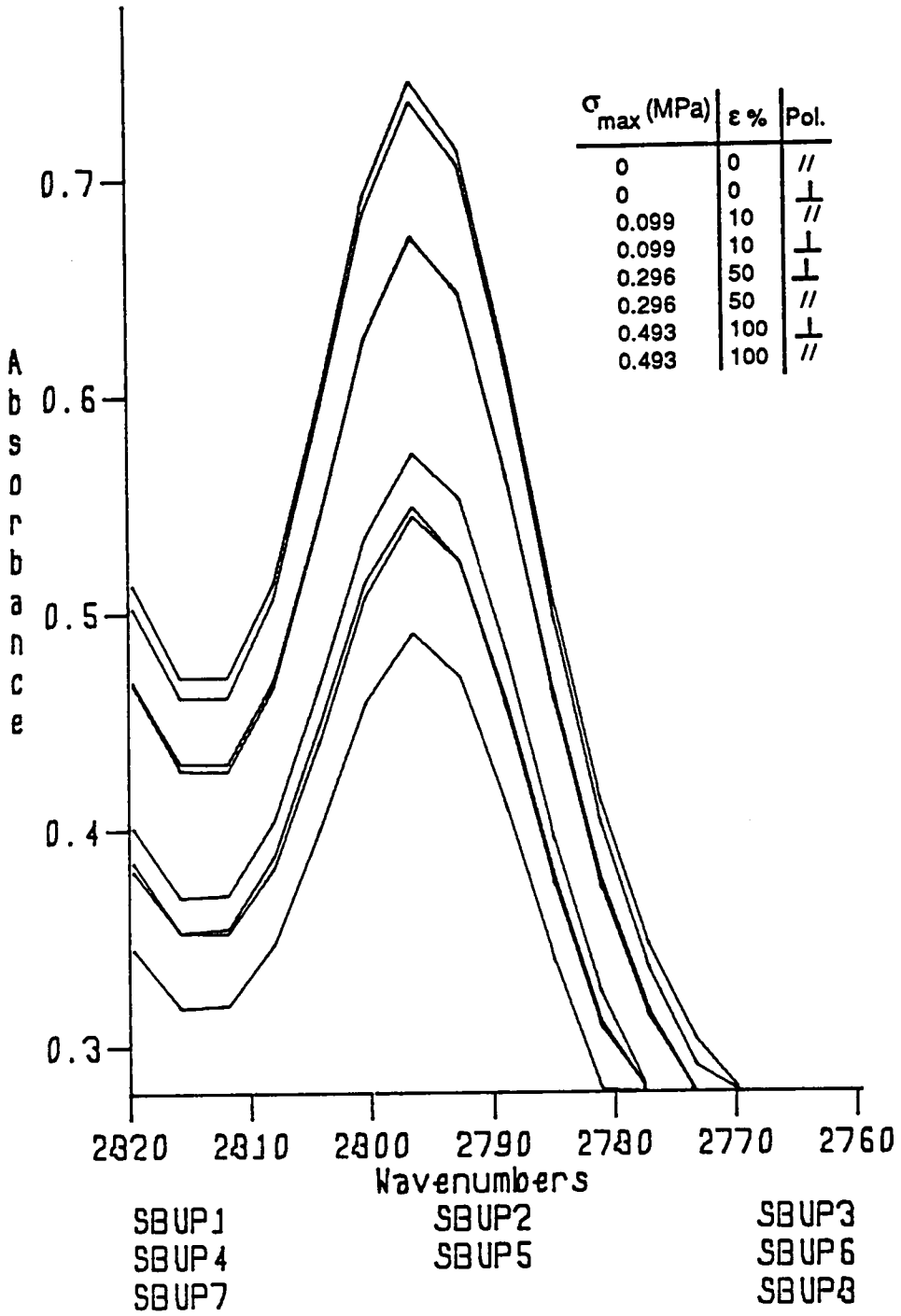

Figure 109: Polarized infrared absorbance spectra for Biomer after 30 days in aqueous calcium chloride solution, at various strains; C-H stretch.

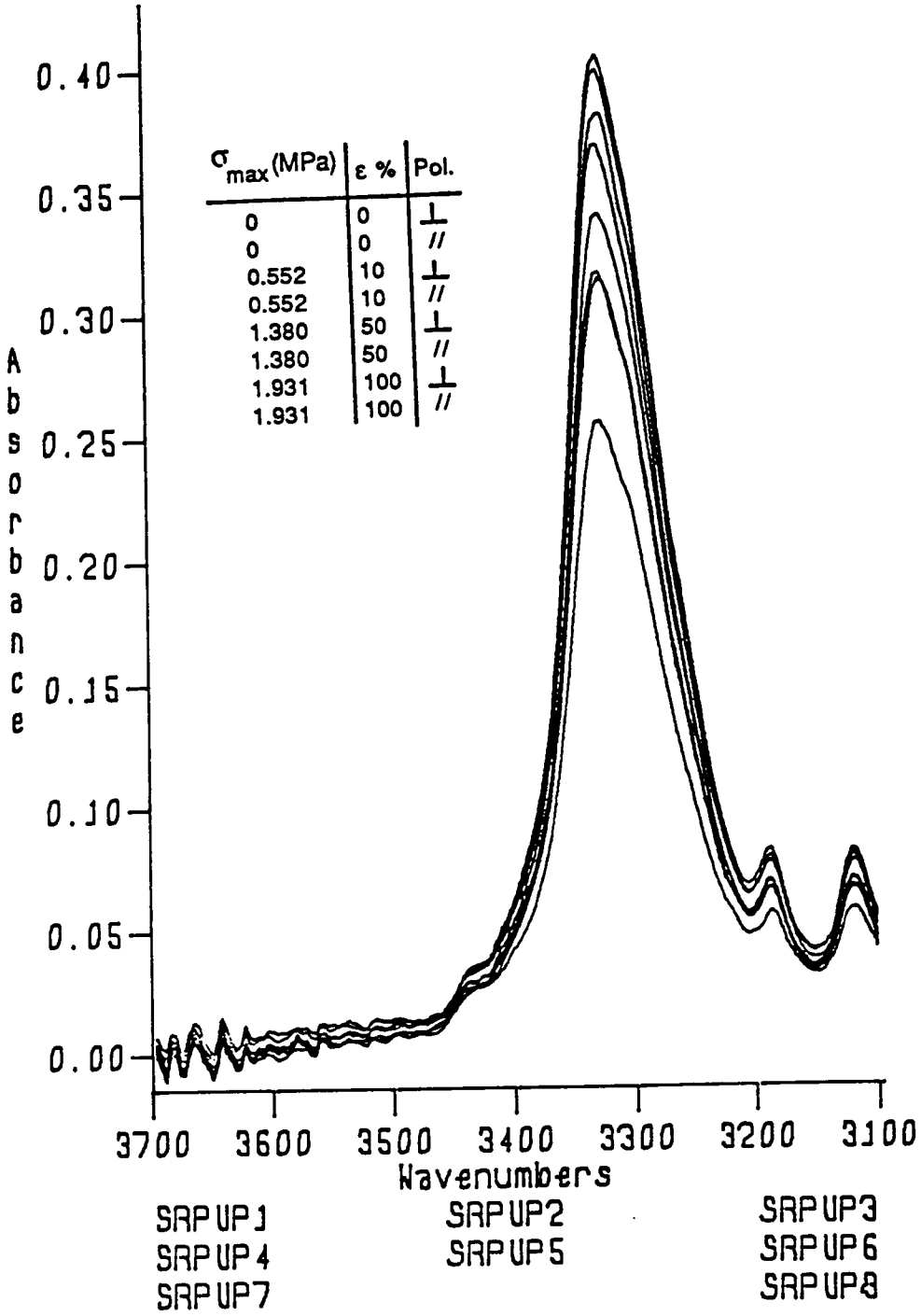

Figure 110: Polarized infrared absorbance spectra for Pellethane after 30 days in aqueous calcium chloride solution, at various strains; N-H stretch.

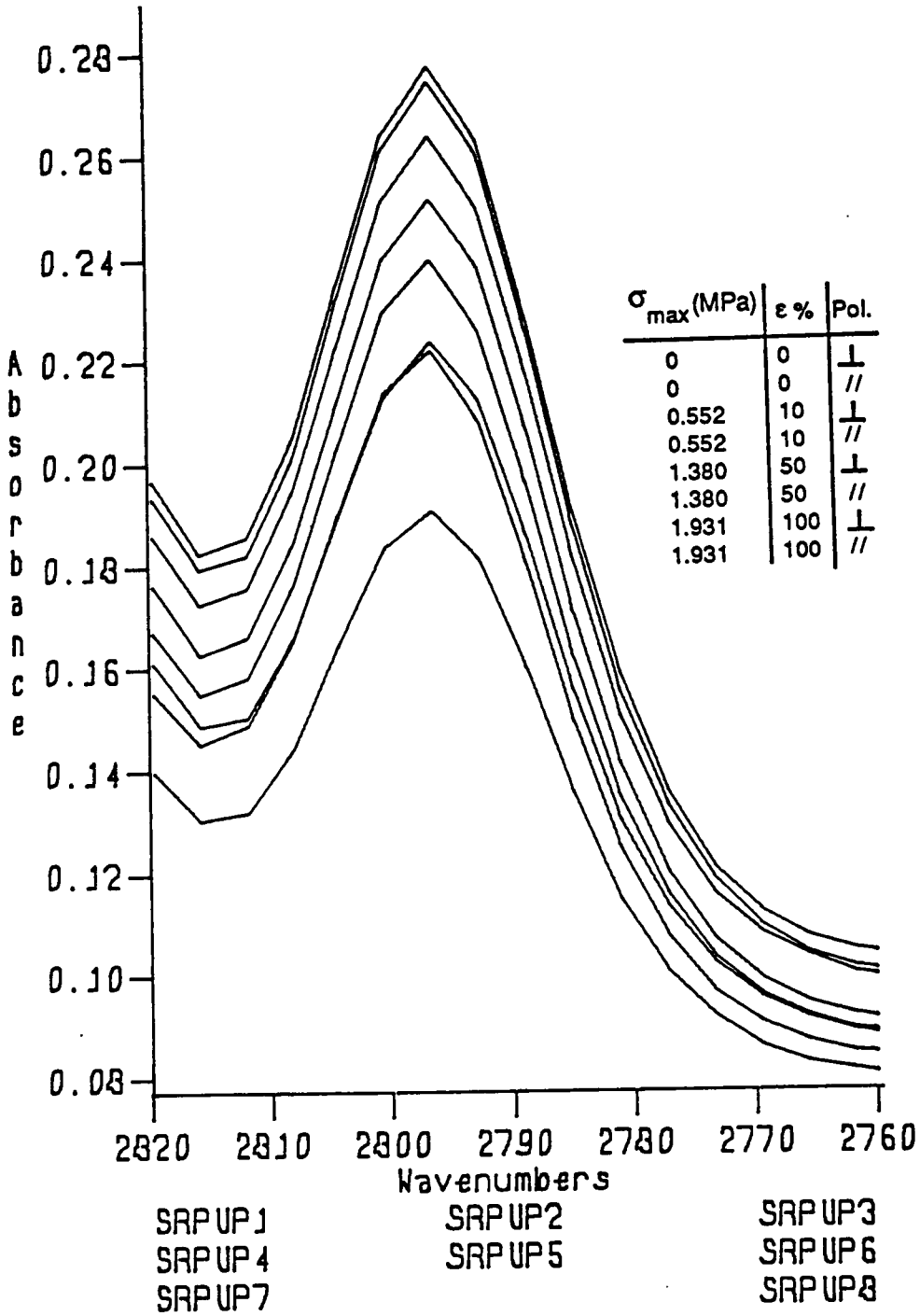

Figure 111: Polarized infrared absorbance spectra for Pellethane after 30 days in aqueous calcium chloride solution, at various strains; C-H stretch.

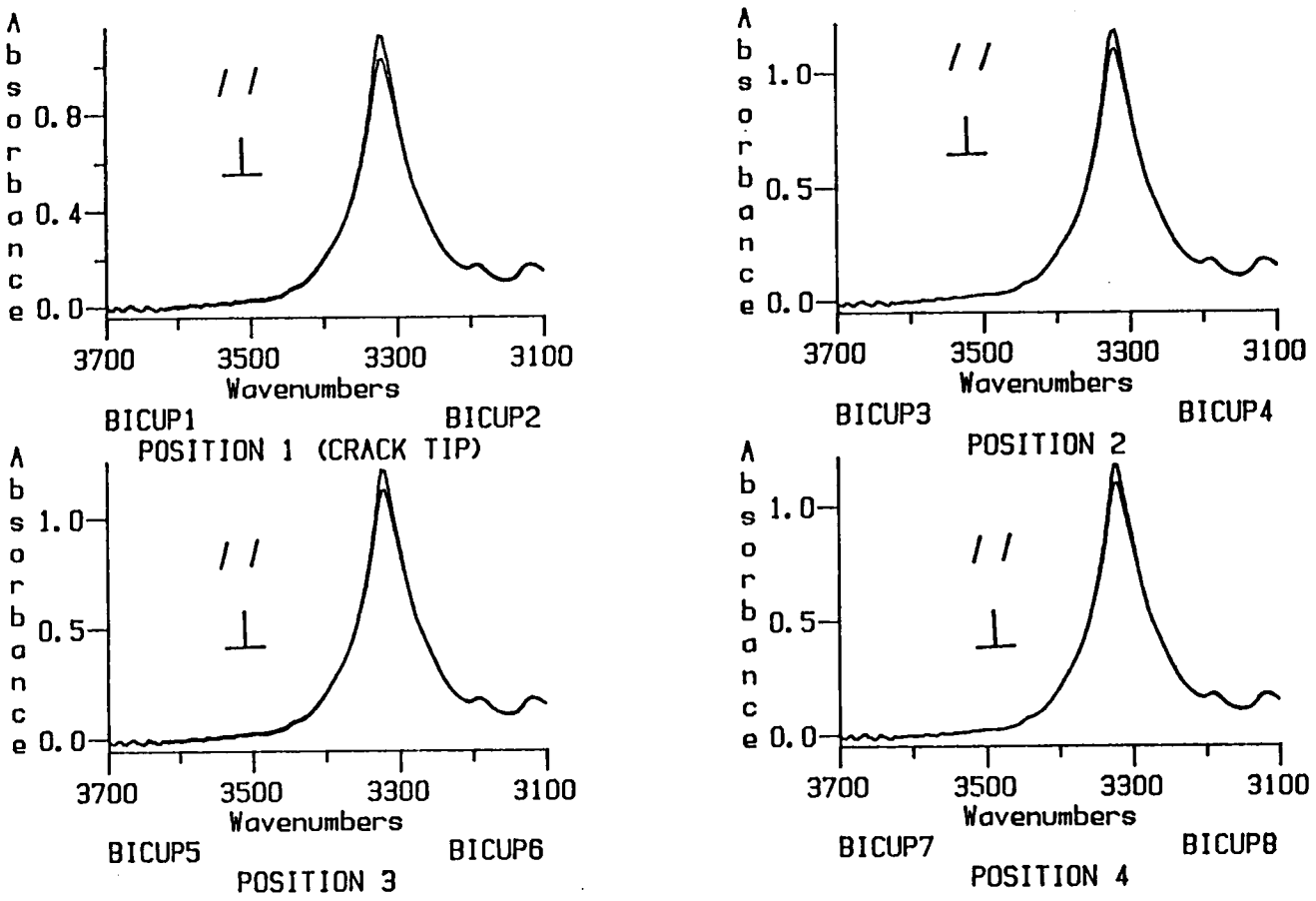

Figure 112: Polarized infrared absorbance spectra for Biomer after 30 days in aqueous calcium chloride solution, surrounding the crack tip; N-H stretch.

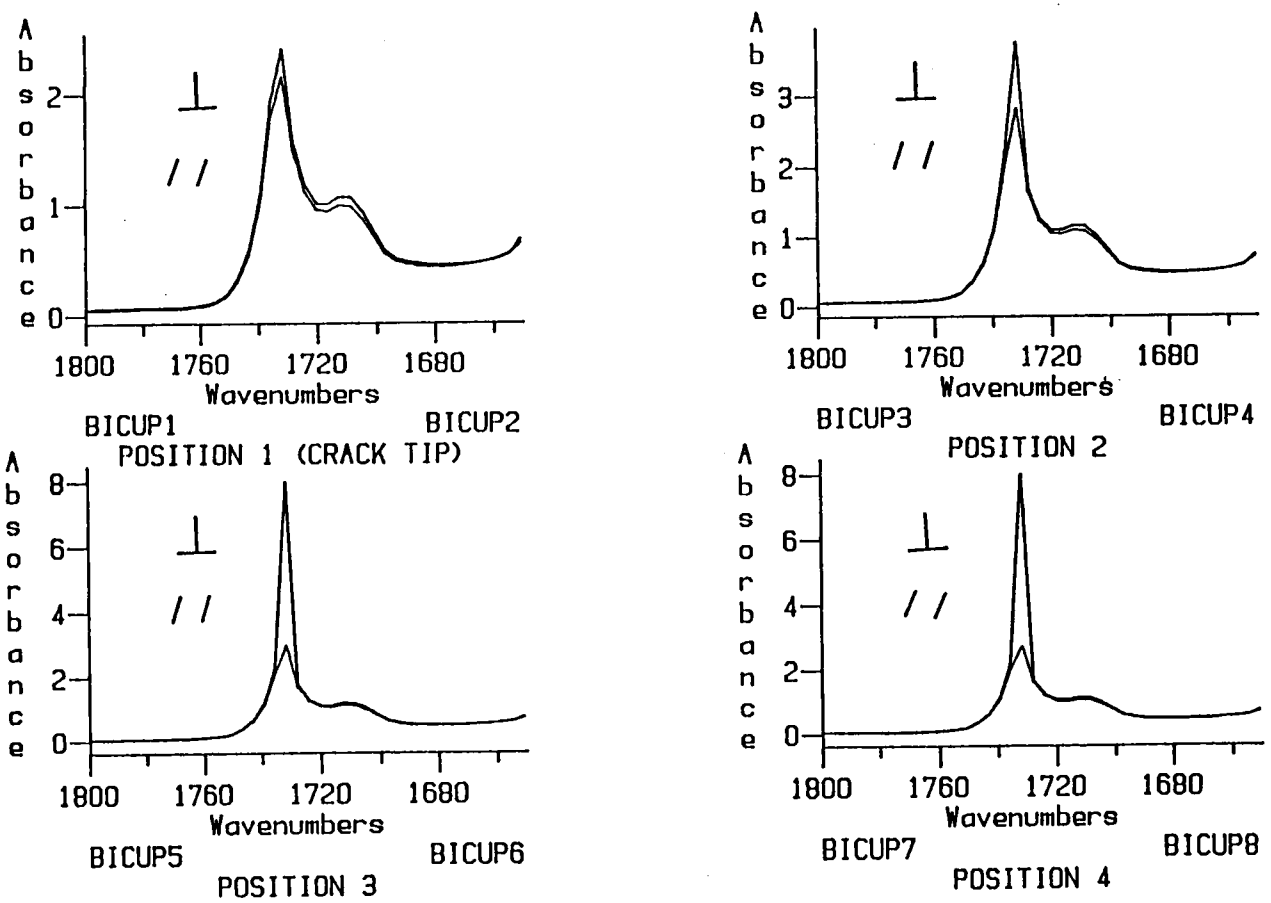

Figure 113: Polarized infrared absorbance spectra for Biomer after 30 days in aqueous calcium chloride solution, surrounding the crack tip; C=O stretch.

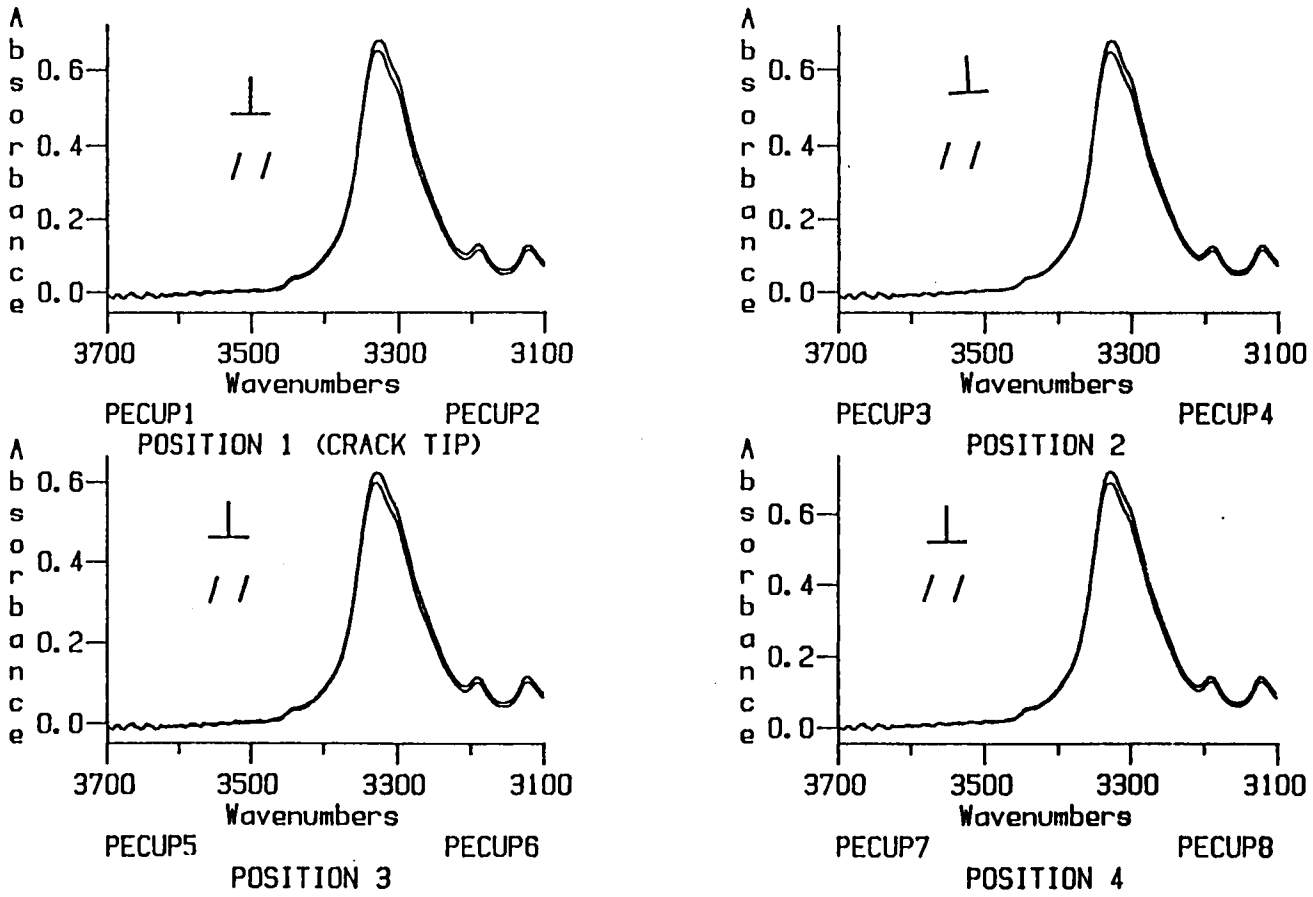

Figure 114: Polarized infrared absorbance spectra for Pellethane after 30 days in aqueous calcium chloride solution, surrounding the crack tip; N-H stretch.

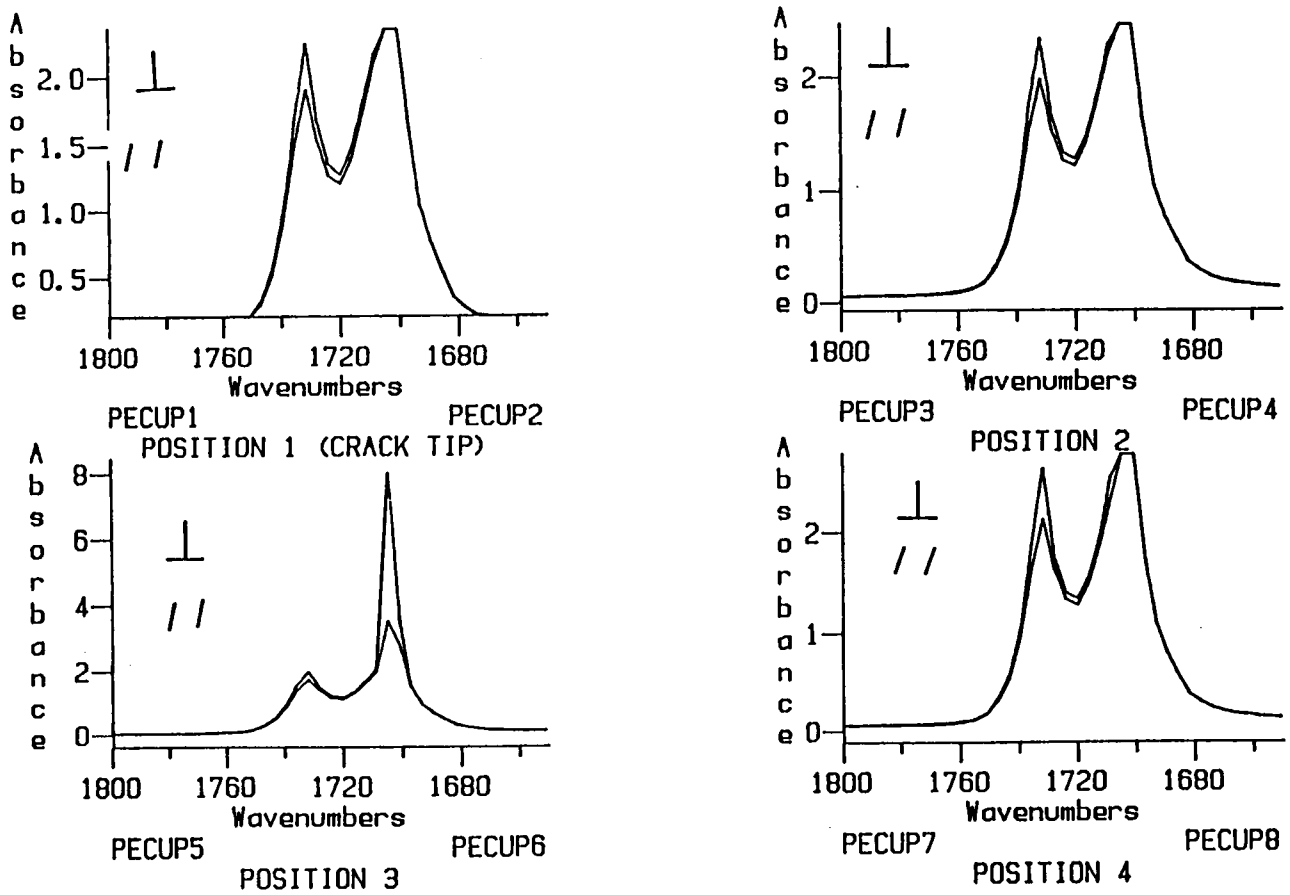

Figure 115: Polarized infrared absorbance spectra for Pellethane after 30 days in aqueous calcium chloride solution, surrounding the crack tip; C=O stretch.

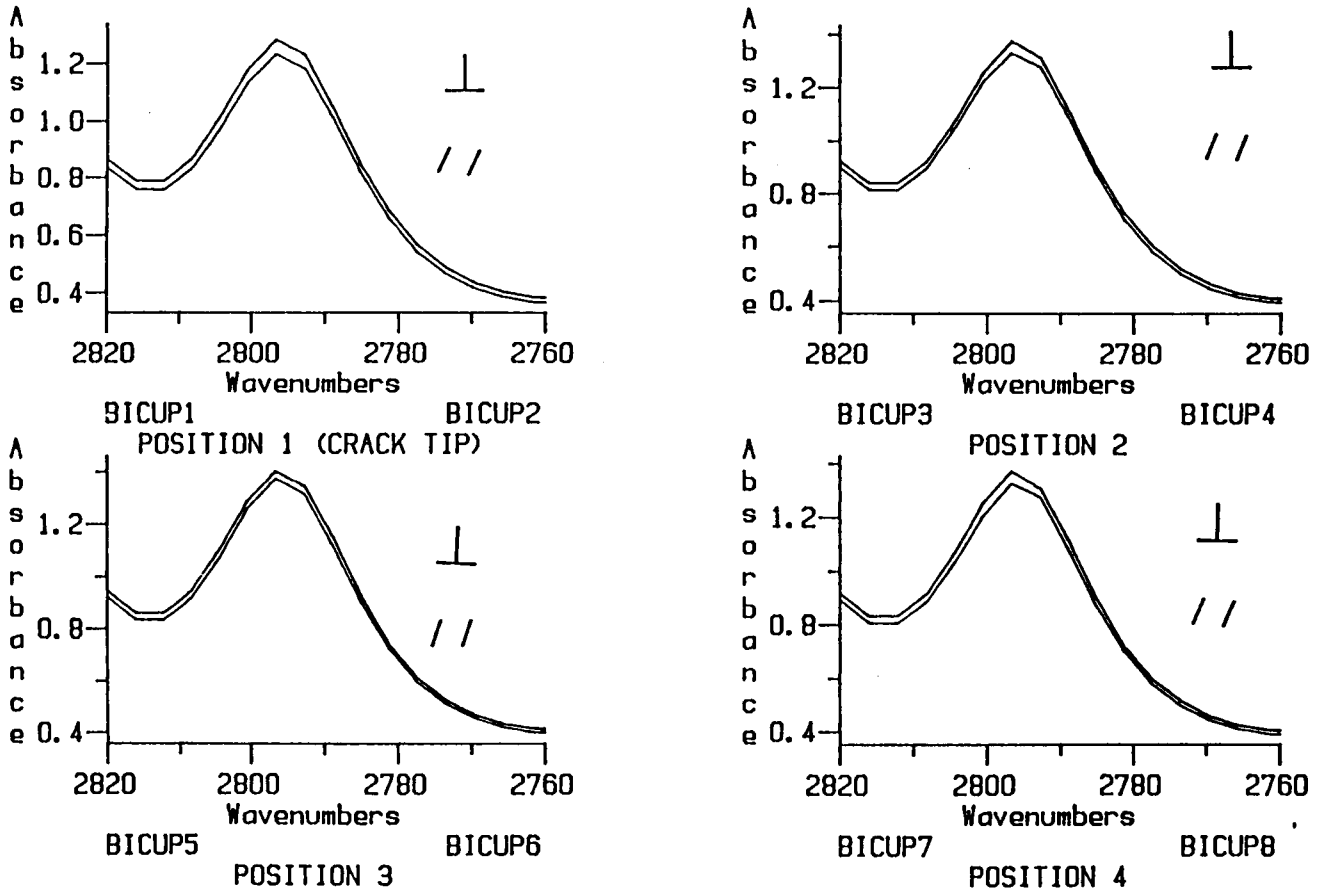

Figure 116: Polarized infrared absorbance spectra for Biomer after 30 days in aqueous calcium chloride solution, surrounding the crack tip; C-H stretch.

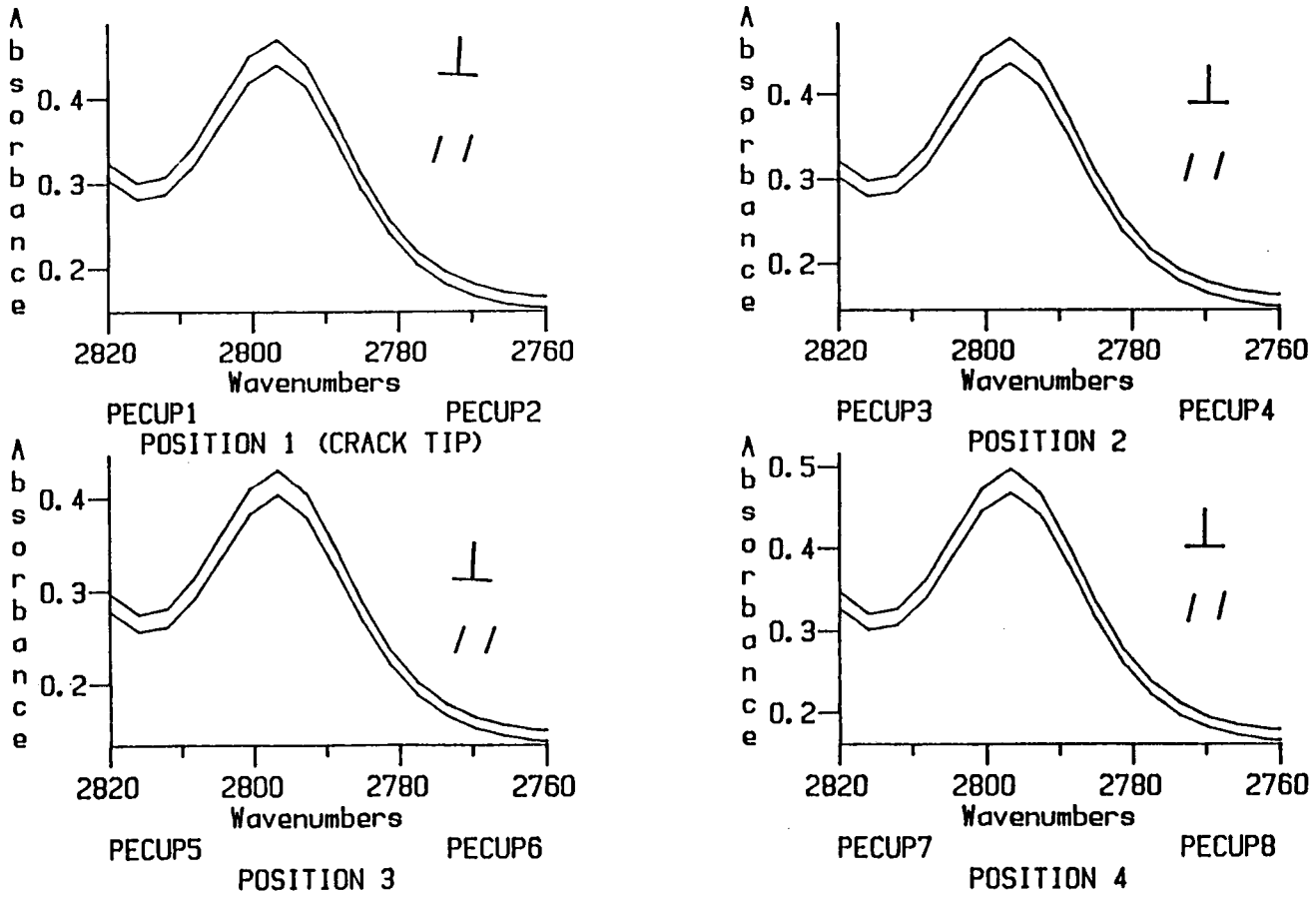

Figure 117: Polarized infrared absorbance spectra for Pellethane after 30 days in aqueous calcium chloride solution, surrounding the crack tip; C-H stretch.

H stretch vibration for the Biomer uptake sample. Figure 117 shows the same information for Pellethane.

5. DISCUSSION

A discussion of the results presented in the previous chapter requires an interpretation of the data as well as a consideration of the ramifications of this work. It is therefore necessary to consider a primary analysis of the data as well as an overall summary of the engineering significance of this study. This chapter examines the mechanical/orientation behavior of the blends of calcium chloride and polyurethane. Based on the information gained from the known blends, an attempt was made to understand the polyurethanes exposed to the aqueous calcium chloride solutions.

5.1. Fracture Testing

The strain energy curves shown in chapter 3 were re-calculated to account for the length of the uncracked ligament in an attempt to formulate J integral curves which could be used to assign critical conditions to the fracture behavior. The strain energy to failure had significant contributions from two material properties. The first was tensile drawing in which the material absorbed strain energy in the form of molecular orientation or deformation. The second was strain energy absorbed through the propagation of a crack. The second term was the desired quantity, J. To account for the first term, finite element fracture mechanics studies are

under development to correct for material deformation before crack propagation. The corrections allow for the fact that deformation (non-crack propagating) energy was more dominant at shorter crack lengths than at longer crack lengths. It should be noted that several references in the literature[89,93] do not differentiate between the strain energy contributions and designate J integral values without regard to the definition.

Because of the large strain energy absorbed by polyurethanes for short cracks, the strain energy for crack propagation alone could not be determined directly. As a result, it was not possible to directly determine true J integral values. The normalized strain energy plots, however, have yielded a clear method for determining instability conditions. Furthermore, the shape and smoothness of the $\mathcal{J}$ curves give an indication of the relative properties of the polyurethanes.

In order to differentiate it from the proper J integral the symbol $\mathcal{J}$ will be used for the values calculated in this study where:

$$\mathcal{J} = (\text{Strain Energy})(W)(l_o)/(W-a)$$

Note that the units of $\mathcal{J}$ are the same as J. $\mathcal{J}$ is analagous to the Rivlin-Thomas tearing energy except that the mode of fracture is tensile (mode I) in this case, rather than in shear (mode III).

5.1.1. Fracture Property Changes with Calcium Chelation

The pure samples of Biomer displayed rubber elastic type behavior during tensile testing to fracture. This was true even at longer initial crack lengths where one might not expect an unstable crack growth dominated tensile behavior to continue to display rubber elastic properties. This behavior was shown in Figure 34. Figure 118 indicates a steady decrease in $\mathcal{J}$ with increasing initial crack length and consequently, Δa. Instability conditions occurred for crack lengths exceeding 5 mm. The strain energy curves indicate that Biomer had a stronger resistance to crack propagation than Pellethane, prior to reaching an instability crack length.

The addition of 1%wt. of $CaCl_2$ to Biomer led to changes in the stress-strain behavior of the cracked samples. At strains below 60%, the anticipated rubber type curvature was maintained. For specimens with short initial cracks (and thus longer strains to failure), the tensile curves deviated from an ideal rubber curve at high strains into a more linear elastic type behavior. This is seen in Figure 37 for Δa values of 3.55, 3.50 and 3.45 cm at strains greater than 60%. The non-rubber behavior can be attributed to molecular behavior which causes deviations from ideal rubber elasticity. These factors include strain induced orientation which may be enhanced by the presence of $CaCl_2$. The calcium chloride binds the

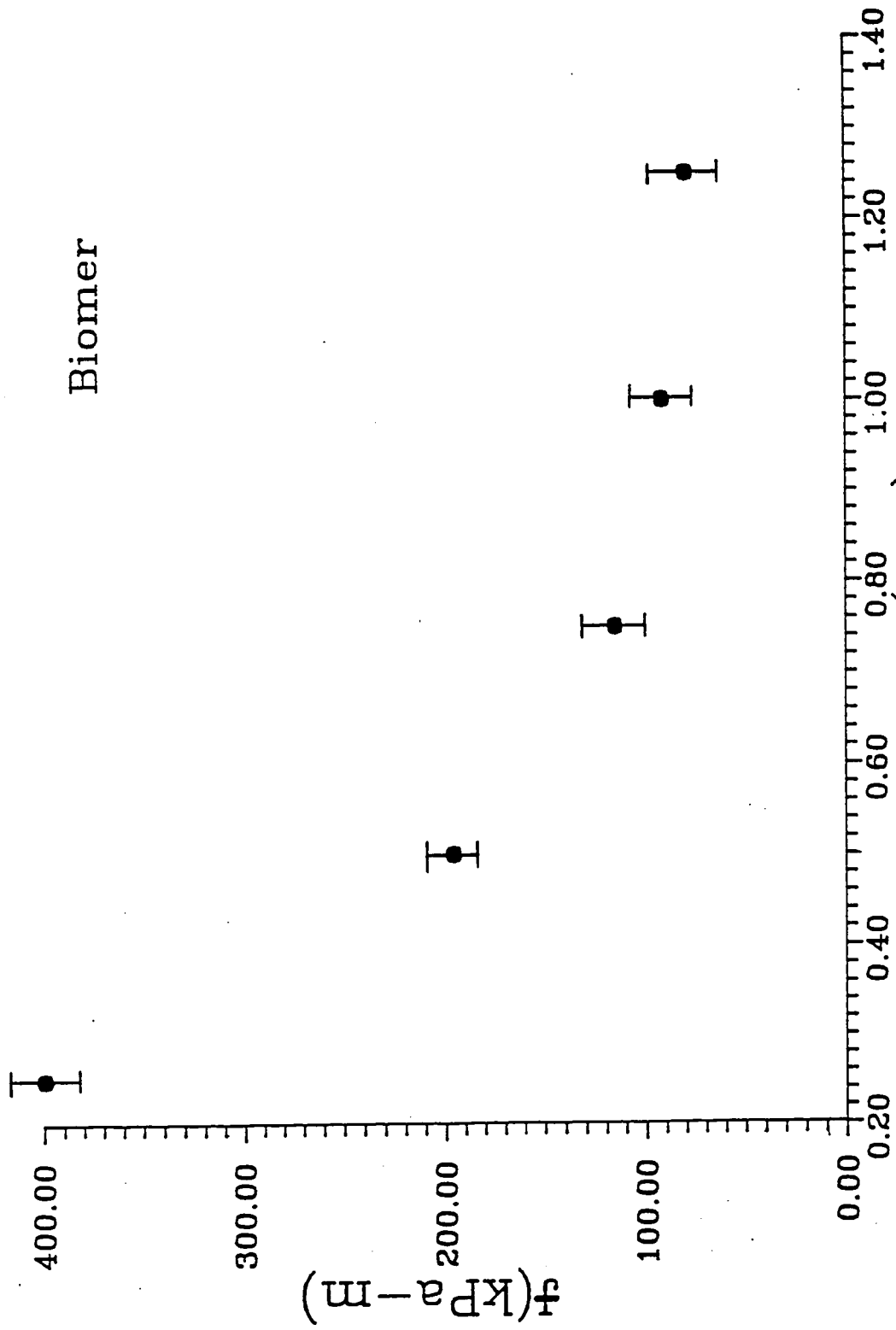

Figure 118: Normalized strain energy to failure versus initial crack length for pure Biomer.

polyether into a more ordered structure which deviates from the assumption of the freely rotating molecule. At high strains, soft segment orientation causes deviations from ideal rubber behavior for the same reason.

At 1%wt. concentration, the $\mathcal{J}$ values were least for all the $CaCl_2$ blends with Biomer as shown in Figure 119. The strain energy to failure fell sharply between 3 and 3.5 mm, indicating that Biomer blended with $CaCl_2$ at low concentrations is weakened by the interaction of the polymer with the salt.

At 5%wt. calcium chloride concentrations, Biomer was plasticized as seen in the stress-strain behavior in Figure 40. The fracture process involved more steady tearing to failure along these curves rather than the stretching followed by immediate failure observed in the 0 and 1% concentrations. The upswing in the stress-strain curves above 150% strain is indicative of the reduction in free volume associated with strain orientation. This is possible because of the initial breakdown in the domain structure which allows molecules to slide with respect to each other; it also indicates a weakening of the hydrogen bonding of the hard segment domains.

The $\mathcal{J}$ values of the 5% concentration were significantly greater than the 1% concentration for Biomer as seen in Figure 120. This was a result of the plasticization of the elastomer; failure was not as rapid

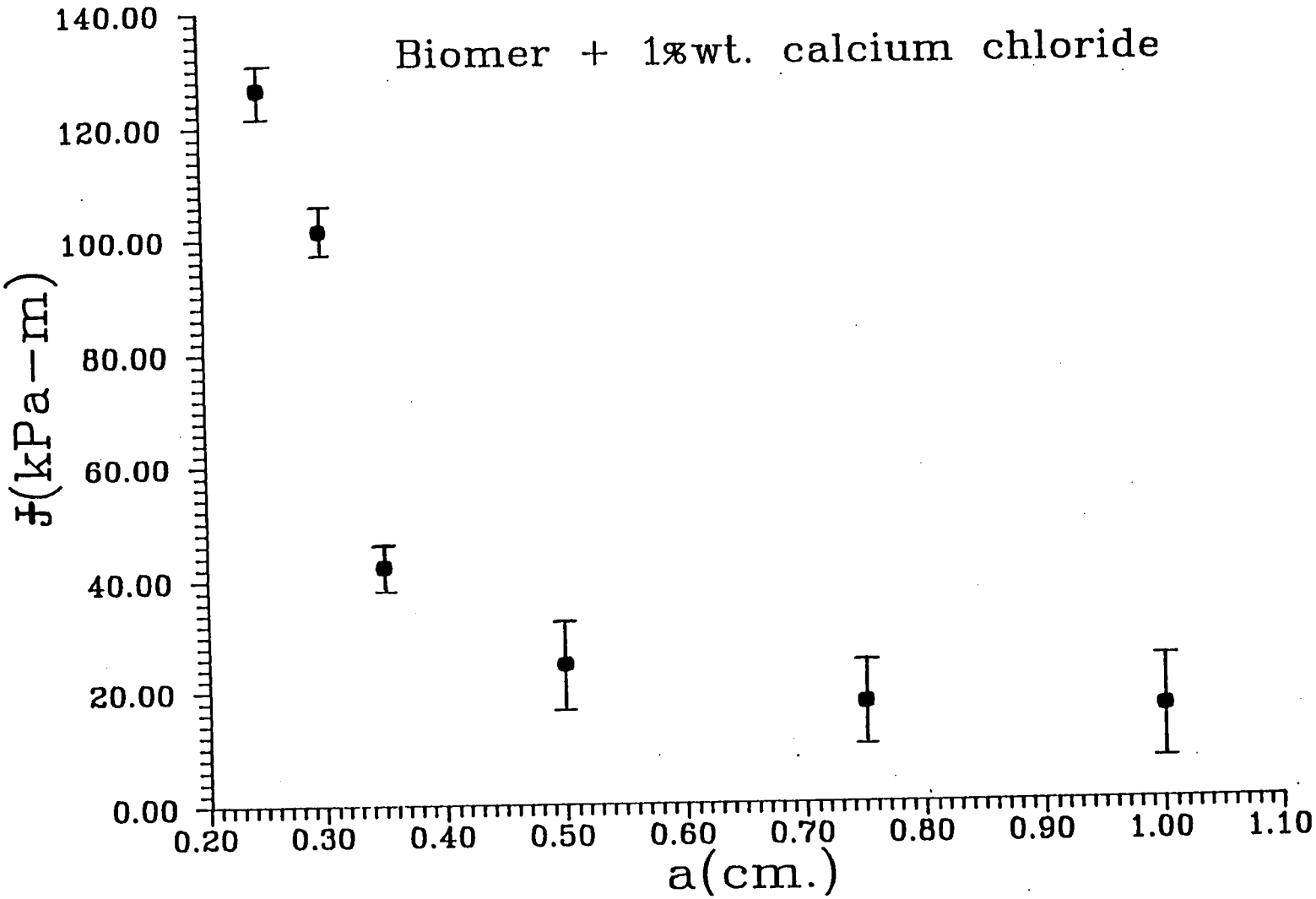

Figure 119: Normalized strain energy to failure versus initial crack length for Biomer blended with 1% wt. calcium chloride.

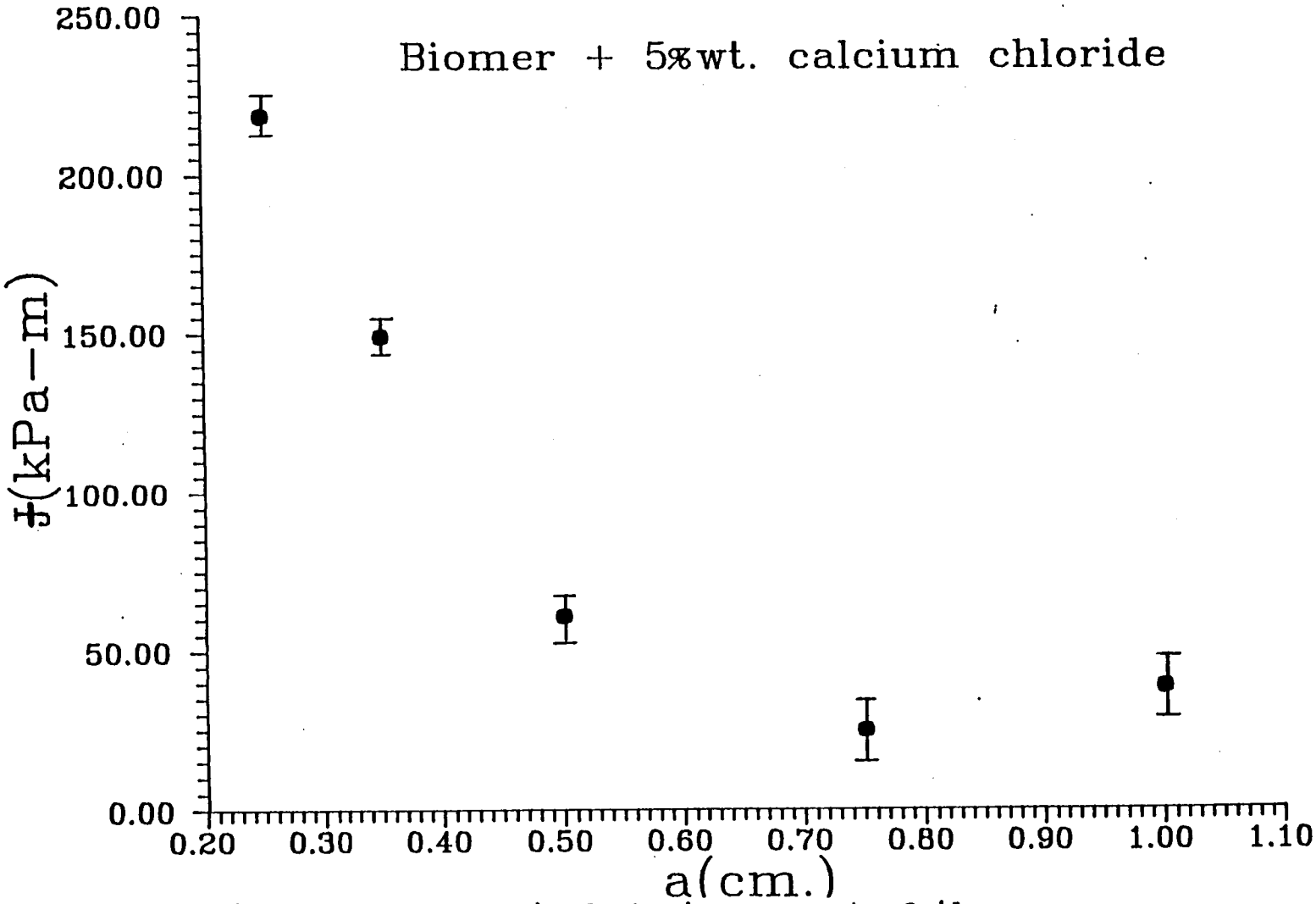

Figure 120: Normalized strain energy to failure versus initial crack length for Biomer blended with 5% wt. calcium chloride.

as the flexible polyether group reached it's strain limit. Instead, molecules slide slowly to absorb the strain energy. The breakdown of the hydrogen bonding was observed in the infrared spectra. Furthermore, a greater percentage of the overall strain energy may be absorbed in the form of material deformation. The overall energy to reach the critical energy for crack propagation is therefore larger. In this case, the crack instability occurred at roughly 5 mm.

At 10%wt. $CaCl_2$ concentration, the plasticization effects observed at 5% were not as apparent with the absence of the stress upswing prior to failure. At this high a level of salt concentration, the tensile test was also measuring a large contribution from the salt crystals. The normally transparent polyurethane films were slightly opaque, indicating crystallization of salt and/or polymer. The salt crystals inhibited the plasticization causing failure to be more abrupt as in the case of the pure rubber. This is apparent in the σ plot in Figure 121. There also appeared to be a broad distribution of stress levels, depending on the initial crack length. This may be due to the variations in the stress fields surrounding the crack tip which varied with local salt concentration. The strain energy values were comparable to the 5% concentration before the instability crack lengths but were greater at large initial crack

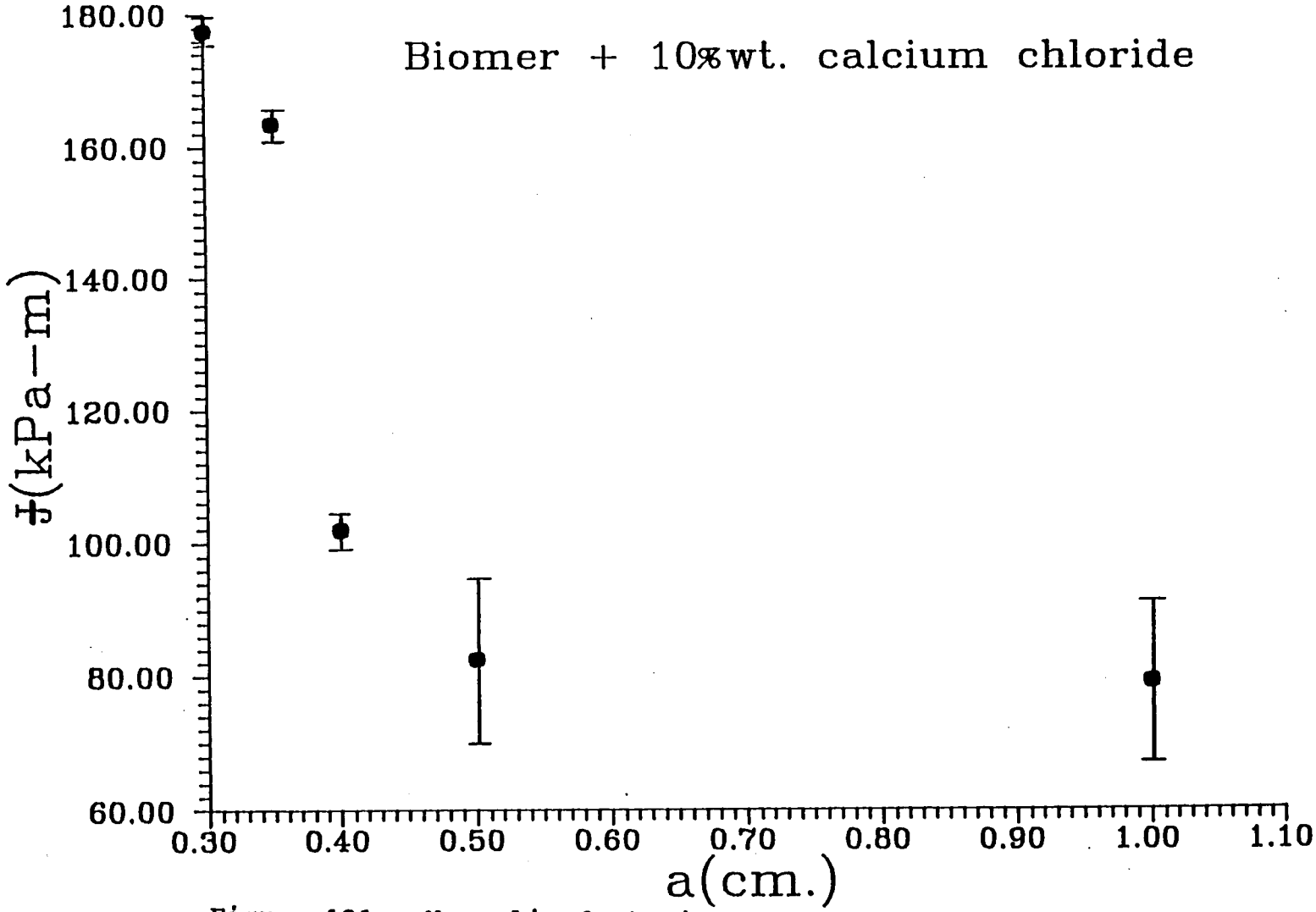

Figure 121: Normalized strain energy to failure versus initial crack length for Biomer blended with 10% wt. calcium chloride.

lengths. In this case, the large salt crystals probably aided in arresting crack propagation. The instability crack length was approximately 4 mm. A comparison plot of $\mathcal{J}$ is shown in Figure 122 which summarizes the fracture discussion of Biomer.

The tensile data of Pellethane had fewer data points per curve because of the much lower strain to failure of the material. Pure Pellethane had a rubbery behavior with no observable non-ideal rubber elastic effects prior to failure. The stress levels were much lower than for Biomer and the films failed much more rapidly than pure Biomer. The transition at the instability conditions shown in Figure 123 was abrupt between 3.5 and 5 mm.

The strain energy values for $CaCl_2$ blended with Pellethane were less than for pure Pellethane at initial crack lengths less than the instability point. At cracks larger than the instability lengths, the calcium blends displayed greater strain energy to failure. Again the binding of the salt to the soft segment and the plasticization of the hard segment by $CaCl_2$ caused an averaging of the critical fracture properties.

According to Figure 49, at 1%wt. $CaCl_2$, Pellethane appeared to have a reduction in rubbery behavior upon drawing, approaching a linear stress-strain behavior. One should recall that the second order term in rubber elasticity theory (equation 2.3.1.9) has negligible

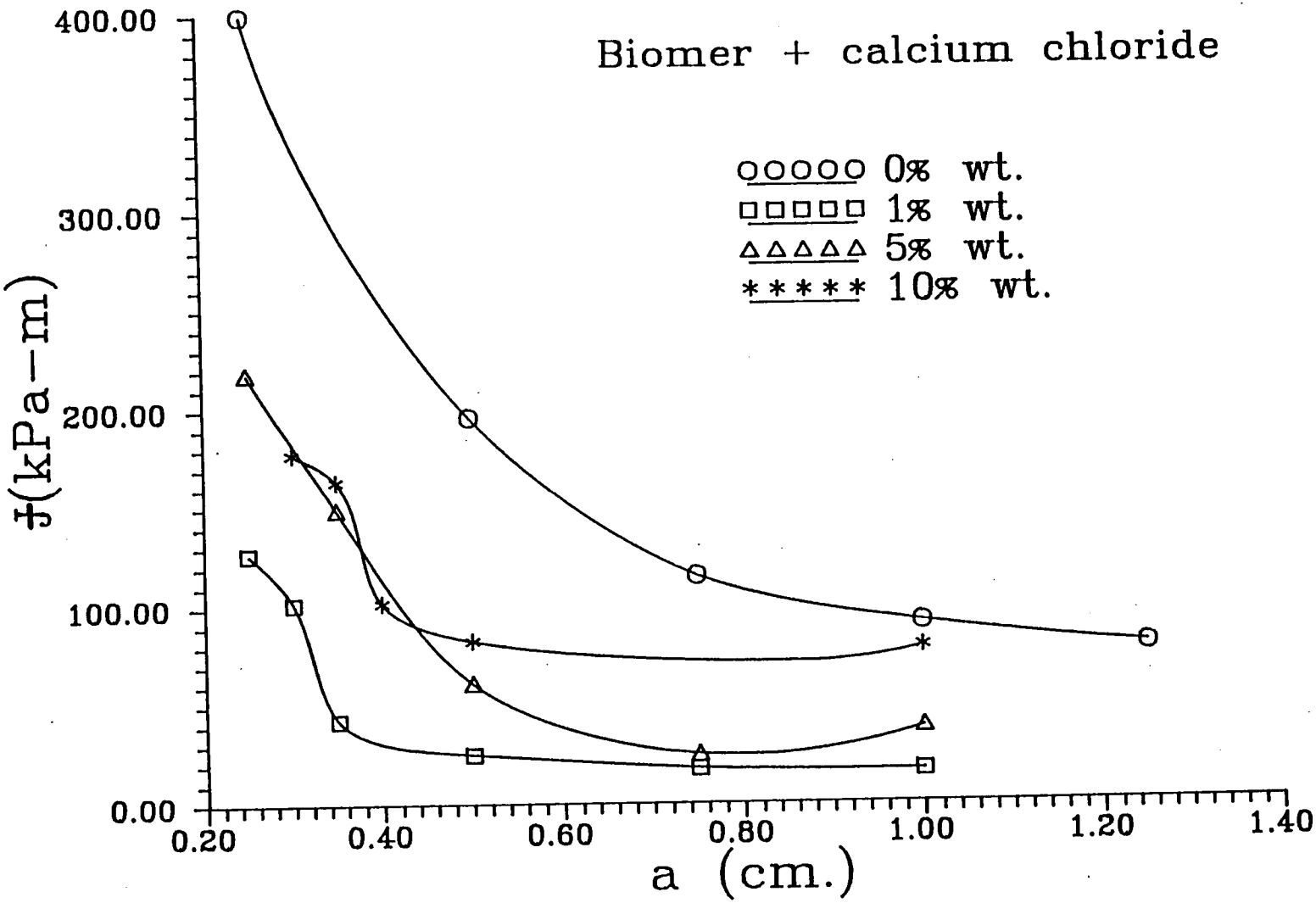

Figure 122: Comparison plot of normalized strain energy to failure versus initial crack length for Biomer blended with various calcium chloride concentrations.

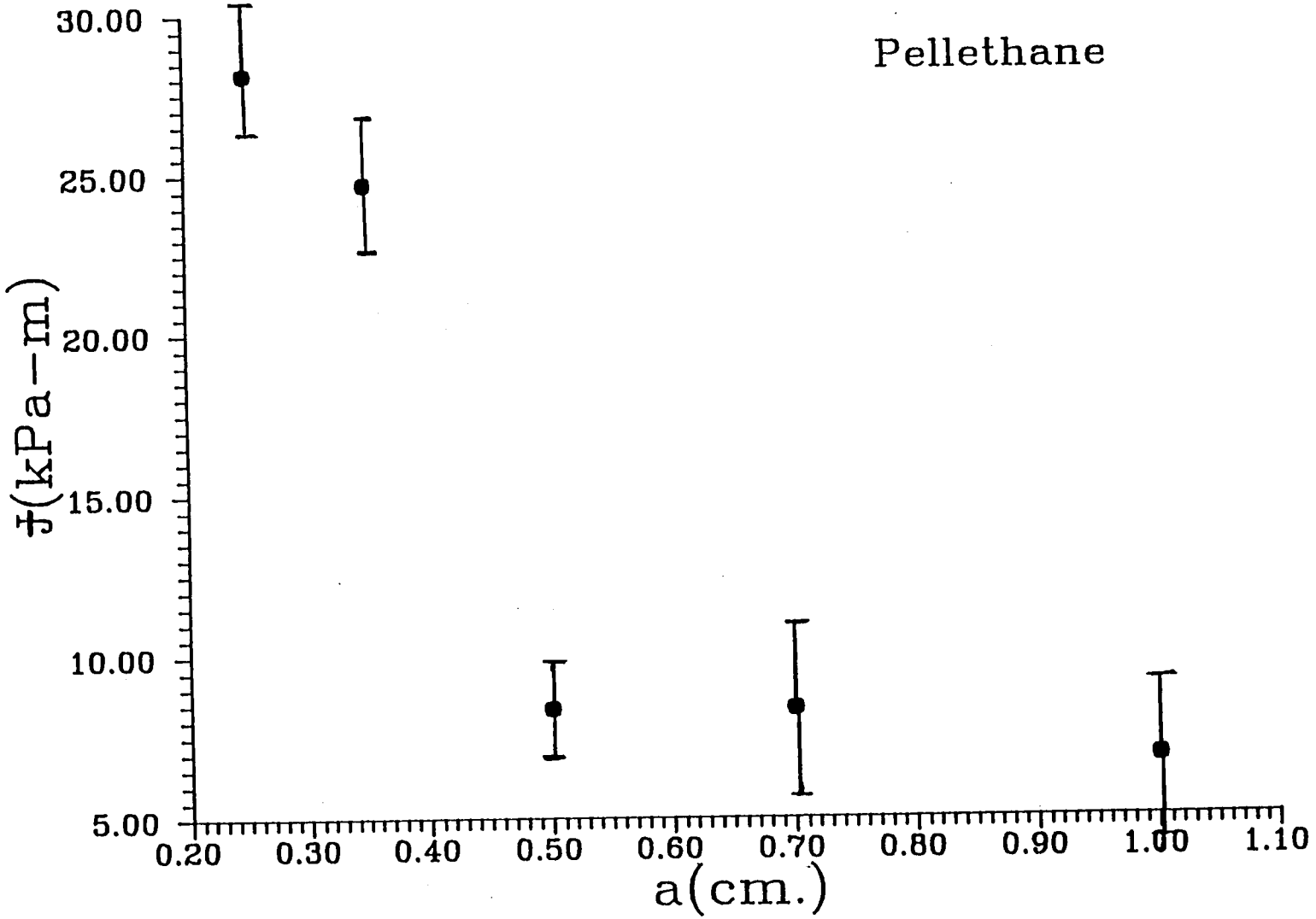

Figure 123: Normalized strain energy to failure versus initial crack length for pure Pellethane.

contributions at small strains. Since Pellethane failed at much lower strains than Biomer at all $CaCl_2$ concentrations, one might expect that the first order term would dominate. The $\mathcal{J}$ curve appeared to have a less abrupt transition at the instability point as shown in Figure 124. The transition was estimated to be 4 mm.

The linearization of the stress-strain behavior continued at 5% $CaCl_2$ as seen in Figure 52. The loss of the second order dependence of the stress-strain curves also resulted in the lowest of $\mathcal{J}$ values and a reduction in the sharpness of the discontinuity point. In other words, the discontinuity is not as abrupt at $CaCl_2$ concentrations of 5 and 10%. The instability point was estimated from Figure 125 at 4.5 mm for the 5% concentration.

At 10% $CaCl_2$ the stress-strain curves for Pellethane appeared to continue their linear behavior. It is significant that the $\mathcal{J}$ values (shown in Figure 126) increased from the 5% $CaCl_2$ concentrations. At this high a $CaCl_2$ concentration, the mechanical test measures less of a molecular fracture phenomena and more of a molecular disentanglement and sliding of molecules. The longer instability was estimated at 6.5 mm from Figure 126. This results in lower strain energies at cracks shorter than the instability length and greater strain energies at crack lengths longer than the instability length. The $\mathcal{J}$ results for Pellethane are compared in Figure 127.

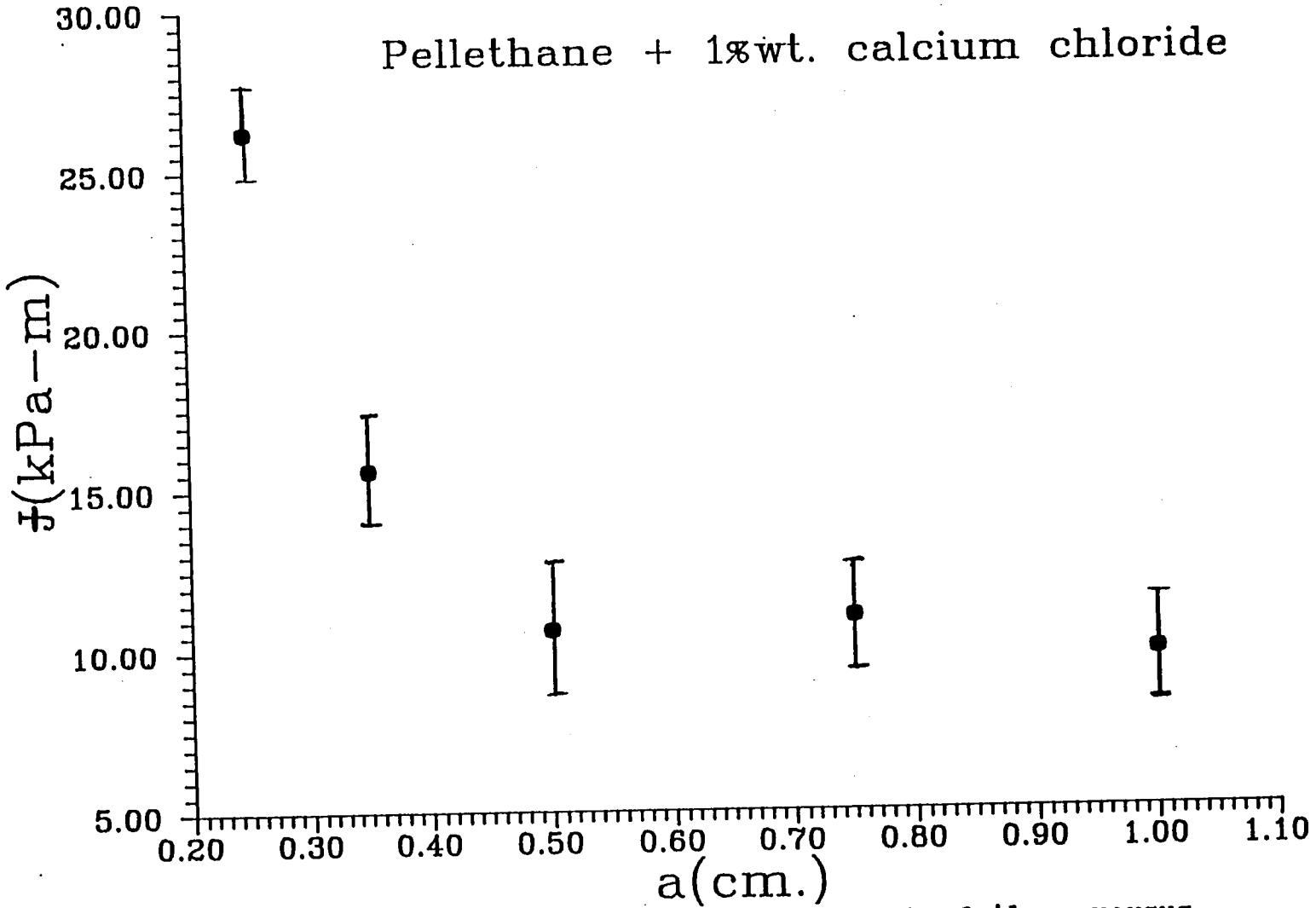

Figure 124: Normalized strain energy to failure versus initial crack length for Pellethane blended with 1% wt. calcium chloride.

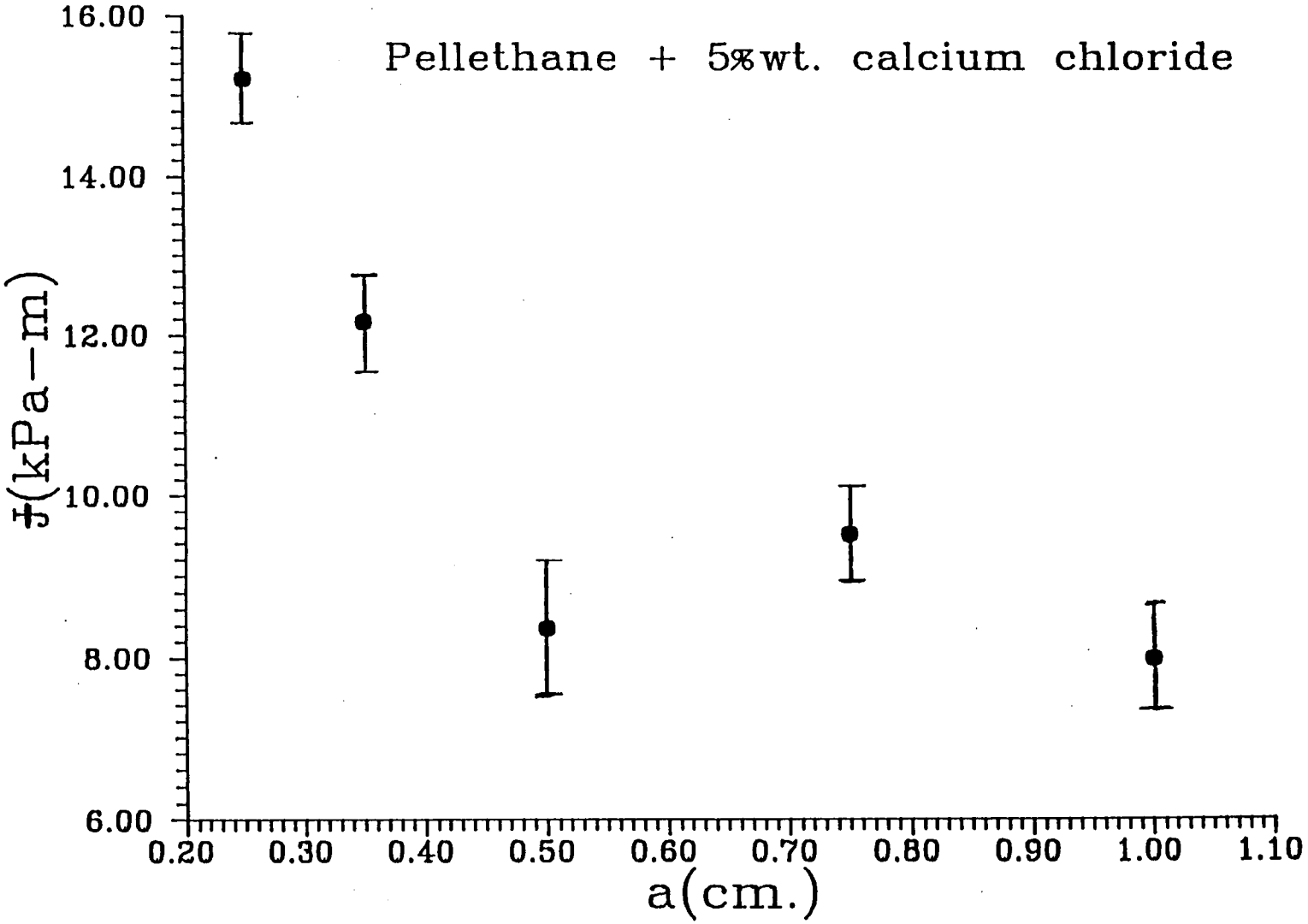

Figure 125: Normalized strain energy to failure versus initial crack length for Pellethane blended with 5% wt. calcium chloride.

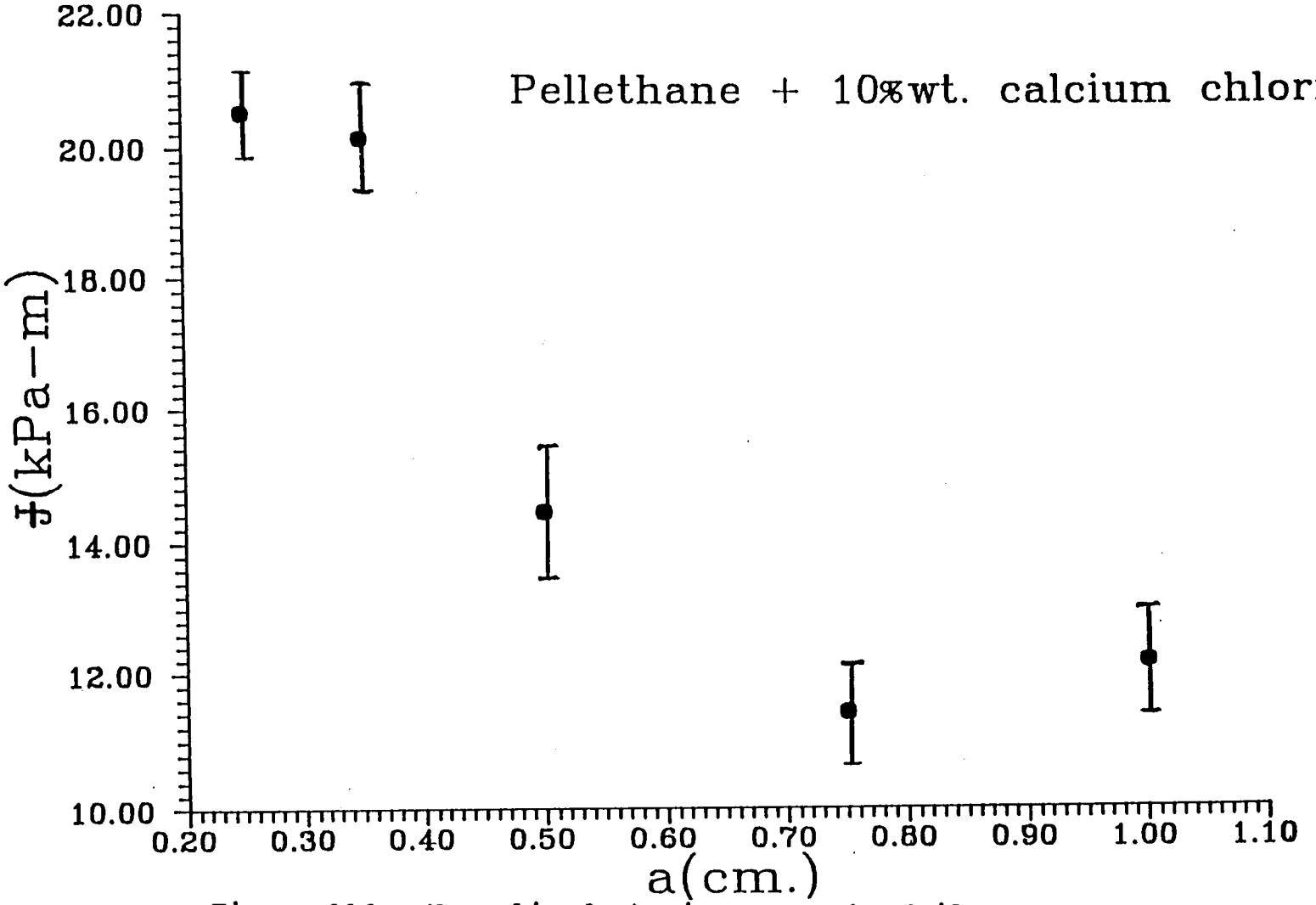

Figure 126: Normalized strain energy to failure versus initial crack length for Pellethane blended with 10% wt. calcium chloride.

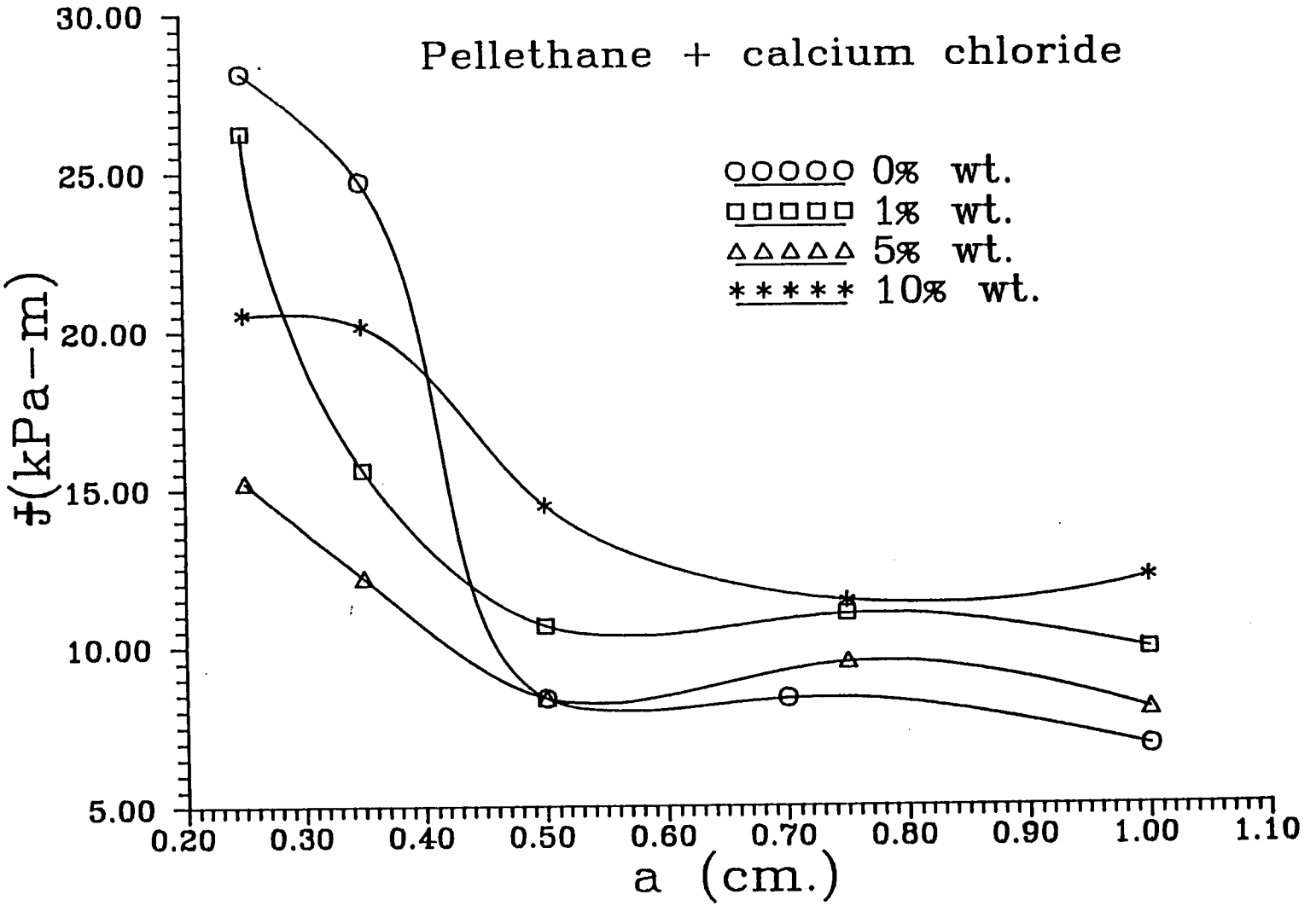

Figure 127: Comparison plot of normalized strain energy to failure versus initial crack length for Pellethane blended with various calcium chloride concentrations.

The instability crack lengths used in the crack tip orientation measurements are summarized in Table IV. Although critical crack lengths are less than ideal fracture toughness criteria, some general observations can be made from the data of Table IV. The addition of 1% calcium chloride to Biomer and Pellethane lowered the critical crack length by roughly 20%. This means that calcium salts lowered the amount of energy required to reach unstable crack propagation, thus making it easier for the crack to propagate. This can be attributed to soft segment binding of calcium chloride. At higher salt concentrations, the greater critical crack lengths resulted from increased plasticity due to the disruption of the domain structure. This will be discussed in greater detail in section 5.2.

5.1.1. Summary of Fracture Testing

Fracture testing of calcium blended polyurethanes has led to several important points. At physiologically low levels of $CaCl_2$ blends, there are significant changes in mechanical properties. The fracture results indicate that $CaCl_2$ has two roles in effecting changes in mechanical properties. At the lower concentrations, there is a significant reduction in toughness and the strain energy to failure. It is therefore possible that such a rapid reduction may accelerate fatigue crack growth or stress cracking under physiological conditions. This is

particularly significant because the body's calcification mechanism is not by passive diffusion but by an active transport mechanism. Pellethane appeared to be more susceptible to the degradation process because it had less extensive hydrogen bonding in its domain structure.

The second role of $CaCl_2$ is in changing the strain energy behavior. Because $CaCl_2$ causes changes in intermolecular forces of the domains and matrix, the fracture mechanical properties are affected. In the hard segment domains, the hydrogen bond is disrupted. In the soft segment matrix, $CaCl_2$ binds to the polyether and changes it's strain orientation properties. These structural changes are apparent in mechanical property changes like strain energy to failure. The changes depend on the $CaCl_2$ concentration and the point at which saturation of the matrix leads to disruption of the domains.

The biomedical engineering ramifications are also significant. Regardless of the mechanism of calcification in the body, a small deposit of calcium salts will increase stress cracking. The stress cracking can be attributed to two modes of embrittlement. The first mode is a reduction in rubber elastic properties due to large mineral deposits which were noted in the literature review. The second is the chelation of salts at the molecular level which leads to reductions in free rotation

of the polyether. The bound salt may also serve as a nucleation site for calcification of the first mode.

5.2. Molecular Orientation of Polyurethanes

In Figures 60 through 67, the effects of several phenomena are depicted as they relate to the N-H stretch vibration. Changes in the peak absorbance values associated with polarization and orientation were quite noticeable in each lettered figure. A more important feature, however, is the peak broadening with increasing $CaCl_2$ concentration. This is a clear indication that calcium chloride is disrupting the formation of the hydrogen bonds which give polyurethanes their elastomeric behavior. The broadening is attributed to the increase of free (non hydrogen bonded) N-H groups which are depicted in Figure 128. In the case of the free N-H, there are no secondary bonding effects which allow for a short period, high frequency vibration. The sharpness of the peak is therefore an indication of the breadth of a distribution of N-H bonds vibrating at different frequencies. Because the additional urea segment in Biomer enhances hydrogen bonding, the disruption did not become significant until concentrations reached 5% wt. (Figure 62). In Pellethane, significant broadening was observed at the 1% concentrations (Figure 65), confirming that the additional urea group enhanced hydrogen bonding. Similarly, Biomer with 10% wt. calcium chloride appeared to retain a small

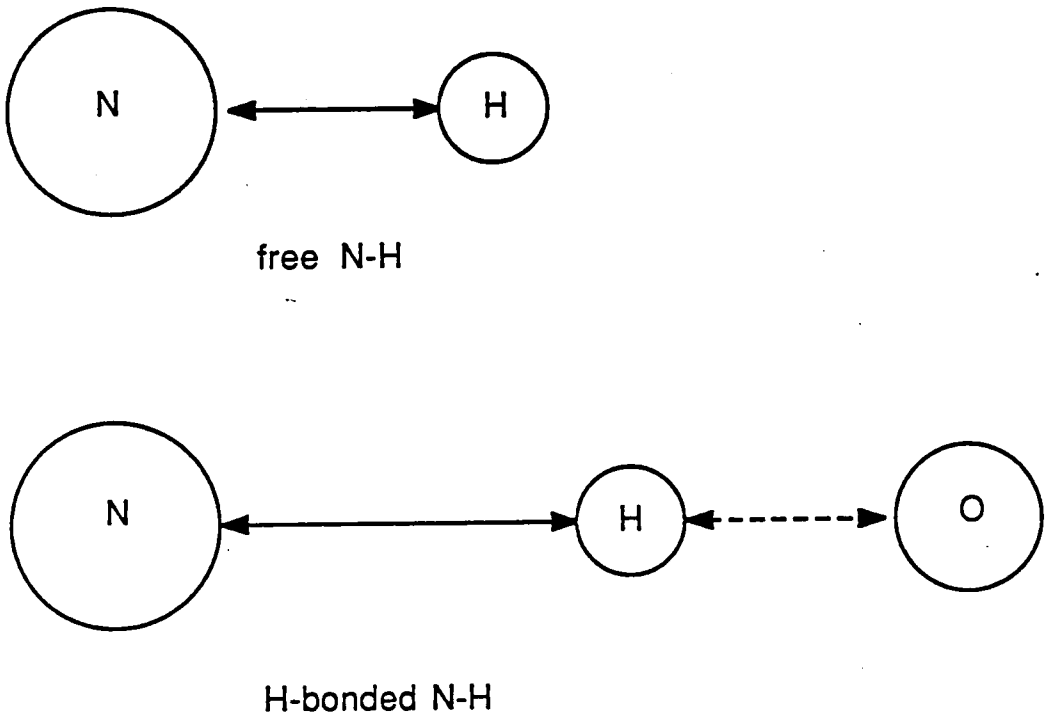

Figure 128: The N-H stretch vibration. High frequency (shorter period) vibration corresponds to free N-H; low frequency (longer period) vibration corresponds to hydrogen bonded N-H.

concentration of hydrogen bonded N-H, while Pellethane at 5% wt. concentration already had a severe breakdown in hydrogen bonding as the appearance of the free N-H peak appeared at the higher frequencies above the hydrogen bonded N-H in Figure 66.

Figure 67 which shows the data for Pellethane at 10% wt. is presented to address a limitation of the instrumentation. The absorbance saturation of the N-H bands implies that the film sample was too thick for the high intensity IR source to produce a spectrum. This is perhaps due to the $CaCl_2$ crystals which may have scattered a portion of the beam, producing an excessive absorbance condition. Producing a thinner specimen, however, would have brought the mechanical properties into question. The specimen broke between strain values of 50% and 100%, indicating that, in fact, the specimen was already too thin. (Increasing the sample width would not allow a fair mechanical comparison to other samples). It can be concluded that highly IR absorbing or scattering materials present limitations to stress-strain-orientation measurements by FTIR dichroism. Possible solutions include the use of higher intensity sources or the use of optical methods for collecting dispersive IR spectra such as diffuse reflectance spectroscopy (DRIFTS). Higher intensity sources are not readily available for laboratory use, nor will they solve the problem of losses from

scattering light. Current diffuse reflectance techniques have the problem that they cannot allow for dichroic ratio measurements because their optics affect the direction of the electric vector.

Using the data that was acceptable, orientation functions for the stretched films were calculated. The change in orientation functions, (Δf), from 0% strain were plotted as functions of strain in Figures 129 and 130. The hard urethane segment for Biomer tended to orient perpendicularly to the draw direction, indicating that the extensive hydrogen bonding had created domains with long axes perpendicular to the chain axis. Negative orientation of the urethane hard segment has been observed by others in recent studies of polyurethanes using visible and infrared dichroism.[119,120] As a result, the addition of calcium chloride reduced the hydrogen bonding and lessened the domain orientation at 5% and 10% concentrations.

Because of it's domain structure, Pellethane displayed positive hard segment orientation upon drawing. As shown in Figure 130, the domain orientation was reduced for $CaCl_2$ concentrations of 1 and 5%. At 10%, however, the hard segment orientation increased rapidly with strain beyond values of pure Pellethane. Recalling that at 10% $CaCl_2$ there is nearly a complete disruption of the N-H hydrogen bonding by large crystals of $CaCl_2$, one may

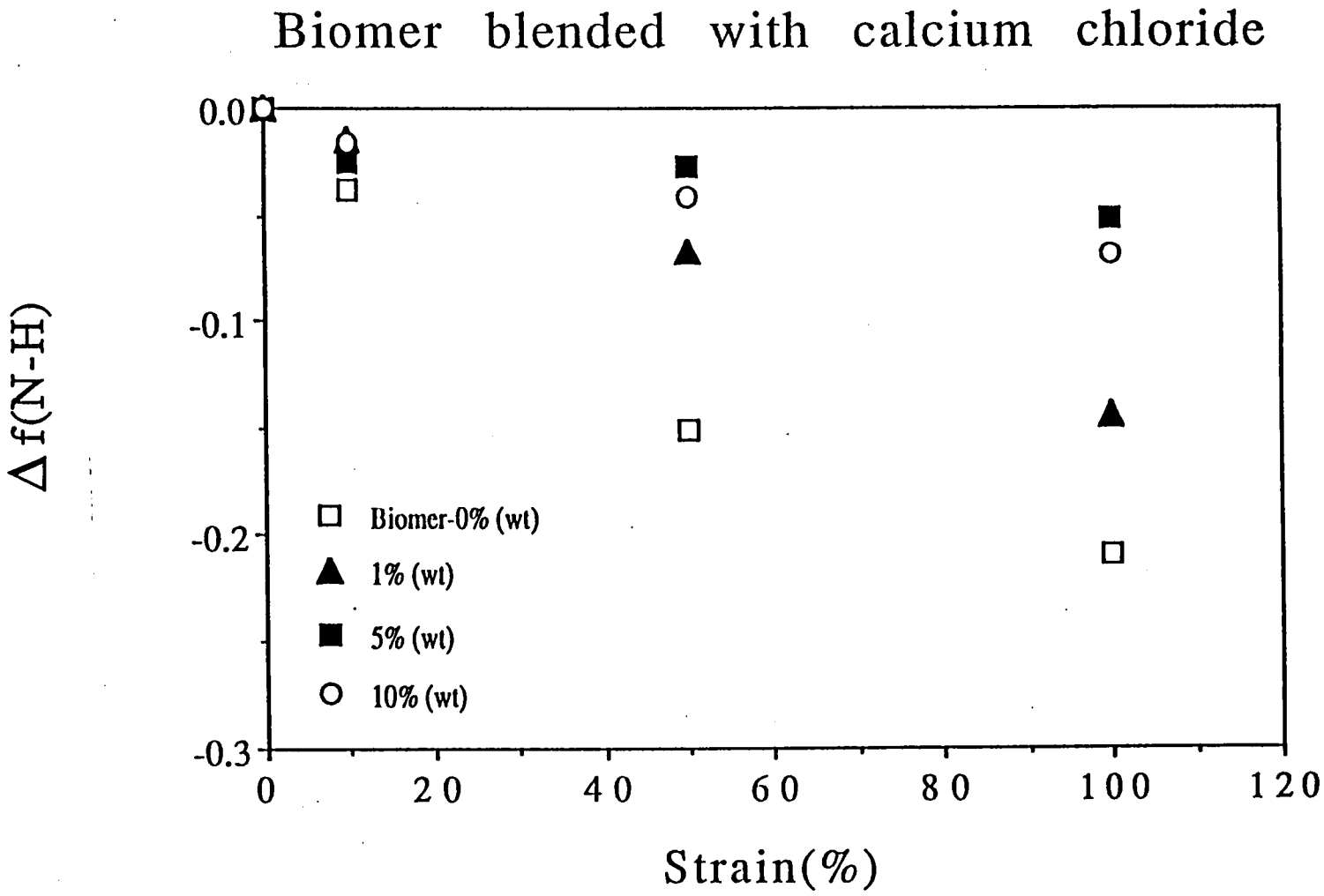

Figure 129: Change in N-H orientation function with strain for various calcium chloride concentrations in Biomer.

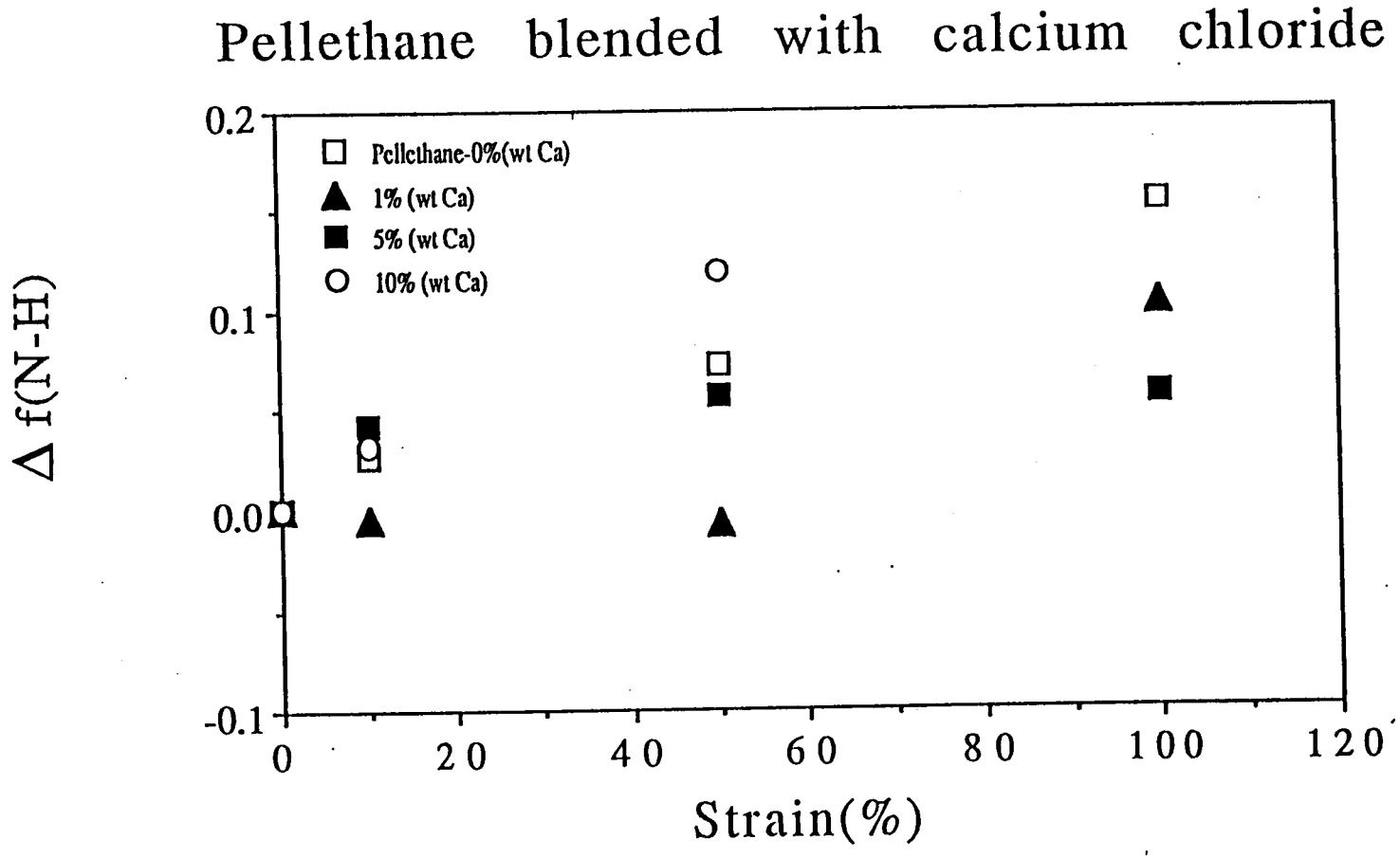

Figure 130: Change in N-H orientation function with strain for various calcium chloride concentrations in Pellethane.

expect that these same crystals are allowing the molecules to slide by each other more easily. Furthermore, since the 10% concentration sample broke between 50 and 100% strain, one might expect orientation to develop faster (at lower strains). This would occur with a reduction of intermolecular forces between molecules.

The discussion of the hard segment domain orientation is summarized in sketches in Figures 131 and 132. Note that at the same $CaCl_2$ concentrations, Biomer always maintains a more extensive hydrogen bonded structure. This was true even at the higher 10% concentration.

The C-H stretch spectral data of Figures 68 through 75 were calculated into Δf values shown in Figures 133 and 134. The soft segment of Pellethane displayed similar positive orientation behavior to the hard segment within experimental error. The soft segment of Biomer also displayed a positive orientation in contrast to the negative orientation of the hard segment. The orientation change with strain was consistent and linear for the 0, 5, and 10% $CaCl_2$ concentrations. The 1% $CaCl_2$ concentration of Pellethane displayed higher values and more scatter with increasing strain. The cause of this behavior is not clear at this time, however, there are some possible explanations. In the previous section, it was observed that 1% of $CaCl_2$ had little effect on the hydrogen bonding of Biomer. One may expect, therefore, that the $CaCl_2$

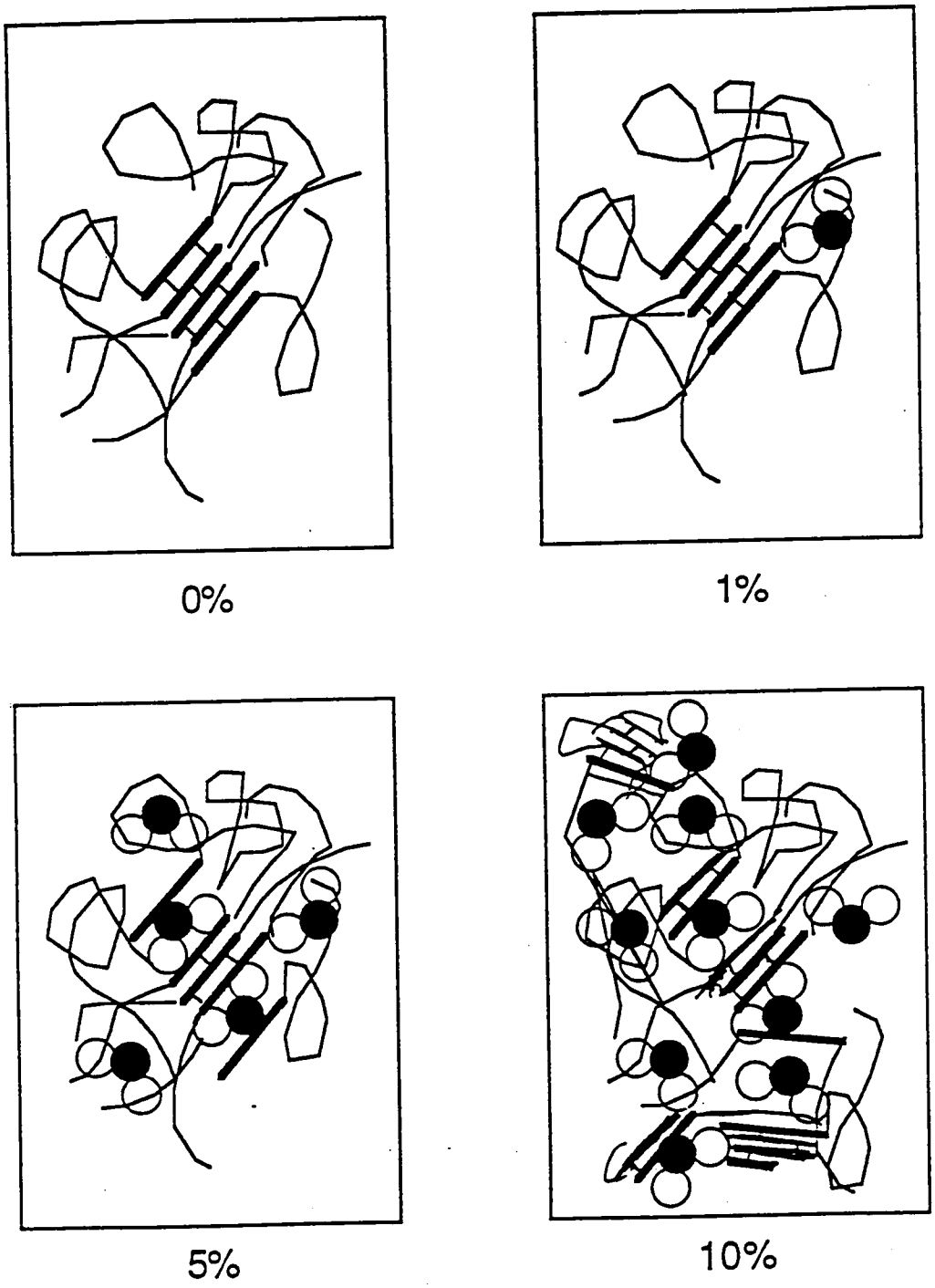

Figure 131: Schematic depiction of hard segment domains for Biomer. Disruption of hydrogen bonding due to calcium chloride.

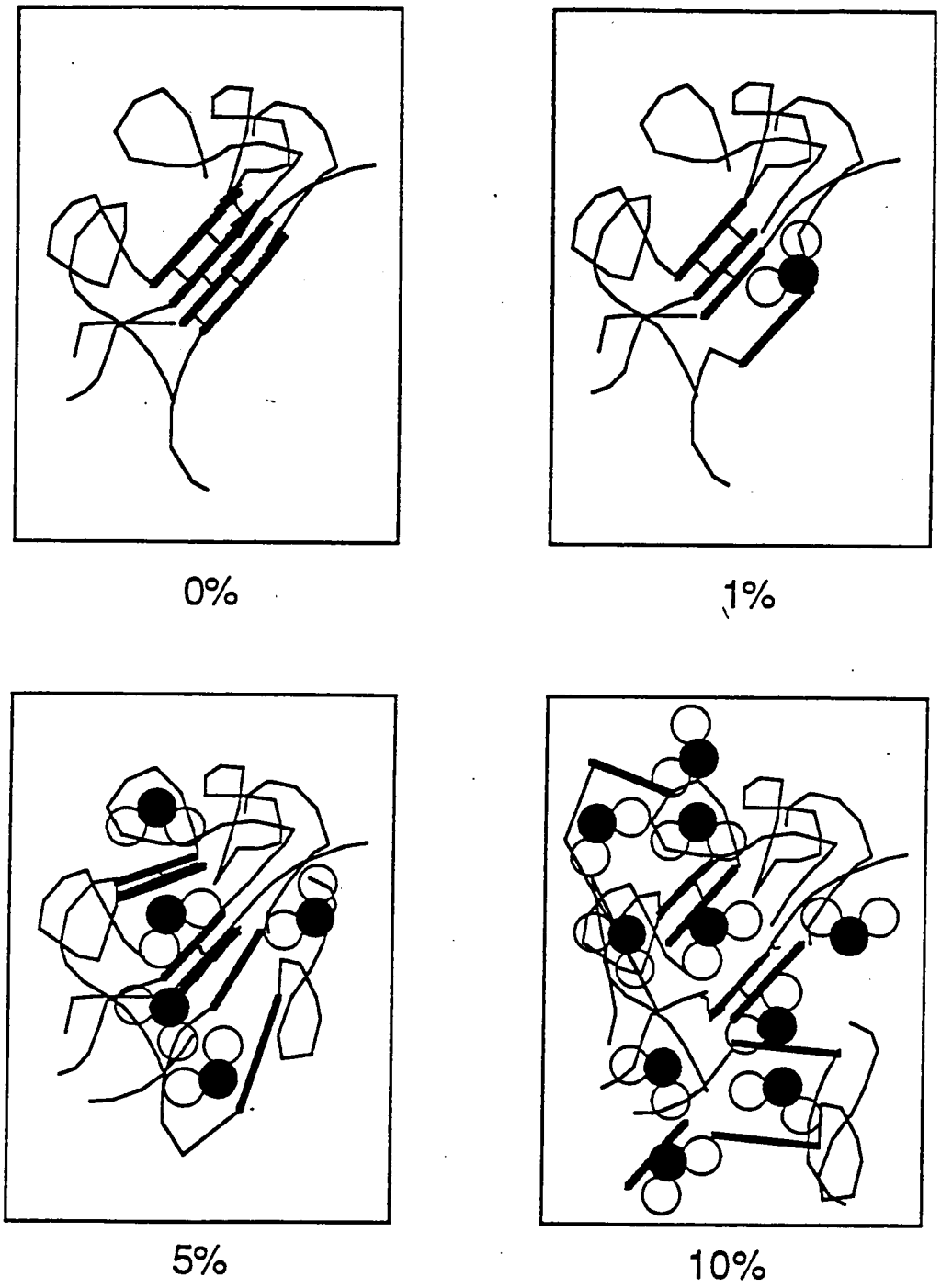

Figure 132: Schematic depiction of hard segment domains for Pellethane. Disruption of hydrogen bonding due to calcium chloride.

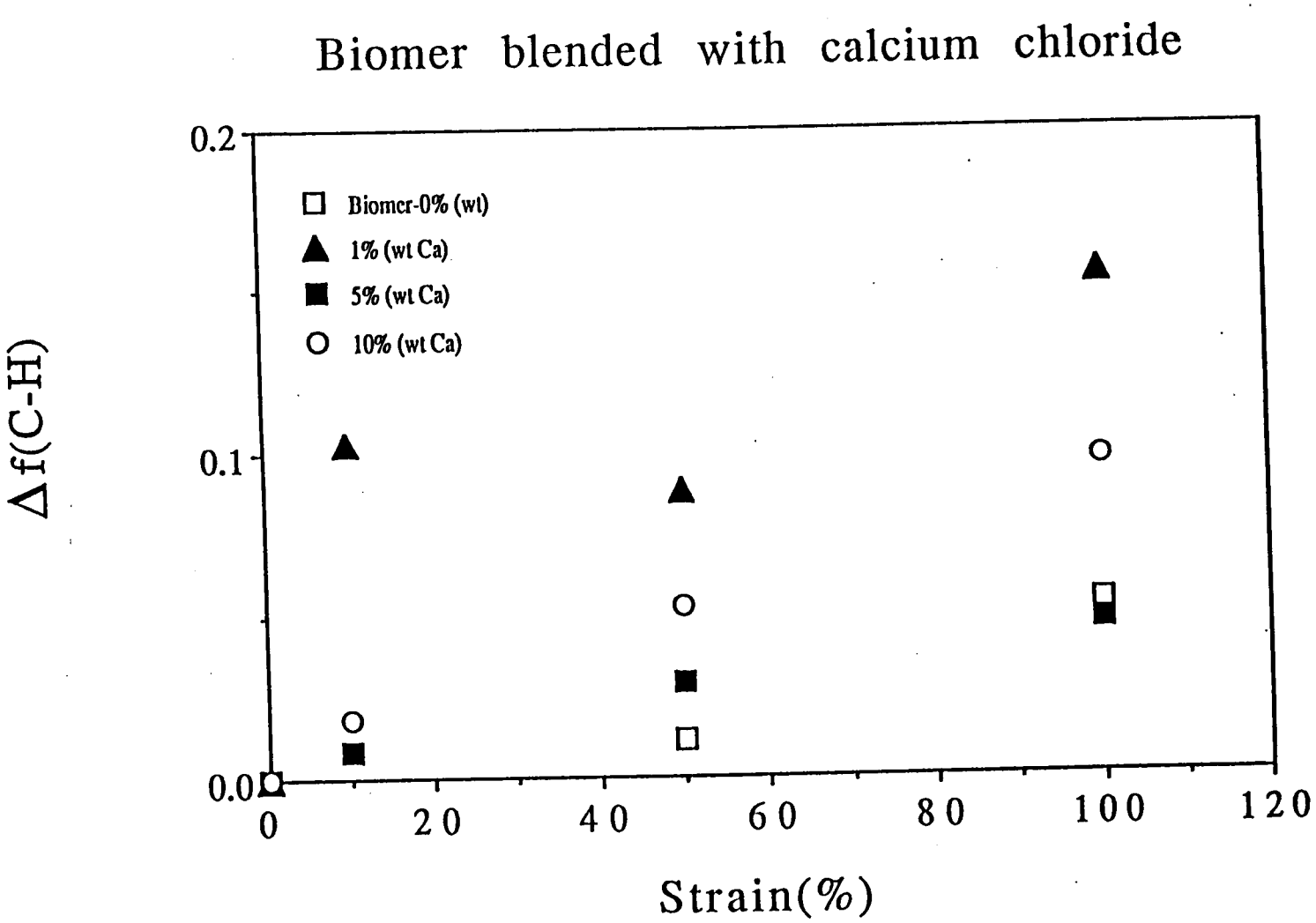

Figure 133: Change in C-H orientation function with strain for various calcium chloride concentrations in Biomer.

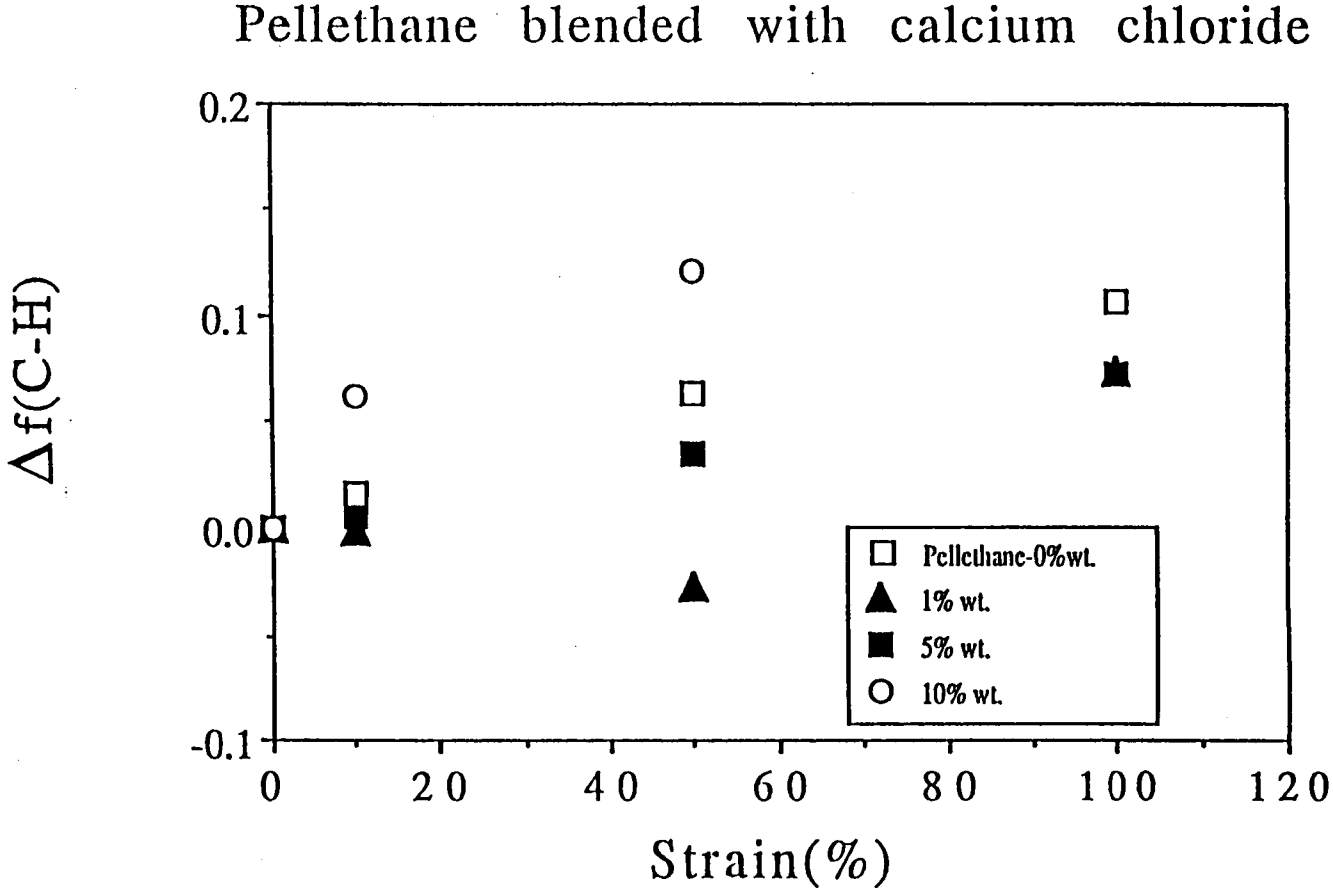

Figure 134: Change in C-H orientation function with strain for various calcium chloride concentrations in Pellethane.

migrated or preferred interaction with the polyether segment at low concentrations. The 1% $CaCl_2$ concentration may have saturated the matrix of polyether segments upon removal of the solvent; the incompatibility of the soft and hard segments may also have contributed to the migration of the calcium chloride to the matrix. If this is indeed the case, one would expect to observe a reduction in the free rotation of the elastomeric chains. This reduction in elasticity correlates well with the $\bar{\sigma}$ curves in Figure 122. This is also consistent with the negative orientation of the hard segment observed in the previous section.

Plots of the maximum stress with strain are shown in Figures 135 and 136 for Biomer and Pellethane, respectively. For Biomer, the 1% $CaCl_2$ was bound by the soft segment matrix resulting in a stiffening effect observed even at 10% strain. At 5 and 10% concentrations, the disruption of hydrogen bonds dominated the mechanical behavior. At the 10% concentration, the $CaCl_2$ binding to the matrix began to replace the urethane as a mode of preventing the polyether chains from sliding. This is exactly in agreement with the fracture results discussed previously and the FTIR spectral data presented in this section. It is also in agreement with previous initial modulus studies.[8] A similar stress-strain behavior occurred for varying $CaCl_2$ concentrations of Pellethane,

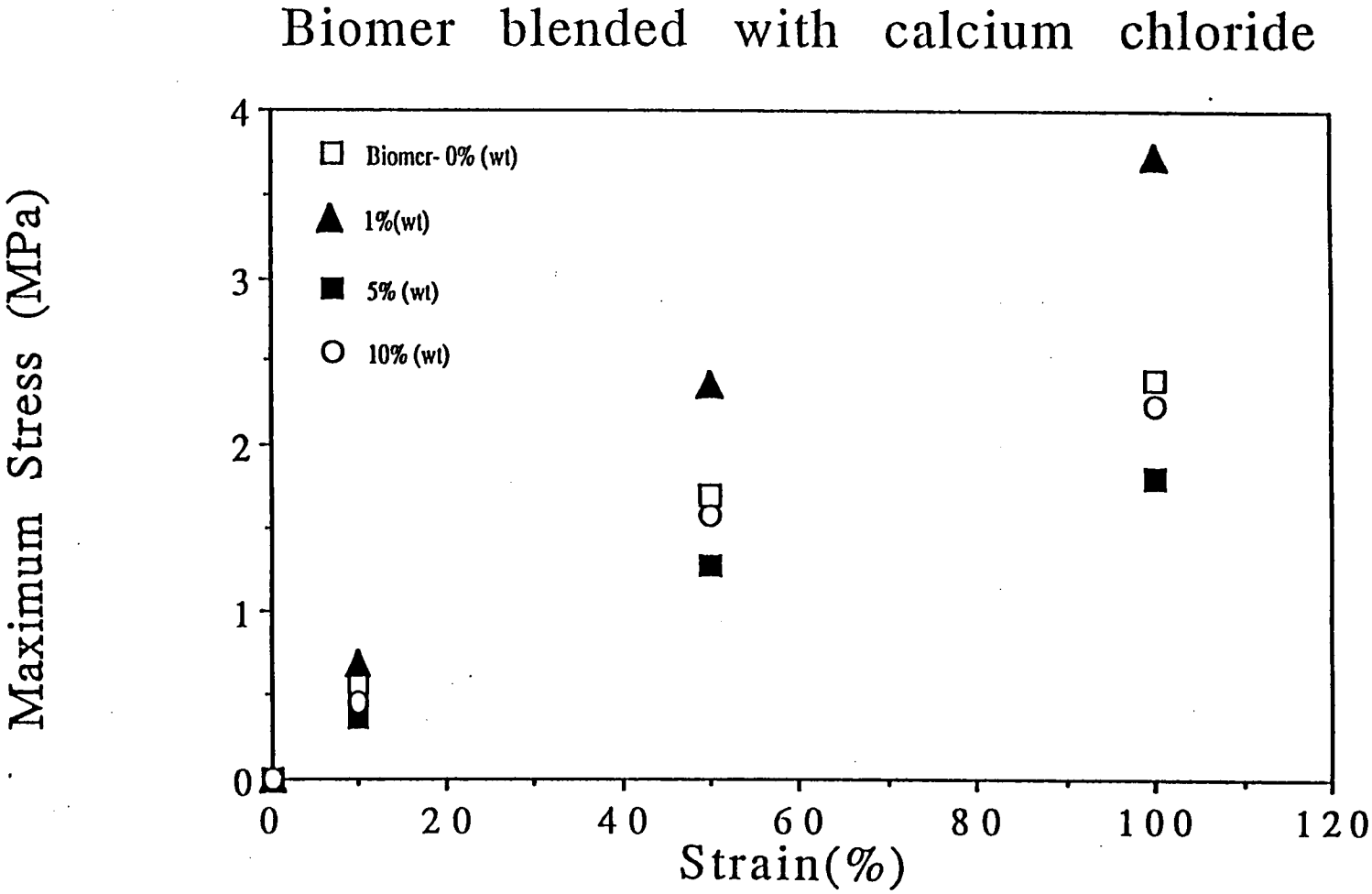

Figure 135: Maximum stress at fixed strain for various calcium chloride concentrations in Biomer.

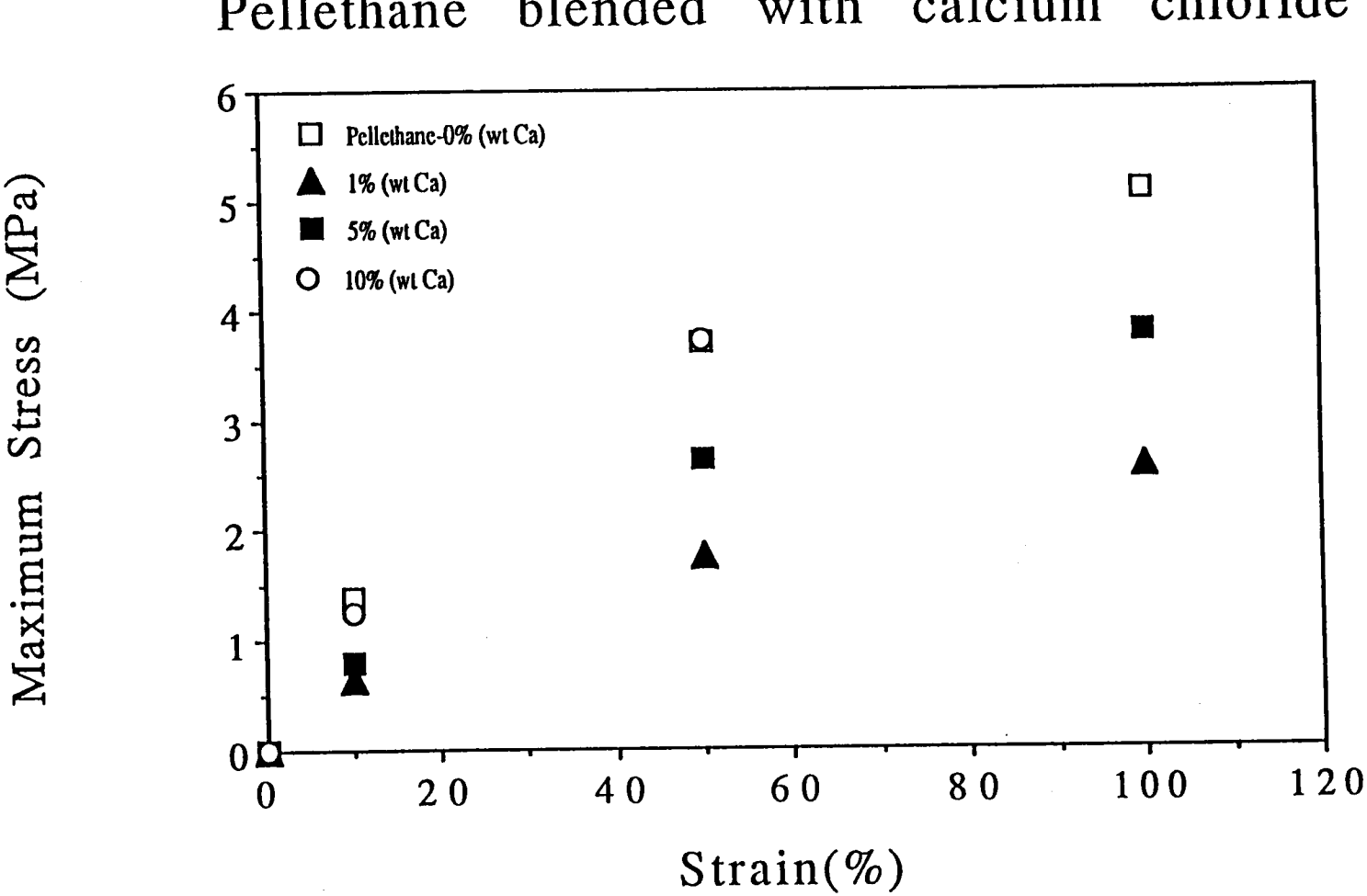

Figure 136: Maximum stress at fixed strain for various calcium chloride concentrations in Pellethane.

shown in Figure 136. Note that the 10% $CaCl_2$ concentration had almost identical tensile behavior as pure Pellethane, except that the sample broke between 50 and 100% strain. This illustrates the importance of examining the fracture properties, such as $\mathcal{J}$. Materials may display similar tensile curves yet have completely different fracture properties.

5.3. Orientation of the Crack Tip Fields

Simultaneous measurements of crack tip orientation and stress at fixed strain allowed the development of crack tip orientation maps. Crack lengths were selected based on the instability values obtained in the fracture studies; these values were shown in Table IV.

Molecular orientation surrounding the crack tip is a function of stresses developed within the material. In equations 2.4.2.7 and 2.4.2.8, the HRR stress singularities were shown to be a strong function of J, the power law exponent, n, and the distance from the crack tip, r. In this study, the value of J depended on the loading conditions and geometry, n varied with calcium chloride concentration and r was varied by positions 1 through 4.

To insure that the cracked specimen was not relaxing significantly during the orientation measurements, stress relaxation data was collected during the FTIR sampling. As seen in Figures 76 and 77, after the actuators were

stopped, there was a slight relaxation during the first 20 seconds during which no spectral data was collected. The stress relaxation data has low levels of background noise which were detected by the load cell. The noise was due to dry air currents from the micro FTIR purge gas. They are not attributable to molecular relaxation, nor were the extremely low background stresses induced by the purge gas considered to be significant. The relaxation data presented indicates that no significant stress relaxation occurred during collection of spectral data at all four crack tip positions. Broadening of N-H peaks continued to be observed with addition of $CaCl_2$ as was observed in the preceeding orientation study.

The crack tip dichroic spectral data were calculated into orientation functions and mapped according to position in Figures 137 to 142. Figures 137 and 138 show the Biomer orientation maps for N-H and C=O, respectively. Recalling that with increasing stress and strain, the N-H orientation decreases for Biomer, the high domain stress regions of the crack tip are the positions with the smallest orientation values. For pure Biomer, the high stress region is at positions perpendicular to the crack tip plane as predicted by the HRR fields with the maximum stress at position 2. This was true for both the N-H and C=O stretch vibrations. At 1% $CaCl_2$, the minimum orientations were at position 2 for N-H but at position 1

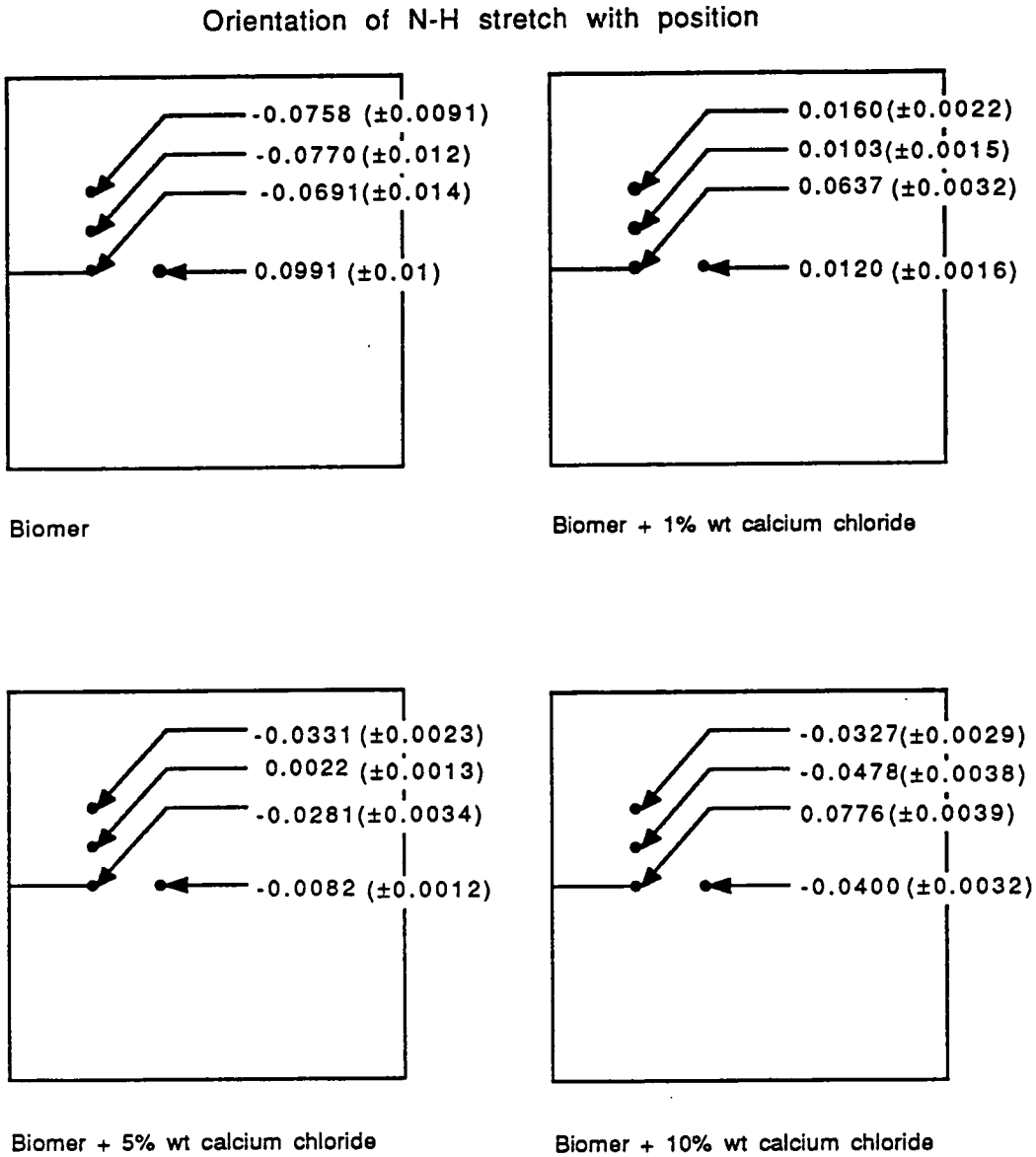

Figure 137: Crack tip N-H orientation maps of Biomer for various calcium chloride concentrations.

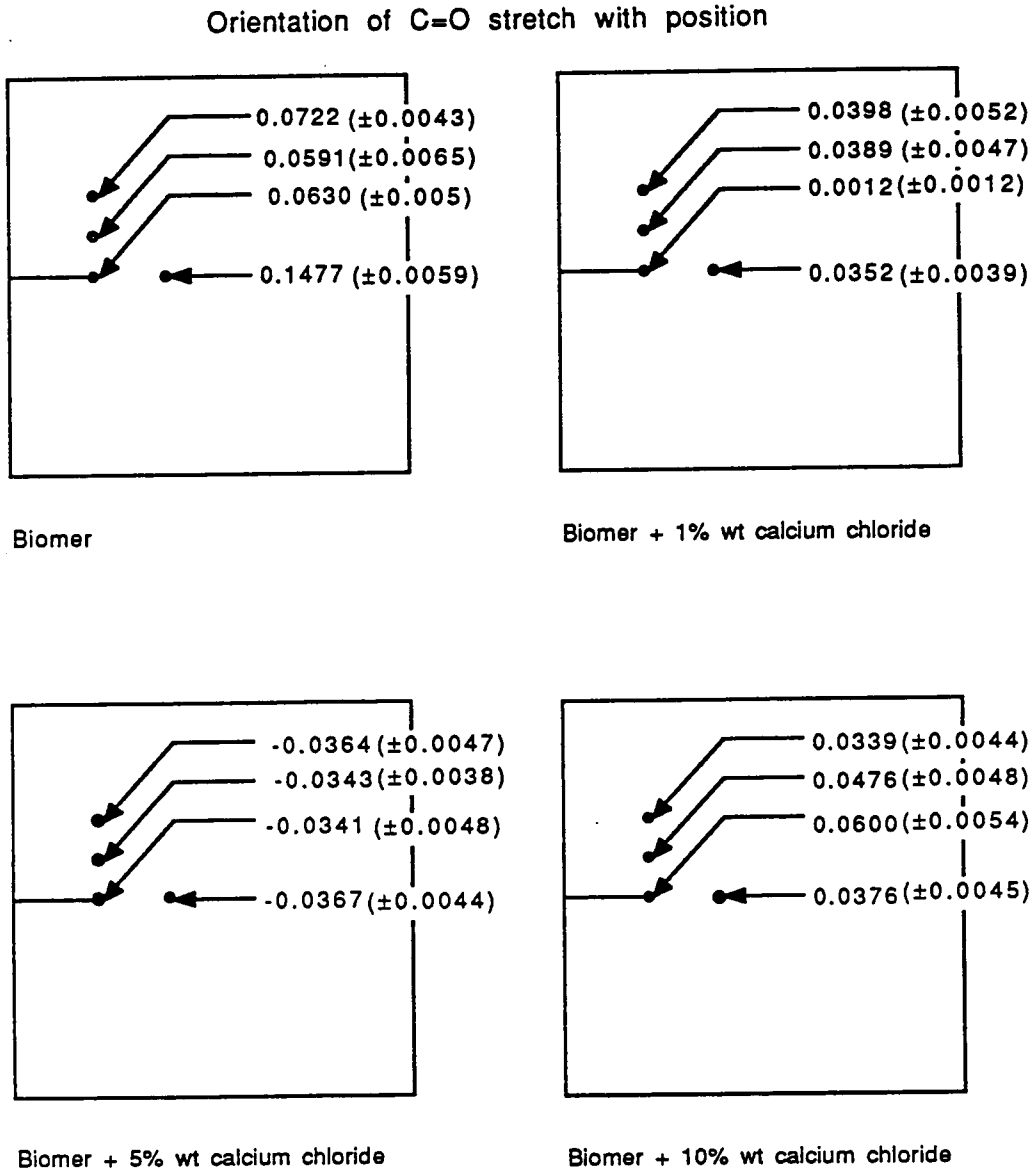

Figure 138: Crack tip C=O orientation maps of Biomer for various calcium chloride concentrations.

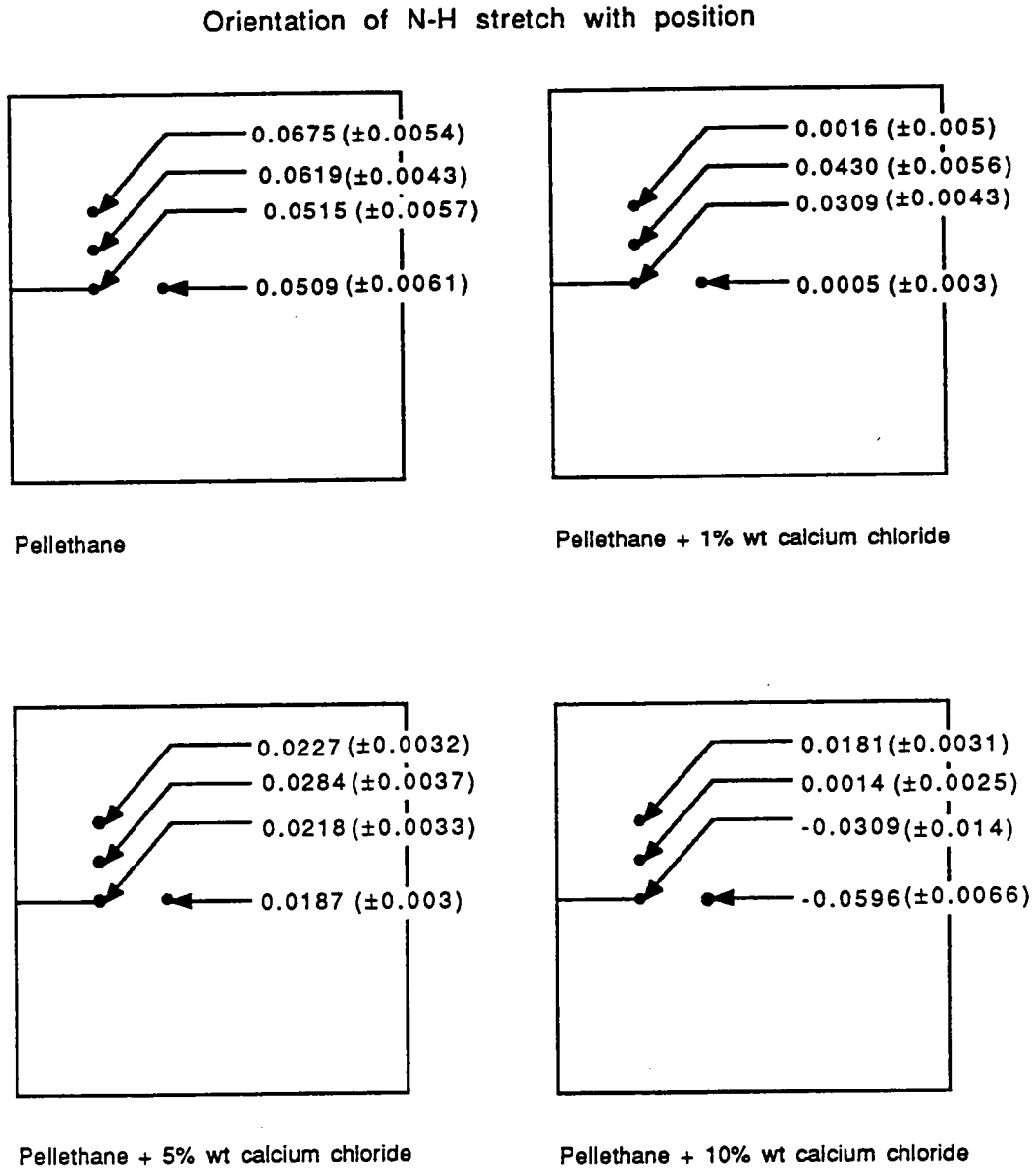

Figure 139: Crack tip N-H orientation maps of Pellethane for various calcium chloride concentrations.

Orientation of C=O stretch with position

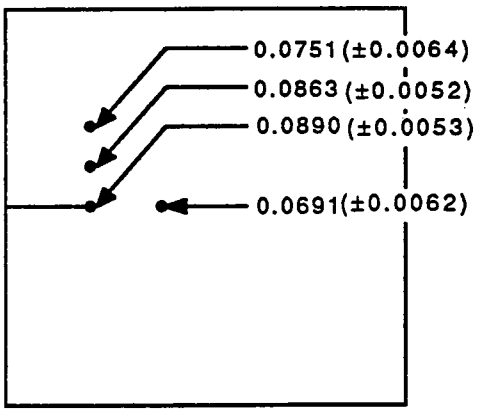

Pellethane

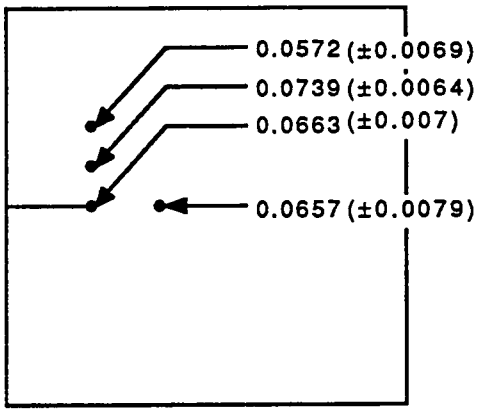

Pellethane + 1% wt calcium chloride

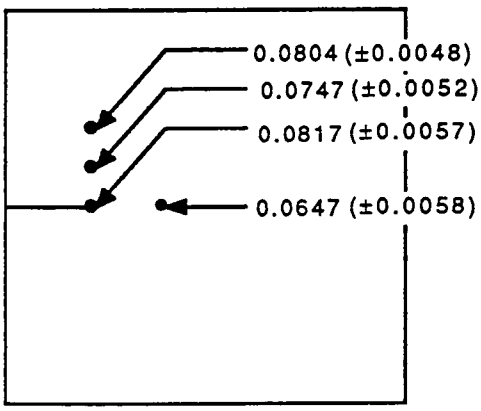

Pellethane + 5% wt calcium chloride

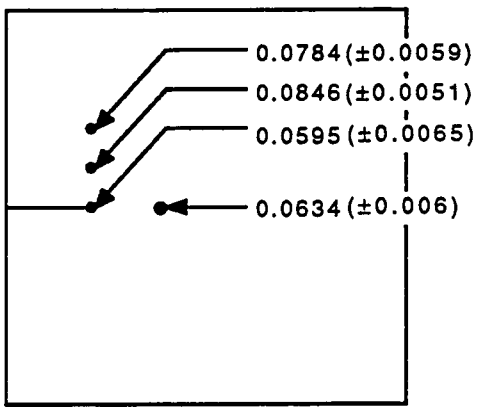

Pellethane + 10% wt calcium chloride

Figure 140: Crack tip C=O orientation maps of Pellethane for various calcium chloride concentrations.

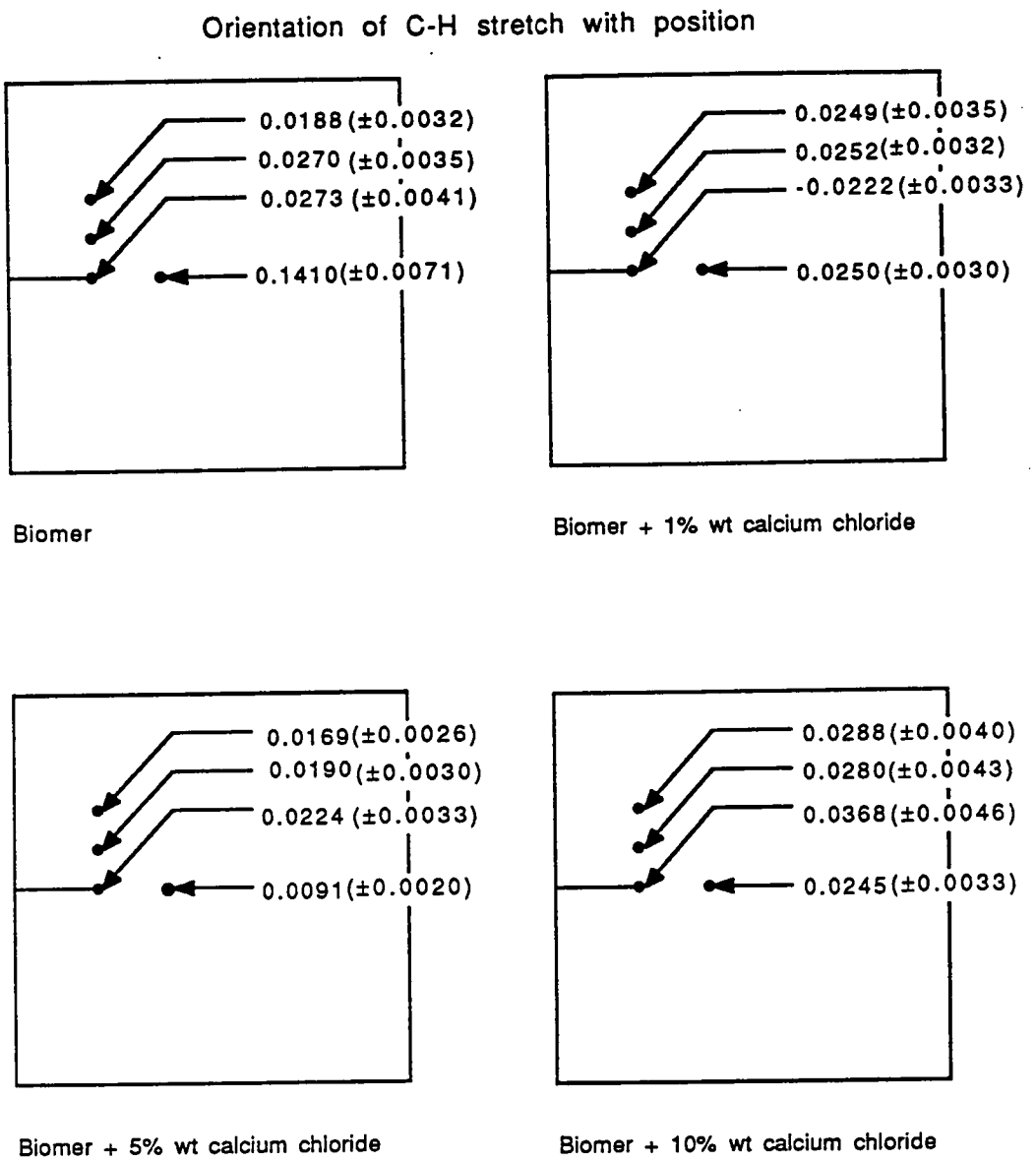

Figure 141: Crack tip C-H orientation maps of Biomer for various calcium chloride concentrations.

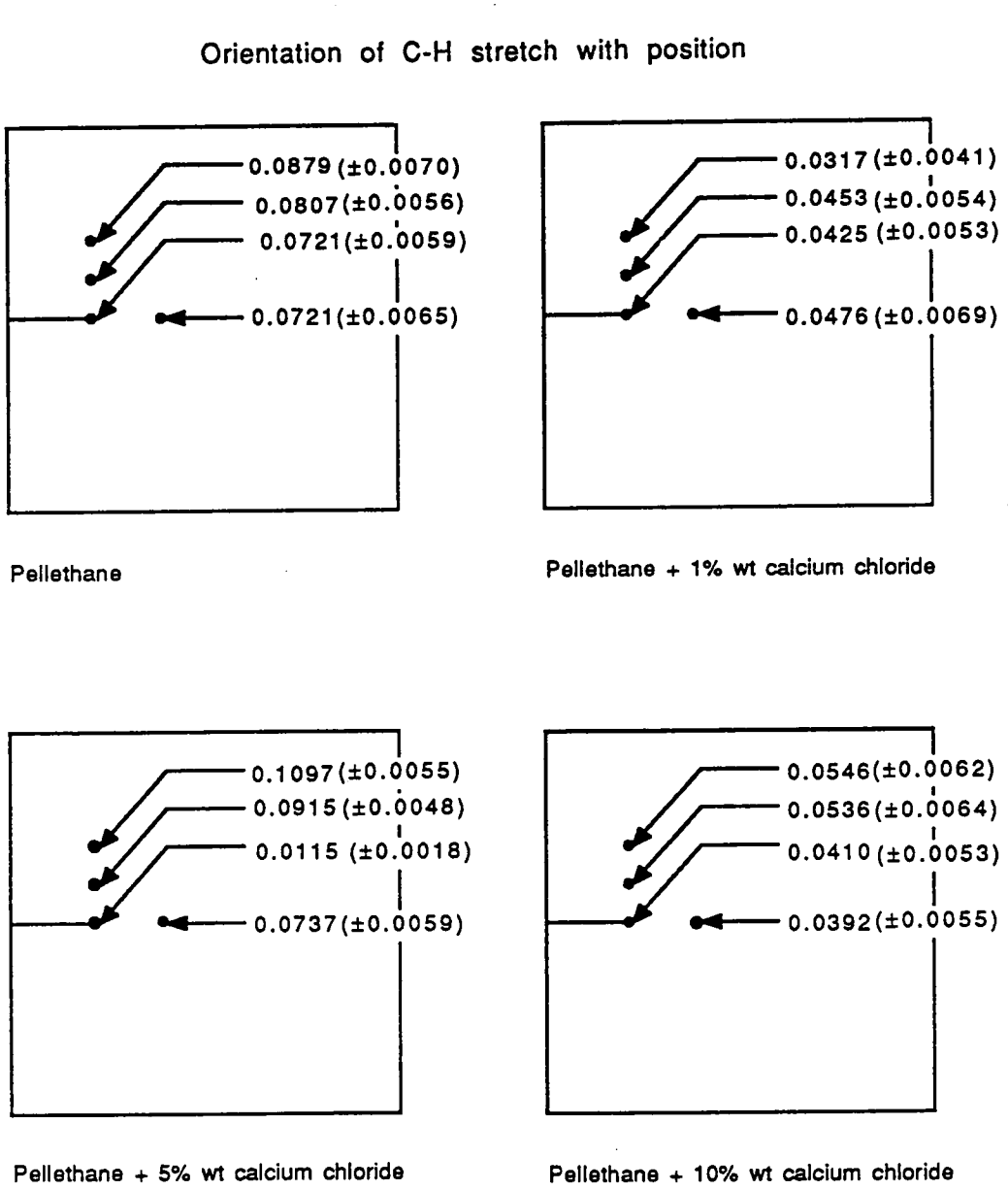

Figure 142: Crack tip C-H orientation maps of Pellethane for various calcium chloride concentrations.

(the crack tip) for C=O. This may be attributed to the $CaCl_2$ binding with N-H to disrupt hydrogen bonding. The interference with the C=O may be due more to steric hindrance effects. This is seen in the 5% $CaCl_2$ case where breakdown of the domain structure becomes significant. For the N-H based orientation function, the minimum value was at position 3 while there was a negligible variation by position for the C=O orientation. At 10% $CaCl_2$, the minimum N-H orientation was at positions 2 and 4 while the minimum C=O orientation was at positions 3 and 4. The low stress values at the crack tip indicate that crazing may have occurred with some elastic recoil from the breaking or sliding actions of the oriented chains. The molecular recoil caused a reduction in measured orientation.

The hard segment maps for Pellethane are shown in Figures 139 and 140, based on the N-H and C=O stretch vibrations. In the case of Pellethane, the domain long axis is the same as the chain axis, therefore, the hard segment orientation is directly related to the stress and strain. For pure Pellethane, the highest stress region was position 3 for N-H and the crack tip for the C=O although these values deviated only slightly from other positions. At 1% $CaCl_2$ the maximum values occurred at position 2 for the N-H orientation and the C=O orientation. The differences were much larger and more

significant for the amine than for the carbonyl vibrations. The low N-H orientation at position 4 (0.0005) did not appear to correlate with the C=O orientation. The difference may be attributed to greater steric restrictions imposed on the N-H group from the adjacent diphenyl methylene group. The maximum stress region is in the HRR fields (at positions 1,2, and 3) for both N-H and C=O for 5% wt. $CaCl_2$. The lower orientation at position 4 indicates that stresses are lower in the plane of the crack and that the crack tip plastic zone is smaller at the 5% concentration. At the 10% concentration, stresses increased away from the plane of the crack; again the phenomena appeared more significant for the N-H rather than the C=O

The soft segment orientation was examined with variation in position for Biomer in Figure 141. For pure Biomer, the high stress region was at position 4 ahead of the crack tip. Upon the addition of 1% $CaCl_2$, the orientation values were not significantly different with position. (The low crack tip value was due to the recoil or broken chains or domain structure). This sudden change is a result of the salt saturation of the matrix at 1% $CaCl_2$. At 5% and 10% concentrations, the expected orientation effects returned to the crack tip (position 1), as the plasticization of the cross links allows the crack tip soft segments to deform plastically.

The Pellethane soft segment orientation is mapped in Figure 142. Pure Pellethane has a soft segment orientation distribution which is similar to the hard segment distribution with the higher orientations away from the crack plane. The addition of 1% $CaCl_2$ caused the soft segment orientation to increase with position away from the crack plane. This deviated from the hard segment behavior which showed lower orientations in the crack plane. At 5% $CaCl_2$, the breakdown of the domains begins to return the soft segments to higher orientations with some recoil of soft segments occurring at the crack tip. This was in spite of the fact that the hard segment orientation was maintained. At 10% $CaCl_2$, the soft segment returns to an orientation distribution similar to pure Pellethane with the large orientation changes having occurred in the N-H map.

Although the orientation maps are quite variable in behavior, some conclusions can be drawn. As critical conditions are approached, molecular orientation is not necessarily the greatest in the highly nonlinear zone ahead of the crack tip. Higher orientations have been detected in the high stress HRR fields perpendicular to the crack plane. The craze zone orientation depends on material structure (Biomer versus Pellethane), calcium chloride concentration, and the mechanical test conditions. It may also be observed that the differences

in orientation of the domain and matrix along the draw axis indicate that each segment is absorbing different levels of strain energy based on the relative segment flexibility (hard versus soft) and intermolecular forces present.

Crack propagation may occur at relatively low levels of HRR crack tip orientation; this will be determined by the loading conditions, the initial crack length, the sample thickness and geometry. These conditions are the same which govern the stress and strain singularities discussed in sections 2.4.1 and 2.4.2.

5.4. Summary of Polyurethane-Calcium Chloride Blend Studies

By varying the concentrations of $CaCl_2$ in Biomer and Pellethane, a model of the degradative effects of calcium salts on these materials has been achieved. At relatively low concentrations of salt, disruption of the rubber elastic network has led to significant differences in the tensile mechanical properties. It is believed that the physiologically low levels of calcification in these blends has demonstrated that degradation takes place in the polyether segment initially and in the urethane segments over the long term, particularly in dynamically loaded systems. If the matrix of polyether is saturated beyond its ability to bind the calcium salts, there is a

disruption of the physical cross linking (hydrogen bonding) of the domains.

The changes in intermolecular interactions translates into changes in the tensile, fracture and orientation properties of each polyurethane. The data presented gives an indication of the relative degrees of degradation that are encountered in the study of polyurethane calcification. This information can be used to set criteria for acceptable levels of calcification before mechanical properties are compromised.

5.5. Polyurethane Uptake of $CaCl_2$

After 30 days in a physiological concentration of $CaCl_2$(aq.), property changes were observed in Biomer and Pellethane. Because this was a diffusion and surface type experiment, large scale calcium deposition was not anticipated. It is believed that most of the salt deposits formed on the surface because of the tendency of polyether segments to aggregate on the surface. The salt deposits formed during the drying process as chloride ions re-associated with the bound calcium to form $CaCl_2$. During the thirty day process, the Ca^{++} ions had an opportunity to diffuse into the bulk and form salts upon drying as well.

The tensile data for the Biomer uptake indicated much lower stresses and shorter strains at break than for the Biomer control. The normalized strain energies to

failure, $\mathcal{J}$, fell by about a factor of 3 for all crack lengths as seen in Figure 143. This is indicative of a large scale binding of $CaCl_2$ by the soft segments.

For the Pellethane uptake study, the control sample unexpectedly appeared to have a greater loss in fracture properties than the calcified sample, as shown in Figure 144. Pellethane may have been more susceptible to swelling by water; the calium deposits may, therefore, be acting to toughen the swollen sample by binding adjacent polyethers. Upon removal of water from the control sample, the swelling effects persisted. The $\mathcal{J}$ values for the calcified samples increased in accordance with a 1% $CaCl_2$ blend. That is, significant polyether binding of the salt has occurred which reduces the ability of the soft segments to disentangle. The low concentration did not lead to disruption of the domain structure however.

The tensile orientation behavior of Biomer after calcium salt uptake confirmed the low level calcification hypothesis. Although much lower levels of stress were achieved, increased hard segment orientations were observed in Figure 145. The hard segment domains did not orient as readily after calcium salt uptake as compared to the control specimens. This behavior may be attributed to $CaCl_2$ which was bound by the Biomer. At low stress levels, most of the strain orientation energy was absorbed in the form of orientation of the soft segment shown in

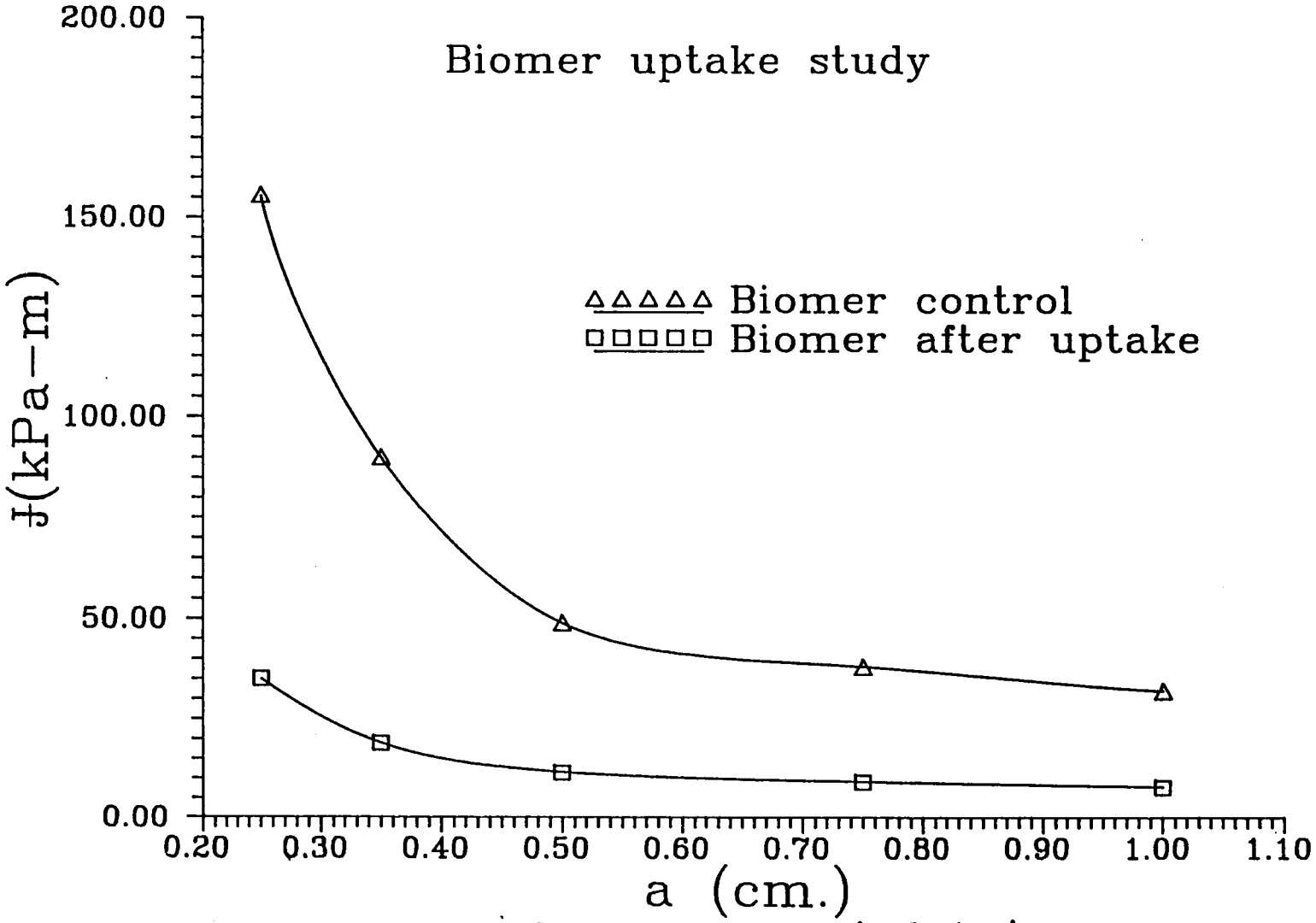

Figure 143: Comparison plot of normalized strain energy to failure versus initial crack length for pure Biomer and the Biomer uptake study.

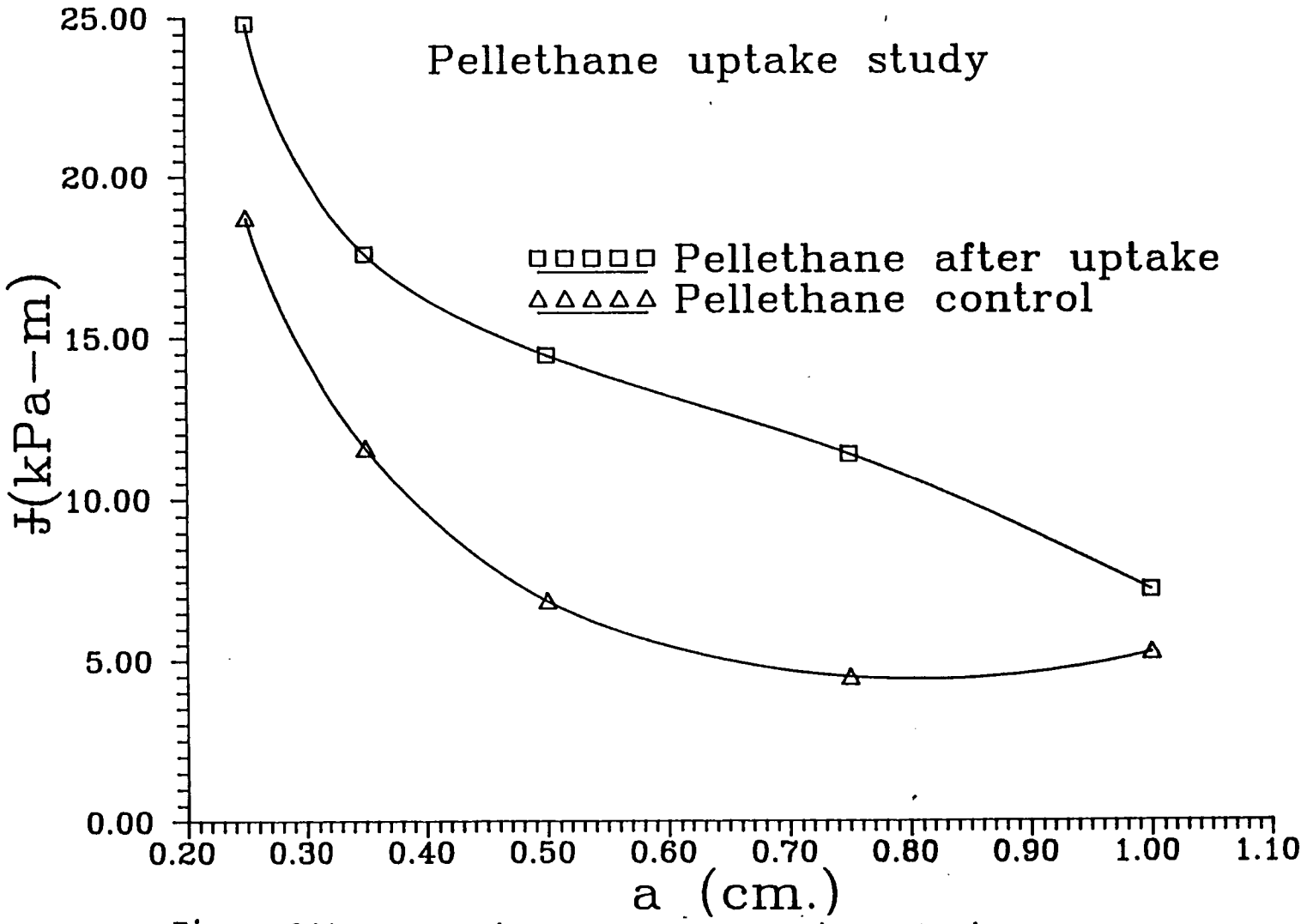

Figure 144: Comparison plot of normalized strain energy to failure versus initial crack length for pure Pellethane and the Pellethane uptake study.

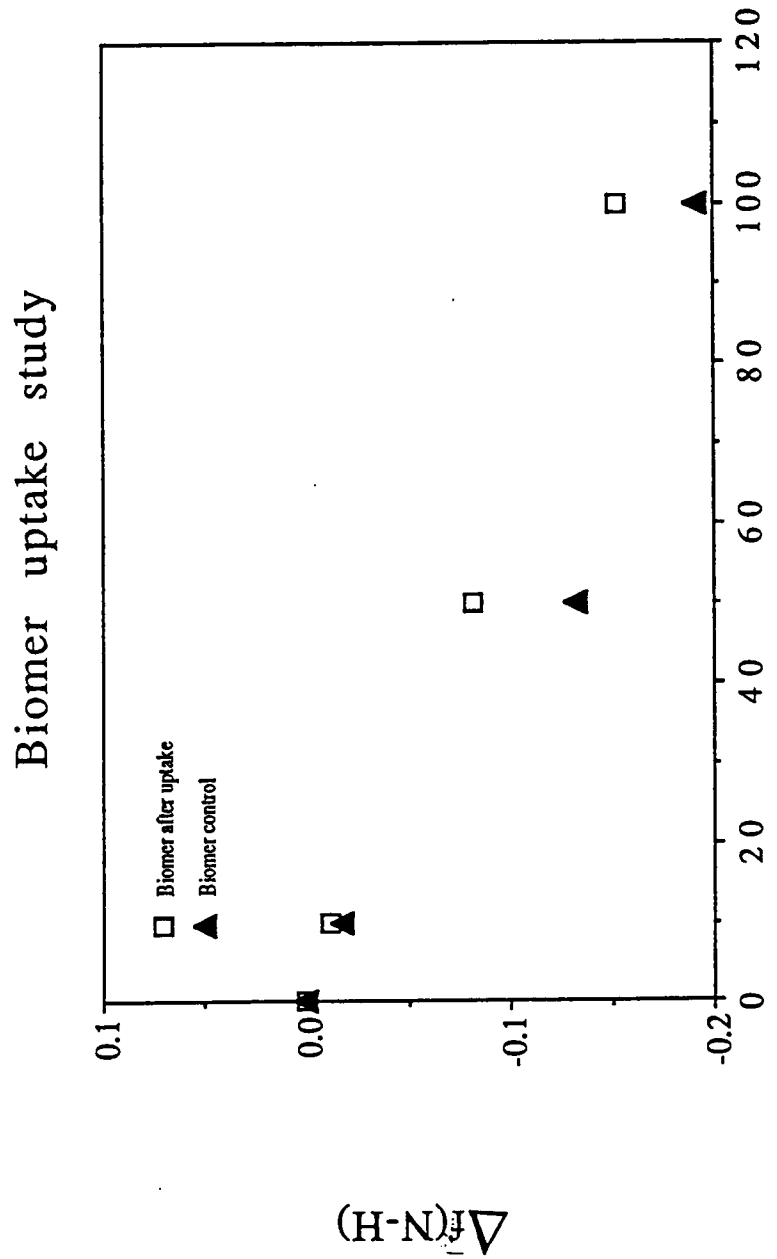

Figure 145: Change in N-H orientation function with strain for Biomer and the Biomer uptake study.

Figure 146. $CaCl_2$ causes a reduction in entropy by restricting the polyether. The hard segment orientation is less negative, indicating that the salt binding to the polyether was slightly restricting the domain orientation.

A similar mechanical orientation behavior was observed for Pellethane in Figures 147 and 148. Marginal changes in hard segment orientation were observed in Figure 147. In Figure 148, however, the soft segment orientation appeared to have large orientation differences. For the uptake sample, at low strains, the soft segment orientation increased suddenly, after which it increased more steadily for increasing strains. Because crosslinking in Pellethane is less extensive and not as tightly binding, a sudden increase in orientation at low strains can be attributed to small conformational changes which have an effect on the measured orientation.

There was a reduction in maximum stress values with strain after the uptake from solution for Biomer, compared to the control sample. This is shown in Figures 149. Chelation of the calcium by the polyether segments at concentrations high enough to disrupt orientation of hard segments and soft segments without disrupting hydrogen bonding of the domains may account for the changes in mechanical behavior. In Figure 150, the increase of maximum stress values of calcified Pellethane compared to

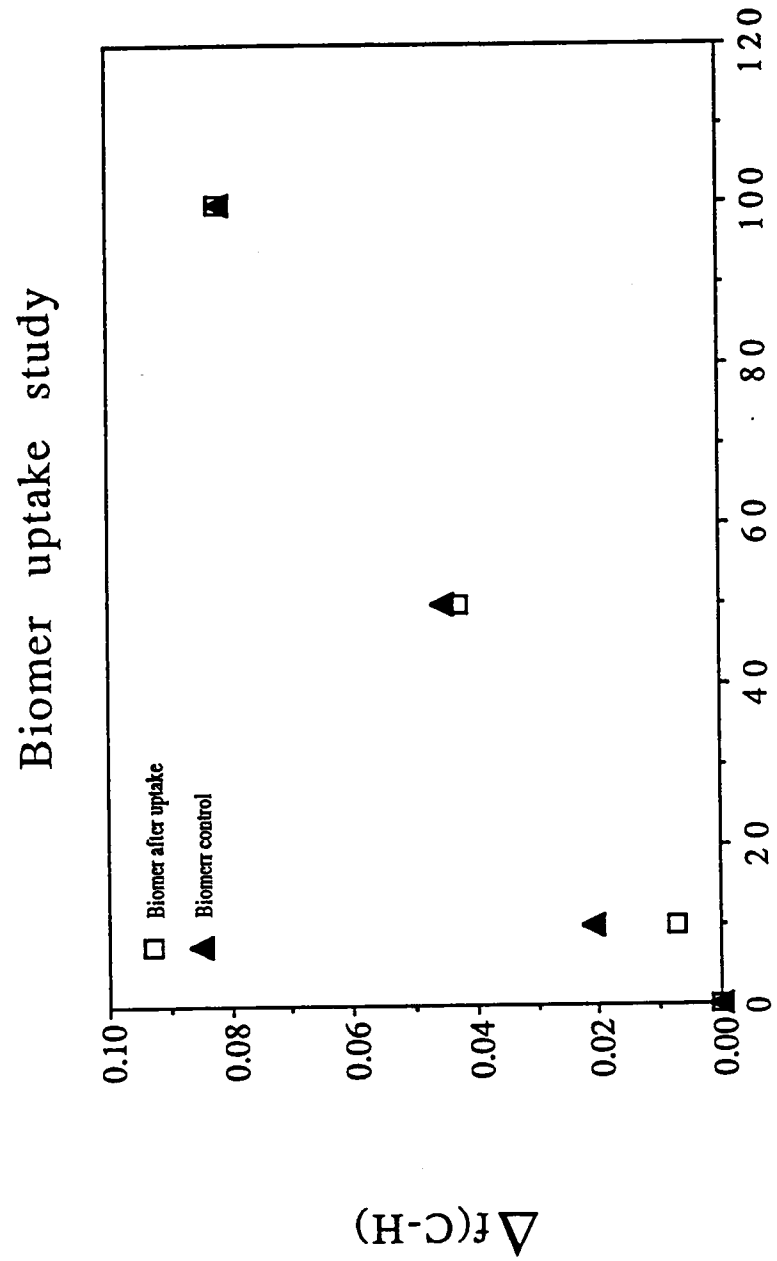

Figure 146: Change in C-H orientation function with strain for Biomer and the Biomer uptake study.

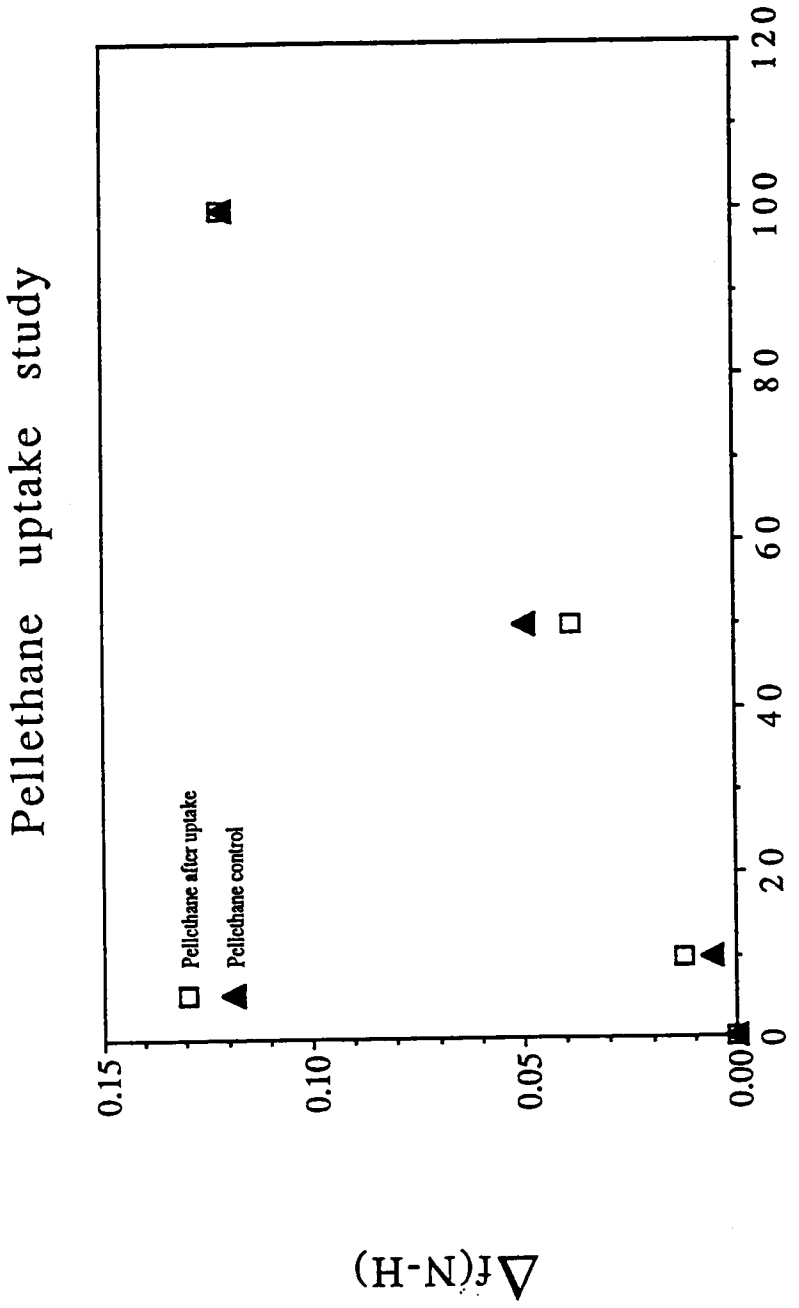

Figure 147: Change in N-H orientation function with strain for Pellethane and the Pellethane uptake study.

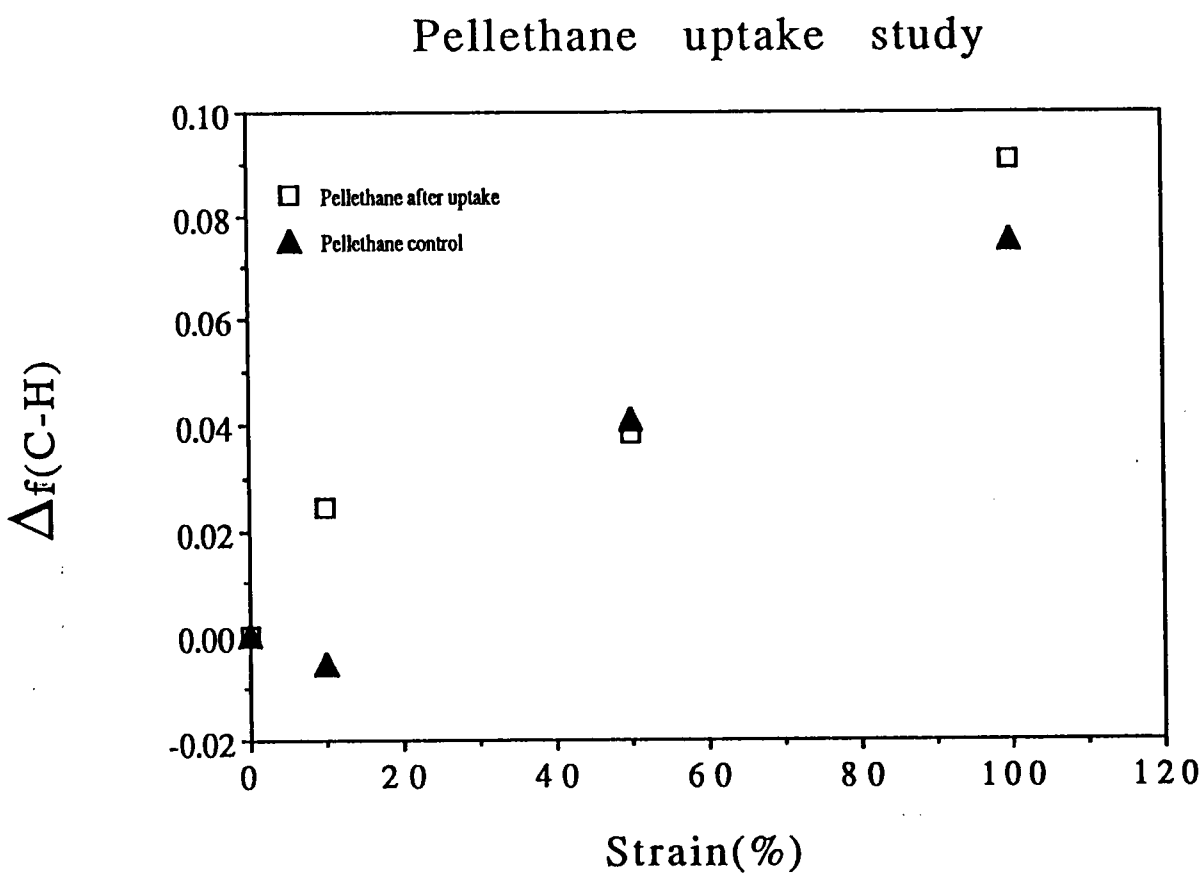

Figure 148: Change in C-H orientation function with strain for Pellethane and the Pellethane uptake study.

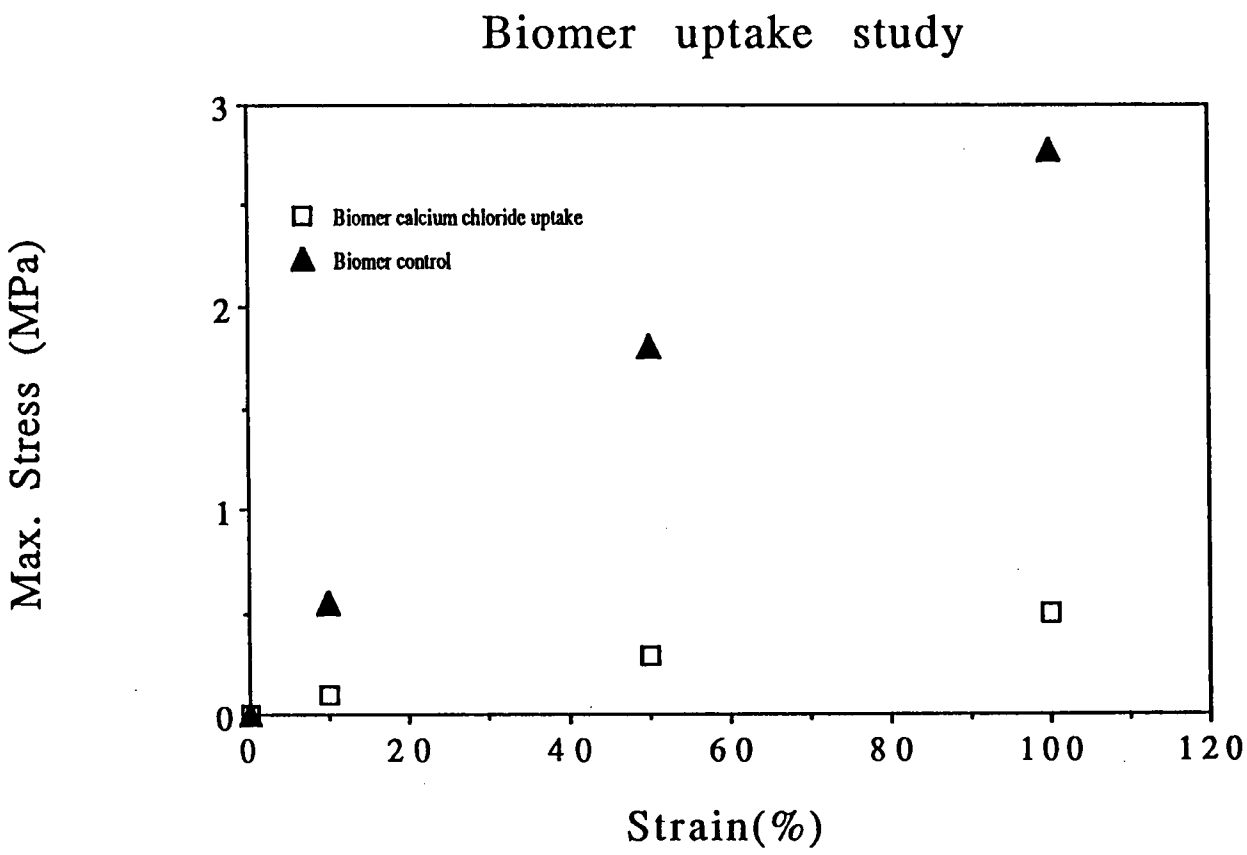

Figure 149: Maximum stress at fixed strain for Biomer and the Biomer uptake study.

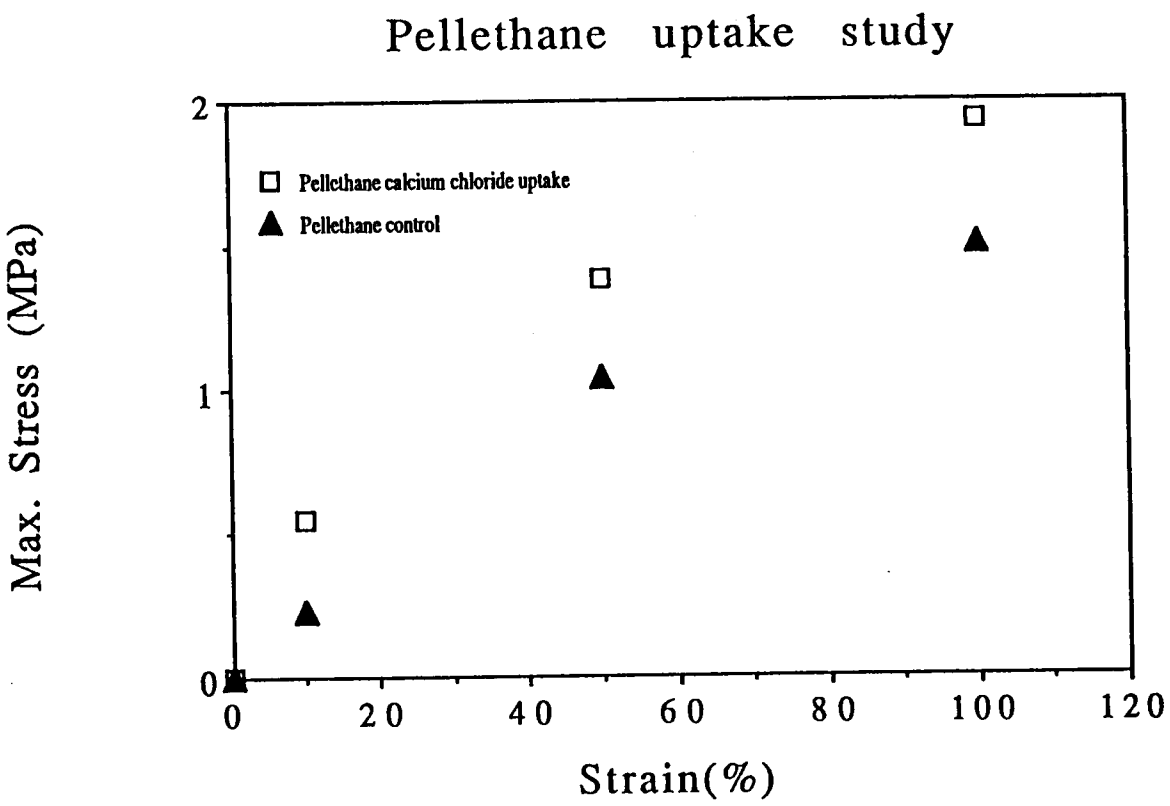

Figure 150: Maximum stress at fixed strain for Pellethane and the Pellethane uptake study.

the control sample is consistent with the effect observed in the fracture study.

The crack tip orientation maps of the control Biomer hard segments show that high tensile stresses were in the HRR fields as indicated by a decreasing N-H orientation. The data for the N-H stretch based orientation and the C=O stretch orientation are shown in Figures 151 and 152. After treatment in calcium chloride solution, the orientation distribution appears to have shifted toward equal crack tip plane orientation as the lower stresses were not able to produce large orientation differences with position. The carbonyl orientation, shown in Figure 152, appears to have greater orientation values away from the crack tip, probably due to the negative orientation behavior of the hard segments with increasing tensile stress.

Similar hard segment results were obtained for Pellethane as lower stresses in the calcium chloride uptake study resulted in a lower disparity in orientation values surrounding the crack tip. This was determined from the N-H data shown in Figure 153. The C=O orientation, shown in Figure 154, appears to indicate higher values at position 4 (in the crack plane) after uptake. Although the cause of the discrepency is not clear, the high orientation may be a combined effect of the interface of the domain and matrix since the C=O may

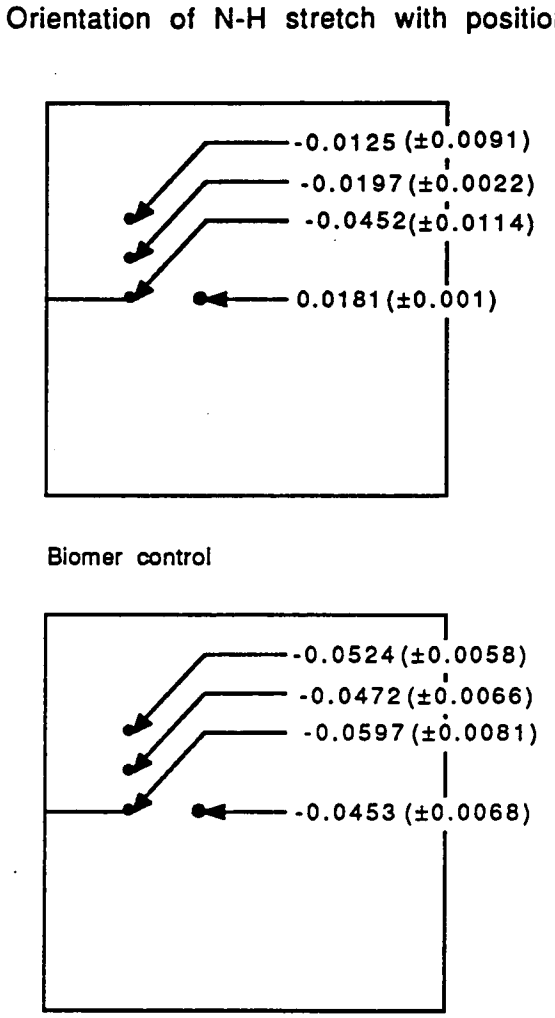

Figure 151: Crack tip N-H orientation maps for Biomer and the Biomer uptake study.

Orientation of C=O stretch with position

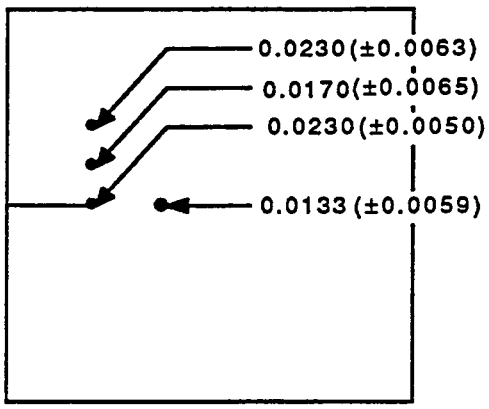

Biomer control

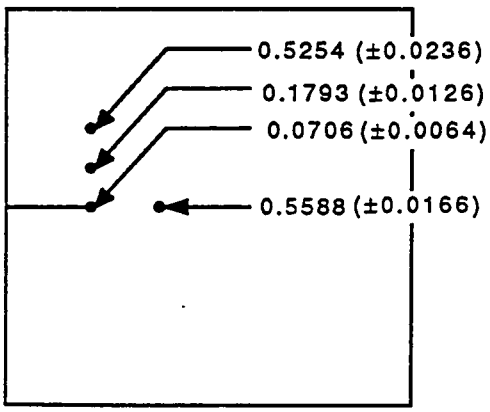

Biomer after 30 days in calcium chloride solution

Figure 152: Crack tip C=O orientation maps for Biomer and the Biomer uptake study.

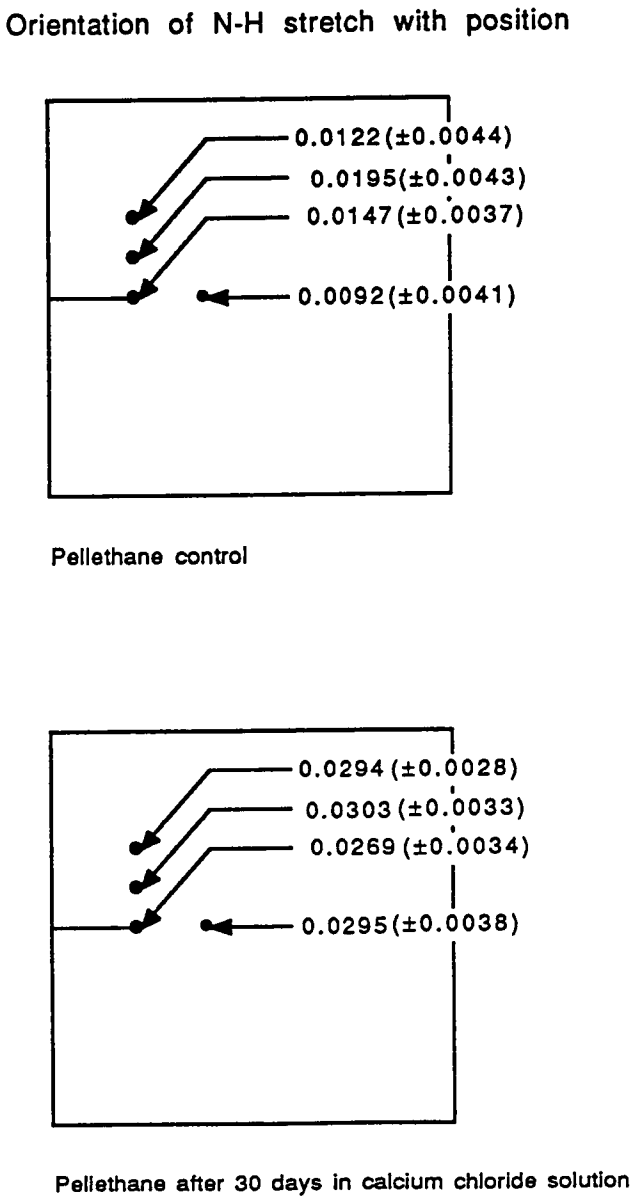

Figure 153: Crack tip N-H orientation maps for Pellethane and the Pellethane uptake study.

Orientation of C=O stretch with position

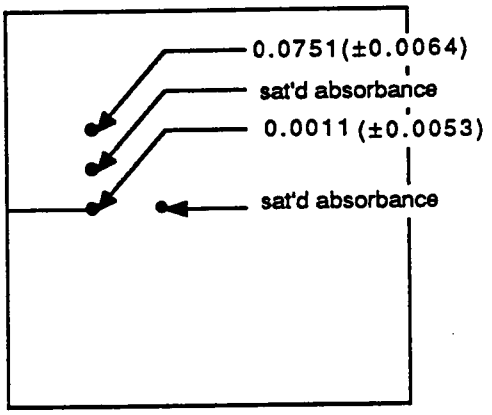

Pellethane control

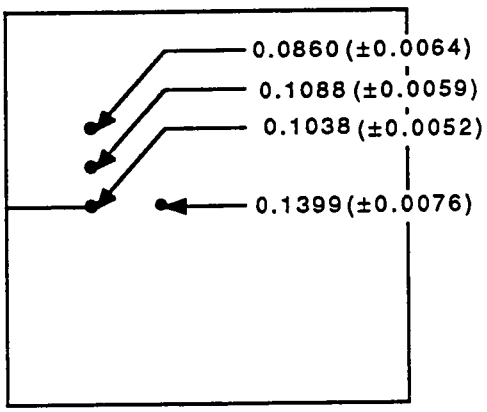

Pellethane after 30 days in calcium chloride solution

Figure 154: Crack tip C=O orientation maps for Pellethane and the Pellethane uptake study.

not be hydrogen bonded although it is chemically part of the hard segment.

The soft segment of Biomer after calcium chloride uptake showed a similar behavior to the hard segment. Crack tip orientation measurements, shown in Figure 155, had different distributions in the HRR fields in the control sample and after calcium chloride uptake. In the calcified sample in the crack plane at position 4, there was a reduction in orientation ahead of the crack tip which may have been related to the overall reduction in stress which reduced the zone of plastic deformation.

The HRR orientations fields were not significantly different after calcium chloride uptake for the Pellethane soft segments. This is shown in Figure 156. This is in contrast to the control Pellethane which showed favorable orientations in HRR position 2. Again, the reduction in overall stress which resulted from the calcification may have also reduced orientation stresses as well.

In the case of Pellethane and Biomer the formation of complexes with the flexible soft segment was in agreement with earlier studies.[8] In both cases, saturation of the polyether segment by calcium salts caused the mechanical properties to pass through maxima; the additional calcium salts caused plasticization.

Orientation of C-H stretch with position

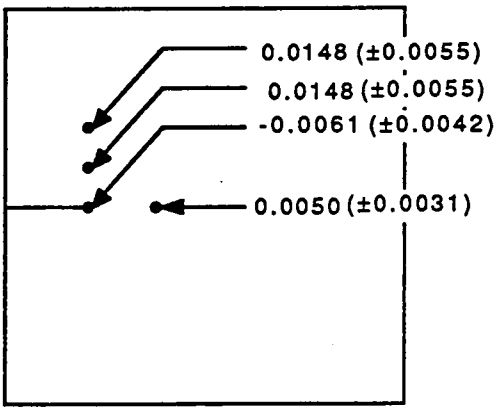

Biomer control

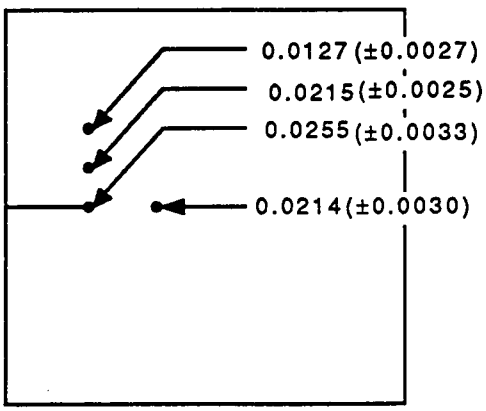

Biomer after 30 days in calcium chloride solution

Figure 155: Crack tip C-H orientation maps for Biomer and the Biomer uptake study.

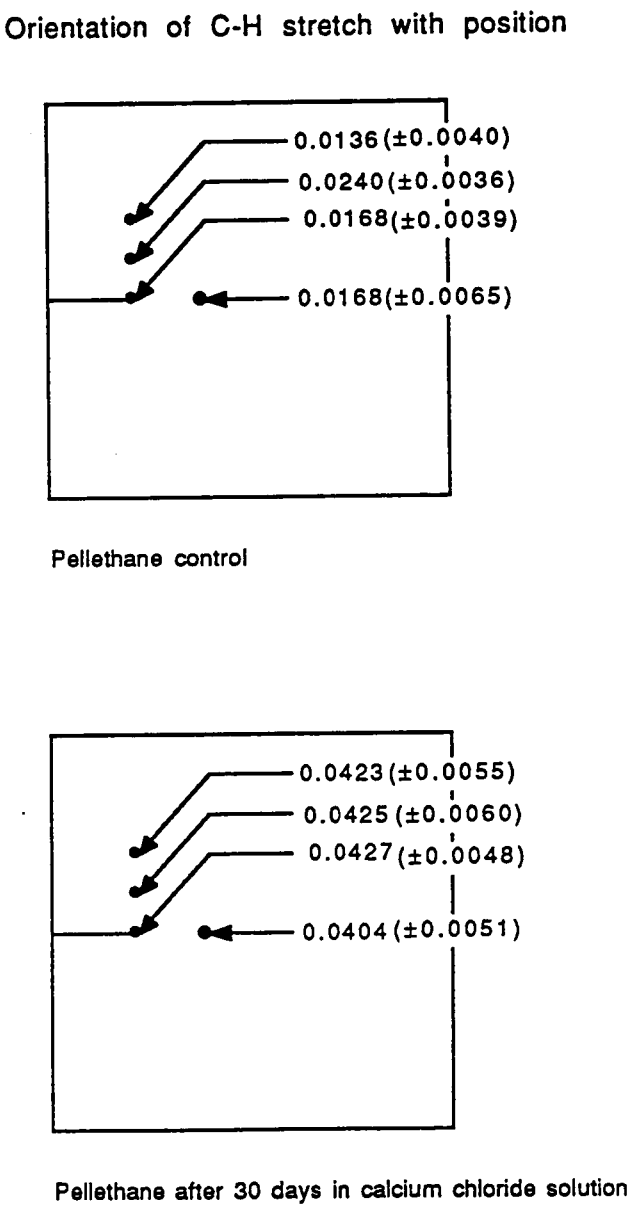

Figure 156: Crack tip C-H orientation maps for Pellethane and the Pellethane uptake study.

6. CONCLUSIONS

Mechanical properties of biomedical polyurethanes were explored in this study as they relate to the presence of calcium chloride. Because mechanical properties are ultimately determined by the polymer's chemical and microstructure, the conclusions from this study reflect an attempt to understand how calcium chloride interacts with the hard and soft segments of Biomer and Pellethane.

(1) Blending calcium chloride with the polyurethanes in known concentrations caused changes in fracture toughness and stress distributions surrounding cracks. The effects were attributed to salt saturation of the soft segment matrix with calcium chloride followed by disruption of the domain structure at higher salt concentrations. The disruption of the domain structure was shown by FTIR studies of the free and hydrogen bonded N-H stretch. The disruption of the microstructure became apparent during tensile mechanical-orientation testing. The presence of the salt disrupted normal sliding and disentanglement of the matrix, causing changes in rubber elastic properties or strain induced orientation. The disruption of the domains caused a loss of the physical crosslinking which led to more sliding prior to fracture. The molecular sliding motion, however, absorbed more tensile strain energy, slowing crack propagation.

(2) The uptake study of calcium chloride from a physiological aqueous solution showed that low concentrations of calcium chloride may cause significant reductions in mechanical properties. Because no evidence of domain disruption was observed in the uptake study, the changes in mechanical properties were mediated by the soft segment matrix. This involved chelation of the calcium chloride to surface polyether segments.

(3) Because of chemical structure differences between Biomer and Pellethane, their domain structure was found to be quite different in mechanical strain orientation studies. The additional urea segment in Biomer allows for a higher degree of hydrogen bonding. The domains, therefore, tend to have their long axes in a direction perpendicular to the chain axes. Upon drawing, the domains orient positively in the draw direction, causing the chain axes to display a negative orientation. Pellethane domains have their long axes in the chain direction, causing the chain axes to display normal positive orientation upon drawing.

(4) Fourier transform infrared dichroism techniques were successfully applied to mechanical orientation studies. Simultaneous measurements of stress, strain and orientation were correlated to elucidate microstructural changes with tensile and fracture mechanical properties.

(5) FTIR dichroism measurements of crack tip orientation can be a useful tool for identifying stress intensification. The technique is useful to identify microstructural, stress induced changes which lead to changes in ultimate properties.

This study has elucidated one of the problems in degradation of polymeric implants. Because significant calcification was shown to occur in as few as 30 days of exposure to a less degradative environment, one must question the current methods of long term implant materials selection. This is not to say that polyurethanes are to be completely dismissed as an implant material; polyurethanes are still the best biocompatible materials for cardiovascular applications. It is clear, however, that selection must account for a polyether segment which resists binding by metal ions. This may be accomplished through the attachment of pendent groups to the polyether chain, however, the changes in resulting mechanical properties may require adjustments to the molecular weight.

It may be necessary to accept the fact that blood components will penetrate the soft segment matrix. If the polyether segment persists in binding metal ions, it may be necessary to more closely examine the structure of the domain, matrix, and the interface. The domain disruption may be reduced by enhancing crystallinity of the domains,

possibly through annealing as was seen by Rek and Govorcin.[60] Hydrogen bonding may be enhanced by selection of urethane-urea segments which will bring the hydrogen bonding groups into crystallographic register. In either case, a reduction in free volume will prevent blood components from reducing the elasticity of the polyurethane through domain disruption.

Each of these proposed variations must be considered carefully. It will be necessary to maintain mechanical properties through fracture mechanics testing. Variations in chemical and microstructure may lead to adverse immune, toxic, and carcinogenic effects which must be prevented. If these factors continue to be favorable for the new polyurethanes, however, there will be dramatic improvements in the longevity of polyurethanes in the human body.

7. FURTHER WORK

The results of this research have laid the groundwork for a number of future pursuits in the fields of biomedical polymers, fracture mechanics, and mechanical properties of polymers.

Several important questions remained beyond the scope of this research in the field of biomedical polymers, specifically in regard to calcification. Having an understanding of the interaction of calcium salts with polyurethanes, there remains a need to understand all the biological causes of calcification of synthetic polymers in the body. At the molecular level, future work may center on the effect of molecular orientation, stress and strain to determine how it is sensed by the body's immune system. The function and geometry of an implant under cyclic loading must be taken into account as the elastomer undergoes dynamic changes in molecular structure. Based on this knowledge, polymer chemical and physical properties could be specified and implemented by precise control of the processing. It may then be possible to prevent calcification in soft tissue implant materials and enhance calcification in hard tissues such as bone.

In the field of fracture mechanics of elastomers, several future goals are possible. The high elastic strain energy absorbed by the material in the case of

short cracks is currently a subject of ongoing research. Corrections for the deformation prior to fracture would allow engineers to make fair comparisons of polymer fracture toughness to other materials based on a J_{Ic} criteria. They could be calculated directly from non-linear elastic finite element methods.

Another goal in fracture mechanics may be to understand the effects of processing, fatigue, and thermal history on fracture toughness. It is important to develop reliable test methods for quantifying the contribution of each of these factors as they affect toughness. Although there is an extensive body of data for metals in each of these areas, there is a great need for developing a similar data base for polymers with an understanding of polymer science as well as engineering. This is particularly important as polymers replace metals in many engineering applications.

For the study of polymer mechanical properties, there are several directions in which this research may be extended. The study of stress-strain-orientation behavior should be persued with other polymers, processing conditions, and testing conditions (such as temperature, strain rate, and thermal history). While varying polymers and processing conditions can be addressed immediately, varying the test conditions would require an improvement on the current instrumentation.

Dynamic studies of molecular orientation during the fracture process will be possible with the advent of higher rates of FTIR data acquisition in the near future, including simultaneous measurements of polarized spectra. Information regarding real time crack tip orientation measurements will be useful in developing polymer structures which have greater fracture toughness.

LIST OF REFERENCES

LIST OF REFERENCES

1. Knutson, K.; Lyman, D.J. In Biomaterials: Interfacial Phenomena and Applications; S.L. Cooper; N.A. Peppas, Eds., Advances in Chemistry Series, No. 199; American Chemical Society: Washington, DC, 1982.

2. Szycher, M.; Poirer, V.L.; Dempsey, D.J. J. Elast. Plast. **1983**, 15, 81.

3. Hung, G.W.C.; Nunez, L.J.; Autian, J. J. Pharm. Sci. **1975**, 64, 1493.

4. Graham, S.W.; Hercules, D.M. J. Biomed. Mat. Res. **1981**, 15, 465.

5. Coleman, D.; Meuzelaar, H.L.C.; Kessler, T.R.; McClennen, W.H.; Richards, J.M.; Gregonis, D.E. J. Biomed. Mat. Res. **1986**, 20, 417.

6. Duncan, E. Biomaterials Forum **1990**, 12, (July-August), 4.

7. Stoppert, J.R. Biomaterials Forum **1990**, 12, (July-August), 4.

8. Warner, C.A.; Wong, R.P.; Benson, R.S. Abstract of Papers, 196th National Meeting of the American Chemical Society, Los Angeles, CA; American Chemical Society: Washington, DC 1988; PMSE 59.

9. Warner, C.A. PhD Dissertation Proposal, University of Utah, unpublished.

10. Harasaki, H. Abstract of Papers, 13th Annual Meeting of the Society for Biomaterials, New York, NY; The Society for Biomaterials: Birmingham, AL, 1987; page 280.

11. Hamon, R.F.; Khan, A.S.; Chow, A. Talenta **1982**, 29, 313.

12. Benson, R.; Yoshikawa, S.; Knutson, K.; Lyman, D.J. In Biomaterials: Interfacial Phenomena and Applications; S.L. Cooper; N.A. Peppas, Eds., Advances in Chemistry Series, No. 199; American Chemical Society: Washington, DC, 1982.

13. Lyman, D.J. J. Polym. Sci. **1960**, 45, 49.

14. Benson, R.S.; Wong, R.P. Abstract of Papers, 13th Annual Meeting of the Society for Biomaterials, New York, NY; The Society for Biomaterials: Birmingham, AL, 1987; page 121.

15. Golomb, G.; Wagner, D. Abstract of Papers, 16th Annual Meeting of the Society for Biomaterials, Charleston, SC; The Society for Biomaterials: Birmingham, AL, 1990; page 129.

16. Lo, H.B.; Herold, M.; Reul, H.; Muckter, H.; Taguchi, K.; Surmann, M.; Hildinger, K.H.; Lambertz, H.; De Haan, H.; Handt, S.; Hollweg, G.; Messmer, B.J.; Rau, G. Trans. Am. Soc. Artif. Intern. Organs **1988**, 35, 839.

17. Paris, P.C. Fracture Mechanics in the Elastic-Plastic Regime, Flaw Growth and Fracture, ASTM STP 631, American Society for Testing and Materials, Philadelphia: 1977, pp. 3-27.

18. Rice, J.R.; Rosengren, G.F. J. Mech. Phys. Solids **1968**, 16, 1.

19. Hutchinson, J.W. J. Mech. Phys. Solids **1968**, 16, 13.

20. Basic and Clinical Immunology, 5th ed.; Stites, D.P.; Stobo, J.D.; Fudenberg, H.H.; Wells, J.V. Eds.; Lange Medical Publications; Los Altos, CA, 1984.

21. Park, J.B. Biomaterials: An Introduction; Plenum: New York, 1979; Chapter 8.

22. Stewart, S.F.C. PhD. Dissertation, University of Utah, 1987.

23. Born, L.; Hespe, H.; Crone, J.; Wolf, K.H. Colloid Polym. Sci. **1982**, 260, 819.

24. Briber, R.M.; Thomas, E.L. J. Macromol. Sci., Phys. **1983**, B22(4), 509.

25. Fridman, I.D.; Thomas, E.L. Polymer **1980**, 21, 388.

26. Chau, K.W.; Geil, P.H. Polymer **1985**, 26, 490.

27. Blackwell, J.; Gardner, K.H. Polymer **1979**, 20, 13.

28. Blackwell, J.; Lee, C.D. J. Polym. Sci., Polym. Phys. Ed. **1984**, 22, 759.

29. Cooper, S.L.; Tobolsky, A.V. J. Appl. Polym. Sci. **1966**, 10, 1837.

30. Senich, G.A.; MacKnight, W.J. Macromolecules **1980**, 13, 106.

31. Seymour, R.W.; Cooper, S.L. Macromolecules **1973**, 6, 48.

32. Wilkes, C.E.; Yusek, C.S. J. Macromol. Sci., Phys. **1973**, B7(1), 157.

33. Blackwell, J.; Nagarajan, M.R. Polymer **1981**, 22, 202.

34. Chang, A.L.; Briber, R.M.; Thomas, E.L.; Zdrahala, R.J.; Critchfield, F.E. Polymer **1982**, 23, 1060.

35. Miller, J.A.; Lin, S.B.; Hwang, K.K.S.; Wu, K.S.; Gibson, P.E.; Cooper, S.L. Macromolecules **1985**, 18, 32.

36. Xu, M.; MacKnight, W.J.; Chen, C.H.Y.; Thomas, E.L. Polymer **1983**, 24, 1327.

37. Blackwell, J.; Nagarajan, M.R.; Hoitink, T.B. Polymer **1983**, 24, 1327.

38. Blackwell, J.; Ross, M. J. Polym. Sci., Polym. Lett. Ed. **1979**, 17, 447.

39. Bonart, R.; Morbitzer, L.; Hentze, G. J. Macromol. Sci., Phys. **1969**, B3(2), 337.

40. Bonart, R.; Morbitzer, L.; Muller, E.H. J. Macromol. Sci., Phys. **1974**, B9(3), 447.

41. Born, L.; Crone, J.; Hespe, H.; Muller, E.H.; Wolf, K.H. J. Polym. Sci., Polym. Phys. Ed. **1984**, 22, 163.

42. Multiphase Polymers; Cooper, S.L.; Estes, G.M., Eds. Advances in Chemistry Series 176; American Chemical Society: Washington, D.C., 1981.

43. Urethane Chemistry and Applications; Edwards, K.N. Ed.; ACS Symposium Series 172; American Chemical Society: Washington, D.C., 1981.

44. Hwang, K.K.S.; Hemker, D.J.; Cooper, S.L. Macromolecules **1984**, 17, 307.

45. Knutson, K. PhD. Dissertation, University of Utah, 1981.

46. Koutsky, J.A.; Hien, N.V.; Cooper, S.L. J. Polym. Sci., Polym. Lett. Ed. **1970**, 8, 353.

47. Onder, K.; Peters, R.H.; Spark, L.C. Polymer **1977**, 18, 155.

48. Ophir, Z.; Wilkes, G.L. J. Polym. Sci., Polym. Phys. Ed. **1980**, 18, 1469.

49. Schneider, N.S.; Desper, C.R.; Illinger, J.L.; King, A.O.; Barr, D. J. Macromol. Sci., Phys. **1975**, B11(4), 527.

50. Wang. C.B.; Cooper, S.L. Macromolecules **1983**, 16, 775.

51. MacKnight, W.J.; Yang, M. J. Polym. Sci., Polym. Symp. **1973**, 42, 817.

52. Chen, C.H.Y.; Briber, R.M.; Thomas, E.L.; Xu, M.; MacKnight, W.J. Polymer **1983**, 24, 1333.

53. Ishihara, H.; Kimura, I.; Saito, K.; Ono, H.; J. Macromol. Sci., Phys. **1974**, B10(4), 591.

54. Atwood, J.L.; Davies, J.E.D.; MacNicol, D.D. eds. Inclusion Compounds, vol. 2, Academic: London, 1984.

55. Atwood, J.L.; Davies, J.E.D.; MacNicol, D.D. eds. Inclusion Compounds, vol. 3, Academic: London, 1984.

56. Killis, A.; LeNest, J.F.; Gandini, A.; Cheradame, H. J. Polym. Sci. Polym. Phys. Ed. **1981**, 19, 1073.

57. Walsh, D.J.; Higgins, J.S.; Hall, R.H. Polymer **1979**, 20, 951.

58. Dzierza, W. J. Appl. Polym. Sci. **1982**, 27, 1487.

59. Wilkes, G.L.; Dziemianowicz, T.S.; Ophir, Z.H.; Artz, E.; Wildnauer, R. J. Biomed. Mat. Res. **1979**, 13, 189.

60. Rek, V.; Govorcin, E. 33rd IUPAC International Syposium on Macromolecules, MACRO 90, Montreal, 1990, Session 2.1.7.

61. Kambour, R.P. Polymer **1964**, 5, 143.

62. Flory, P.J. Principles of Polymer Chemistry; Cornell University: Ithaca, NY, 1953; Chapter 11.

63. Boyd, R.H. University of Utah, class notes, personal communication, 1984.

64. James, H.M.; Guth, E. J. Chem. Phys. **1943**, 11, 455.

65. Treloar, L.R.G. Trans. Faraday Soc. **1944**, 40, 59.

66. Ward, I.M. Mechanical Properties of Solid Polymers, 2nd ed.; Wiley: Chichester, 1983; Chapter 12.

67. Argon, A.S.; Salama, M.M. Phil. Mag. **1977**, 36, 1217.

68. Donald, A.M.; Kramer, E.J. Phil. Mag. A **1981**, 43, 857.

69. Caspary, R.; Schencko, H. Makromol. Chem. **1981**, 182, 2109.

70. Donald, A.M.; Kramer, E.J. Phil. Mag. A **1981**, 43, 857.

71. Brown, N.; Bhattacharya, S.K. J. Mat. Sci. **1985**, 20, 4553.

72. Bernier, G.A.; Kambour, R.P. Macromolecules **1968**, 1, 393.

73. Andrews, E.H.; Bevan, L. Polymer **1972**, 13, 337.

74. Adamson, A.W. Physical Chemistry of Surfaces, Wiley Interscience: New York, 1960.

75. Inglis, C.E. Proc. Inst. Naval Architects **1960**, 60.

76. Bartenev, G.M.; Zuyev, Y.S. Strength and Failure of Visco-elastic Materials; Pergammon: Oxford, 1968.

77. Orowan, E. Phys. Soc. Rep. Prog. Phys. **1948**, 12, 186.

78. Irwin, G.R. Fracture, Handbuch der Physik VI, Flugge Ed., Springer: Munich , 1958, pp.551-590.

79. Westergaard, H.M. J. Appl. Mech. **1939**, 61, A49.

80. Broek, D. Elementary Engineering Fracture Mechanics, 4th ed.; Martinus Nijhoff: Dordrecht, 1986.

81. Rivlin, R.S.; Thomas, A.G. J. Polym. Sci. **1953**, 10, 291.

82. Andrews, E.H. J. Appl. Phys. **1961**, 32, 542.

83. McClintock, F.A. J. Appl. Mech. **1958**, 25, 582.

84. Andrews, E.H. Proc. Phys. Soc. (London) **1961**, 77, 483.

85. Begley, J.A.; Landes, J.D. Fracture Toughness, ASTM STP 514 **1972**, 1.

86. Landes, J.D.; Begley, J.A. Fracture Toughness, ASTM STP 514 **1972**, 24.

87. Lake, G.J. The Yield, Deformation and Fracture Conference Proceedings, Oxford **1966**, 134.

88. Lindley, P.B. J. Strain Analysis **1972**, 7, 132.

89. Oh, H.L. Mechanics of Crack Growth, ASTM STP 590 **1976**, 104.

90. Wang, N.M. Int. J. Solids. Structures **1973**, 9, 1211.

91. Chang, S. J. Appl. Math. Phys. **1972**, 23, 149.

92. Knowles, J.K.; Sternberg, E. Arch. Rational Mech. Analysis **1972**, 44, 187.

93. Hashemi, S.; Williams, J.G. Polymer **1986**, 27, 384.

94. Hashemi, S.; Williams, J.G. Polym. Sci. Eng. **1986**, 26, 760.

95. Huang, D.D.; Williams, J.G. J. Mat. Sci. **1987**, 22, 2503.

96. Moskala, E.J.; Tant, M.R. Abstract of Papers, National Meeting of the American Chemical Society, Washington, D.C.; American Chemical Society: Washington, DC 1990; PMSE 63, 522.

97. Griffiths, P.R.; deHaseth, J.A. Fourier Transform Infrared Spectrometry, John Wiley & Sons: New York, 1986.

98. Fraser, R.D.B. J. Chem. Phys. **1953**, 21, 1511.

99. Fraser, R.D.B. J. Chem. Phys. **1958**, 28, 1113.

100. Read, B.E.; Stein, R.S. Macromolecules **1968**, 1, 116.

101. Stein, R.S.; Norris, F.H. J. Polym. Sci. **1956**, 22, 381.

102. Ishihara, H.; Kimura, I.; Saito, K.; Ono, H. Rep. Prog. Polym. Phys. Japan **1970**, 13, 409.

103. Seymour, R.W.; Estes, G.M.; Cooper, S.L. Macromolecules **1970**, 3, 579.

104. Seymour, R.W.; Allegrezza, A.E. Jr.; Cooper, S.L. Macromolecules **1973**, 6, 896.

105. Tanaka, T.; Yokoyama, T.; Yamaguchi, Y. J. Polym. Sci., Part A-1 **1968**, 6, 2137.

106. Trifan, D.S.; Terenzi, J.F. J. Polym. Sci. **1958**, 28, 443.

107. Laptij, S.V.; Lipatov, Y.S.; Kercha, Y.Y.; Kosenko, L.A.; Vatulev, V.N.; Gaiduk, R.L. Polymer **1982**, 23, 1917.

108. Wong, R.P. MS Thesis, University of Utah, 1986.

109. Young, P.H. Spectroscopy **1988**, 3, 24.

110. 3200 Data Station User's Manual 091-0260E, Bio-Rad Laboratories, Digilab Division, 1989.

111. The Infrared Spectra of Complex Molecules 3rd. ed.; Bellamy, L.J., Ed.; Chapman and Hall: London, 1975; Vol.1.

112. Engineering Mathematics Handbook 2nd. ed.; Tuma, J.J., Ed.; McGraw-Hill: New York, 1979.

113. Taber's Cyclopedic Medical Dictionary; Thomas, C.L. , Ed; F.A. Davis: Philadelphia, PA, 1981, p. 223.

114. Rice, J.R. J. Appl. Mech. **1968**, 35, 379.

115. Andrews, E.H. Abstract of Papers, 196th National Meeting of the American Chemical Society, Los Angeles, CA; American Chemical Society: Washington, DC 1988; POLY 29.

116. Griffith, A.A. Phil. Trans. Roy. Soc. London A **1921**, 221, 163.

117. Griffith, A.A. Proc. 1st Int. Congress. Appl. Mech. **1924**, 55.

118. Koenig, J.L. Chemical Microstructure of Polymer Chains; Wiley: New York, 1980.

119. Hammond, P.T.; Nallicheri, R.A.; Rubner, M.F. Abstracts of Papers, 33rd IUPAC International Symposium on Macromolecules, Montreal, Canada 1990; Session 2.2.6.

120. Moreland, J.C.; Wilkes, G.L. Abstracts of Papers, Southeastern Graduate Polymer Conference, Atlanta, GA 1989; 2, abstract 45.

121. Andrews, E.H.; Kinloch, A.J. Proc. Roy. Soc. Lond. A. **1973**, 332, 385.

122. Andrews, E.H.; Kinloch, A.J. Proc. Roy. Soc. Lond. A. **1973**, 332, 401.

123. Gent, A.N.; Kinloch, A.J. J. Polym. Sci. A 2 **1971**, 9, 659.

124. Andrews, E.H. J. Mat. Sci. **1974**, 9, 887.

APPENDICES

APPENDIX A. SOFTWARE MACROS DEVELOPED FOR THE DIGILAB 3240-SPC MICROCOMPUTER

The source code for each macro may be examined by typing:

```
% cat macroname <ret>
```

in the IR2 directory. Each macro may be executed by typing it's name at the % sign followed by <ret>.

amicro	Steps user through the operation of the UMA-300 microscope attachment.
dich	Steps user through collection of infrared dichroism spectra in the main compartment.
lock	Restricts file access to the file owner.
main	Sets SETUP parameters to standard operation of main compartment, then executes the SETUP program.
microdich	Steps user through collection of infrared dichroism spectra from the UMA-300 microscope attachment.
microscope	Sets SETUP parameters to standard operation of the UMA-300 microscope attachment, then executes the SETUP program.
timed	Steps the user through the collection of spectra as a function of time.
windo	Creates a second window to accept IDRIS commands.

APPENDIX B. SOURCE CODE OF PASCAL PROGRAMS FOR TENSILE TESTING

The following are the source codes of three programs written for the tensile testing hardware. The code was compiled by a Borland Turbo Pascal 5.5 compiler using software units from Borland Turbo Pascal Graphix Toolbox 4.0 and Data Translation ATLAB device drivers.

CONTROL.PAS is a program which communicates with the motor controller through a serial communications port (COM1:) in the Dell System 200. Instructions are sent and responses are received using string variables. The program can be used to set motor speed (i.e. strain rate), step ramping, reposition the clamps, reset step values, read step positions (to calculate strain), and scale steps into useful units (i.e. centimeters or inches). The program can also be used to set input values to non-volatile random access memory (NVRAM). The values stored in NVRAM are retained when the controller is turned off.

```
     CONTROL.PAS {Compiler Directives}
{$R+}     {Range checking on}
{$B+}     {Boolean complete evaluation on}
{$S+}     {Stack checking on}
{$I+}     {I/O checking on}
{$N+}     {Numeric coprocessor present}

program control; {Program to pass ASCII characters to
COM1:}

Uses Dos,Crt,Graph;

var
```

```
   MCU2Instruction,answer :  string;  {Command strings
for actuators}
   FilVar,FilVar1,MCU2: Text;
   XCon,YCon,XDell,YDell : byte;

procedure DellWindow;  {Set up a window for input}
begin
     XCon:=WhereX;
     YCon:=YDell;
     Window(1,4,35,25);
     GotoXY(XDell,YDell);
     TextBackground(Blue);
end;

procedure MCU2Window;  {Set up a window for responses from
the motor controller}
begin
     XDell:=WhereX;
     YDell:=WhereY;
     Window(46,4,80,25);
     GotoXY(XCon,YCon);
     TextBackground(Red);
end;

procedure SetupWindows;
begin {SetupWindows}
     TextBackground(Black);
     TextColor(White);
     ClrScr;
     Writeln('                        Serial Communications
through COM1:');Writeln;
     Write(' Dell System 200
MCU-2 Controller Response');
     GotoXY(1,1);
     MCU2Window;
     ClrScr;
     DellWindow;
     ClrScr;
end;

procedure TalkToController; {Use serial communications
port to exchange information}
var
   finished : Boolean;

  procedure SetupController;
  begin
      Assign(MCU2,'COM1');
  end;{SetupController}

begin {TalkToController}
     SetupController;
```

```
     finished:=False;
     Repeat
          DellWindow; Write('Instruction:  ');
Readln(MCU2Instruction);
          Writeln;
          If (Pos('q',MCU2Instruction)=1) or
             (Pos('Q',MCU2Instruction)=1) then
finished:=True;  {When finished, the user types q}
          If not finished then
          begin
               Rewrite(MCU2);
               Write(MCU2,MCU2Instruction,#13);
               Close(MCU2);
               If (Pos('1',MCU2Instruction)=2) or
                  (Pos('2',MCU2Instruction)=2) then
               begin
                    Reset(MCU2);
                    Read(MCU2,answer);
                    Close(MCU2);
               end
               else if Copy(MCU2Instruction,1,2)='**'
then
                   answer:='**'
               else
                   answer:='Error: command ignored';
               MCU2Window;
               Writeln('MCU-2:  ',answer,^G);
               Writeln;
          end;
     Until finished;
{Stop all motor motion to initiate in auto mode}
     Rewrite(MCU2);
     Writeln(MCU2,'**Q',#13);
     Close(MCU2);
end;

begin {Main Program}
      SetupWindows;
      TalkToController;
      Window(1,1,80,25);
      TextBackground(Black);
      TextColor(LightGray);
      ClrScr;
end.→
```

MYATLEX.PAS is a program which continuously converts the analog load cell signal to a digital value for analysis by the Dell System 200. The average of every 100

scans is displayed with the time. This value is updated roughly every 0.2 seconds. This program was used to calibrate and zero the load cell.

```
     MYATLEX.PAS
{ ATLAB single-value A/D example program in PASCAL }

PROGRAM ATLEX01 ( INPUT, OUTPUT );

uses Dos,Crt,Graph,ATLDEFS,ATLERRS,ATLEXSUB;

const
     trials=100;
VAR
     ad_channels : CHANNEL_LIST;          { channel scan
list }
     ad_gains : GAIN_LIST;                { gains for
channels }
     configuration : AL_CONFIGURATION;    { unit
configuration data }
     max_channel,status : INTEGER;
     data_value,Hour,Minute,Second,Sec100 : WORD;
        data_string,force_string,time_string : STRING;
        force,average : REAL;
        time : EXTENDED;
        count,sum,bad_values : LongInt;

procedure SetupGraphics;
var
   GraphDriver,GraphMode  :  Integer;
begin
     GraphDriver:=Detect;
     InitGraph(GraphDriver,GraphMode,'C:\tp');
     If GraphResult <> grOK then Halt(1);
     SetTextStyle(TriplexFont,HorizDir,5);
     SetColor(Red);
     SetBkColor(White);
end; {SetupGraphics}

BEGIN

        SetupGraphics;

{ Initialize the ATLAB subroutines. }

     status := al_initialize ;

{ Select board 1, the first unit. }
```

```
     status := al_select_board ( 1 );

{ Perform a reset on the device. }

     status := al_reset ;

{ Set channel and gain.}

                ad_channels[0]:=0;
          ad_gains[0] := 8;

{ Read the channel and display it. }

           OutTextXY(0,20,'Load Cell & A/D Status');
           OutTextXY(0,100,'Gain set at 8');
           OutTextXY(0,200,'time:
secs.');
           OutTextXY(0,250,'Data value:
(max=2048)');
           OutTextXY(0,300,'Value read was
pounds');
           OutTextXY(0,400,'Press any key to terminate:');
           SetTime(0,0,0,0);
           Repeat
                GetTime(Hour,Minute,Second,Sec100);
                sum:=0; bad_values:=0;
                For count:=1 to trials do
                begin
                     status := al_adc_value (
ad_channels[0], ad_gains[0],
               data_value );
                     data_value:=4096-data_value;
                     If data_value > 2049 then
                     begin
                          data_value:=0;
                          Inc(bad_values);
                     end;
                sum:=sum+data_value;
                end;
                If trials <= bad_values then
bad_values:=0;
                average:=sum/(trials-bad_values);
                force:=12.5*sum/(trials-bad_values)/2048;

time:=Hour*3600.0+Minute*60.0+Second+Sec100/100.0;
                Str(time:10:2,time_string);
                Str(Round(average):4,data_string);
                Str(force:5:2,force_string);
                OutTextXY(320,200,time_string);
                OutTextXY(250,250,data_string);
          OutTextXY(350,300,force_string);
                SetColor(GetBkColor);
```

```
                OutTextXY(320,200,time_string);
                OutTextXY(250,250,data_string);
                OutTextXY(350,300,force_string);
                SetColor(Red);
            Until Keypressed;

{ Terminate ATLAB operations. }

     status := al_terminate ;

{ end ATLEX01.PAS }

        CloseGraph;

END.→
```

STRETCH3.PAS is a program which controls the tensile experiment. The user is prompted for sample identification, dimensions, and testing conditions. The conditions are stored in a header file. By setting the appropriate test conditions, the user may conduct a standard tensile experiment or a stress relaxation experiment. After the data is collected, it is stored on disk in a data file and displayed graphically on the computer screen.

STRETCH 3.PAS

```
{$R+}     {Range checking on}
{$B+}     {Boolean complete evaluation on}
{$S+}     {Stack checking on}
{$I+}     {I/O checking on}
{$N+}     {Numeric coprocessor}
{$M 32768,0,655360}  {Set memory requirements}

program Stretch; {Program to control tensile experiments}
        {by R.P. Wong}

Uses Dos, Crt, ATLDEFS, ATLERRS, ATLEXSUB, GDriver,
GKernel, GWindow, GShell;

const
```

```
     MaxPoints = 400;  {Number of stress-strain data
points}
     MaxLoad = 200.169945;{Newtons = 45 lb (for a 50 lb
load cell)}
     MaxElongation = 0.30480; {meter corresponds to 12
inches}
     StepsPerMeter = 1.574803150e5;
type
    dattype = array[0..MaxPoints] of Real;   {Define the
arrays for data}

var
   stress,strain,time  :  dattype;     {Declare
stress,strain & time arrays}
   area,lo,width,thickness,force,elongation,
   StrainRate,MaxStrain,MaxStress,PreCrackLength,DTime :
Double;
   Smax : Real;
   i,j,MaxNumberOfPoints  :  Integer;    {Define data
point counting integers}
   done,relaxing  :  Boolean;     {Declare flags for
experimental conditions}
   SampleName,HeadName,FileName : string[14];
                                   {Names of data files
for I/O}
   FilVar,FilVar1,MCU2: Text;
     configuration : AL_CONFIGURATION;  { unit
configuration data }
     data_value : WORD;
     status : INTEGER;
     ad_channels : CHANNEL_LIST;        { channel scan
list }
     ad_gains : GAIN_LIST;              { gains for
channels }

procedure beep;  {Sound an obnoxious tone to signal input
errors}
begin
     TextColor(Yellow+Blink); Write(' *
');TextColor(White);
     Sound (300); Delay (100);
     Sound (440); Delay (100);
     NoSound;
end;

procedure SetColors;  {Set screen colors}
begin
     TextColor(White);
     TextBackground(Blue);
     ClrScr;
end;
```

```
procedure GetSampleData; {Input sample information}
begin
     Writeln('Get Sample Data'); Writeln;
     Write ('Input sample name (no extensions): ');
     Readln (SampleName);
            HeadName := 'c:'+SampleName+'h.dat';
            FileName := 'c:'+SampleName+'d.dat';
     Write ('Input the initial length (in cm): ');
     Readln (lo);
            lo:=lo/100.0;  {convert lo units : cm to
meters}
     Write ('Input the initial width (in cm): ');
     Readln (width);
            width:=width/100.0;  {convert lo units : cm to
meters}
     Write ('Input the initial film thickness (in mils or
1/1000"): ');
     Readln (thickness);
            thickness:=thickness*2.54e-5;
                {convert thickness units : mils to meters}
     Write ('Input the initial crack length (in cm): ');
     Readln (PreCrackLength);
            PreCrackLength:=PreCrackLength/100.0;
                 {convert PreCrackLength units : cm to
meters}
            While PreCrackLength >= width do
            begin
                 beep;
                 Write('Re-enter initial crack length (in
cm): ');
                 Readln(PreCrackLength);
                 PreCrackLength:=PreCrackLength/100.0;
            end;
     area:=width*thickness;  {area in square meters}
end;

procedure PrintInput;  {Output the user defined
experimental conditions}
begin
     Writeln;
     Writeln(
     'Initial length lo = ',lo:7:5,' meters');
     Writeln(
     'Initial width = ',width:7:5,' meters');
     Writeln(
     'Initial thickness = ',thickness:9,' meters');
     Writeln(
     'Initial crack length = ',PreCrackLength:7:5,'
meters');
     Writeln(
     'Strain rate = ',StrainRate:6:3,' per second');
     Writeln;
```

```
     Write(
     'Type <ret> to continue: ');
     Readln;
end;

procedure SaveConditions; {Write initial conditions to a
file}
begin
     Assign(FilVar1,HeadName);
     Rewrite(FilVar1);
     Writeln(FilVar1,
     'Initial length lo = ',lo:7:5,' meters');
     Writeln(FilVar1,
     'Initial width = ',width:7:5,' meters');
     Writeln(FilVar1,
     'Initial thickness = ',thickness:9,' meters');
     Writeln(FilVar1,
     'Initial crack length = ',PreCrackLength:7:5,'
meters');
     Writeln(FilVar1,
     'Strain rate = ',StrainRate:6:3,' % per second');
     Close(FilVar1);
end;

procedure SetUpController;
          {For details of documentation, consult the MCU-2
Manual}
var
   BaseRate : String[15];
begin
     Assign(MCU2,'COM1');
     Rewrite(MCU2);
     {Setup strain rate for actuators}
     Str(Round(StrainRate*lo*StepsPerMeter/2.0),BaseRate);
     Write(MCU2,'**B=',BaseRate,#13);
     Delay(50);
end;

procedure SetUpLoadCell;
begin
{ Initialize the ATLAB subroutines. }
     status := al_initialize ;
{ Select board 1, the first unit. }
     status := al_select_board ( 1 );
{ Perform a reset on the device. }
     status := al_reset ;
{ Get the unit configuration for the number of A/D
channels. }
     status := al_get_configuration ( configuration );
        ad_channels[0]:=0;
     ad_gains[0] := 8;
```

```
                    {Scale A/D output to read in lbs
(recalc later in N)}
end;

procedure SetupExperiment;  {Input conditions of stress-
strain test}
begin
     GetSampleData;
     Writeln;Writeln ('Test Conditions');Writeln;
     StrainRate:=0.0;
Repeat
      Write ('Input the initial strain rate (in % per
second): ');
      Readln (StrainRate);
      StrainRate:=Abs(StrainRate/100.0);
                           {Convert %/sec. to a
fraction/sec.}
            If StrainRate=0.0 then
            begin
                 beep;
                 Write('Only non-zero values accepted for
strain rate.');
                 Writeln('  Please try again.');
            end;
Until StrainRate <> 0.0;
      Write ('Input the maximum strain (in %): ');
      Readln (MaxStrain);
            MaxStrain:=Abs(MaxStrain/100.0);  {Convert
from % to a fraction}
            If MaxStrain > (MaxElongation-lo)/lo then
            begin
                 beep;
            Write('Strain value exceeds actuator limit:
default value = ');
                 MaxStrain:=(MaxElongation-lo)/lo;
                 Writeln(MaxStrain:5:2,' x 100%');
            end;
     Write ('Input the maximum stress (in MPa): ');
     Readln (MaxStress);
            MaxStress:=Abs(MaxStress*1e6); {Convert
MaxStress units : MPa to Pa}
            If MaxStress > MaxLoad/area then
            begin
                 beep;
            Write('Stress value exceeds load cell limit:
default value = ');
                 MaxStress:=MaxLoad/area;
                 Writeln(MaxStress:10,' Pa');
            end;
     Write ('Input the time between data points (in secs):
');
     Readln (DTime);
```

```
     DTime:=Abs(DTime);
     PrintInput;
     SaveConditions;
     SetUpController;
     SetUpLoadCell;
end;

procedure SaveData;  {Save collected stress-strain-time
data to disk}
begin
     Writeln('Saving data...');
     Assign(FilVar,FileName);
     Rewrite(FilVar);
     For i:=0 to MaxNumberOfPoints do
     begin
          stress[i]:=stress[i]/1.0e6;   {Convert to MPa}
          Writeln(FilVar, time[i],'  ',strain[i],'
',stress[i]);
     end;
     Close(FilVar);
     Write('Number of points saved =
',MaxNumberOfPoints+1);
end;

procedure TestEnd;  {Test conditions to see if experiment
is completed}

procedure StopMotors;
begin
     beep;  {If any of these conditions are met, sound the
alarm}
     Rewrite(MCU2); Write(MCU2,'**Q',#13);  {Stop all
motor motion}
     Delay(50);
     Rewrite(MCU2); Write(MCU2,'**G-0',#13);
end;

begin {TestEnd}
     If KeyPressed then  {Pressing any key terminates the
experiment}
     begin
          Writeln('Experiment terminated by user.');
          StopMotors;
          done:=True;
     end;
     If stress[i] <= 0.20*Smax then
     begin
          Writeln('Stress <= to 20% of maximum stress.');
          StopMotors;
          done:=True;
     end;
```

```
     If i >= MaxPoints then  {Number of data points
cannot exceed array size}
     begin
          Writeln('Maximum number of ',MaxPoints,' data
points collected.');
          StopMotors;
          done:=True;
     end;
end; {TestEnd}

procedure StretchFilm;  {Stretch the sample and call
relative procedures}
var
   l1,l,lamda,position,OldTime  :  Double;
          {Define the values of length of actuator
motion}
   s1,code : Integer; {Actuator indices}
   Response : String[10];
   Hour,Minute,Second,Sec100 : word;

procedure WaitDTime;
begin
     Repeat
          GetTime(Hour,Minute,Second,Sec100);

time[i]:=Hour*3600.0+Minute*60.0+Second+Sec100/100.0;
     Until Abs(time[i]-OldTime) >= DTime;
end;

procedure CheckPosition;
begin
     Write(MCU2,'01P',#13);
     Reset(MCU2);
     Read(MCU2,Response);  Delete(Response,1,4);
     Val(Response,s1,code);
     l1:=(lo/2.0)+Abs(s1)/StepsPerMeter;
     l:=2.0*l1;    {Double the elongation (for 2
actuators)}
end;

procedure ReadLoad;
const
     trials = 100;
var
   count,sum,bad_values : LongInt;
begin
     sum:=0; bad_values:=0;
     For count:=1 to trials do
     begin
          { Read the channel }
          status := al_adc_value ( ad_channels[0],
ad_gains[0],
```

```
                data_value );
            data_value:=4096-data_value;
            If data_value > 2048 then
            begin
                data_value:=0;
                Inc(bad_values);
            end;
            sum:=sum+data_value;
        end;
        If trials <= bad_values then bad_values:=0;
        force:=2.714978638e-2*sum/(trials-bad_values);
           {or 4.448221 (N/lb)*12.5 (lb-full scale with gain
at 8)
             *data_value/2048.0} {Read load cell in
Newtons}
        stress[i]:=force/area;  {in Pa}
end;

begin
        ClrScr; Writeln('Collecting data...please watch the
experiment.');
        Writeln('Press any key to stop experiment.');
{Set preliminary values of defined variables}
        i:=0; done:=False; relaxing:=False;
        time[0]:=0.0; stress[0]:=0.0;
strain[0]:=0.0;Smax:=0.0;
        Hour:=0; Minute:=0; Second:=0; Sec100:=0;
                {Store max values of stress time for
relaxation model}
        Rewrite(MCU2);
        Write(MCU2,'**L-',#13);
        SetTime(Hour,Minute,Second,Sec100);
        Close(MCU2);
        While not done do
        begin
            i:=i+1;                    {Cycle subscript of
data points}
            If not relaxing then   {Increment displacement
&/or strain}
            begin
                Rewrite(MCU2);
                WaitDTime;
                CheckPosition;
                ReadLoad;
                If stress[i]> Smax then Smax:=stress[i];
            end;
            strain[i]:=(l-lo)/lo;
            If relaxing then
            begin
                WaitDTime;
                ReadLoad;
            end;
```

```
          If (strain[i] > MaxStrain-(StrainRate*DTime))
              or (force >= MaxLoad) then
              begin
                   relaxing:=True;
                   Rewrite(MCU2);
                   Write(MCU2,'**Q',#13);
              end;
          Writeln(time[i]:8:2,' secs.  ',
                    100.0*strain[i]:8:2,'% strain    ',
                    stress[i]/1e6:8:4,' MPa     ',
                    force/4.448221:8:4,' lbs');
          MaxNumberOfPoints:=i;
          OldTime:=time[i];
          TestEnd;   {Call the TestEnd procedure to see if
experiment if done}
     end;
     Close(MCU2);
     status := al_terminate ;  { Terminate ATLAB
operations. }
     SaveData;  {If experiment is done save all the data}
end;

procedure OnePolygon;
procedure PolygonPlot;
var
  A : PlotArray;

procedure GenerateFunction;
{ Generate a stress-strain polygon }
begin
  for i := 1 to MaxNumberOfPoints do
  begin
    A[i, 1] := strain[i-1];
    A[i, 2] := stress[i-1];
  end;
end; { GenerateFunction }

begin
  ClearScreen;
  GenerateFunction;       { Generate the polygon }
  DefineWindow(1, 0, 0, XMaxGlb, YMaxGlb);
  DefineHeader(1, 'SAMPLE: '+SampleName);    { Set up the
screen }
  DefineWorld(1, 0.0, 0.0, Round(strain[MaxNumberOfPoints]

+0.2*strain[MaxNumberOfPoints]),
                          Round(0.5+Smax/1e6));
  SelectWorld(1);
  SelectWindow(1);
  SetForegroundColor(Blue);
  SetBackgroundColor(White);
  SetHeaderOn;
```

```
  DrawBorder;
  DrawAxis(8, -8, 0, 0, 0, 0, 0, 0, True);  { Draw the
axes }
  DrawPolygon(A, 1, MaxNumberOfPoints, 3, 2, 0);  { Draw
the polygon }
  DrawText(45,15,1,'Stress (MPa)');
  DrawText(550,330,1,'Strain');
end; { PolygonPlot }

begin
  InitGraphic;                          { Initialize the
graphics system }
  PolygonPlot;                          { Do the plot }
  Repeat until KeyPressed;              { Wait until a key
is pressed }
  LeaveGraphic;                         { Leave the
graphics system }
end; { OnePolygon }

begin          {Main Program}
     SetColors;
     Writeln('Program to control tensile
experiments');Writeln;
     SetupExperiment;
     StretchFilm;
     OnePolygon;
end.
```

APPENDIX C. MECHANICAL DRAWINGS USED TO MACHINE VERTICAL POSITIONING AND CLAMPS FOR STEP MOTOR LINEAR ACTUATORS

The following diagrams and drawings were used to design the tensile stretching device. The most important design criteria was that the film samples had to be focused under the infrared microscope with a minimum of modification to the microscope.

Infrared Microscope Dimensions

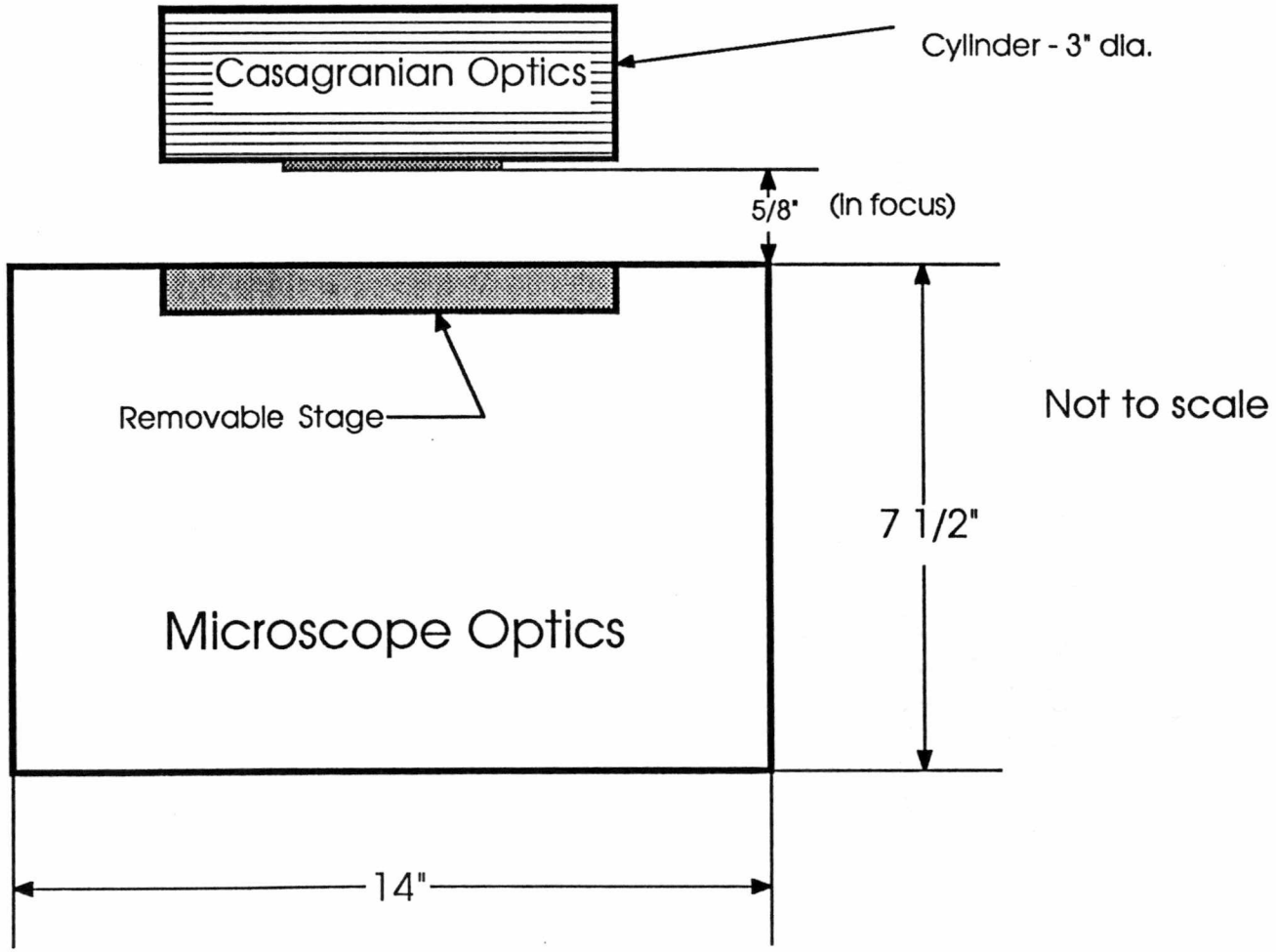

Height Details

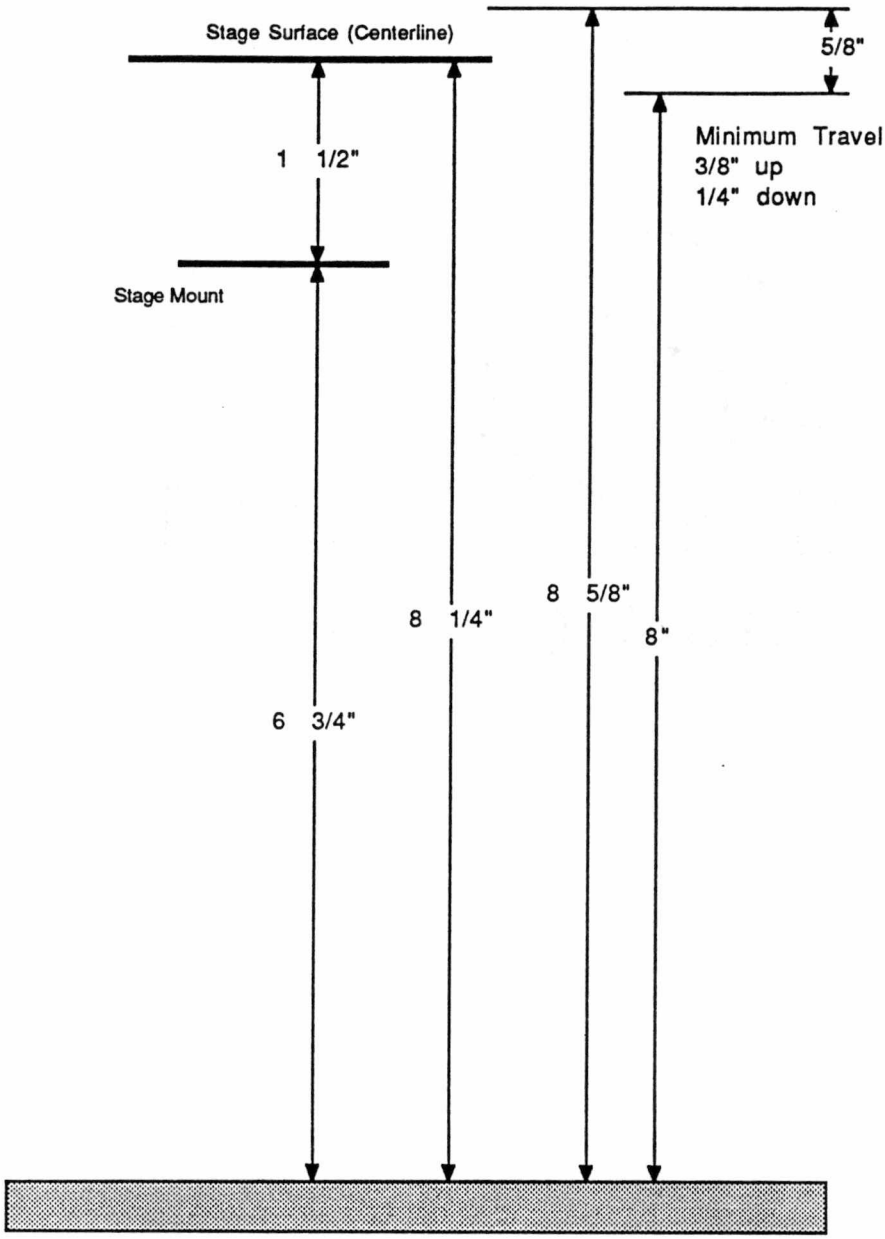

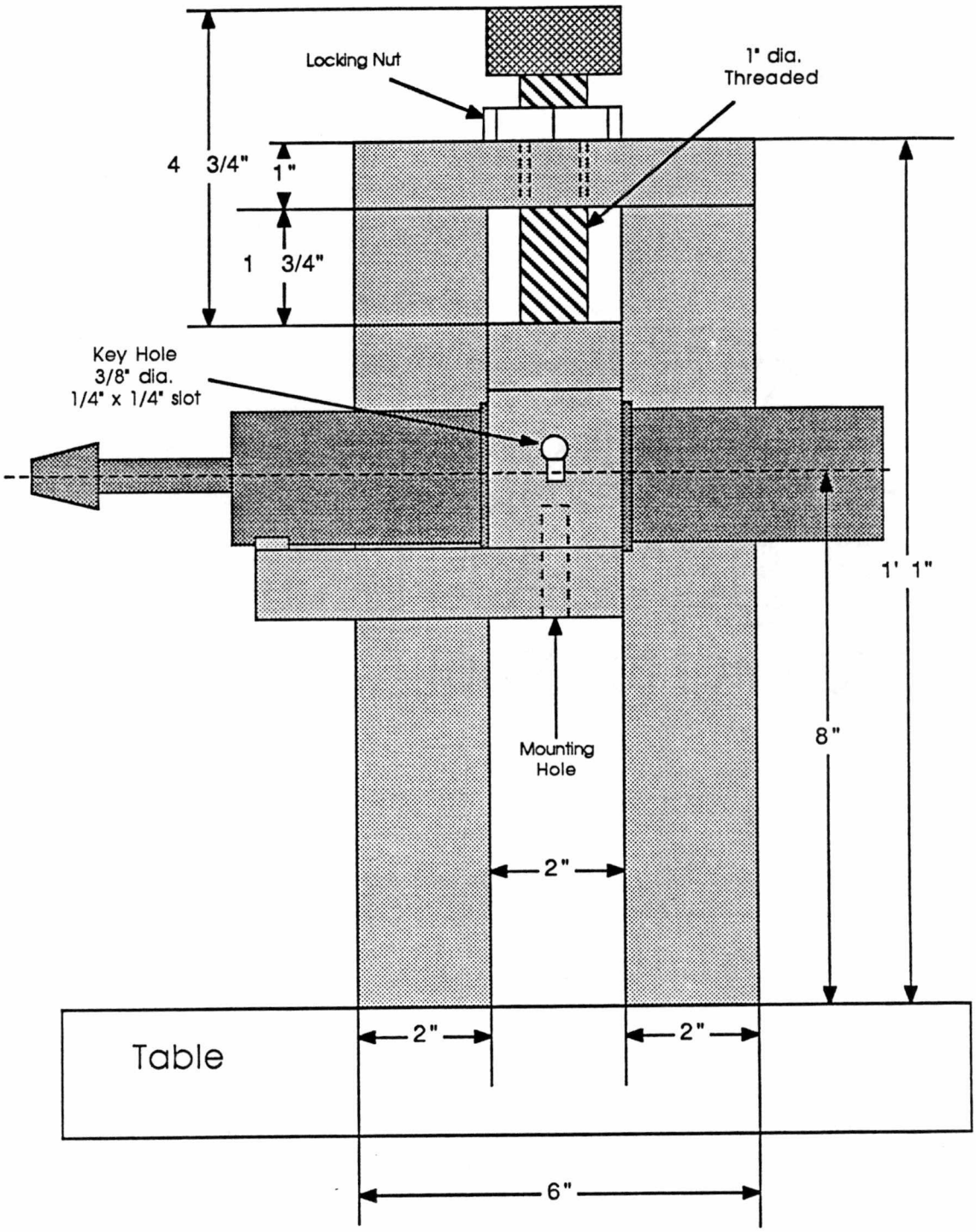
Locking Nut
1" dia.
Threaded
4 3/4"
1"
1 3/4"
Key Hole
3/8" dia.
1/4" x 1/4" slot
1' 1"
8"
Mounting
Hole
2"
2"
2"
Table
6"

Clamp for IR Microscope Film Stretcher

2 req'd

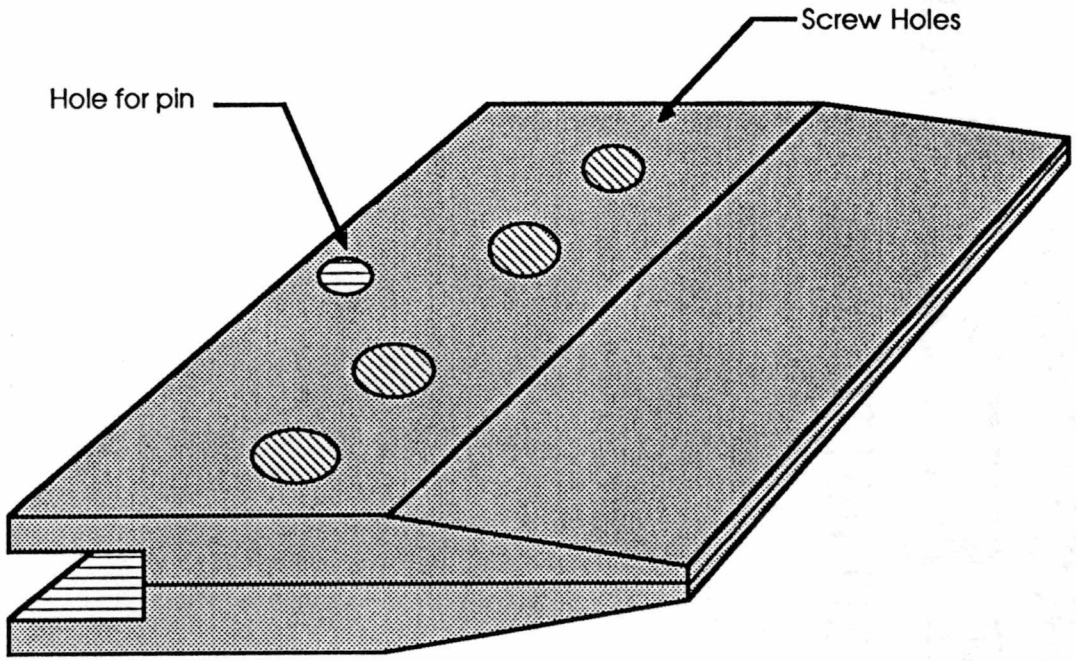

Clamps for IR Microscope Film Stretcher - Top View

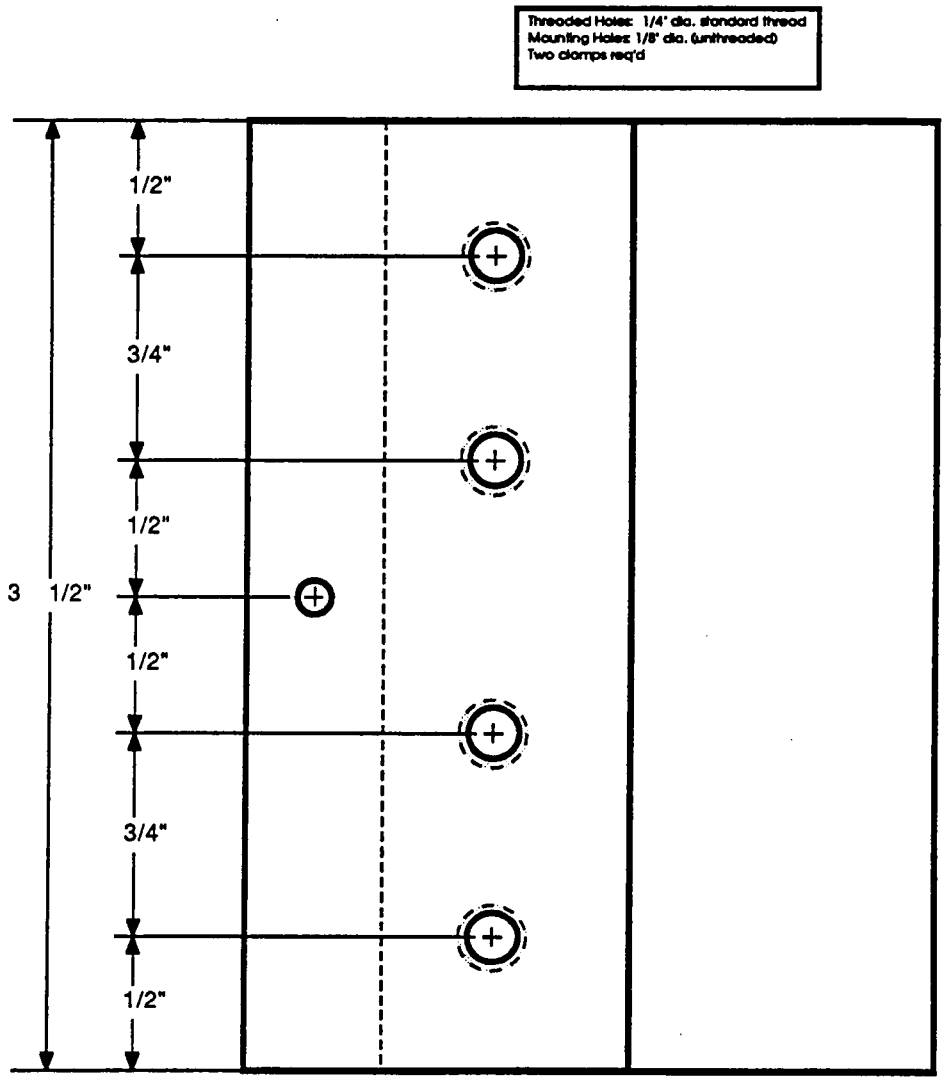

Drawn by R.P.Wong

Drawn by R.P.Wong

Clamps for IR Microscope Film Stretcher - Front View

Threaded Holes: 1/4" dia. standard thread
Mounting Holes: 1/8" dia. (unthreaded)
Two clamps req'd

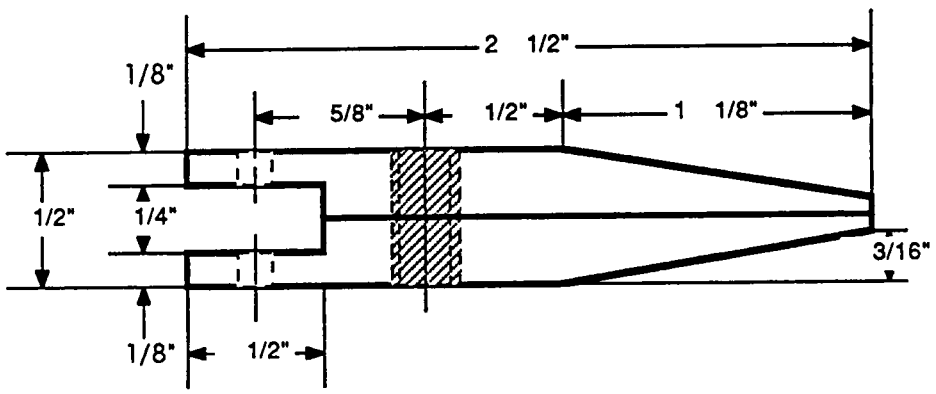

VITA

Russell Paul Wong was born in Brooklyn, New York on February 8, 1961. He attended Brooklyn Technical High School where he specialized in the chemical program. Upon graduation from Brooklyn Tech in June of 1979, he attended The Cooper Union for the Advancement of Science and Art in New York City where he served as president of the student chapter of the American Chemical Society and member of the admissions committee to the School of Engineering. He received his Bachelor of Engineering degree in chemical engineering from Cooper Union in May of 1983. He began his graduate education the following September at the University of Utah with Dr. Donald J. Lyman and Dr. Roberto S. Benson in the field of biomedical polyurethanes. He received his Master of Science in bioengineering there in April of 1986. He then joined Dr. Benson at the University of Tennessee-Knoxville in the Department of Materials Science and Engineering for further studies of biomedical polyurethanes. He received his Doctor of Philosophy degree in Polymer Engineering in May of 1991. Dr. Wong is currently a Senior Research Engineer at Monsanto Chemical Company in Springfield, Massachusetts.